

## PDF hosted at the Radboud Repository of the Radboud University Nijmegen

The following full text is a publisher's version.

For additional information about this publication click this link.

<http://hdl.handle.net/2066/74874>

Please be advised that this information was generated on 2017-12-06 and may be subject to change.

**Distributed Read-Out Imaging Device  
array for astronomical observations in  
UV/VIS**

*Richard A. Hijmering  
([rhijmeri@rssd.esa.int](mailto:rhijmeri@rssd.esa.int))*

This thesis has been printed on environmental friendly BioTop paper by

Ridderprint, Ridderkerk (<http://www.ridderprint.nl>)

*ISBN: 978-90-5335-231-1*

*Cover: Tools of the trade*

Depicts the tools required for the research. The pen and paper used for the theoretical derivations and notes, the PC for the simulations and writings, calculator for the quick calculations, cryogenic set-up for the measurements and coffee for the inspiration.

# **Distributed Read-Out Imaging Device array for astronomical observations in UV/VIS**

Een wetenschappelijke proeve op het gebied van de  
Natuurwetenschappen, Wiskunde en Informatica

PROEFSCHRIFT

ter verkrijging van de graad van doctor  
aan de Radboud Universiteit Nijmegen  
op gezag van de rector magnificus prof. mr. S.C.J.J. Kortmann,  
volgens besluit van het College van Decanen  
in het openbaar te verdedigen op maandag 21 december 2009  
om 13:30 precies

door

Richard Arnold Hijmering

geboren op 7 september 1978  
te Boxmeer



**Promotor:** Prof. dr. P.J. Groot

**Copromotor:** Dr. P. Verhoeve  
ESTEC/ESA, Noordwijk

Dr. D.D.E. Martin  
ESTEC/ESA, Noordwijk

**Manuscriptcommissie:** Prof. dr. T.H.M. Rasing

Prof. dr. T.M. Klapwijk  
Delft University

Dr. A.A. Golubov  
University of Twente

Dr. P.A.J. de Korte  
SRON, Utrecht

Dr. J.H.J de Bruijne  
ESTEC/ESA, Noordwijk

---

# Contents

---

1.	Introduction .....	1
1.1	Low Temperature Detectors .....	3
1.2	Superconducting Tunnel Junctions.....	3
1.3	Distributed Read Out Imaging Devices .....	6
1.4	S-Cam .....	7
1.5	Aim and outline of the thesis.....	8
2.	Theoretical introduction .....	11
2.1	Superconductivity .....	12
2.2	Quasiparticle excitations and density of states.....	15
2.3	Photon absorption .....	17
2.4	Current-voltage characteristics.....	19
2.4.1	Josephson current.....	19
2.4.2	Quasiparticle Tunneling.....	21
2.5	Proximity effect.....	24
3.	Experimental set-up .....	27
3.1	Fabrication .....	28
3.2	Cryostats .....	30
3.2.1	Heliox system ( $^3\text{He}$ cooler).....	31
3.2.2	Bradford cryostats with $^4\text{He}/^3\text{He}$ sorption coolers .....	32
3.2.3	Adiabatic Demagnetisation Refrigerator (ADR).....	34
3.3	Read out electronics .....	35
3.3.1	IV curve tracer.....	36
3.3.2	DROID photo-pulse analyser.....	37
3.3.3	Pulse sampling.....	38
3.3.4	S-Cam 3 120-channel read out electronics.....	40
3.4	Illumination.....	41
3.4.1	Double grating monochromator.....	41
3.4.2	S-Cam optical unit .....	42
4.	Dynamics of nonequilibrium quasiparticles in narrow-gap superconducting tunnel junctions.....	43
4.1	Introduction .....	44
4.2	Kinetic description of nonequilibrium quasiparticles and phonons in a superconducting tunnel junction.....	45
4.3	Time-dependent spectral balance equations .....	47
4.4	Experiment and modelling.....	51
4.5	Analysis and discussion of results .....	52
4.5.1	Bias voltage dependence of dc current.....	52
4.5.2	Responsivity and rise time: Bias voltage dependence .....	54
4.5.3	Responsivity and rise time: Photon energy dependence.....	55
4.5.4	Responsivity and rise time: Temperature dependence .....	56
4.6	Summary.....	58
5.	Efficiency of quasiparticle creation in proximised superconducting photon detectors .....	59
5.1	Introduction .....	60
5.2	Quasiparticle relaxation in the final stage of the downconversion process..	61

5.3	Phonon emission rate in BCS and proximised structures.....	63
5.4	Quasiparticle creation efficiency .....	65
5.5	Experimental investigation of the quasiparticle yield in the BCS absorber and proximised STJ of a DROID.....	67
	Discussion.....	70
5.6	Conclusion .....	71
6.	Position dependent spatial and spectral resolution measurement of distributed read-out superconducting imaging detectors.....	73
6.1	Introduction .....	74
6.2	Modelling of DROID response.....	75
6.3	Experimental details.....	78
6.4	Results.....	81
6.5	Discussion.....	88
6.6	Conclusion .....	89
7.	Experimental and theoretical response of Distributed Read-Out Imaging Devices with imperfect confinement .....	91
7.1	Introduction .....	92
7.2	Modelling of DROID response.....	93
7.3	Experimental set-up and data reduction .....	99
7.4	Testing of the model with the experimentally obtained results .....	101
7.5	Discussion.....	106
7.6	Conclusion .....	107
8.	First results of a cryogenic optical photon counting imaging spectrometer with use of a DROID array .....	109
8.1	Introduction .....	110
8.2	Operation of the DROID array.....	111
8.3	Full array test set-up .....	113
8.4	Data reduction .....	115
8.5	Imaging quality of the DROID array detector .....	117
8.6	Discussion.....	120
8.7	Conclusion .....	121
	References .....	123
	Summary.....	129
	Samenvatting .....	133
	Acknowledgements .....	137
	List of Publications.....	139
	First Author: .....	139
	Second Author: .....	140
	Co-Author:.....	140
	Curriculum Vitae .....	141

# Chapter 1

---

## Introduction

---

*L*ike in all aspects of life there is in astronomy a drive for better observation techniques and instrumentation. Initially observations were conducted using the human eye only, which is actually a very good optical photon detector. In 1608 Hans Lippershey and Zacharias Janssen both developed the telescope independently. On July 26, 1609, Thomas Harriott was the first to use the telescope for astronomic observations of the moon<sup>1</sup>. For long this was credited to Galileo Galilei, who allegedly found a telescope on a market, improved the quality and used it to observe the moon, stars and the moons of Jupiter which he described in his *Siderius Nuncius*, being the first to report the observation. Development of photographic plates in 1837 by Louis Daguerre made it possible to capture objective images of the night sky of which the first was produced by 1840 by John William Draper with a photograph of the Moon. Due to the possible long exposure times and sensitivity to a broader wavelength range, photographic plates can reveal objects that are impossible to observe with the naked eye. Unfortunately photographic plates have very low quantum efficiency (1-2%), a non-linear response to light intensity and they are difficult to analyse.

In the 1960s AT&T Bell Labs were working on the development of the picture phone for which Willard Boyle and George Smith developed memory which could transfer charge along the surface of a semiconductor<sup>2</sup>. It was immediately clear that this charge could be created in the semiconductor itself by absorption of photons using the photoelectric effect which could be used to create electronic images. The Charge Coupled Device, or CCD, was born. When photons are absorbed in silicon a photoelectron is released which is confined within the pixel by potential barriers. At the end of the integration the potential barriers are alternated and the collected charge is shifted towards the output stage where the charge is converted into a voltage which is stored digitally. The CCD is linear in response, has a high quantum efficiency (up to 90%) and is sensitive over a broad wavelength range (infrared to X-rays).

The CCD or photographic plate provide information on position and intensity but has no wavelength discrimination (at UV/VIS wavelengths). Color filters can be used to obtain images in different wavelength bands. When making multiple images using different color filters a measure of spectral information can be obtained.

For accurate spectral information a spectrograph, developed in the early 19<sup>th</sup> century, needs to be used which disperses the light into a spectrum at the cost of the positional information and efficiency. The first spectrographs consisted of a prism to split the light into different wavelengths and on to a photographic plate.

The ideal detector would be photon counting providing temporal, positional, energy and polarisation information on each individual photon. The combination of photon counting and temporal information makes it possible to explore rapid changing systems and simultaneously adding the spectral information provides extra constraints on the geometry and dynamics.

With the current development of cryogenics detectors, explained in 1.1, which can provide temporal, spectral and positional information on photon to photon basis, the ideal detector seems to become reality. With the S-Cam project<sup>3</sup>, handled in 1.4, the European Space Agency is developing a series of prototype photon-counting imaging spectrometers to be used for ground based astronomy in the visible/UV based on superconducting tunnel junctions, explained in 1.2. Three prototypes have successfully been used for observations on the telescope on several campaigns during which several objects have been observed. For instance the accretion flow and location of the hotspot of cataclysmic variables have been mapped using the high temporal resolution and spectral information. Or the period of the optical pulse of pulsars has been determined accurately using the high temporal resolution and photon counting capability.

The next step in the S-Cam project would be to increase the field of view while maintaining the same number of read out wires. This would be achieved using distributed read-out devices which contain an absorber strip, to absorb the incident photon, and a sensor at either end, to measure the produced charge. The development of such devices is the topic of this thesis.

## 1. Introduction

---

### 1.1 Low Temperature Detectors

Apart from the polarisation the ideal detector appears to become possible with the current development in low temperature detectors. The low temperature is needed to reduce the thermal signal or to facilitate the required phase of operation. The properties of these low temperature detectors allow for noise free photon counting with high timing accuracy and energy discrimination. These next generation detectors can be divided into thermal detectors, depending on the change of temperature due to the absorption of photons, and pair breaking detectors, where the absorption of photons break Cooper pairs. Both have short response times and intrinsic energy resolving power.

In the case of thermal detectors the high energy resolving power is due to the much reduced thermal fluctuations at low operating temperatures ( $\sim 100\text{mK}$ ) enabling detection of extremely small temperature changes. Bolometers<sup>4</sup> measure the integrated rise in temperature due to the energy of the absorbed photons within the integration time. Bolometers are successfully being used for ground based applications like: SCUBA II<sup>5</sup> (TES based filled array, submillimeter), South Polar Telescope<sup>6</sup> (horn coupled TES based spiderweb array, large-area millimeter and submillimeter) and LABOCA<sup>7</sup> on APEX (NTD-Ge semiconductors, sensitive at 345GHz with a bandwidth of 60GHz). For space applications they are used as the detectors in SPIRE<sup>8</sup> (horn coupled NTD-Ge based spiderweb array, sensitive in the submillimeter) and on PACS<sup>9</sup> (two bolometer filled arrays of doped Si bolometers sensitive in 60-210 $\mu\text{m}$ ) on the recently launched Herschel satellite. Microcalorimeters also use the change in temperature to detect the absorption of a photon but do this on the individual photon level. The Transition Edge Sensor<sup>10</sup> (TES) is biased in temperature on the transition from superconducting to normal metal where the electrical resistance is greatly dependent on temperature. The small rise in temperature due to the absorption of a single photon will produce a considerable change in resistance which is proportional to the absorbed energy. These detectors are mainly developed for space X-ray applications like the IXO<sup>11</sup> mission which is currently being investigated. However, Stanford university has been developing a ground based instrument based on TES for NIR/UV<sup>12</sup>.

In the case of pair breaking detectors the high energy resolving power is due to the low excitation energy, in the order of a meV, which is 3 orders of magnitude lower compared to semiconductors. Kinetic Inductance Devices<sup>15</sup> (KID) operate in the superconducting phase where the absorption of a single photon will break up Cooper pairs into several thousands of quasiparticles per eV of photon energy. This produces a change in inductance which is measured using the corresponding change in resonance frequency when placed in a resonant circuit. The number of created quasiparticles and thus the change in resonance is proportional with the absorbed energy. Superconducting Tunnel Junctions<sup>16</sup> (STJ) also rely on the creation of quasiparticles due to the absorption of a single photon. However, in this case the signal is produced by quasiparticles tunneling across a tunnel barrier creating a current pulse of which the height is proportional to the absorbed energy. These detectors are being developed for ground based UV-NIR applications by RIKEN<sup>13</sup>, and the European Space Agency<sup>14</sup>.

### 1.2 Superconducting Tunnel Junctions

In 1986 Twerenbold detected 6keV X-rays using a Sn-based STJ<sup>16</sup> which started the development of STJs for photon detection. The first detection of an optical photon was shown by our group in 1996 using a Nb-based STJ<sup>17,14</sup>.

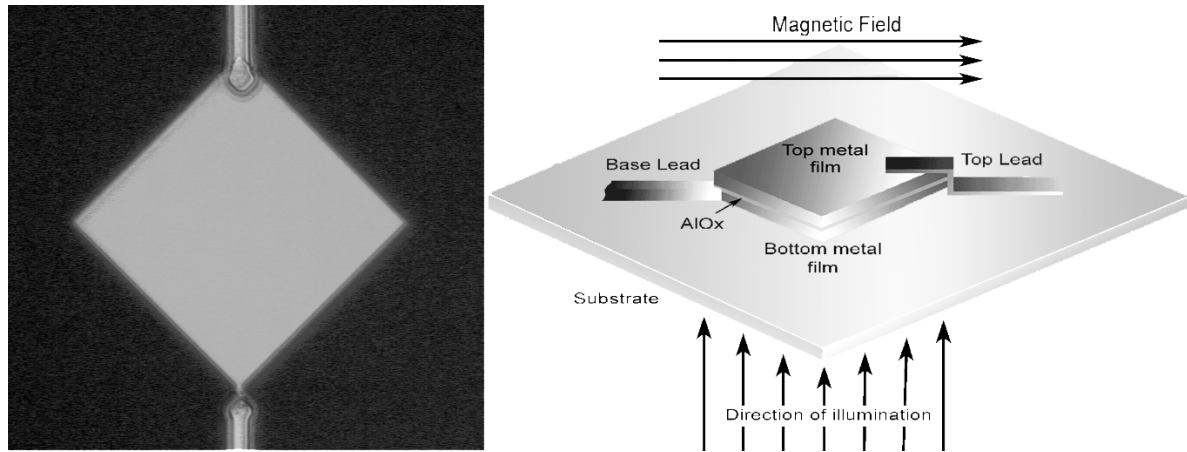


Figure 1-1 Micrograph and a schematic representation of a single Superconducting Tunnel Junction.

An STJ (Figure 1-1) consist of two superconducting layers, with a thickness of  $\sim 100\text{nm}$ , separated by a thin insulating layer,  $\sim 1\text{nm}$  (tunnel barrier). Generally the STJs are a few of tens to a few hundreds of micrometers in size. When the superconducting material is cooled below its critical temperature,  $T_{op} < T_c$ , electrons form pairs known as Cooper pairs<sup>18</sup>. When a photon is absorbed these Cooper pairs are broken into excitations called quasiparticles which can tunnel across the tunnel barrier and, under the influence of a constant bias voltage, produce a measurable tunnel current pulse. Since the basic excitations from the superconducting groundstate have energies in the order of only a few meV the absorption of an optical photon with energy of a few eV will create several thousands of quasiparticles. The exact number is proportional to the absorbed energy providing the detector with its spectrographic capabilities (eq. 1-1).

$$N = \frac{E_o}{\varepsilon} \quad 1-1$$

with  $N$  the number of created quasiparticles,  $E_o$  the energy of the absorbed photon and  $\varepsilon = 1.75\Delta_g$  the mean energy needed to create a quasiparticle<sup>19</sup>, with  $\Delta_g$  being the energy gap of the material. Applying a small bias voltage across the junction, which favours the tunnel current to flow into the direction of the applied bias voltage, produces a measurable current which is proportional to the energy of the absorbed photon. A magnetic field is applied parallel to the tunnel barrier to suppress all Josephson currents, tunnelling of Cooper pairs across the tunnel barrier at zero voltage bias predicted by Josephson<sup>20</sup>. In order to reduce the thermally excited quasiparticle population the STJ needs to be cooled well below the critical temperature ( $T_{op} \sim 0.1T_c$ ). For the widely used tantalum the operating temperature is around 300mK. The need for this low operating temperature also puts constraints on the number of read out wires which run from the readout electronics at ambient temperature into the cold stage where the junctions are located. Because each STJ forms a separate detector, requiring dedicated electronics to apply the necessary bias voltage and read out the tunnel current, the number of STJs in an array which can be read out is limited. At present the largest array of STJs used is the 10x12 S-Cam 3 array<sup>21,22</sup>.

The theoretical limit for the intrinsic energy resolution is given by:

## 1. Introduction

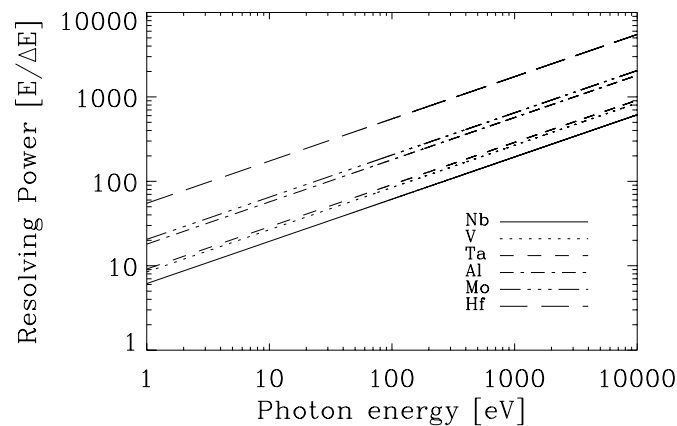
$$\Delta E = 2.355\sqrt{\varepsilon E_0 (F + G)}$$

1-2

The factor 2.355 arises from the conversion of root mean square (RMS) resolution to full width at half maximum (FWHM) resolution.  $F=0.2$ <sup>19,23</sup> is the Fano factor<sup>24</sup> which accounts for the statistical variations in the quasiparticle creation. Similarly  $G$ <sup>25</sup> accounts for statistical variations in the tunnel process. Generally  $G$  can range from 0 to  $\gg 1$ , depending on the tunnel probabilities in the electrodes, but in a typical symmetrical STJ with quasiparticle life times much longer than the tunnel time,  $G=(1+1/n)$  with  $n$  being the average number of tunnel events for each charge carrier.

**Table 1-1 Energy gap, critical temperature and theoretical energy resolution at 2.48 eV, 1 keV and 6keV**

Material	$\Delta_g$ [ $\mu\text{eV}$ ]	$T_c$ [K]	$\Delta E@2.48\text{eV}$ [eV]	$\Delta E@1\text{keV}$ [eV]	$\Delta E@6\text{keV}$ [eV]
Nb	1550	9.3	0.208	4.2	10.2
V	820	5.4	0.15	3.0	7.5
Ta	700	4.5	0.14	2.8	7
Al	180	1.2	0.07	1.4	3.5
Mo	139	0.915	0.06	1.25	3.1
Hf	19.4	0.128	0.023	0.47	1.15



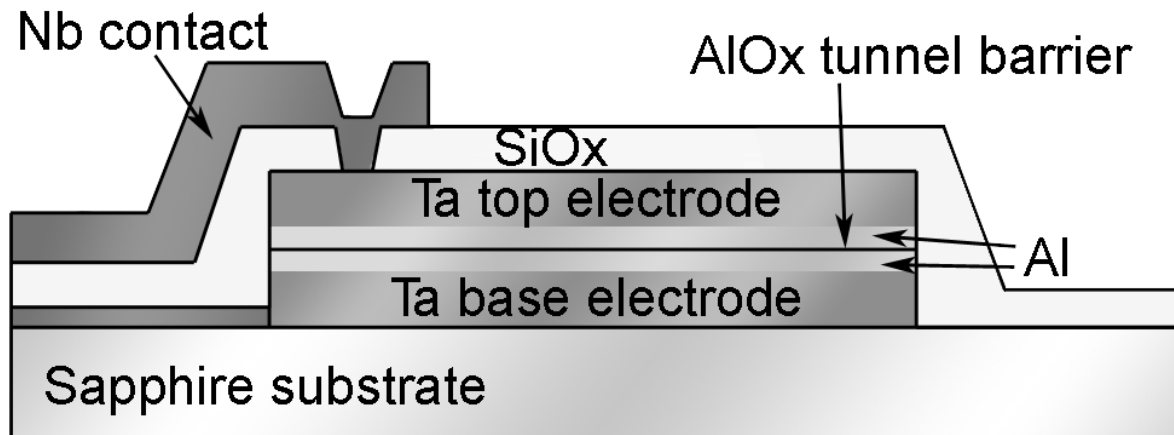
**Figure 1-2 Theoretical limit of the resolving power with photon energy for six different superconducting materials**

Table 1-1 shows the energy gap, critical temperature and energy resolutions ( $G=1$ ) at three different characteristic photon energies for different superconducting materials and Figure 1-2 shows the energy resolving power against photon energy for the same materials. The best achievable energy resolution varies as the square root of the energy gap. Since the critical temperature decreases proportional to the energy gap this increase in energy resolution demands lower operating temperatures, which complicates the operation.

As can be seen from Figure 1-2 the energy resolving power in the visible ( $<100$ ) is far below the highest energy resolution requirements for astronomy, for which a spectrograph is used (resolving power $\sim 100,000$ ). However for normal imaging astronomy in the visible the spectral information is usually obtained by taking three sequentially images in different wavelength bands using filters. Using STJs will provide this information within a single integration and with a higher energy resolving power.



For X-Ray astronomy semiconductors Si detectors are used which have an energy resolution of  $110\text{eV}@6\text{KeV}$ . As can be seen in Table 1-1 the energy resolution using superconductors exceeds this number by at least an order of magnitude.



**Figure 1-3 Schematic cross-cut of the used STJ geometry. The vertical scale has been enhanced for clarification.**

In our group proximised Ta/Al junctions are used with the following lay-out: Ta/Al/AlOx/Al/Ta (see Figure 1-3). The aluminium is added in-between the tantalum layer and tunnel barrier to confine the quasiparticles near the tunnel barrier and increase the tunnel probability<sup>26</sup>. The presence of the aluminium modifies the properties of the tantalum, and vice versa, due to the proximity effect<sup>27</sup> (explained in more detail in section 2.5) by suppressing the energy gap over the complete superconducting layer. Suppression of the energy gap is dependent on the thickness of the aluminium which gives the possibility to tune the energy gap.

### 1.3 Distributed Read Out Imaging Devices

In order to overcome the limitation on the sensitive area the Distributed Read-Out Imaging Device (DROID)<sup>28</sup> configuration is being developed (Figure 1-4). The DROID consists of a superconducting strip, which acts as an absorber, and a STJ on either side. When a photon is absorbed in the absorber quasiparticles are created which diffuse through the DROID. When they reach the STJ they will tunnel across the barrier producing the desired signal. Due to losses inside the absorber the signal will decrease with distance between the absorption site and the STJ providing the detector with positional information. However, one does not want the losses to be too big since this will diminish the signal and thus the energy resolution. The sum of the signal of the two STJs is a measure of the absorbed energy while the ratio of the signals is a measure for the absorption position.

An important issue for DROIDS is confinement of quasiparticles inside the STJs, called trapping. When trapping is absent the quasiparticles are able to quickly diffuse out of the STJ into the absorber. This reduces the time they can spend tunnelling across the barrier and they are subjected for longer to losses inside the absorber, thereby reducing the signal and energy resolution. When the loss rate in the absorber is low, the quasiparticles can travel between the two STJs, which produces crosstalk and reduces any positional information. On the other hand when trapping in the STJ is perfect the quasiparticles entering the STJ will stay in the

## 1. Introduction

STJ which prevents crosstalk between the STJs and the quasiparticles are near the tunnel barrier where they will tunnel adding to the signal. This will improve both the energy and the position resolution of the DROID. In order to optimise trapping the STJs are manufactured to have a lower energy gap than the absorber. Kraus<sup>28</sup>, in his pioneering work on DROIDS, used Sn ( $\Delta=580\mu\text{eV}$ ) absorbers with Al ( $\Delta=180\mu\text{eV}$ ) STJs. The difference in energy gap is sufficiently large to facilitate perfect trapping of quasiparticles inside the aluminium STJs. Segall<sup>29</sup> used tantalum absorbers with aluminium STJs with the same result. In our group we use proximised Ta/Al STJs with a pure tantalum absorber. Depending on the aluminium thickness the trapping of quasiparticles inside the STJs can be anything from non-existing to perfect.

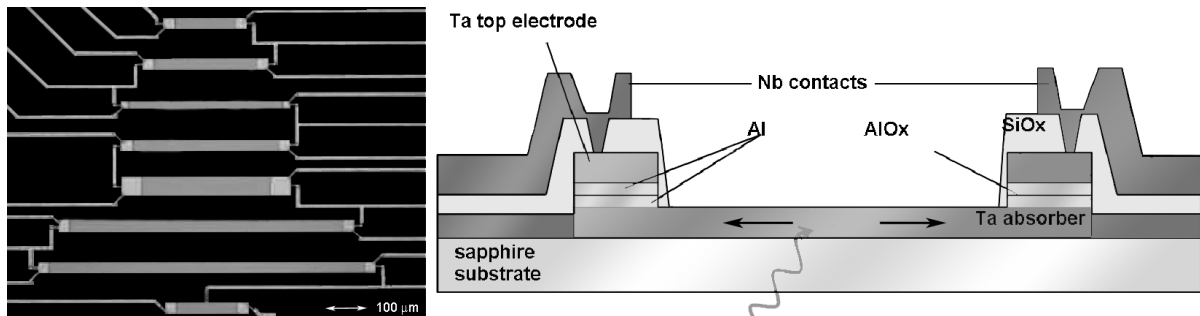


Figure 1-4 Micrograph of different geometries (left) of and a schematic cross-cut (right) of Distributed Read Out Devices.

Because the position is measured using two signals the position resolution and energy resolution are linked. For DROIDS with perfect trapping the relation is given by<sup>28</sup>:

$$\frac{E_0}{\Delta E} = \frac{2L}{\Delta x} \quad 1-3$$

with  $E_0$  the absorbed photon's energy,  $\Delta E$  the energy resolution,  $L$  the length of the absorber and  $\Delta x$  the position resolution.

### 1.4 S-Cam

Within the S-Cam program<sup>3</sup> we develop photon-counting spectrometers for ground-based astronomical applications in the optical. Three prototypes have been fabricated and used with success on telescopes such as the 4.2m William Herschel Telescope (WHT), La Palma, and the 1m Optical Ground Station (OGS), Tenerife.

The first two instruments, S-Cam 1 and S-Cam 2 (Figure 1-5a), used a 6x6 array of 25x25 $\mu\text{m}$  Ta/Al junctions. S-Cam 1<sup>30</sup> was a technology demonstrator which showed the potential of this new kind of spectrometer. S-Cam 2<sup>31</sup> was an improvement in energy resolution ( $E_0/\Delta E=8$  instead of 6 as with S-Cam 2). S-cam 2 had two observing campaigns on the WHT in the years 1999 and 2000. S-Cam 3<sup>21,22</sup> (Figure 1-5b) was again based on an array of single Ta/Al junctions but was an improvement on S-Cam 2 in many ways. The format of the array was 10x12 pixels of 35x35  $\mu\text{m}$  corresponding to a field of view on the sky of 9''x10'' when used at the WHT or OGS. The energy resolution was drastically improved to  $E_0/\Delta E=12@500\text{nm}$ , the optical bandpass of the IR suppression filters was increased and the count rate per pixel was increased from 5 to 8 kHz. The cryogenic capabilities were improved to have a longer hold time and easier operation. The readout electronics were redesigned to be much more

stable and flexible for future detectors. The S-Cam 3 system had one campaign on the WHT and five campaigns on the OGS.

During these campaigns several objects have been observed. For instance cataclysmic variables are binary systems which consist of a white dwarf primary and a main sequence secondary with an orbital period of between  $\sim 80$  and 700 min. The two stars are so close to each other that the gravity of the white dwarf distorts the secondary and matter flows from the secondary to the white dwarf forming an accretion disk. On the position where the matter falls on to the outer edge of the accretion disk a hotspot is formed. To map the accretion flow and location of the hot spots high temporal resolution is required. The addition of spectral information allows to distinguish matter of different temperatures and helps to constrain the description of the geometry of the system<sup>32,33,34</sup>.

A pulsar is a rapidly spinning neutron star which emits two beams of radio waves seen as pulses. The beams sweep past earth in a similar fashion as the beams of a lighthouse. Next to pulsars emitting radio waves some pulsars have been detected which emit visible light, X-ray or even gamma rays. The period of pulsars range from a few milliseconds up to around 12 seconds. To produce accurate models of the spatial distribution of the various emission regions precise timing of the pulsar light curve is required and a detector with high temporal resolution and photon counting capabilities is needed<sup>34,35</sup>. A detailed description of the design and performance of all aspects of S-Cam 3, along with examples of astronomical observations, is given in ref 21.

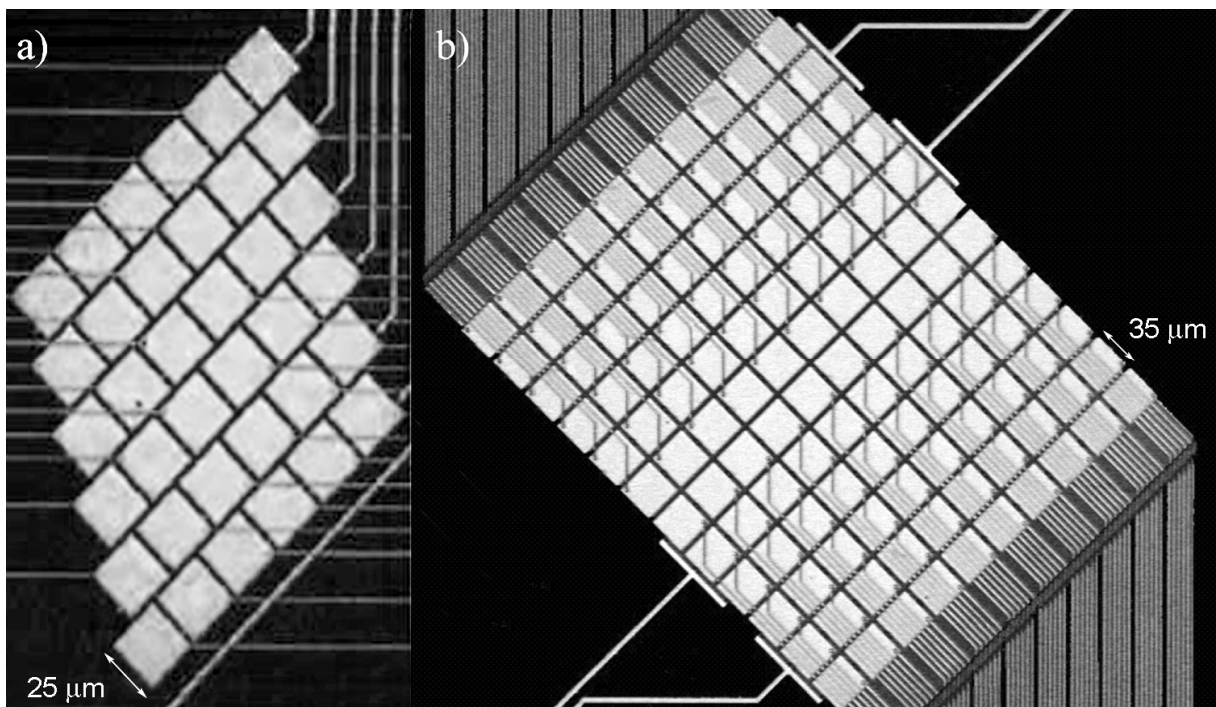


Figure 1-5 Micrograph of: a) the 6x6 S-Cam 1 and S-Cam 2 array (25x25 micron pixels) and b) the 10x12 S-Cam 3 array (35x35 micron pixels).

### 1.5 Aim and outline of the thesis

The next step in the S-Cam program is to further increase the field of view while maintaining the number of readout channels by using an array of DROIDS instead of single STJs. Within a DROID the quasiparticles will diffuse throughout the absorber towards the STJs and the added effect on the photon detection due to this diffusion process needs to be understood.

## 1. Introduction

---

The use of DROIDS will also put extra constraints on the responsivity (number of excited quasiparticles per eV photon energy). Firstly two signals are added together with each their own noise contribution. Secondly due to the larger sensitive area the tunnel probability decreases. Thirdly there will be extra losses inside the absorber. And finally the larger sensitive area of the detectors will increase the possibility of pile up, two photon absorptions within the integration time of the detector, and thereby reduce the maximum count rate.

The aim of this thesis is to develop the next cryogenic detector in the S-Cam programme which is based on an array of DROIDS. The requirements of such a detector are: an increase of field of view of a factor 5, and energy resolution comparable to the previous S-Cam detectors (RP~6@500nm or higher), position resolution equal to the width of the absorber at 500nm and microsecond time resolution. In order to develop such a detector an adequate knowledge of the processes involved with photon detection with DROIDS is needed. This involves the processes related to producing the tunnel signal inside the STJs such as the diffusion of quasiparticles in the absorber strip and confinement of the quasiparticles inside the STJs. The measured photon energy and absorption position needs to be reconstructed from two signals and the correct correlation between the two signals and the absorption position and photon energy need to be obtained. This includes the relation between the spectral and position resolution of the DROIDS.

In chapter 2 a theoretical overview is provided on the physical phenomena underlying photon detection with STJs and DROIDS. First superconductivity, a fundamental property of many cryogenic detectors, is briefly discussed. This is followed by the process of converting the energy of an absorbed photon into a number of quasiparticles which, in an STJ, tunnel across the tunnel barrier and produce the tunnel current to be measured. Finally the proximity effect, which is used in DROIDS to lower the energy gap in the STJ for confinement of the quasiparticles near the tunnel barrier, is explained.

Chapter 3 gives an overview of the production process of the devices, the experimental set-ups and measurement techniques that were used in the different experiments. It starts with the production process of the different devices. This is followed by the different cryostats available in the laboratories of the Advanced Studies & Technology Preparation Division within the Directorate of Science & Robotic Exploration of the European Space Agency. Thirdly, the readout electronics and methods used with DROIDS are discussed, followed by a description of the illumination methods.

Chapter 4 is the result of a detailed study in the quasiparticle dynamics involved with photon detection using STJs. It describes detailed theoretical analyses of the spectral and temporal evolution of the non-equilibrium quasiparticle and phonon distribution excited by the absorption of a single photon. Although the STJs of a DROID are open structures, i.e. at higher energy levels the quasiparticles are no longer confined in the STJ and can diffuse out of the STJ, the different processes described in this chapter are of equal importance for DROIDS.

The DROIDS described in this thesis use proximised STJs in order to confine the quasiparticles inside the STJ due to the lower energy gap. Due to the affected density of states of a proximised STJ the creation of quasiparticles following the absorption of a photon is less efficient as one would expect from its energy gap (eq. 1-1). Chapter 5 investigates this increased inefficiency in quasiparticle creation in proximised STJs. DROIDS provide an ideal configuration to verify this experimentally by comparison of the responsivity of the proximised STJ and the pure elemental absorber.

Several theoretical relations between the spectral and positional resolution are available but these have never been tested experimentally. Chapter 6 shows an experimental method to measure the spectral and positional resolution using optical light. The experimentally found resolutions are tested against the available theoretical relations and provide a good insight for further theoretical development.

Theoretical descriptions of photon detection with DROIDs published to date have been inadequate for the DROID geometry used in this thesis or did not fully describe all relevant processes involved. Chapter 7 presents a model to describe the responsivity from DROIDs with imperfect trapping (confinement of quasiparticles in the STJs). The model describes all processes relevant for photon detection in absorber and top or base film of the STJ.

The final chapter, chapter 8, describes the results of a system test using an actual array of 60 DROIDs in the geometry as would be used for S-Cam 4. The set-up of S-Cam 3 is used without modifications, except for the detector chip. Reconstruction of the DROID signals is done completely off-line by using the available position and time tags in the data to find coincident events. The test demonstrated the imaging capabilities of a DROID array in the optical. The results and experience provided much insight into operating a DROID array as a detector and possible improvements of the system as a whole.

# *Chapter 2*

---

## Theoretical introduction

---

*I*n this chapter we explain the different processes involved with photon detection using STJs or DROIDs in more detail. The basics of superconductivity and quasiparticle excitations are discussed. This is followed by the energy down conversion process which describes the creation of a quasiparticle distribution following the absorption of a photon. In the STJ these quasiparticles tunnel across the barrier and the four different tunnel processes that are possible are explained. In this thesis the electrodes of the STJs are Ta/Al bilayers and the proximity effect in such layers is explained in the final section of this chapter.

## 2.1 Superconductivity

Superconductivity, discovered by Kamerlingh Onnes in 1911<sup>37</sup>, lies at the basis of pair-breaking low temperature detectors. Below the critical temperature  $T_c$  the electrical resistance in a superconductor rapidly decreases to zero. At the same time the Meissner effect, discovered by Meissner and Ochsenfeld in 1933<sup>38</sup>, sets in: below  $T_c$  any magnetic field, constant or changing, below a critical field strength  $H_0$  is expelled by the superconductor. Actually the magnetic field penetrates the superconductor by a small distance called the London penetration depth discovered in 1935<sup>39</sup> by the brothers London.

In 1957 Bardeen, Cooper and Schrieffer presented a macroscopic theory of superconductivity which is known as the BCS theory<sup>40</sup>. At zero Kelvin temperature the electrons in a metal, which obey the Pauli Exclusion Principle, will occupy the lowest available energy levels up to a level equal to the Fermi energy forming a Fermi sea. When an electron moves through the positively charged ion lattice it will leave behind a higher ion density, due to oscillations in the ion lattice, forming an oscillating charge which is attractive to another electron. This second electron will break the oscillations and a phonon is exchanged between the two electrons by means of ion oscillation. This phonon exchange produces coherence between the two electrons, which results in an attractive potential between them and pairs of electrons with opposite spin and momentum are formed, called Cooper pairs<sup>41</sup>.

The characteristic length scale of the interaction within a Cooper pair is given by the coherence length,  $\xi_0$ , introduced by Pippard in 1953<sup>42</sup>. He argued that the superconducting wave function should have a characteristic length similar to the mean free path  $l$  in normal conducting metals which could be estimated by an uncertainty principle argument. Only electrons within  $\sim kT_c$  of the Fermi energy could play a major role in a phenomenon that sets in at  $T_c$  which have a momentum range  $\Delta p \sim kT_c/v_F$ , with  $v_F$  the Fermi velocity. Thus,

$$\Delta x \geq \frac{\hbar}{\Delta p} \approx \frac{\hbar v_F}{kT_c} \quad 2-1$$

which leads to the definition of the coherence length:

$$\xi_0 = a \frac{\hbar v_F}{kT_c} = \frac{\hbar v_F}{\pi \Delta_g} \quad 2-2$$

where  $2\Delta_g$  is the energy required to break a Cooper pair and  $a$  is a numerical constant found experimentally by Pippard<sup>43</sup> to be equal to 0.15. The right hand term of eq. 2-2 was derived by Bardeen *et al*<sup>40</sup>. They show that  $\Delta_g = 1.76kT_c$  for which the value for  $a$  becomes 0.18, confirming the value found by Pippard. This coherence length ( $\sim 100\text{nm}$  for the widely used tantalum) is typically much larger than the inter-atomic distance of the lattice, showing the strong overlap of the Cooper pairs in the superconductor.

The potential energy of the bound electrons outweighs the total excess kinetic energy of the individual electrons relative to the Fermi energy. Thus although the individual kinetic energy of the paired electrons is larger than the kinetic energy of electrons at the Fermi level the total energy of the paired electrons is negative compared to the free electron energy at the Fermi level. Therefore, the electrons will start to condense into Cooper pairs until equilibrium is reached, called the BCS ground state, which is responsible for the superconducting properties like perfect electric conductivity and diamagnetism. The equilibrium point is reached when

## 2. Theoretical introduction

---

the state of the system has changed from the Fermi sea such that the binding energy of an additional pair has gone to zero.

The BCS ground state is described by the BCS waveform:

$$|\psi_G\rangle = \prod_{\vec{k}=\vec{k}_1, \dots, \vec{k}_M} (u_{\vec{k}} + v_{\vec{k}} c_{\vec{k}\uparrow}^* c_{-\vec{k}\downarrow}^*) |\varphi_0\rangle \quad 2-3$$

With  $\phi_0$  the vacuum state with no particles present,  $u_{\vec{k}}^2$  the probability of the pair  $|\vec{k}\uparrow, -\vec{k}\downarrow\rangle$  being empty,  $v_{\vec{k}}^2 = 1 - u_{\vec{k}}^2$  the probability of the pair  $|\vec{k}\uparrow, -\vec{k}\downarrow\rangle$  being occupied.  $c_{\vec{k}\sigma}^*$  and  $c_{\vec{k}\sigma}$  (which is used later) are the creation and annihilation operator for an electron with wave vector  $\vec{k}$  and spin  $\sigma$  ( $\uparrow$  or  $\downarrow$ ). With this wave function it is assumed that the occupancy of a Cooper pair state  $|\vec{k}\uparrow, -\vec{k}\downarrow\rangle$  only depends on the average occupancy of all the other paired states (*mean field approximation*) because the number of pairs is large.

The BCS theory assumes that the electrons in a superconductor can be described by a free electron gas with a weak interaction potential between pairs of electrons leading to the so-called *reduced Hamiltonian* or *pairing Hamiltonian*:

$$\mathcal{H} = \sum_{\vec{k}\sigma} \varepsilon_{\vec{k}\sigma} c_{\vec{k}\sigma}^* c_{\vec{k}\sigma} + \sum_{\vec{k}\vec{l}} V_{\vec{k}\vec{l}} c_{\vec{k}\uparrow}^* c_{-\vec{k}\downarrow}^* c_{-\vec{l}\downarrow} c_{\vec{l}\uparrow} \quad 2-4$$

With  $\varepsilon_{\vec{k}\sigma}$  the free electron energy relative to the Fermi energy  $E_F = (\hbar^2 \vec{k}_F^2 / 2m^*)$  where  $m^*$  is the effective electron mass\*

$$\varepsilon_{\vec{k}\sigma} = \frac{\hbar^2 \vec{k}^2}{2m^*} - E_F \quad 2-5$$

$V_{\vec{k}\vec{l}}$  is the interaction potential of the two electrons in  $\vec{k}$ -space given by:

$$V_{\vec{k}\vec{l}} = \frac{1}{\Omega} \int V(\vec{r}) e^{i(\vec{l}-\vec{k})\vec{r}} d\vec{r} \quad 2-6$$

with  $\Omega$  the normalisation volume and  $V(\vec{r})$  the usual interaction potential of two electrons at a relative distance  $\vec{r}$ . In order to find the superconducting ground state the Hamiltonian of eq. 2-4 is operated on the ground state wave function of eq. 2-3 to obtain the total energy which is minimized. The interaction term of the result is given by:

$$\langle V \rangle \equiv \langle \psi_G | \sum_{\vec{k}\vec{l}} V_{\vec{k}\vec{l}} c_{\vec{k}\uparrow}^* c_{-\vec{k}\downarrow}^* c_{-\vec{l}\downarrow} c_{\vec{l}\uparrow} | \psi_G \rangle = \sum_{\vec{k}\vec{l}} V_{\vec{k}\vec{l}} u_{\vec{k}\uparrow} v_{-\vec{k}\downarrow} u_{-\vec{l}\downarrow} v_{\vec{l}\uparrow} \quad 2-7$$

---

\* Within a solid material the movement of an electron is affected by forces between atoms and Newton's law does not apply. The effective mass is the mass the particle seems to carry in the semiclassical model of transport in a crystal



In order for the term  $V_{\vec{k}\vec{l}}$  to scatter from a state with  $|\vec{l}\uparrow, -\vec{l}\downarrow\rangle$  to one with  $|\vec{k}\uparrow, -\vec{k}\downarrow\rangle$  requires the initial state to have the  $\vec{l}$  pair occupied and the  $\vec{k}$  pair empty. The probability amplitude for such an initial state is  $u_{\vec{k}\uparrow}v_{\vec{l}\uparrow}$  and for the final state it is  $u_{\vec{k}\downarrow}v_{\vec{l}\downarrow}$ .

The wave function of the state with the lowest total energy is found by minimizing  $\langle \psi_G | \mathcal{H} | \psi_G \rangle$ , while keeping the number of electrons fixed and BCS defined at zero temperature the so-called gap parameter  $\Delta_{\vec{k}}$  as:

$$\Delta_{\vec{k}} \equiv -\sum_{\vec{l}} V_{\vec{k}\vec{l}} u_{\vec{l}} v_{\vec{l}} \quad 2-8$$

and the excitation energy  $E_{\vec{k}}$  of a quasiparticle of momentum  $\vec{k}$  as:

$$E_{\vec{k}} \equiv \left( \Delta_{\vec{k}}^2 + \varepsilon_{\vec{k}}^2 \right)^{1/2} \quad 2-9$$

By substituting eq. 2-9 and eq. 2-8 into eq. 2-7 in order to evaluate  $\Delta_{\vec{k}}$  leads to the condition for self-consistency:

$$\Delta_{\vec{k}} = -\frac{1}{2} \sum_{\vec{l}} \frac{\Delta_{\vec{l}}}{E_{\vec{l}}} V_{\vec{k}\vec{l}} \quad 2-10$$

Next to the trivial solution  $\Delta_{\vec{k}}=0$  it also has a non-trivial solution which is expected when the potential is negative. Following BCS a negative constant attractive interaction potential is assumed between pairs of electrons up to energy equal to  $\hbar\omega_D$  and zero above energy  $\hbar\omega_D$ :

$$V_{\vec{k}\vec{l}} = \begin{cases} -V & \text{for } |\varepsilon_{\vec{k}}| \text{ and } |\varepsilon_{\vec{l}}| \leq \hbar\omega_D \\ 0 & \text{otherwise} \end{cases} \quad 2-11$$

this makes  $\Delta_{\vec{k}}$  independent of  $\vec{k}$ . Replacing the summation by an integration from  $-\hbar\omega_D$  to  $\hbar\omega_D$  and approximating the single spin electronic density of states with the single spin density of states at the Fermi level,  $N(0)$ , which is justified in the weak-coupling limit,  $\Delta_g$  becomes:

$$\Delta_g = \frac{\hbar\omega_D}{\sinh\left(N(0)^{-1} V^{-1}\right)} \quad 2-12$$

The coefficients  $u_{\vec{k}}$  and  $v_{\vec{l}}$  which specify the optimum BCS wave function can then be calculated to be:

$$u_{\vec{k}}^2 = \frac{1}{2} \left( 1 + \frac{\varepsilon_{\vec{k}}}{E_{\vec{k}}} \right) \quad 2-13$$

## 2. Theoretical introduction

$$v_k^2 = \frac{1}{2} \left( 1 - \frac{\varepsilon_k}{E_k} \right) \quad 2-14$$

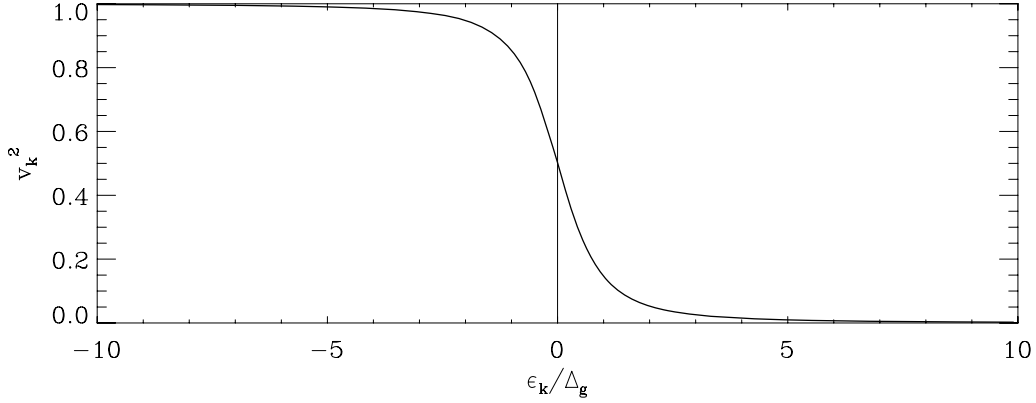


**Figure 2-1 Occupational probability  $v_k^2$  as a function of electron energy as a function of free electron energy  $\varepsilon_k$  for a BCS superconductor at zero Kelvin.**

Figure 2-1 shows a plot of  $v_k^2$  at zero Kelvin, which shows that even at zero Kelvin still some of the electrons are bound into Cooper pairs occupying states above the Fermi level. This distribution does not show much variation in the range  $0 < T < T_c$  and any change in the metal on cooling from  $T_c$  to  $T=0$  cannot be usefully described in terms of changes in  $v_k^2$ .

For a more detailed description of superconductivity and the BCS theory the reader is referred to chapter 3 of *Introduction to Superconductivity* by M. Tinkham<sup>44</sup>.

## 2.2 Quasiparticle excitations and density of states

Excitations of the superconducting ground state, called Bogoliubov quasiparticles or simply quasiparticles, have been calculated in 1958 by Bogoliubov<sup>45</sup> and Valatin<sup>46</sup> by introducing a linear pair of orthonormal operators which form an orthogonal set of excitations.

$$\begin{aligned} \gamma_{\vec{k}0}^* &= u_{\vec{k}} c_{\vec{k}\uparrow}^* - v_{\vec{k}} c_{-\vec{k}\downarrow} \\ \gamma_{\vec{k}1}^* &= u_{\vec{k}} c_{-\vec{k}\downarrow}^* + v_{\vec{k}} c_{\vec{k}\uparrow} \end{aligned} \quad 2-15$$

The operator  $\gamma_{\vec{k}0}^*$  creates an electron with momentum  $\vec{k}$  and spin up, either by creating an electron with momentum  $\vec{k}$  and spin up if the pair state  $|\vec{k}\uparrow, -\vec{k}\downarrow\rangle$  was initially empty or annihilating an electron with momentum  $-\vec{k}$  and spin down if the pair state was initially occupied. The operator  $\gamma_{\vec{k}1}^*$  is similar but creates an excitation with momentum  $-\vec{k}$  and spin down. As mentioned above, the energy is given by eq. 2-9 with minimum excitation energy equal to  $\Delta_g$ , which acts as an energy gap below which no excitations can exist.

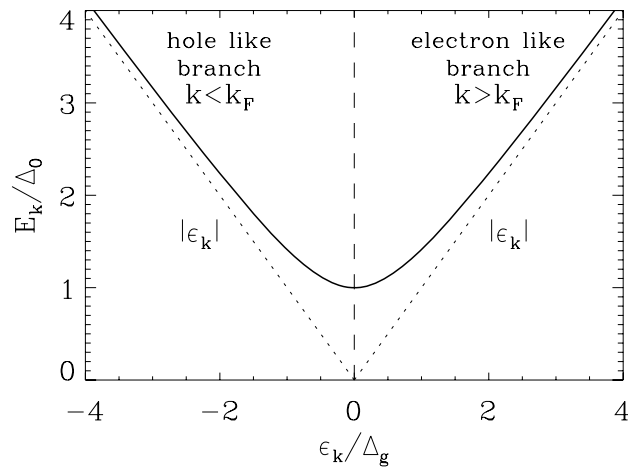


**Figure 2-2** Quasiparticle excitation energy as a function of the free electron energy relative to the Fermi energy for the superconducting state (solid line). The excitation energy for the normal state (holes and electrons) is shown (dotted line) for comparison.

Figure 2-2 shows the excitation energy of a quasiparticle as a function of the free electron energy relative to the Fermi energy. It shows that for each quasiparticle excitation energy above the gap energy two quasiparticle states are possible: a hole-like quasiparticle ( $|\vec{k}| > |\vec{k}_F|$ ) and an electron-like quasiparticle ( $|\vec{k}| < |\vec{k}_F|$ ). In order to conserve the particle number the quasiparticles are always created or annihilated in pairs, by breaking or creating a Cooper pair, in which the quasiparticles have opposite electron energy relative to the Fermi energy. Thus the minimum energy required to create an excitation in a superconductor is  $2\Delta_g$ .

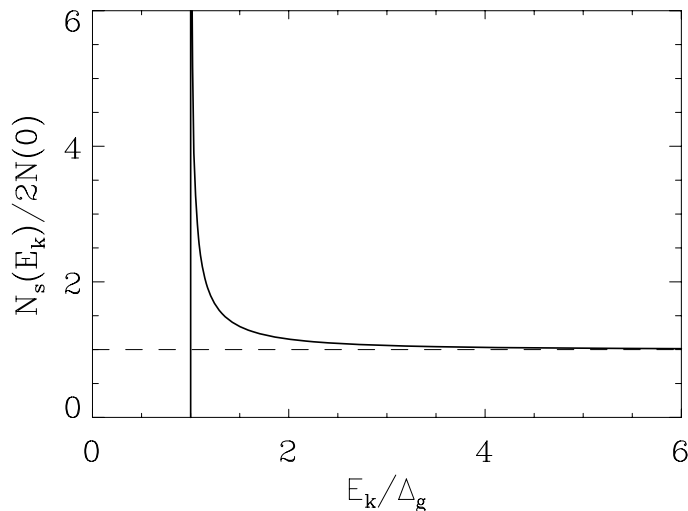


**Figure 2-3** Density of states in a BCS superconductor (solid line) compared to the normal state (dashed line).

The superconducting density of states ( $N_s(E)$ ) can be obtained by equating:

## 2. Theoretical introduction

$$N_s(E)dE = N_n(\varepsilon)d\varepsilon \quad 2-16$$

Because we are only interested in energies  $\varepsilon$  close to the Fermi energy we can take the single spin electronic density of states in the normal material equal to the single spin electronic density of states at the Fermi energy in the normal material,  $N_n(\varepsilon)=2N(0)$  (The factor 2 accounts for both spin orientations), leading to the simple result:

$$\frac{N_s(E_{\vec{k}})}{2N(0)} = \begin{cases} \frac{E_{\vec{k}}}{\sqrt{E_{\vec{k}}^2 - \Delta_g^2}} & E_{\vec{k}} > \Delta_g \\ 0 & E_{\vec{k}} < \Delta_g \end{cases} \quad 2-17$$

This relation is plotted in Figure 2-3.

### 2.3 Photon absorption

The process in which the energy of an absorbed photon is converted into a distribution of quasiparticles is called the downconversion process<sup>47,48,49</sup>, schematically represented in Figure 2-4. Because cryogenic detectors can be used for a wide range of photon energies we will discuss the downconversion process starting from an energy which results from the absorption of an X-ray photon. Optical photons only possess several electron volts of energy and the downconversion process will start from that energy and will follow the steps described from that energy downwards.

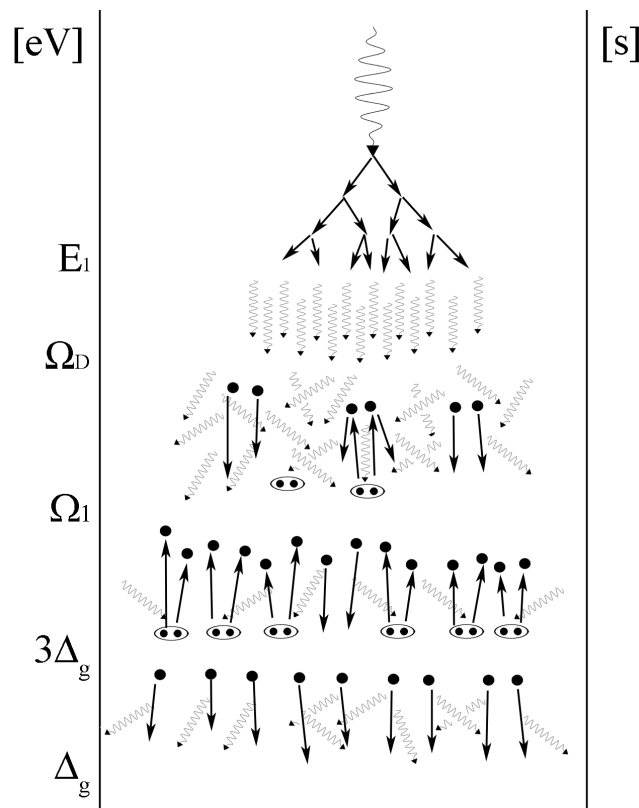


Figure 2-4 Schematic representation of the different stages of the downconversion.

When a photon is absorbed in a superconducting film it interacts with one of the electrons in the shells of an atom. This electron leaves the atom with energy equal to the difference of the absorbed photon energy and binding energy of the electron. Via strong electron-electron interactions, dominated by secondary ionization and cascade plasmon emission, the energy is quickly distributed over a number of electrons until a characteristic energy  $E_I$ ,  $\sim 1$  eV, is reached. Below this energy the electron-electron scattering rate ( $\tau_{ee}^{-1}(\varepsilon)$ ) becomes slow and the electron phonon rate ( $\tau_s^{-1}(\varepsilon)$ ) takes over. The energy  $E_I$  is defined as the energy at which  $\tau_{ee}^{-1}(E_I) = \tau_s^{-1}(E_I)$  resulting into the following expression for  $E_I$ :

$$E_I = 2.82\Omega_D r_s^{-1/4} \left( \frac{\lambda}{3} \frac{\varepsilon_F}{\Omega_D} \right)^{1/2} \quad 2-18$$

where we used:

$$\tau_{ee}^{-1}(E_I) = \frac{\varepsilon^2}{\hbar \varepsilon_F} \frac{r_s^{1/2}}{7.96} \quad 2-19$$

$$\tau_s^{-1}(E_I) = \begin{cases} \frac{1}{3} \lambda \Omega_D \left( \frac{\varepsilon}{\Omega_D} \right)^{1/3} & \varepsilon < \Omega_D \\ \frac{1}{3} \lambda \Omega_D & \varepsilon > \Omega_D \end{cases} \quad 2-20$$

Here  $r_s$  is the radius of a sphere in atomic units which encloses one electron charge and  $\lambda$  the dimensionless electron-phonon coupling strength and  $\Omega_D$  the Debye energy\*.

Below  $E_I$  the electrons first emit phonons with energy equal to  $\Omega_D$  in a long cascade containing several tens of phonons, until they reach into the last spectral interval below  $\Omega_D$ . Each step takes  $\tau_s(E_I)$  and in total the cascade takes  $\tau_1 \cong (3/\lambda\Omega_D)(E_I/\Omega_D)$ .

At the end of this phase there will be a large phonon distribution with energies around  $\Omega_D$  because the life time of a Debye phonon,  $\tau_D$ , is larger than  $\tau_I$ ,  $\tau_D > \tau_I$ . From the energy  $\Omega_D$  down the breaking of Cooper pairs is the main mechanism governing the downconversion. First the relaxation of high energy quasiparticles and emission of phonons happens very fast and the Cooper pair breaking rate is the limiting factor producing a large distribution of phonons. As the phonon energy degrades the relaxation of quasiparticles and thus emission of phonons becomes more slow and breaking the Cooper pairs takes over as being the faster process producing a distribution of quasiparticles. The energy  $\Omega_1$ , which indicates the turnaround energy, is defined as the energy at which the phonon emission rate is equal to the Cooper pair breaking rate  $^{1/3}\lambda(\varepsilon^3/\Omega_D^2) = \lambda_1 \varepsilon|_{\varepsilon=\Omega_1}$  resulting into:

$$\Omega_1 = \Omega_D \sqrt{\frac{3\lambda_1}{\lambda}} \quad 2-21$$

with

---

\* Debye energy is the highest energy of a phonon in a lattice determined by the lattice structure

## 2. Theoretical introduction

---

$$\lambda = \frac{1}{\Omega_D \tau_0} \left( \frac{\Omega_D}{k_b T_c} \right)^3, \text{ and } \lambda_1 = \frac{\lambda v_e}{2v_{ph}} \quad 2-22$$

where  $v_e$  is the electron density of states at the Fermi level in the normal metal, while  $v_{ph}$  is the phonon density of states in the Debye approximation  $v_{ph}=3\Omega_D^2/2\pi^2c^3$  ( $c$  is the mean sound velocity). The end of the electron-phonon interaction stage is when the quasiparticles reach an energy equal to  $3\Delta_g$ . Phonons emitted by quasiparticles relaxing from this energy to  $\Delta_g$  do not possess enough energy ( $\epsilon_{ph}<2\Delta_g$ ) to break a Cooper pair and are lost from the system. This loss in energy in the downconversion process is the reason for the factor 1.75 when calculating the number of created quasiparticles from the photon energy using eq. 1-1.

### 2.4 Current-voltage characteristics

An STJ consists of two superconducting layers separated by a thin insulating tunnel barrier. Via a quantum mechanic effect Cooper pairs and quasiparticles are able to tunnel across the barrier to the opposite superconducting layer<sup>50,51</sup>. The tunnel current over a junction is given by two major contributions<sup>52</sup>

$$J = J_J + J_{qp} \quad 2-23$$

In which  $J_J$  is the pair tunnelling and  $J_{qp}$  is the quasiparticle tunnelling.

#### 2.4.1 Josephson current

In 1950 (before Bardeen *et al* presented their theory on microscopic level) Ginzburg *et al*<sup>53</sup> presented a macroscopic theory which was a generalization of the London theory. They introduced a pseudo wave function  $\Psi(\mathbf{r})$  as a complex order parameter.  $|\Psi(\mathbf{r})|^2$  was to represent the local density of superconducting electrons. From the microscopic BCS theory this can be seen as a macroscopic wave function since wave functions of Cooper pairs overlap and they find it energetically favourable to lock all their phases. Thus the superconductor can be described by its condensed many-particle wave function  $\Psi(\mathbf{r})=|\Psi(\mathbf{r})|e^{i\varphi}$  which maintains its phase coherence over macroscopic distances.

In 1962 Josephson<sup>52</sup> showed that between two superconducting electrodes separated by a thin insulating barrier a current,  $J_j$ , should flow through the junction:

$$J_J = J_{J1} \sin \varphi + J_{J2} \cos \varphi \quad 2-24$$

$J_{J2}$  is given by:

$$J_{J2} = \frac{G_{nn}}{\pi} \int_{-\infty}^{\infty} \frac{\Delta_1 \Delta_2}{E(E-eV)} [f(E-eV) - f(E)] dE_{\vec{k}} \quad 2-25$$

where  $G_{nn}$  is the conductance when both electrodes are in the normal state (equal to the inverse of the normal barrier resistivity,  $1/R_{nn}$ , which is a measure of the barrier quality) of the junction and  $f$  the Fermi distribution. The  $\cos\varphi$  term oscillates as  $\cos(2eVt/\hbar)$  and will

average to 0 in the typical low frequency I-V measurements and it will not be considered further.

The  $\sin\varphi$  term in eq. 2-24 is responsible for the supercurrent at 0 voltage bias.  $J_{J1}$ , the critical current or the maximum current the junction can support, is given by:

$$J_{J1} = \frac{G_{nn}}{\pi} P \int_{-\infty}^{\infty} \int_{-\infty}^{\infty} \frac{\Delta_1 \Delta_2}{E_1 E_2 (E_1 - E_2 + eV)} [f(E_1) - f(E_2)] dE_{1\bar{k}} dE_{2\bar{k}} \quad 2-26$$

With  $\Delta_{1/2}$  the gap and  $E_{1/2}$  the energy level of electrode 1 or 2. When  $V=0$  and  $\Delta_1=\Delta_2=\Delta$  we get:

$$J_{J1} = \frac{\pi\Delta(T)}{2eR_{nn}} \tanh \frac{\Delta(T)}{2kT} \quad 2-27$$

At  $T=0$  the maximum supercurrent corresponds to the current in the normal state junction, biased at  $eV=\pi\Delta/2$  providing the relation:

$$J_{J1}(0) = \frac{\pi\Delta}{2eR_{nn}} \quad 2-28$$

For the case  $\Delta_1 \neq \Delta_2$  Ambegaokar and Baratoff<sup>54</sup> have derived the following expression for the same situation.

$$J_{J1}(0) = \frac{\Delta_1(T)}{2eR_{nn}} K \sqrt{1 - \frac{\Delta_1^2(T)}{\Delta_2^2(T)}} \quad 2-29$$

with  $K$  a coupling constant which reduces to  $\pi/2$  at  $x=0$ . In 1964 Fiske<sup>55</sup> discovered that when applying a voltage across the junction a series of steps (so-called Fiske steps) appeared at constant voltage. Together with Coon<sup>56</sup> he showed that these structures arise from interaction between the Josephson current density-waves with the electromagnetic fields in the junction acting as a resonator. If a voltage difference  $V_0$  is maintained across the junction the phase difference  $\varphi$  would evolve according to:

$$\frac{d\varphi}{dt} = 2e \frac{V_0}{\hbar} \quad 2-30$$

and an oscillating current is produced. One expects a corresponding oscillating voltage  $\delta V$ , supposing a junction capacity  $C$  (since  $I=CdV/dt$ ), whose fundamental component (at  $\omega_0 = 2eV_0 / \hbar$ ) is

$$\delta V = \frac{I_{J1}}{\omega_0 C} \cos(\omega_0 t + \alpha) \quad 2-31$$

This voltage will correspondingly produce electromagnetic radiation, both at the fundamental  $\omega_0$  and at its overtones  $n\omega_0$ .

## 2. Theoretical introduction

---

Suppression of the supercurrent, and Fiske steps, can be achieved by applying a magnetic field parallel to the tunnel barrier. This can be optimised by the choice of STJ geometry and the orientation with respect to the magnetic field<sup>57</sup>. The Josephson current dependence on the applied magnetic field can be calculated using the following relations:

$$\nabla\varphi = \frac{2e(2\lambda + d)}{\hbar} (\vec{B} \times \vec{n}) \quad 2-32$$

$$I_c = \iint dx dy J_c \sin \varphi f(x, y) \quad 2-33$$

with  $\lambda$  the London penetration depth,  $d$  the thickness of the barrier,  $\vec{B}$  the applied magnetic field and  $\vec{n}$  the unit vector normal to the junction plane and  $f(x, y)$  the function which defines the junction area. As function of the applied magnetic field the amplitude of the Josephson current displays a Fraunhofer like pattern. The separation of the minima in amplitude depends on the size of the junction and the maxima in amplitude show a linear or faster decay with magnetic field.

### 2.4.2 Quasiparticle Tunneling

The total quasiparticle current  $J_{qp}$ , the second term in eq. 2-23, is given by:

$$J_{qp} = G_{nn} \int_{-\infty}^{\infty} \frac{N_{S_1}(E_{\vec{k}})}{2N_1(0)} \frac{N_{S_2}(E_{\vec{k}} + eV)}{2N_2(0)} [f(E_{\vec{k}}) - f(E_{\vec{k}} + eV)] dE_{\vec{k}} \quad 2-34$$

The four tunnel processes, presented in Figure 2-5, in which quasiparticles can tunnel are independent and can be evaluated separately.

The first process is direct tunnelling of a quasiparticle across the barrier from layer 1 to layer 2 in the direction of the bias voltage. The corresponding tunnel current  $J_{qp1}$  is given by:

$$J_{qp1} = G_{nn} \int_{-\infty}^{\infty} \frac{N_{S_1}(E_{\vec{k}})}{2N_1(0)} f(E_{\vec{k}}) \frac{N_{S_2}(E_{\vec{k}} + eV)}{2N_2(0)} [1 - f(E_{\vec{k}} + eV)] dE_{\vec{k}} \quad 2-35$$

In process 2 a Cooper pair is annihilated in layer 1 creating two quasiparticles. One of these quasiparticles tunnels across the barrier to layer 2 where it recombines into a Cooper pair with another quasiparticle. Since a quasiparticle has been annihilated in layer 2 and a quasiparticle is created in layer 1 the quasiparticle flow is effectively from layer 2 to layer 1. However, physically an electron has tunnelled from layer 1 to layer 2, as in process 1. The corresponding tunnel current  $J_{qp2}$  is given by:

$$J_{qp2} = G_{nn} \int_{-\infty}^{\infty} \frac{N_{S_1}(E_{\vec{k}} + eV)}{2N_1(0)} f(E_{\vec{k}} + eV) \frac{N_{S_2}(E_{\vec{k}})}{2N_2(0)} [1 - f(E_{\vec{k}})] dE_{\vec{k}} \quad 2-36$$



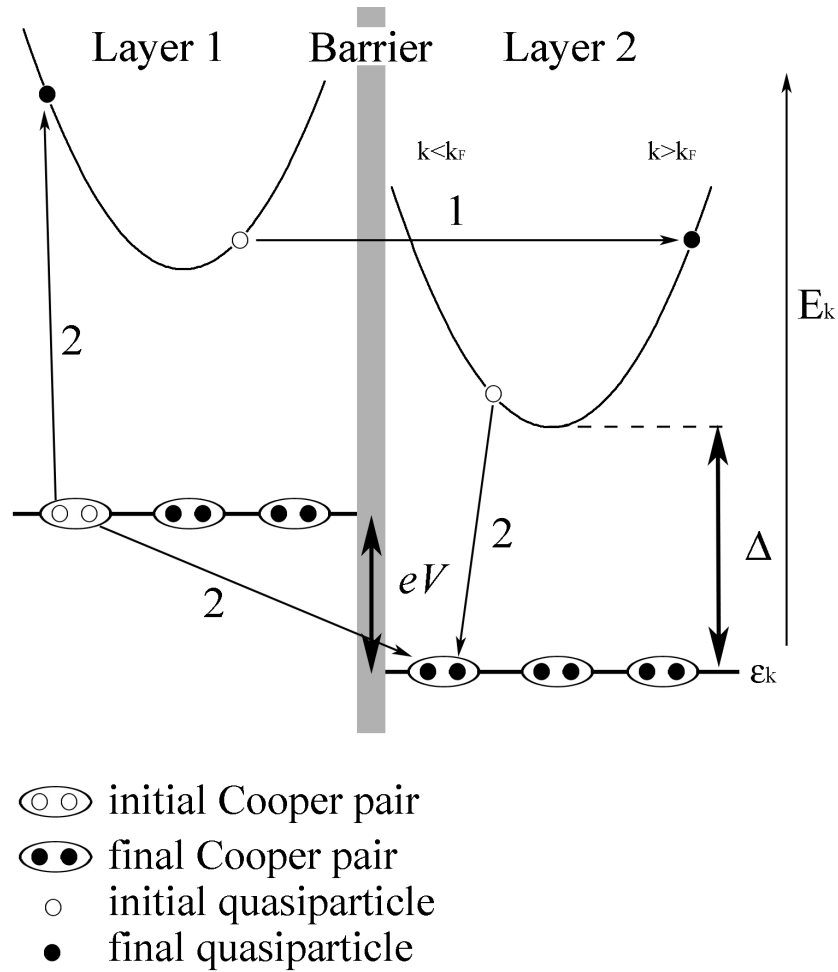


**Figure 2-5 Different tunnel processes in a superconducting tunnel junction. Processes 1 and 2 indicate forward and back tunnelling. Processes 3 and 4 are not shown but are the reverse of resp. process 1 and 2.**

Process 3 is the same as process 1 but in opposite direction. Due to the applied bias voltage only the quasiparticles at higher energy levels can tunnel following this process, which reduces its probability. The corresponding tunnel current  $J_{qp3}$  is:

$$J_{qp3} = G_{nn} \int_{-\infty}^{\infty} \frac{N_{S_1}(E_{\bar{k}} + eV)}{2N_1(0)} [1 - f(E_{\bar{k}} + eV)] \frac{N_{S_2}(E_{\bar{k}})}{2N_2(0)} f(E_{\bar{k}}) dE_{\bar{k}} \quad 2-37$$

Process 4 is the opposite of process 2 but since it requires quasiparticles with energy level larger than  $eV + \Delta$  it will vanish rapidly. The tunnel current  $J_{qp4}$  is given by:

$$J_{qp4} = G_{nn} \int_{-\infty}^{\infty} \frac{N_{S_1}(E_{\bar{k}} + eV)}{2N_1(0)} f(E_{\bar{k}} + eV) \frac{N_{S_2}(E_{\bar{k}})}{2N_2(0)} [1 - f(E_{\bar{k}})] dE_{\bar{k}} \quad 2-38$$

The process of back tunnelling (process 2) produces an internal amplification of the tunnel signal because the quasiparticles can tunnel back and forth while adding to the signal<sup>58</sup>. This is of importance for the detection of an optical photon since the absorbed energy is low. Important to note is that with the preferred tunnel processes, process 1 and 2, the

## 2. Theoretical introduction

quasiparticles are promoted in energy with each tunnel cycle by an amount equal to  $2eV_b$ , with  $V_b$  being the applied bias voltage. They continue to gain energy by tunnelling until the quasiparticle relaxes by emitting a phonon of which the rate is dependent on the number of states available. These two processes produce a broadened quasiparticle energy distribution which is bias voltage dependent.

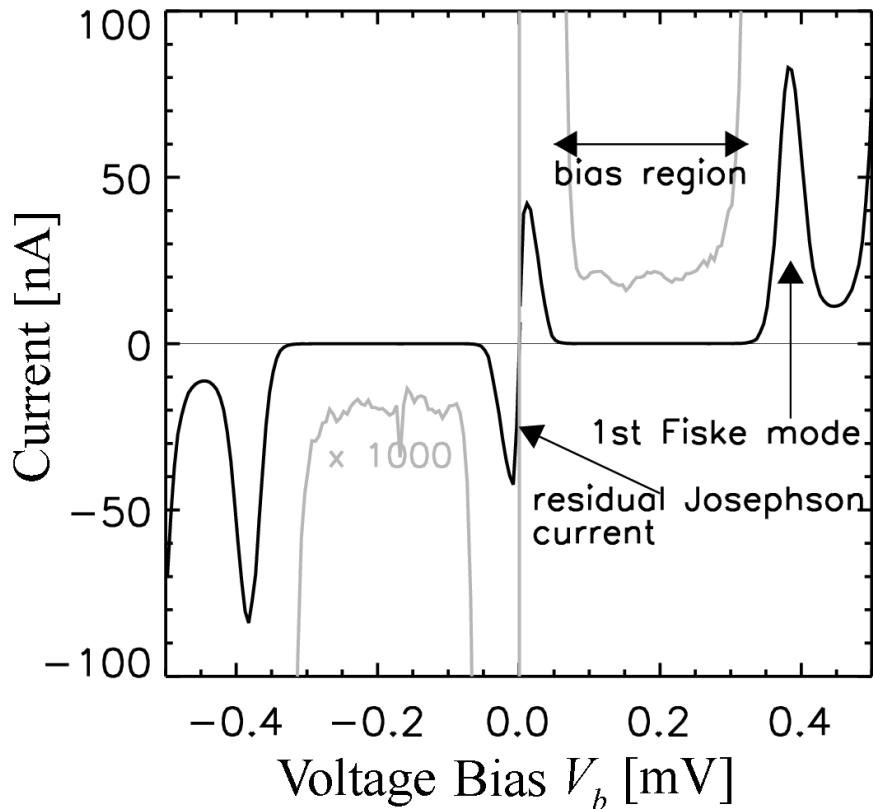


Figure 2-6 IV curve of a  $25 \times 25 \mu\text{m}^2$  STJ. An amplification of the current of 1000x has been shown to highlight the subgap region in which the device can be biased.

For  $\Delta/kT \gg 1$  a simple relation between the subgap current and the quasiparticle densities can be derived:

$$I_{\text{subgap}} = \frac{N(T)(eV + \Delta)}{2N(0)eR_m \left( (eV + \Delta)^2 - \Delta^2 \right)^{1/2}} \quad 2-39$$

With  $R_m$  the junction's normal state resistance and  $N(T)$  is the density of thermally excited quasiparticles given by<sup>59</sup>:

$$N(T) = N(0)(8\pi\Delta kT)^{1/2} e^{-(\Delta/kT)} \quad 2-40$$

For a more detailed description of the tunnel currents in STJs the reader is referred to chapter 3 of *Principles of electron tunnelling spectroscopy* by E.L. Wolf<sup>60</sup>.

## 2.5 Proximity effect

With tantalum STJs an aluminium layer is added in between the tantalum layer and tunnel barrier in order to confine the quasiparticles near the tunnel barrier and increase the tunnel probability<sup>26</sup>. The two superconducting materials will influence each other within a distance of several coherence lengths of the bulk material. The film thicknesses of the used detectors are generally comparable to the coherence length and the properties of the formed bi-layer differ considerably from the bulk properties of the materials. The mean free path is limited by the thickness of the film and the granularity of the surface and the dirty superconductor limit, the electronic mean free path is short compared to the coherence length ( $l \leq \xi_0$ ), can be assumed. The proximity effect of two dirty superconductors can be described using the Usadel equations<sup>61,27</sup> (eq. 2-41).

$$\frac{\hbar D_{S_i}}{2} \frac{\partial^2 \theta_{S_i}}{\partial x^2}(\varepsilon, x) + i\varepsilon \sin \theta_{S_i}(\varepsilon, x) + \Delta_{S_i}(x) \cos \theta_{S_i}(\varepsilon, x) = 0 \quad 2-41$$

With  $D_{S_i}$  the normal state diffusion constant in material  $S_i$  ( $i=1,2$ ),  $\varepsilon$  the energy and  $x$  the coordinate perpendicular to the interface between the two layers with the origin at the interface. The pair potential  $\Delta_{S_i}(x)$  is determined by the self-consistency relation:

$$\Delta_{S_i}(x) \ln \frac{T}{T_{c,S_i}} + 2 \frac{T}{T_{c,S_i}} \sum_{\omega_n} \left[ \frac{\Delta_{S_i}(x)}{\hbar \omega_n} - \sin \theta_{S_i}(i\hbar \omega_n, x) \right] = 0 \quad 2-42$$

With  $\omega_n = (2n+1)\pi kT/\hbar$  the Matsubara frequency, which relates to the quasiparticle energy by  $\hbar \omega_n = -i\varepsilon$ . The function  $\theta_{S_i}(\varepsilon, x)$  is a unique Green's function which defines the density of states ( $DoS$ ) as the real part of the function  $G_{S_i} = \cos \theta_{S_i}(\varepsilon, x)$  (eq. 2-43).

$$\frac{DoS_{S_i}(\varepsilon, x)}{2N_{S_i}(0)} = \text{Re} \left[ \cos \theta_{S_i}(\varepsilon, x) \right] \quad 2-43$$

With  $N_{S_i}(0)$  the electronic density of states in the normal state Fermi surface of superconductor  $i$ . One also defines the function  $\text{Im}F(\varepsilon, x)$ , which is the imaginary part of the function  $F_{S_i} = \sin \theta_{S_i}(\varepsilon, x)$ :

$$\frac{\text{Im}F_{S_i}(\varepsilon, x)}{2N_{S_i}(0)} = \text{Im} \left[ \sin \theta_{S_i}(\varepsilon, x) \right] \quad 2-44$$

eq. 2-41 and eq. 2-42 need to be solved for the two superconducting films  $S_1$  and  $S_2$ , for which  $T_{c,S1} > T_{c,S}$ , using the boundary conditions at the free interfaces:

$$\theta'_{S_1}(x = d_{S1}) = 0, \quad \theta'_{S_2}(x = -d_{S2}) = 0 \quad 2-45$$

And at the interface of the two materials the boundary conditions are<sup>66</sup>:

## 2. Theoretical introduction

$$\gamma_{S_2}^* \theta'_{S_2} = \xi_{S_1}^* \theta'_{S_1}, \quad \gamma_{BN} \xi_{S_2}^* \theta'_{S_2} = \sin(\theta_{S_1} - \theta_{S_2}) \quad 2-46$$

Where  $\gamma$  and  $\gamma_{BN}$  are the interface parameters describing the nature of the interface between the two materials, defined by:

$$\gamma_{BN} = \frac{R_B}{\rho_{S_2} \xi_{S_2}^*}, \quad \gamma = \frac{\rho_{S_1} \xi_{S_1}^*}{\rho_{S_2} \xi_{S_2}^*} \quad 2-47$$

With  $\rho_{S_i}$  the normal state resistivity and  $R_B$  the product of the resistance of the  $S_1$ - $S_2$  boundary and its interface area. Qualitatively  $\gamma$  can be understood as a measure of the strength of the proximity effect between the two layers and  $\gamma_{BN}$  as the transparency of the boundary.

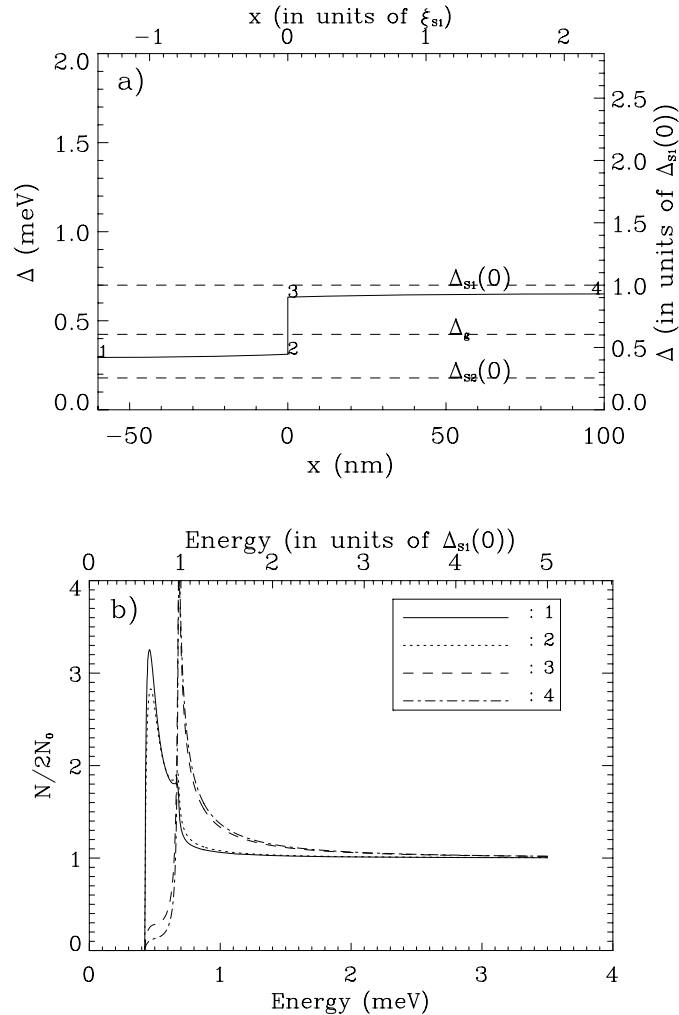


**Figure 2-7 a) The pair potential as function of position in the bi-layer for and b) the density of states for a proximised Ta/Al sandwich with thicknesses of 100/60nm. The numbers indicate different positions in the bi-layer with: 1) in the Al layer at the tunnel barrier, 2) in the Al layer at the interface with Ta, 3) at the same interface but in the Ta layer and 4) in the Ta layer at the vacuum surface.**

Figure 2-7 shows the resulting pair potential and density of states for a 100nm Ta and 60nm Al bilayer for which eq. 2-41 and eq. 2-42 have been solved numerically. First eq. 2-41 is solved numerically using the bulk values for the order parameter  $\Delta_0$ . The resulting  $\theta_{S_i}(\epsilon, x)$  is introduced into eq. 2-42 which calculates the first iteration of  $\Delta(x)$  which in turn is introduced into eq. 2-41. This is repeated until convergence is achieved.

The density of states on the four locations all show the lowest available state at the same value indicating a constant energy gap throughout the two layers of which the value lies in between the bulk values of the individual materials. Thus proximising a superconducting film by placing a second lower gap superconducting material can be used to lower the energy gap to a desired value which will improve responsivity and resolution of the devices.

The maxima of the density of states are rounded and different in the two materials. In the lower gap material the maximum occurs near the proximised energy gap while for the high gap material it occurs near the bulk value of the energy gap of the higher gap material. The latter causes a considerable concentration of quasiparticles at higher energies which proves to be of importance when proximised STJs are used with DROIDs. When the high gap material in the proximised STJ is the same as the BCS absorber a considerable concentration of the quasiparticles can reside above the energy gap of the absorber and they are free to diffuse out of the STJ. This produces a semi-open structure due to the partial trapping of quasiparticles in the STJs.

## *Chapter 3*

---

### Experimental set-up

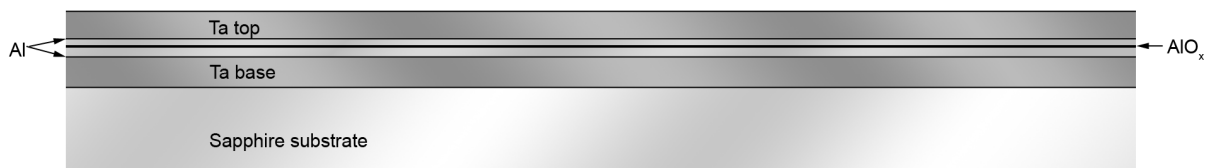
---

All the measurements in this thesis have been conducted in the laboratories of the Advanced Studies & Technology Preparation Division within the Directorate of Science & Robotic Exploration of the European Space Agency. Here a wide range of cryogenic refrigerators, corresponding readout electronics and illumination sources are available and used for testing and the development of the next generation detectors. Chapter 3 describes the fabrication process of the devices and the different apparatus used within the framework of this thesis. These are a  $^3\text{He}$  sorption, a  $^3\text{He}/^4\text{He}$  sorption cooler and an ADR, IV curve tracer, photo-pulse analyzers and pulse sampling electronics and a monochromator optical light source and optical set-up.

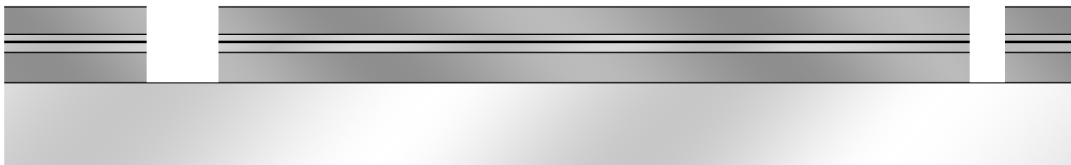
### 3.1 Fabrication

In this thesis two types of detectors from one manufacturer are used: pure Al STJs used in chapter 4 and Ta/Al DROIDs in chapters 5-8 produced by Cambridge MicroFab Ltd ( $\mu\text{fab}$ )<sup>62</sup>. Typically the process can be divided into two main parts. The first is the fabrication of the layers of the junction, mostly a multilayer of Ta/Al/ $\text{AlO}_x$ /Al/Ta where  $\text{AlO}_x$  forms the tunnel barrier. The second part, the post-processing, is forming the different structures which build up the STJ or DROID using several etching and deposition techniques. A general schematic representation of these steps is given in Figure 3-1.

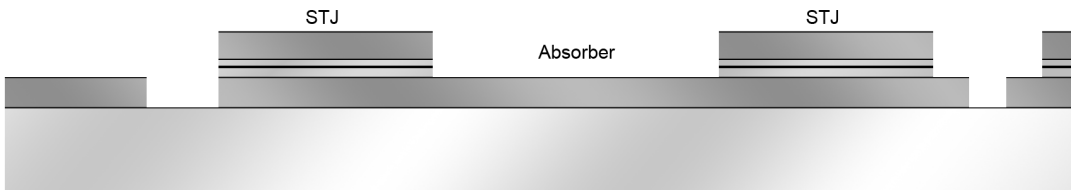
#### Trilayer



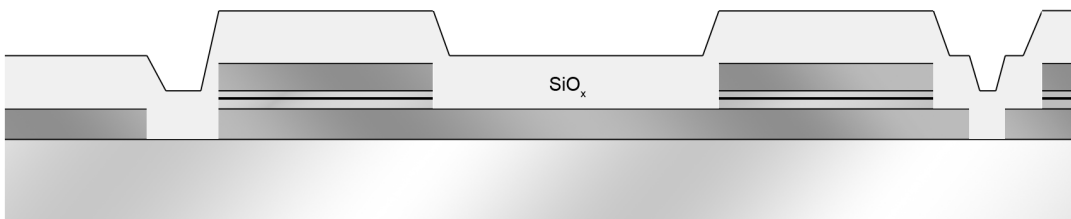
#### Base Etch



#### Mesa Etch



#### SiO<sub>x</sub> insulation



### 3. Experimental set-up

---

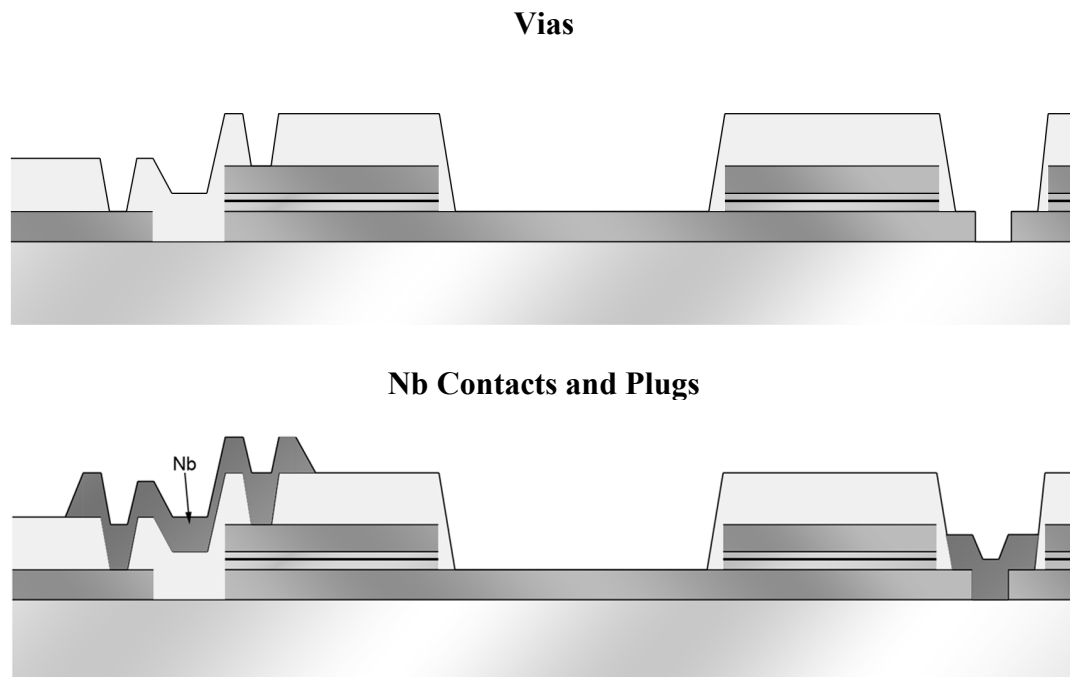


**Figure 3-1** A schematic representation of the different steps in the post-processing procedure. The vertical size is greatly exaggerated as is the size of the STJ compared to the absorber.

Microfab uses 2" diameter r-plane Sapphire wafers with a thickness of 0.5 mm fabricated by Kyocera. The trilayer is fabricated using DC-magnetron sputtering in a few mbar of high purity argon. The deposition system contains 4 processing stations which are loaded with high purity tantalum, niobium (Plansee<sup>63</sup>) and aluminium (TMI<sup>64</sup>) targets respectively while the last station is equipped with an Ion Beam Miller. Epitaxial tantalum is deposited on the substrate at a temperature of 810°C at a rate of 0.039nm/s (optimised for high RRR values). Aluminium is deposited in the second station at a temperature of -120°C at a rate of 0.05nm/s. Oxidation of the aluminium for the tunnel barrier is performed at 60°C for 2 hours under 187mbar oxygen pressure. Cap aluminium is deposited under the same conditions as before followed by depositing the tantalum layer at a temperature of 0°C, to ensure that the barrier stays intact but it produces a polycrystalline structure. The post-processing is performed at wafer level. The wafer is sawn into separate chips after post-processing is completed. Postprocessing involves the following steps (see Figure 3-1):

- 1) **Base etch**, defines the devices and leads. The definition of structures is performed using a Shipley S1813<sup>65</sup> photoresist and UV exposure with mask layer 1. The actual etch is divided into 3 parts. First the top tantalum is removed using plasma etch and the etchstop is optically determined. After rinsing and drying of the wafer the aluminium and barrier layers are removed using a wet etch for a total of 45 seconds. The surface is cleaned using Ion Beam Milling (IBM) for 45 seconds after which the tantalum base layer is removed with plasma etch. Finally the resist is removed using SVC-14.
- 2) **Mesa etch**, which removes the top layers and oxide barrier to form the leads, uses the same process as the base etch but stopping at the base tantalum layer.
- 3) **Passivation** insulates the devices by covering them with a SiO<sub>2</sub> layer and is performed by reactively sputtering silicon from a high purity target in an O<sub>2</sub> atmosphere for 75



minutes. The thickness of the layer is typically equal to the trilayer thickness plus ~160 nm.

- 4) **Vias** are etched into the SiO<sub>2</sub> using CHF<sub>3</sub> Reactive Ion Etching (RIE) for 22 minutes (for an oxide thickness of 440nm).
- 5) **Niobium** plugs are produced in the vias for the top and base contacts by sputtering Nb for 100 minutes at room temperature to a thickness of ~230nm. The high thickness is required due to the steep wall angle of the vias. The layer is patterned via lift-off technique by dissolving the AZ5214E resist underneath the unwanted material
- 6) **Dicing** of the chips is performed after the wiring is complete and the complete wafer is coated with a protective layer of resist. Dicing is performed with a 150μm wide resin bounded diamond blade with water cooling. During the process the wafer is bounded to thermal release tape (Revalpha) and the chips are later released by heating.

The pure aluminium devices are fabricated using roughly the same steps as with the Ta/Al devices except for slight changes in the base etch, mesa etch and etching of the vias. In the base etch only a wet etch is used to remove the aluminium. In the mesa etch IBM is used to etch the aluminium away until just below the barrier. To create the vias SF6 plasma etch is used which has a higher etching rate and stops at the aluminium surface. When used on the Ta/Al trilayer it would rapidly attack the exposed tantalum layer making it unfit for use in the production of these devices.

### 3.2 Cryostats

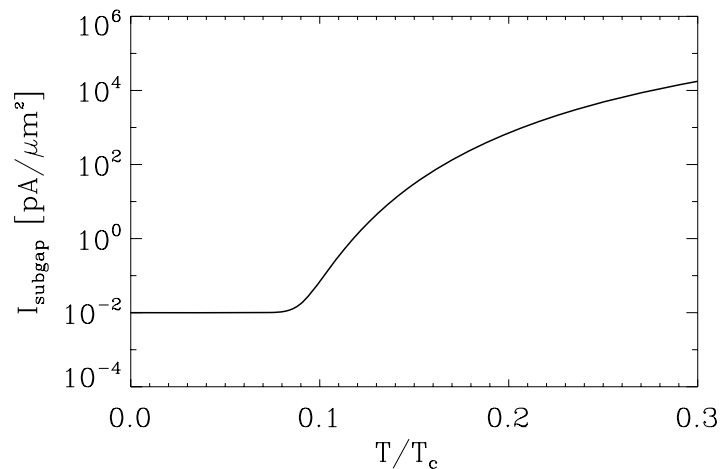


**Figure 3-2** The tunnel current of thermally excited quasiparticles as a function of temperature at a bias voltage of 100μV. A barrier resistivity of  $R_{nn}=2 \mu\Omega\text{cm}^2$  and a leakage current of 0.01 pA/μm<sup>2</sup> is used.

Figure 3-2 shows the theoretically predicted subgap tunnel current in a BCS-type superconducting tunnel junction as function of temperature calculated using eq. 2-39, a normal barrier resistivity, which is a measure of the barrier transparency, of  $R_{nn}=2 \mu\Omega\text{cm}^2$  and a leakage current of 0.01pA/μm<sup>2</sup>. Such a leakage current is typical for a high quality barrier and generally independent of temperature. It shows that in order to sufficiently reduce the thermally excited quasiparticle population, the STJ or DROID needs to be operated at a temperature below a tenth of its critical temperature. For the widely used tantalum STJ ( $T_c=4.5\text{K}$ ) a temperature of 300mK obtained with <sup>3</sup>He sorption coolers is sufficient. However, in tantalum STJs proximised with aluminium the energy gap is reduced and for an aluminium

### 3. Experimental set-up

---

thickness of more than 60nm ( $\Delta_g < 500\mu\text{eV}$ ) the operating temperature of 300mK becomes critical.

Illumination from the outside of the cryostat introduces an extra complication. When imaging or accurate positioning of a light spot is required the devices need to be illuminated directly from the outside through windows and apertures in the different shields. This introduces an extra thermal load of 300K black body radiation. This flux of sub-threshold IR photons causes pile up, which shows up as a broadening of the spectral features, and acts as a noise source similar to electronic noise<sup>67</sup>. The IR radiation can be filtered out using optical filters. Alternatively an optical fibre can be used to transfer the photons into the cryostat. This option will effectively filter out any infrared photons due to the low transmittance of the fibre at these wavelengths. It is also much easier to decouple the device from the warm environment so that the optimum low noise conditions can be achieved. However it is impossible to perform imaging or positional measurement since due to the surface roughness and distance from the detector due to illumination through the substrate the used fibre will spray the light over a wide range of angles. The fibre option is more attractive if a quick assessment of a device performance in responsivity and energy resolution is required.

With all the used cryostats the STJs are read out using electronics at ambient temperature which requires a sufficient amount of signal wires running from ambient temperature to the coldstage of the cryostat. The resistance of these signal wires, which is in series with the junction, need to be low in order to keep the STJ stable during photon detection. The wires are mounted in looms and close to groundplanes ( $\text{N}_2$  tank and He tank) in the cryostat to reduce microphonics and EMI pick-up. No extra EMI filtering is applied since this is currently not a limiting factor in noise performance of the devices.

#### 3.2.1 Heliox system ( $^3\text{He}$ cooler)

The Heliox system (Oxford Instruments) consists of a  $^4\text{He}$  bath producing a 4K environment in which an insert is positioned (see Figure 3-3). When the insert is cooled to 4K the complete insert is evacuated to provide thermal insulation from the 4K bath. The insert contains a  $^4\text{He}$  reservoir (named 1K pot), filled with  $^4\text{He}$  from the bath, which is pumped using a rotary pump and cools down to 1.5K. At this temperature the  $^3\text{He}$  in the closed  $^3\text{He}$  reservoir, which is thermally linked to the  $^4\text{He}$  reservoir, condenses. When most of the  $^3\text{He}$  is condensed a piece of charcoal inside the closed  $^3\text{He}$  reservoir, which has been kept at a temperature of 40K to release all the gaseous  $^3\text{He}$ , is cooled using  $^4\text{He}$  from the bath. When the temperature of the charcoal is below 20K it starts to pump on the condensed  $^3\text{He}$  reducing the pressure. The temperature of the  $^3\text{He}$  decreases to below 300mK as does the temperature of the sample holder which is physically attached to the bottom of the  $^3\text{He}$  reservoir.

The cryostat can be operated in two operation modes. In the first mode the 1K pot is filled with  $^4\text{He}$ , closed and pumped. In this mode the lowest base temperature of 280mK is reached but the hold time is limited by the evaporation of the  $^4\text{He}$  which has to be refilled every 1.5 hour. In the second mode the 1K pot is continuously refilled by properly adjusting a needle valve, while being pumped upon. The hold time is now limited by the  $^3\text{He}$  evaporation which is >30 hours depending on the thermal load. The longer hold time obtained by running the 1K pot in flow mode is at the expense of a higher noise level, originating from the flow of  $^4\text{He}$ , and a higher base temperature of 300mK.

The whole cryostat is shielded from the earth's magnetic field using a double  $\mu$ -metal shield. Submerged in the liquid helium bath a superconducting magnetic coil is present which surrounds the sample space providing a magnetic field parallel to the plane of the tunnel barrier to suppress the Josephson currents of the STJs.

The Heliox systems have a fast turnaround time making it ideal for fast characterisation of the devices. Illumination of the samples is provided using a UV-grade optical fibre (ORIEL 77530). This is in contact with the backside of the transparent sapphire substrate of the STJs on the cold side, and can be coupled to a light source outside the vacuum on the warm side. The transmission curve of this fibre conveniently cuts off at a wavelength of  $\sim 2$  micron. If cooled over a sufficient length, the fibre will effectively block all thermal infrared radiation. The wiring of the heliox contains a single ground line for all devices and individual signal wires for each STJ. At the warm parts of the Heliox the wiring is copper to assure low wire resistance ( $3.5\Omega$  per single wire) and at the cold part it is superconducting wire to reduce the thermal load on the cold stage. From the warm to the cold stage the wires are approximately 1m in length. The devices (STJs or DROIDS) are selected individually at the output of the signal wires and are read out using dedicated electronics at ambient temperature as explained below.

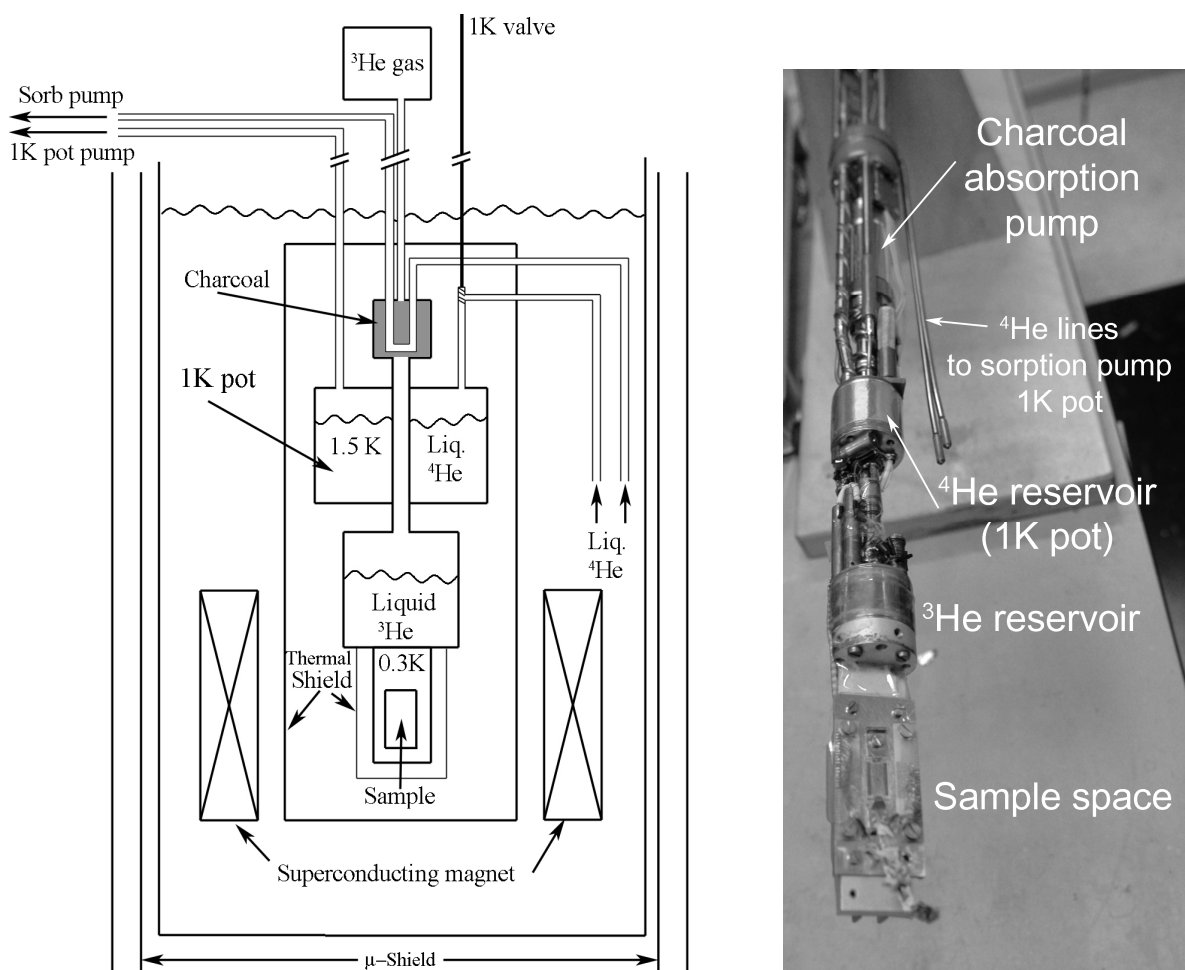


**Figure 3-3 Schematic representation and photograph of the Heliox  $^3\text{He}$  sorption cooler. A liquid nitrogen cooled shield surrounding the liquid helium reservoir is not shown in the schematic representation.**

### 3.2.2 Bradford cryostats with $^4\text{He}/^3\text{He}$ sorption coolers

Two custom-made cryostats (Bradford Engineering BV) built for the different S-Cam systems, have been used for experiments described in chapters 6 and 8, respectively. Rather than quick turnaround time, these systems offer external access for radiation and mobility. They simply provide a liquid He cooled cold plate/sample stage in vacuum at 4K with an

### 3. Experimental set-up

access port for external radiation. Thermal insulation is provided by Multi Layer Insulation (MLI) such that no liquid nitrogen is required. The 4K sample space measures  $\sim 24\text{cm}$  in diameter and 15 cm in height, which provides space for additional coolers, detector holders and magnets. The detector holder is suspended from the cold plate by Kevlar strips which provide the required thermal insulation and sufficient mechanical stability. Copper straps provide the thermal link between coolers and detector holder. Magnets are directly mounted on the 4K cold plate.

Both cryostats are equipped with sorption coolers from CEA, Grenoble. These coolers operate on the same principles as the Heliox systems described above with a closed  $^3\text{He}$  reservoir pumped by charcoal to cool the sample holder to a temperature of  $\sim 300\text{mK}$ .

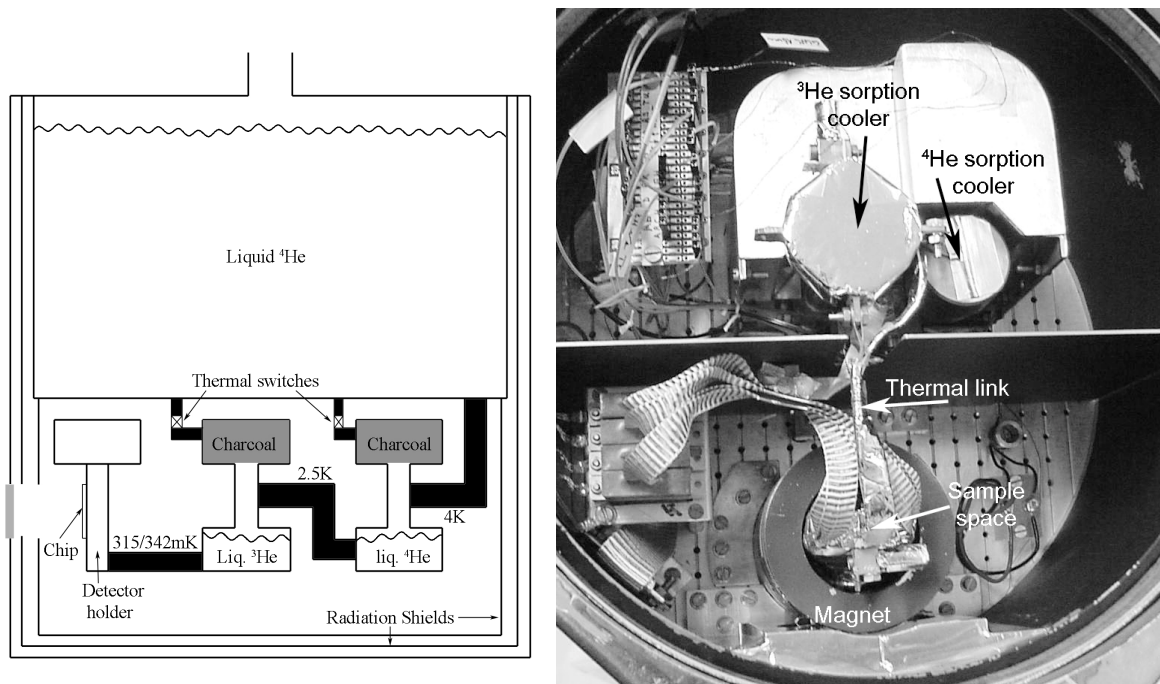


**Figure 3-4 Schematic representation and a photograph of a Bradford cryostat equipped with a double stage  $^4\text{He}/^3\text{He}$  sorption cooler from CEA, Grenoble (France).**

The Bradford I system has a single  $^3\text{He}$  sorption cooler. The liquid helium bath is continuously pumped to maintain a cold plate temperature of 1.9K, sufficiently low to condense the  $^3\text{He}$ . The temperature of the charcoal pump can be controlled with a heater and a gas-gap heat switch. The base temperature of this system is 320mK with a hold time of 6.5 hours (limited by the liquid helium bath) and an additional few hours at 450mK, after refilling the liquid helium bath, without pumping ( $T_{\text{cold plate}}=4\text{K}$ ).

The Bradford II system (Figure 3-4 and Figure 3-10) has an additional sorption cooler containing  $^4\text{He}$  which is thermally linked to the liquid helium bath to liquify the  $^4\text{He}$  in the  $^4\text{He}$  reservoir. This cooler provides a temperature of 2.5K at which the  $^3\text{He}$  from the second sorption cooler can be liquified. This removes the need of pumping the liquid helium bath continuously and also allows to top-up the bath without disturbing the base temperature. In practice, however, a significantly more efficient condensation is achieved if the bath is pumped during the condensation phases of the sorption coolers. In this way an uninterrupted hold time of  $\sim 28$  hours at a base temperature of 290mK is possible. If the bath is continuously pumped, the base temperature drops as low as 260mK, but with limited bath hold time.

The Bradford systems have a thin (110 $\mu$ m)  $\mu$ -metal shield which does not completely surround the sample space to protect the devices from the Earth magnetic field during cool down. Depending on the size of the detector arrays, this is found to be marginally sufficient and complicating the cool down procedure. A separate double  $\mu$ -metal shield is therefore used in which the cryostat is situated during cool down and from which it is lifted after the cool down procedure is finished. The Bradford systems have apertures and windows in place in the different thermal shields which make illumination from the outside possible. An optical relay (explained in 3.4.2) can be placed in front of the cryostat in order to focus the light and project images on the detectors.

Both Bradford cryostats are equipped with signal wiring consisting of manganine (300K-4K) and superconducting Nb-Ti (4K-300mK) with a roundtrip resistance of  $\sim 25\Omega$ . The wires are bundled in woven looms. Each STJ has a dedicated signal wire and up to 30 STJs share a single return wire. Bradford 1 has 36 signal wires and Bradford 2 has 120 signal wires. Bradford 1 can readily be mated with any of the available readout electronics, like the DROID photo analyser (explained in section 3.3.2), used on other cryostats (e.g. Heliox), while Bradford 2 can currently only be combined with the dedicated S-Cam 3 readout system (explained in section 3.3.4). The entire S-Cam 3 cryogenics and readout system, which has been designed to be very flexible, can readily be used in combination with DROIDS making it a perfect test bed for DROID arrays.

### 3.2.3 Adiabatic Demagnetisation Refrigerator (ADR)

To test the low gap aluminium junctions of chapter 1 an Adiabatic Demagnetisation Refrigerator (ADR) build by VeriCold, which reaches a base temperature of 50mK, has been used. The ADR contains two concentric paramagnetic salt pills. The inner salt pill, which is connected to the sample stage, is made of Ferric Ammonium Alum (FAA) and has a base temperature of 50mK. The second is made of Gadolinium Gallium Garnet (GGG), has a base temperature of 1K and functions as a thermal shield from the 4K environment. Both salt pills are suspended using 14 thermal isolating Kevlar strings from the 4K environment, which is cooled using a helium bath. The two salt pills can be thermally linked to the 4K base plate using a mechanical switch operated by a stepper motor. The two paramagnetic salt pills are surrounded by a single superconducting magnet immersed in the helium bath. This magnet is able to produce a magnetic field up to 7 Tesla at its centre magnetising both salt pills simultaneously during the cool down procedure. The sample space is shielded from this magnetic field by a small  $\mu$ -metal box reducing the stray magnetic field to less than a Gauss. During experiments a Helmholtz coil inside the  $\mu$ -metal box creates the magnetic field necessary for the Josephson current suppression in the STJs.

After the complete system is cooled down to 4K by liquid helium the current in the superconducting magnet is slowly ramped up to 36A in 30min producing the maximum field strength and magnetising the two salt pills. The normally random oriented dipoles in the two salts tend to orientate themselves along the applied external field. This process produces heat which is fed to the 4K base by the thermal switch. One and a half hours after the maximum field strength is reached the system is thermalised again to 4K and the switch is opened disconnecting the thermal link thermally isolating the paramagnetic salt pills and the sample space attached to them. The current through the superconducting magnet is ramped down from 36A to 0A in 30min reducing the magnetic field. With the reducing magnetic field the ordered dipoles in the paramagnetic salt pills start to relax into the previous randomness extracting entropy from the crystalline structure and sample space providing adiabatic cooling.

### 3. Experimental set-up

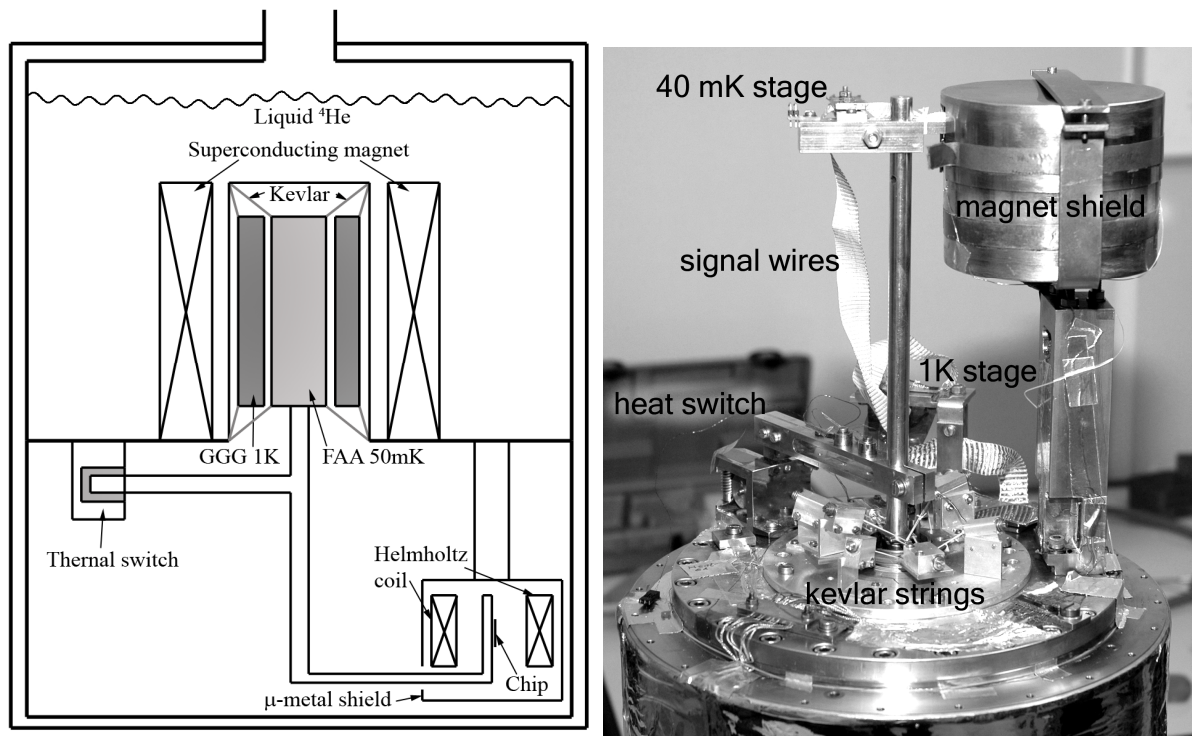


Figure 3-5 Schematic representation of the ADR from VeriCold.

The ADR is equipped with a UV-grade optical fibre similar to the one used in the Heliox system which is in contact with the backside of the transparent substrate of the STJs, and can be coupled to a light source outside the vacuum. The 36 signal wires from the ADR are copper on the warm part (300K-4K), to assure low wire resistance, and superconducting NbTi at the cold part (4K-50mK), to assure good thermal insulation. The wires are in woven looms and grouped in the same way as with the Heliox system (a single ground wire for all devices and individual signal wires for each STJ). The same electronics used with the Heliox system and Bradford 1 system can be used with the ADR system for readout.

### 3.3 Read out electronics

The two main functions of any readout electronics for STJs are:

1. To record current voltage characteristics of an STJ:

The current voltage (IV) curve is a good characterisation tool for the STJs. Before an STJ is used as a detector, it provides information on the subgap currents, normal resistance and sum of the gap of the two superconducting electrodes. It also shows the efficiency of suppression of the Josephson current and Fiske modes by the applied magnetic field and as such it helps in finding the optimum magnetic field and voltage bias for the STJ under investigation. Finally, the IV curve will immediately reveal if a cool down was successful or has resulted in trapped magnetic flux inside the STJ.

2. To detect and record photon-induced current pulses from an STJ:

Most of the physics inside the STJ can be deduced from the current pulses. For instance the responsivity and falltime of the current pulse are important properties which determine the quality of the detector. With these quantities we can determine the average tunnel time and average number of tunnels of the quasiparticles. Two methods are used to detect and record the current pulses. The first is using a charge sensitive pre amplifier, which amplifies the signal, followed by a shaping stage, which provides the trigger signal for the recording and filters the signal. The second method is sampling the current pulse after a preamplifier with which the complete evolution of the current pulse is measured. This method is normally used with X-ray photons because the current pulse is sufficiently above the noise.

For reasons of simplicity and accessibility we have chosen to operate all readout electronics outside the cryostats at room temperature. It should be noted though that there may well be advantages in operating, for example, the input stage of the charge sensitive preamplifiers (described below) much closer to the STJ such that any adverse effects of wiring capacitance and resistance, as well as EMI and microphonics could be reduced.

### 3.3.1 IV curve tracer

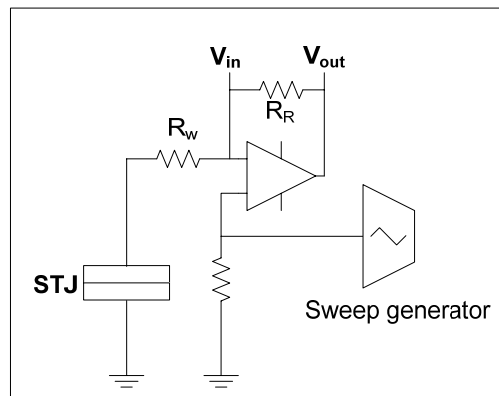


**Figure 3-6 Schematic of the IV-curve tracer set-up.**

In order to measure the IV-curve, Figure 2-6, of a STJ we use an IV-curve tracer as shown schematically in Figure 3-6. In this procedure a voltage  $V_{in}$  is applied to the top electrode of the junction which is increased stepwise to a maximum of  $V_{max}$ , decreased to a minimum voltage of  $-V_{max}$  and increased again to 0V. At every voltage step the voltage  $V_{out}$  is measured. The current  $I_{STJ}$  running through and the voltage  $V_{STJ}$  across the junction are given by:

$$I_{STJ} = \frac{V_{out} - V_{in}}{R_R} \quad 3-1$$

$$V_{STJ} = V_{in} - I_{STJ} R_w \quad 3-2$$

Where  $R_w$  is the wire resistance of the wires between the junction and the electronics at room temperature. The range resistor  $R_R$  can be chosen to be 100Ω, 10kΩ or 1MΩ depending on the required maximum current which has to be supplied to the junction. It is noted that using this circuit the supercurrent at 0V bias voltage can not always be measured since it can saturate



### 3. Experimental set-up

the electronics. However, we are mainly interested in the subgap region of the IV curve, since this is where we will bias or devices, and in the suppression of the Josephson current and Fiskesteps. Thus this will not impose a problem.

#### 3.3.2 DROID photo-pulse analyser

The DROIDS used in this thesis consist of an absorber strip with two proximised STJs, one at each end, for read out. Each of the STJs of a DROID needs a dedicated electronic chain to be read out. However, because a photon absorbed in the DROID produces a signal in both STJs, which are both needed to reconstruct the photon energy and absorption position, the two channels need to be correlated. In other words we need to find nearly coincident events in both channels belonging to the same photon absorption. This correlation can either be performed online in the electronics or offline using time information from the recorded events.

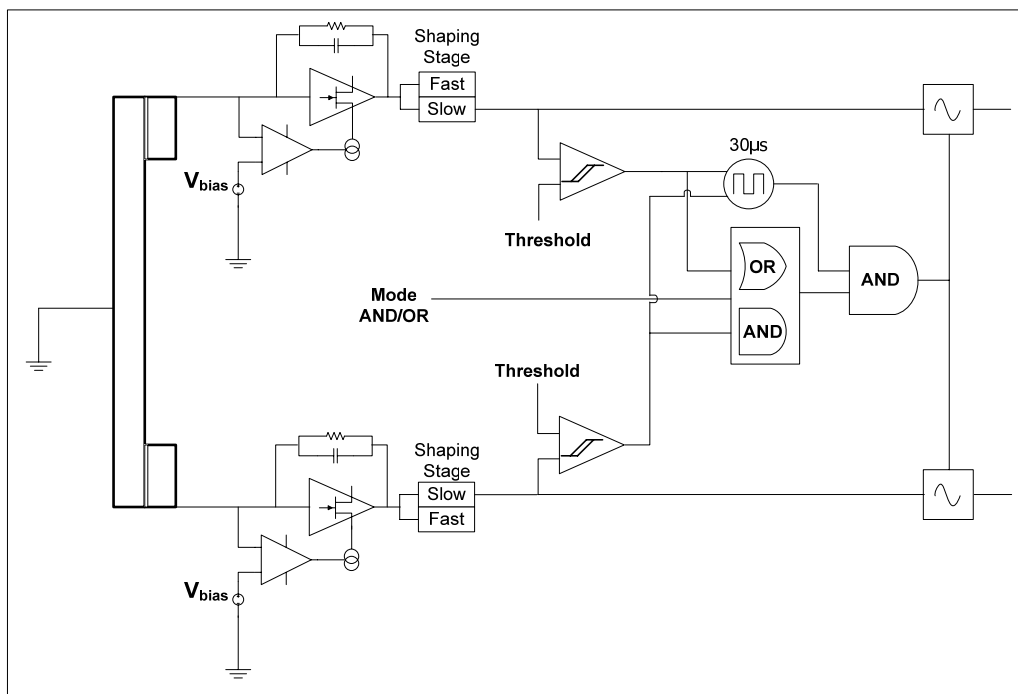


Figure 3-7 Schematic of two paired channels of the DROID photo-pulse analyser.

For the measurement on individual DROIDS a 4 channel readout system is developed which consist of 4 readout chains which are coupled together in pairs (Figure 3-7). Each electronic channel consists of a charge sensitive pre-amplifier with a feedback RC time of  $\tau_{RC}=470\mu s$  which integrates the signal created by the detector. The input stage of the preamplifiers is a J-FET (IF9030). The output of the pre-amplifier is fed into two semi-Gaussian bipolar CR-RC-CR-RC shaping filters which limit the noise bandwidth and pulse duration. The output of the shaping stages provides a bipolar signal with a maximum quickly followed by a minimum. The maxima of these signals are then measured using an analogue to digital converter. The two shaping stages of a single read out channel have different RC time constants, a slow and a fast RC time constant defining the slow and fast signal. Usually the 'slow' signal provides the best spectral information. The 'fast' channel provides a trigger signal for the sample and hold functions in both channels. Originally this design was used with single STJs to provide information on the total tunnelled charge and the fall time of the tunnel current pulse, after



calibration with exponential pulses. However, since the shape of the current pulse in DROIDS is affected by the diffusion of quasiparticles through the absorber and changes with absorption position this method is not accurate when used with DROIDS.

The two channels are combined logically to look for coincident events. When one channel is triggered a clock, with a time window of  $30\mu\text{s}$ , starts. If the second channel is triggered within this time window the two events are defined as coincident and belonging to the absorption of a single photon. The output of the electronics consists of three values per channel: the value of the pulse height of the slow and fast shaping stage and the time elapsed since the first trigger, thus either zero or  $\Delta t$ .

The electronics can be used in two modes. In the first mode, the 'OR' mode, the events are always passed when one of the channels is triggered. When no trigger occurs within the time window in the second channel the values of this channel are set to zero. In this mode the user is sure to detect all events even if the signal in the opposite channel is below the trigger level. In the second mode, the 'AND' mode, the events are only passed if a trigger occurs in both channels within the time window. This mode is a very effective noise filter but requires sufficient responsivity in both channels. Also, if the trapping in the STJs is perfect, no STJ signal will be detected because, following an absorption in one of the STJs a small signal above the threshold should be present in the opposite STJ.

### 3.3.3 Pulse sampling

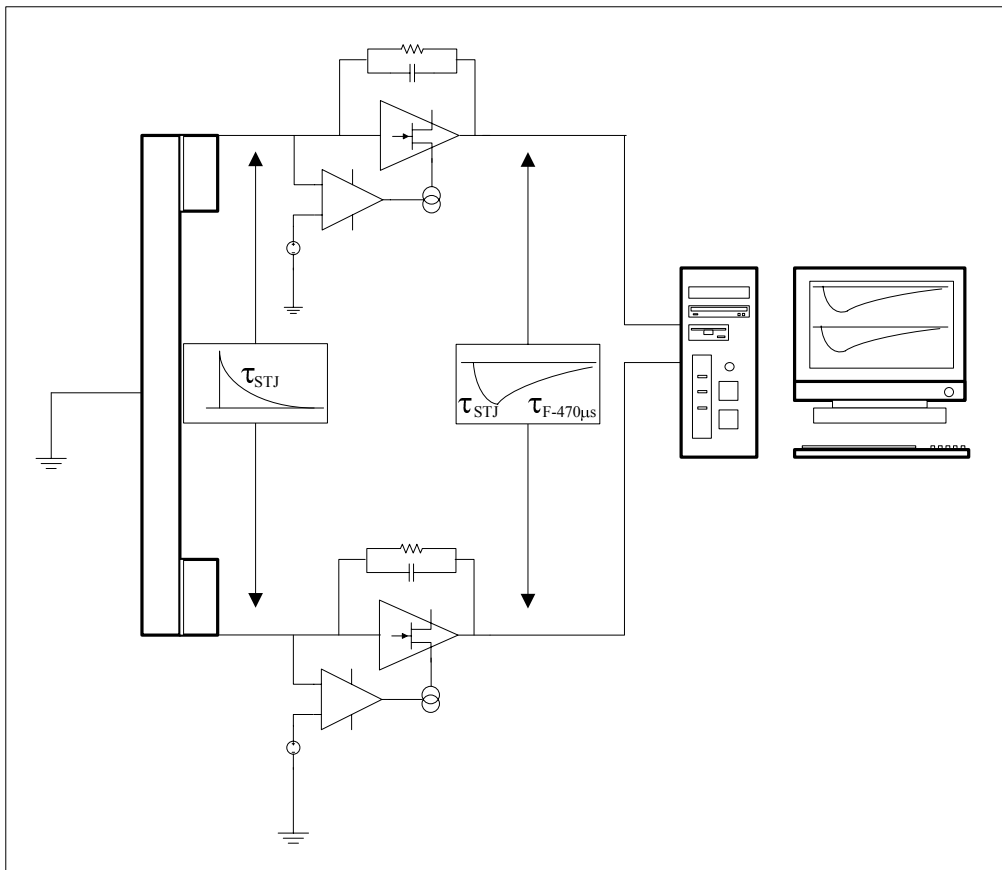


Figure 3-8 schematic representation of the pulse sampling set-up.

In order to obtain true responsivity measurements of the DROID the tunnel current pulses need to be sampled directly. Unfortunately the current pulses resulting from the absorption of

### 3. Experimental set-up

an optical photon are well within the noise levels and thus impossible to detect directly. A charge sensitive preamplifier with a long RC time,  $\tau_{RC}=470\mu s$ , the same as used with the DROID photo-pulse analyser, is used to obtain the integrated pulse profiles. The output of the two preamplifiers is fed into a PC equipped with a GaGe (CS14100) oscilloscope card. The detection threshold is set on one of the channels and when it is triggered the GaGe software stores both pulse profiles on the PC in 4096 samples, from which 1024 are pre-trigger samples. A schematic of the electronic set-up is shown in Figure 3-8.

Offline software is used which mimics a bipolar Gaussian shaping stage to present the data in a similar fashion as the output of the DROID photo-pulse analyser. This data is converted into photon energy and positional data using a model, like the model produced by Kraus *et al*<sup>28</sup> (for DROIDS with perfect trapping in the STJs) or Jochum *et al*<sup>68</sup> (for DROIDS with imperfect trapping in the STJs).

On the basis of the absorption position the data is divided into several sections, in general 11 sections on the absorber and each STJ (Figure 3-9). First the edges of the absorber are determined by eye and the data points in between are separated in equidistant sections using an algorithm. The pulses belonging to the events within a section are averaged to reduce the noise, which is possible as long as the size of the sections is smaller then the position resolution of the DROID. The resulting averaged pulses are de-convoluted to remove the contribution of the pre-amplifier and the true current pulse is obtained. This is then integrated to compute the responsivity.

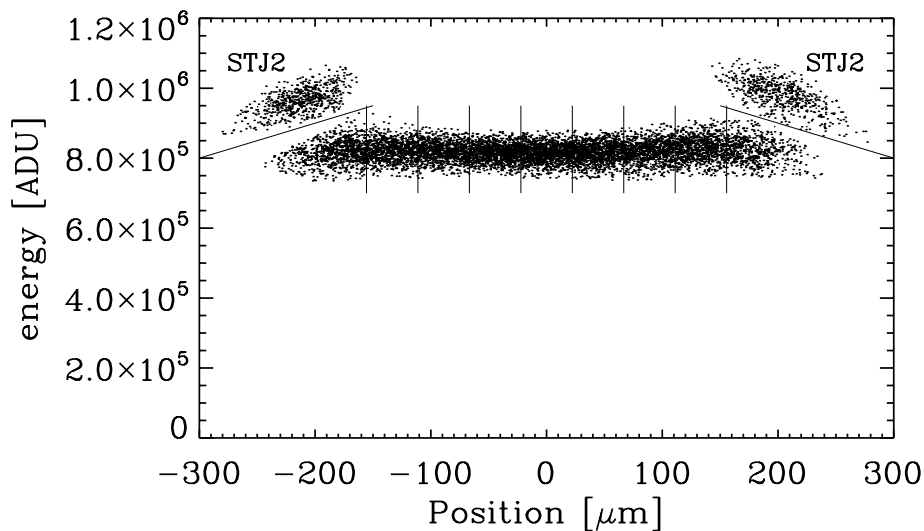


**Figure 3-9** A position versus energy scatter plot, using the model from Jochum *et al*, in which the data is divided into 11 sections.

The method to de-convolute the response from the pre-amplifier is derived in the following steps:

$$H_m = H_{stj} \otimes H_{PA} \quad 3-3$$

Where  $H_m$ ,  $H_{stj}$ , and  $H_{PA}$  are the measured signal, the signal from the STJ and the response from the preamplifier, respectively.

$$L(H_m) = L(H_{stj}) \cdot L(H_{PA}) \quad 3-4$$

where  $L(f(x))$  is the Laplace transformation of the function  $f(x)$ .

$$\begin{aligned} L(H_{stj}) &= \frac{L(H_m)}{L(H_{PA})} \\ &= L(H_m) \cdot \left( s - \frac{1}{\tau_{RC}} \right) \\ &= s \cdot L(H_m) - \frac{1}{\tau_{RC}} L(H_m) \\ &= L\left( \frac{dH_m}{dt} - \frac{1}{\tau_{RC}} H_m \right) \end{aligned} \quad 3-5$$

Here we have taken the response of the preamplifier to be  $L(H_{PA}) = L\left(e^{-t/\tau_{RC}}\right) = 1/(s - 1/\tau_{RC})$  and used the rule for the derivative of  $f(x)$   $L(f'(x)) = sL(f(x))$ . The resulting signal from the STJ is given by:

$$H_{stj} = c \frac{dH_m}{dt} - c \tau_{RC} H_m \quad 3-6$$

Here the factor  $c$  is the voltage-current conversion gain given by the value of the used feedback capacitor.

### 3.3.4 S-Cam 3 120-channel read out electronics

In order to read out an entire array of DROIDS simultaneously multiple readout channels need to be put in parallel preferably in pairs of two channels, one for each STJ on a DROID. Such a system is present as the S-Cam 3 system (Figure 3-10), although it is geared towards the readout of 120 single STJs and the two channels belonging to the STJs of a DROID are not linked.

Four boxes with 32 input pre-amplifiers each are mounted on the Bradford II cryostat. The design of the pre-amplifier is similar to that of the ones used in the DROID photo-pulse analyser with a 470M $\Omega$  resistor and 1pF capacitor. The signals of the pre-amplifiers are immediately sampled by analogue to digital converters at a programmable rate of up to 40 Msamples/s. These digital signals are passed to a Finite Impulse Response (FIR) filter which serves as a shaping stage. The response of a FIR filter is finite because it settles to zero in a finite number of sample intervals. The response  $y[n]$  of the filter on the signal  $x[n]$  is

$y[n] = \sum_{i=0}^N b_i x[n-i]$  where  $N$  is the filter order. The right hand side has  $N+1$  terms which are commonly referred to as taps with tap coefficients  $b_i$ . In the S-Cam filters these are equal to 1 or -2. By changing the length of the filter and/or the sampling rate the effective shaping time can be changed over several orders of magnitude, thus allowing optimizing the system for speed or for energy resolution.

### 3. Experimental set-up

---

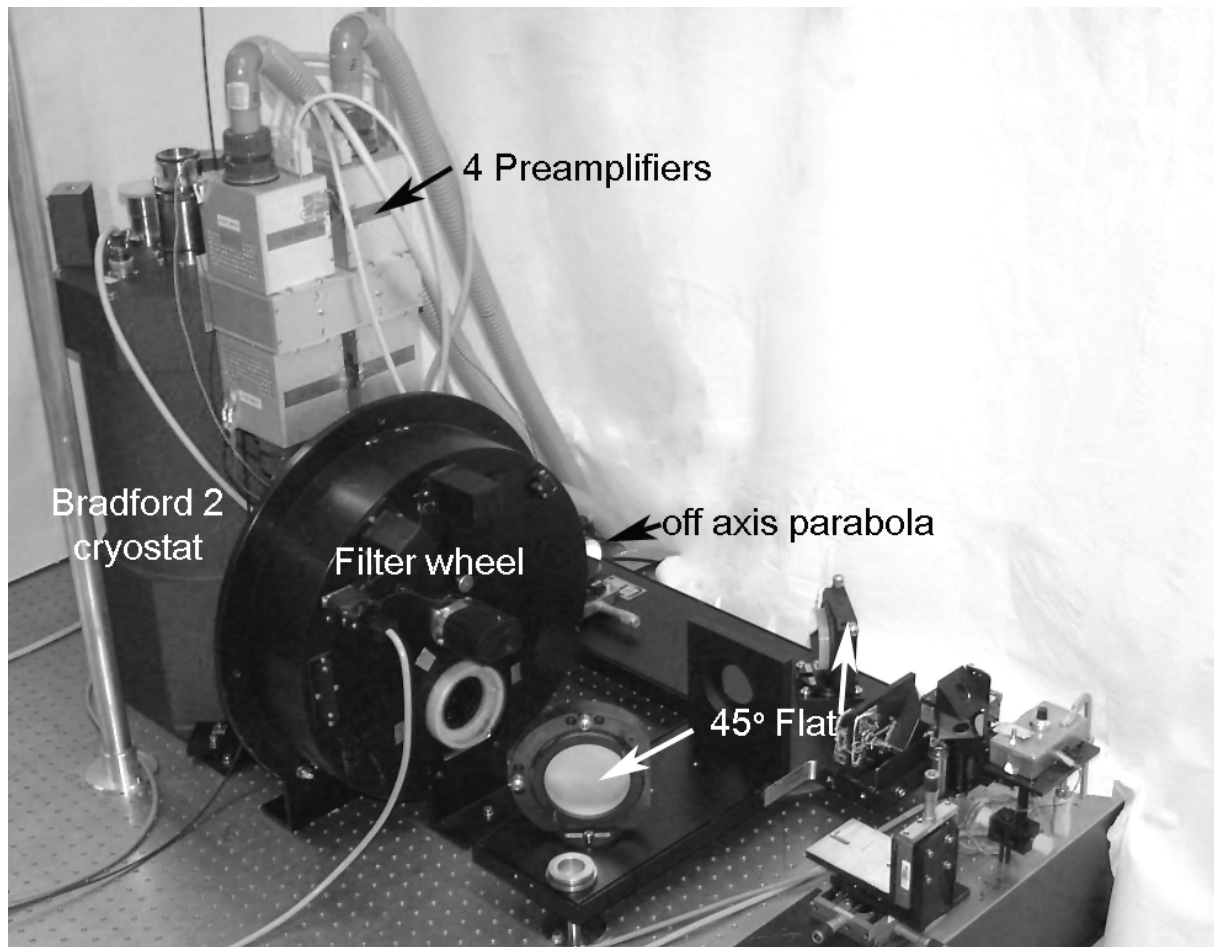


**Figure 3-10** Photograph of the S-Cam 3 set-up displaying the Bradford 2 cryostat with the 4 charge sensitive preamplifiers attached and the optical unit in front.

Each channel reads out a single STJ and when it is triggered it records the time (derived from a GPS receiver) and two measures for the charge, the maximum and minimum of the bi-polar output signal of the FIR filter. As the channels are not linked together the output consists of 120 data arrays in which noise events are scattered arbitrary in time and numbers. Using the absolute timing information, in the two channels reading out the STJs of a single DROID, coincident events have to be found offline in order to reconstruct the responsivity and absorption position.

## 3.4 Illumination

### 3.4.1 Double grating monochromator

In order to perform experiments with optical photons a double grating monochromator is used. The monochromator assembly consists of a Xenon lamp as a light source (ORIEL 7340) in combination with two gratings (ORIEL 77250) to select the desired wavelength. The monochromator is able to produce photons with wavelengths from 200 to 1000nm with a bandwidth of  $\sim 5$ nm. Using a UV-grade optical fibre (ORIEL 77530) the output is coupled to the desired set-up.

### 3.4.2 S-Cam optical unit

The S-Cam 3 optical relay chain (Figure 3-10 and Figure 3-11) which can be used in combination with both Bradford systems uses an off-axis parabolic mirror to produce a collimated beam. Two flat mirrors fold the beam and direct it to the lens assembly attached to the cryostat. A set of 3 infrared filters (10mm KG2 glass and 10mm BK7 glass at 4K and another 10mm BK7 glass at 300mK) inside the cryostats filter out the infrared radiation to reduce thermal load and the low energy photons, resulting in an available wavelength band of 345-750nm. The devices can be illuminated by calibration sources or via a fibre attached to a diffuser, both situated in the focus of the off axis parabola. In astronomical observations the telescope focus (Nasmyth or Coudé) is aligned to the focus of the parabola. A movable pinhole holder is present in the focus of the parabola to project different pinholes or masks onto the detectors.

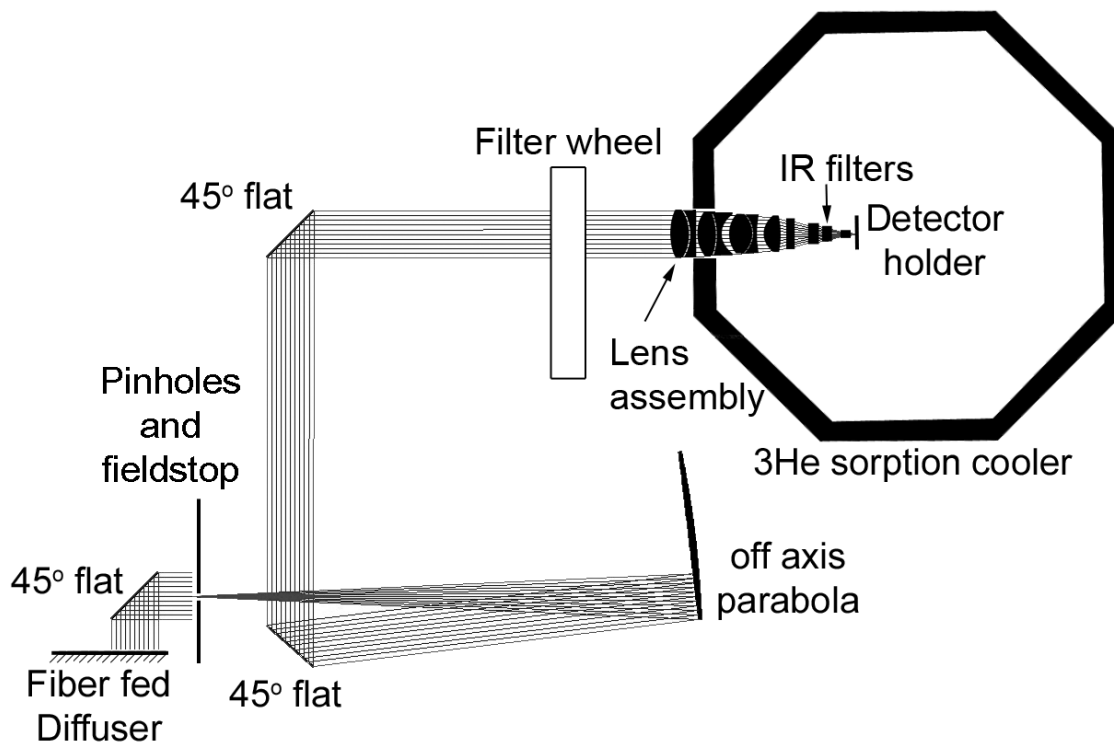


Figure 3-11 Schematic of the S-Cam 3 optical unit.

## Chapter 4

---

# Dynamics of nonequilibrium quasiparticles in narrow-gap superconducting tunnel junctions

---

A. G. Kozorezov, R. A. Hijmering, G. Brammertz, J. K. Wigmore, A. Peacock, D. Martin, P. Verhoeve, A. A. Golubov, and H. Rogalla

Phys. Rev. B **77**, 014501 (2008)

The latest generation of high quality, narrow gap, superconducting tunnel junctions (STJs) exhibits a steady state and time-dependent behaviour which cannot be described satisfactorily by previous treatments of non-equilibrium quasiparticle (qp) dynamics. These effects are particularly evident in experiments using STJs as detectors of photons, over the range from near infrared to X-ray. In this paper, we present a detailed theoretical analysis of the spectral and temporal evolution of the non-equilibrium qp and phonon distributions in such STJs excited by single photons, over a wide range of excitation energy, bias voltage, and temperature. By solving the coupled set of kinetic equations describing the interacting excitations, we show that the non-equilibrium qp distribution created by the initial photon absorption does not decay directly back to the initial undisturbed state in thermal equilibrium. Instead, it undergoes a rapid adiabatic relaxation to a long-lived, excited state, the spectral distribution of which is non-thermal, maintained by a balance between qp creation, recombination, and trapping. The model is able to describe successfully photon absorption data taken on several different aluminium STJs, using a single set of parameters. Of particular note is the conclusion that the local traps responsible for qp loss are situated specifically in the region of Nb contacts.

### 4.1 Introduction

The phenomenon of tunnelling has been widely used as a tool to explore the basic physics of superconductivity, as well as to provide the underlying principle for numerous superconducting devices<sup>60</sup>. There is currently great interest in using high quality superconducting tunnel junctions as single photon detectors for astrophysical and other applications<sup>69</sup>. Such detectors operate under highly non-equilibrium conditions which do not occur in any other experimental scenario. Their performance is very sensitive to microscopic details of the quasiparticle (qp) dynamics and hence provides a unique opportunity for studying non-equilibrium behaviour of the qp population.

As a photon detector, the superconducting tunnel junction (STJ) possesses excellent responsivity (charge output per unit photon energy input), energy resolution, and count rate capability over a broad spectral range, from near infrared to hard X-ray.<sup>70-73</sup> In order to optimize these characteristics, recent work at ESA and elsewhere has been focused on the development of improved devices having smaller energy gaps, highly homogeneous and transparent barriers, and extremely low quasiparticle loss rates. A key parameter is the energy gap, and first generation Nb STJs were succeeded by Ta, then by proximized Nb/Al and Ta/Al ones, and most recently by pure Al structures, with energy gap one-eighth that of Nb. While, as expected, the new devices exhibit significantly improved detector characteristics, several totally new phenomena have also emerged, including internal amplification due to qp back tunneling<sup>74</sup>, enhanced tunnelling and phonon noise<sup>75,25</sup>, and time-dependent tunnelling statistics<sup>76,77</sup>. However, the most exciting discovery has been that of a whole new class of phenomena related to the formation of a non-equilibrium, coupled qp-phonon state due to multiple tunnelling under bias.

The observation of this non-equilibrium situation in steady-state experiments and the explanation of its origins have been reported earlier<sup>78,79</sup>. In a low loss, narrow energy gap, multi-tunnelling device, qps may retain an accumulated energy of  $2eV$ , where  $V$  is the bias voltage, for each cycle of forward and back tunnelling before relaxation. In this context, a narrow gap STJ is the one in which a qp may tunnel several times before relaxing to a lower energy state. This should not be confused with multiple tunnelling, when a qp tunnels several times with or without relaxation, before recombination takes place<sup>79</sup>. As a consequence, a stable non-equilibrium state is established in which many qps may have an energy exceeding the  $3\Delta$  threshold for breaking further Cooper pairs, resulting in an additional excess current and an increase in generation-recombination noise<sup>80,81</sup>. The development of a quantitative theory of the phenomenon required the solution of the coupled system of kinetic equations for the interacting qps and phonons, resulting in a set of spectral balance equations describing the qp populations in different energy intervals.

The objective of the present work has been to carry out parallel calculations for the dynamic situation created by the absorption of a single photon in the energy range between near infrared and X-ray. The time-dependent scenario is significantly more complicated than the stationary one, and a full solution including spectral balance within the qp and phonon distributions has never been achieved previously. Until recently, the only attempts to model the response of a biased STJ to the absorption of a photon creating a population of non-equilibrium qps used the framework of the Rothwarf-Taylor (RT) balance equations<sup>82</sup>. The main assumption of this approach is that during the initial downconversion process, qps relax directly to states at the superconducting edge. However, for the latest STJs, the modelled results for charge output and its rise time as functions of bias voltage and temperature, both of which influence qp distributions, do not agree with the experimental data. Following more realistic calculations based on balancing the two processes of tunnelling and spontaneous

## 4. Dynamics of nonequilibrium quasiparticles in narrow-gap superconducting tunnel junctions

---

phonon emission<sup>83,84</sup>, it is clear that the RT approach is too simplistic to treat satisfactorily a non-equilibrium situation. An attempt to tackle the problem was made recently by Segall *et al.*<sup>85</sup>, beginning from a phenomenologically derived system of rate equations to describe the dynamical situation. However, this formulation did not include the complete kinetic equations for interacting qps and phonons and took no account of non-equilibrium phonon distributions or qp generation effects.

In order to be able to include non-equilibrium phenomena explicitly, we have developed a theoretical approach based on the projection of the exact kinetic equations for the qps and phonons on to a discretized energy space. Interacting distributions of qps and phonons are described in terms of a system of spectral balance equations with all scattering and interaction terms rigorously derived from the corresponding collision integrals. We previously used this approach to model successfully the non-equilibrium qp dynamics for a BCS superconductor in the stationary regime<sup>78,79</sup> and for the general situation of a proximized structure with time evolving distributions<sup>86,87</sup>. However, the latter scheme was incomplete since it did not take account of the qp self generation and used an oversimplified model of qp de-trapping at localized traps. In addition, the effects of the non-equilibrium subgap phonon distribution were not considered. All effects are included in the present work.

In this paper, we develop a general technique for modelling non-equilibrium, time-dependent phenomena in superconducting tunnel junctions. For comparison, we also present recent experimental results taken on several narrow gap STJs of different sizes over a range of photon energy, bias voltage, and temperature. Convincing agreement between experimental results and theoretical predictions is obtained for all devices using a single set of fitting parameters.

The paper is organized as follows. In Sec. 4.2, the various processes involved in the interactions between non-equilibrium and trapped qps and phonons are described. The resultant time-dependent spectral balance equations are derived in Sec. 4.3. Section 4.4 contains details of the experiments and modelling, followed by a comparison of experimental data with theoretical calculations in Sec. 4.5, and a brief summary of our conclusions in Sec. 4.6.

### 4.2 Kinetic description of nonequilibrium quasiparticles and phonons in a superconducting tunnel junction

A fully dynamical description of non-equilibrium qps and phonons in an STJ begins from the kinetic equations for a superconductor with all qp and phonon processes including tunnelling, represented by collision integrals<sup>88,89</sup>. For qps and phonons, respectively, the equations are

$$\frac{\partial f(\varepsilon)}{\partial t} = I_{qp-ph} \{f, N\} + I_{rec} \{f\} + I_{loss} \{f\} + I_{tun} \{f, f'\} \quad 4-1$$

$$\frac{\partial N(\varepsilon)}{\partial t} = I_{ph,loss} \{N\} + I_{qp-ph} \{N, f\} + I_{pb} \{N, f\} \quad 4-2$$

Here,  $f(\varepsilon)$  and  $N(\varepsilon)$  are the respective distribution functions for qps and phonons, where  $\varepsilon$  is the qp energy relative to the Fermi level. The collision integrals in eq. 4-1 describe the following qp processes:  $I_{qp-ph} \{f, N\}$  relates to qp-phonon scattering processes with either emission or absorption of a single phonon,  $I_{rec} \{f\}$  takes into account recombination, while  $I_{loss} \{f\}$  incorporates processes other than recombination which also result in the loss of qps. The latter include trapping with subsequent recombination on the trapping site, and diffusion



and loss in the lead connections. Finally,  $I_{tun}\{f, f'\}$  describes the rate of qp exchange with the other electrode, where the qp distribution function is described by  $f'$ . Collision integrals in the kinetic equation eq. 4-2 for phonons are  $I_{ph,loss}\{N\}$  taking account of phonon escape from the electrode,  $I_{ph-qp}\{N, f\}$  relating to phonon re-absorption by qps, and  $I_{pb}\{N, f\}$  describing the effect of Cooper pair breaking by phonons. The latter is nonzero only for energetic phonons with  $\hbar\Omega > 2\Delta$ , where  $\Delta$  is the superconducting gap.

We showed earlier<sup>90,91</sup> that the kinetics of qps and phonons in non-equilibrium superconductors cannot be adequately described without taking explicit account of the interaction between the mobile qps and phonons and the trapped qps. The microscopic nature of the defects responsible for the trapping states in a particular superconductor is often uncertain. Possible sources are magnetic impurities or clusters, macroscopic regions of locally suppressed gap such as the core regions of trapped magnetic flux, small normal metal inclusions, surface layers of smaller gap natural oxide and suppressed gap regions due to sample geometry. The role of these states in the non-equilibrium kinetics in superconductors can be compared with that of traps or deep levels in semiconductors. Their importance was first demonstrated in Ref. 90, and their effect can be seen in the dynamic response of the STJs to any transient perturbation<sup>91</sup>. Although the production of qps in photon absorption experiments occurs in a tiny excited volume close to the photon absorption site, for a typical STJ only a few tens of microns in size, diffusion rapidly homogenizes their distribution over the whole electrode on a time scale which is much shorter than any of the processes which control subsequent evolution of the qp distribution. Thus, we may omit spatial gradients from the kinetic equations and, equally, we may disregard the positional dependence of qp trapping. We assume that trapping centres of depth  $\Delta_t$  are distributed through the STJ with density  $F_t$ . Thus, the activation energy of the trapped qps is  $\Delta - \Delta_t$ .

As a consequence, the main system of equations must be modified to include additional terms representing the various interactions between the three subsystems, mobile qps, trapped qps, and phonons. Thus, instead of eq. 4-1 and eq. 4-2, we may write

$$\frac{\partial f(\varepsilon)}{\partial t} = I_{qp-ph}\{f, N\} + I_{rec}\{f\} + I_{rec}\{f, f^{trap}\} + I_{loss}\{f\} + I_{tun}\{f, f'\} + I_{trap}\{f, f^{trap}\} - I_{de-trap}\{f^{trap}\} \quad 4-3$$

$$\frac{\partial f^{trap}}{\partial t} = I_{loss}\{f^{trap}\} - I_{trap}\{f, f^{trap}\} + I_{de-trap}\{f, f^{trap}\} - I_{rec}\{f, f^{trap}\} - I_{pb}\{N, f, f^{trap}\} \quad 4-4$$

$$\frac{\partial N(\varepsilon)}{\partial t} = I_{ph,loss}\{N\} + I_{qp-ph}\{N, f\} + I_{ph-trap}\{N, f^{trap}\} + I_{pb}\{N, f\} + I_{pb}\{N, f, f^{trap}\} \quad 4-5$$

Here, we introduce the notation  $f^{trap}$  for the trapped qp density. The collision integrals  $I_{loss}\{f^{trap}\}$ ,  $I_{trap}\{f, f^{trap}\}$ , and  $I_{de-trap}\{f, f^{trap}\}$  describe, respectively, the rate of qp loss due to recombination on the trap, the rate of qp trapping from mobile qp states, and the rate of trap depopulation. We have also split the recombination terms in eq. 4-3 into two parts, the first  $I_{rec}\{f\}$  accounting for the normal recombination of a test qp colliding with another mobile qp and the second  $I_{rec}\{f, f^{trap}\}$  being the contribution due to the collision with a trapped qp. Similarly, in eq. 4-3, we have split the phonon pair breaking term into the two terms with  $I_{pb}\{N, f\}$  describing the process resulting in the creation of two mobile qps, while  $I_{pb}\{N, f, f^{trap}\}$  leads to the creation of one trapped and one mobile qp. In what follows, we will assume that the number of traps is small, so that we may disregard  $I_{rec}\{f, f^{trap}\}$  in comparison with  $I_{rec}\{f\}$  in eq. 4-3 and  $I_{pb}\{N, f, f^{trap}\}$  in comparison with  $I_{pb}\{N, f\}$  in eq. 4-5. Similarly, in eq. 4-4 we will disregard the terms with  $I_{rec}\{f, f^{trap}\}$  and  $I_{pb}\{N, f, f^{trap}\}$ , which describe the

## 4. Dynamics of nonequilibrium quasiparticles in narrow-gap superconducting tunnel junctions

---

population of traps in the processes of recombination and pair breaking and which are small in comparison with  $I_{trap}\{f, f^{trap}\}$ . However, quadratic terms of the kind  $f f^{trap}$  must be retained in  $I_{de-trap}\{f, f^{trap}\}$  since de-trapping may occur either through collision with a thermal phonon, with the strength of the process depending exponentially on temperature, or through depopulation of the trap by one of the non-equilibrium carriers, which may become important at low temperature and high non-equilibrium qp density.

The equation for the phonon distribution function eq. 4-5 is a first order linear differential equation and can be solved in terms of the qp distribution function. It has been shown previously that, after the fast, initial energy down conversion, all succeeding evolution of the non-equilibrium qp distribution is controlled purely by tunnelling loss and recombination, which occur much more slowly. Thus, the qp distribution in the biased STJ remains “frozen-in” and the energetic phonon distribution quickly accommodates itself to the slowly varying qp distribution. In this situation, for pair breaking phonons with energy above  $2\Delta$ , all processes in the phonon system occur much faster than those which control the non-equilibrium qp distribution. Hence, we can use an adiabatic approximation and neglect all effects of temporal dispersion of phonon response. By setting the time derivative of the phonon distribution to zero, we reduce the differential equation to an algebraic one, resulting in a coupled system of equations for mobile and trapped qps. This approach is not valid for lower energy subgap phonons as their loss rate may be very slow and the temporal response may become dispersive<sup>79,93,94</sup>. In addition, their significant accumulation changes the rates of de-trapping through the term  $I_{de-trap}\{f^{trap}\}$ . However, for the moment, we will ignore this group of phonons but will discuss their possible role in the later consideration of real structures and experimental situations.

### 4.3 Time-dependent spectral balance equations

Time-dependent spectral balance equations were previously derived in Refs. 86 and 87 for the general case of a proximised STJ. However, non-equilibrium phonon effects were only partially taken into account, through simplified phonon re-absorption terms in the collision integrals describing the recombination. Conversely, in Ref. 79, the phonon contribution was fully accounted for, but only for the stationary situation. In the previous work, we used the expressions for the collision integrals in eq. 4-3 to eq. 4-5—and projecting these kinetic equations onto energy space as has been described in Refs. 79 and 86, we obtained a system of coupled spectral balance equations for qps. The energy range of interest is split into  $M+1$  ( $M \gg 1$ ) elementary intervals with width  $\delta$ , labelled by the integer  $m$ , so that the  $m$ th elementary interval in energy space becomes  $\varepsilon_m < \varepsilon < \varepsilon_{m+1}$ , where  $\varepsilon_m = \Delta + m\delta$  and the index  $m$  defines the qp energy relative to the gap,  $\Delta$ . The number  $M$  is chosen so that  $M\delta \geq 3\Delta$  falls into the active region defined as  $\varepsilon \geq 3\Delta$ , so that the inelastic relaxation of a qp from this region may release a pair-breaking phonon, leading to qp generation<sup>79</sup>. We take only values of bias voltage which are integer numbers of the elementary width  $\delta$ , that is,  $V_b = v\delta$ . The trap depth measured from the superconducting edge is also assumed to be an integer multiple of  $\delta$ , so that  $\Delta - \Delta_t = t\delta$ . After the transformation of eq. 4-3 and eq. 4-4, our main equations for mobile (eq. 4-6) and trapped (eq. 4-7) qps become

$$\begin{aligned}
 \frac{\partial P_m^i}{\partial t} &= \frac{P_m^i}{\tau_m} + \sum_{s=m+1}^M \frac{P_s^i}{\tau_{s \rightarrow m}} - \frac{P_m^i - P_m^0}{\tau_{l,m}} - \Gamma_{m \rightarrow m+\nu} P_m^i + \Gamma_{m+\nu \rightarrow m} P_{m+\nu}^j \\
 &- \Theta(m - \nu + 0) \left[ \Gamma_{m \rightarrow m-\nu} P_m^i - \Gamma_{m-\nu \rightarrow m} P_{m-\nu}^j \right] - 2\bar{N}(0)\Delta \sum_{s=0}^M R_{m,s}^* \left[ P_m^i P_s^i - P_m^0 P_s^0 \right] \\
 &- \frac{P_m^i}{\tau_{m \rightarrow \text{trap}}} \left( 1 - \frac{f^t}{F^t} \right) + \frac{f^t}{\tau_{\text{trap} \rightarrow m}} + f^t \sum_{s=m+t}^M \int_0^t \frac{dt'}{\tau_0} P_s^i(t') K_{m,s}(t-t') + \sum_{s=m+\text{ceil}(2\Delta/\delta)}^M \frac{P_s^i}{\tau_{g,s}} \\
 \frac{\partial f^t}{\partial t} &= -\frac{f^t - f_0^t}{\tau_{\text{trap-loss}}} + \sum_{s=0}^M \frac{P_s^i}{\tau_{s \rightarrow \text{trap}}} \left( 1 - \frac{f^t}{F^t} \right) - \frac{f^t}{\tau_{de-\text{trap}}} - f^t \sum_{s=0}^M \sum_{s'=s+t}^M \int_0^t \frac{dt'}{\tau_0} P_{s'}^i(t') K_{s,s'}(t-t') \\
 &- 2\bar{N}(0)\Delta \sum_{s=\text{ceil}(\Delta_l/\delta)}^M R_{\text{trap},s} \left[ P_s^i f^t - P_s^0 f_0^t \right]
 \end{aligned} \tag{4-6}$$

where  $\text{ceil}(x)$  is the smallest integer greater than or equal to  $x$ . Here, we have introduced  $P_s^i$ , which is the dimensionless density in units of  $2\bar{N}(0)\Delta$  of qps which belong to the  $s^{\text{th}}$  interval, and  $P_s^0$  is its value for thermally excited qps. The superscript  $i$  labels the base and  $j$  the top STJ electrodes, and  $\bar{N}(0)$  is the density of states at the Fermi level in the normal state, per spin. Similarly,  $f^t$  is the dimensionless density of trapped qps in the same units,  $f_0^t$  is its equilibrium value, and  $F^t$  is the overall dimensionless trap density including both occupied and vacant traps.

Other kinetic parameters in eq. 4-6 and eq. 4-7 are defined as follows<sup>79</sup>:

$$\frac{1}{\tau_m} = \frac{1}{\tau_0} \left( \frac{\Delta}{k_B T_c} \right)^3 \int_{\Delta}^{\varepsilon_{\max}} \frac{d\varepsilon'}{\Delta} \rho(\varepsilon') \bar{B}(\varepsilon', \varepsilon_m) \tag{4-8}$$

where  $B(\varepsilon, \varepsilon') = [(\varepsilon - \varepsilon')/\Delta]^2 (1 - \Delta^2/\varepsilon\varepsilon') \theta(\varepsilon' - \varepsilon)$  and  $\theta(\varepsilon' - \varepsilon)$  is the Heaviside function, so that

$$\bar{B}(\varepsilon', \varepsilon_m) = \frac{1}{\rho_m} \int_{\varepsilon_m}^{\varepsilon_{m+1}} d\varepsilon \rho(\varepsilon) B(\varepsilon', \varepsilon)$$

is the average over the  $m$ th spectral interval, where

$$\rho_m = \int_{\varepsilon_m}^{\varepsilon_{m+1}} \frac{d\varepsilon}{\Delta} \rho(\varepsilon)$$

Here,  $T_c$  is critical temperature,  $\tau_0$  is the characteristic electron-phonon relaxation time in the superconductor, and  $\rho(\varepsilon)$  is the qp dimensionless density of states. It is seen from eq. 4-8 that  $\tau_m$  is the lifetime of a qp with respect to scattering from the initial state in the  $m$ th interval down to any lower lying state with the spontaneous emission of a phonon. Similarly,

#### 4. Dynamics of nonequilibrium quasiparticles in narrow-gap superconducting tunnel junctions

$$\frac{1}{\tau_{s \rightarrow m}} = \frac{1}{\tau_0} \left( \frac{\Delta}{k_B T_c} \right)^3 \int_{\varepsilon_m}^{\varepsilon_{m+1}} \frac{d\varepsilon'}{\Delta} \rho(\varepsilon') \bar{B}(\varepsilon', \varepsilon_s) \quad 4-9$$

where  $\tau_{s \rightarrow m}$  describes the rate of electronic transition of a qp with the spontaneous emission of a phonon from an initial state in the  $s$ th interval to any state in the  $m$ th interval. The loss rate for qps belonging to the  $m$ th interval is

$$\frac{1}{\tau_{l,m}} = \frac{1}{\rho_m} \int_{\varepsilon_m}^{\varepsilon_{m+1}} d\varepsilon' \rho(\varepsilon') \frac{1}{\tau_l(\varepsilon)} \quad 4-10$$

The matrix  $R_{m,s}^*$  defining the recombination contribution from qps, one in the  $m$ th and the other in the  $s$ th interval, to the total recombination rate can be written as

$$R_{m,s}^* = \frac{1}{4N\Delta\tau_0} \left( \frac{\Delta}{k_B T_c} \right)^3 \int_{\varepsilon_m}^{\varepsilon_{m+1}} \frac{d\varepsilon}{\Delta} \frac{\rho(\varepsilon)}{\rho_m} \int_{\varepsilon_s}^{\varepsilon_{s+1}} \frac{d\varepsilon'}{\Delta} \frac{\rho(\varepsilon')}{\rho_s} B(\varepsilon - \varepsilon') [\Gamma(\varepsilon + \varepsilon') \tau_e(\varepsilon + \varepsilon')]^{-1} \quad 4-11$$

where  $\Gamma(\varepsilon) = \tau_e^{-1}(\varepsilon) + \tau_{ph}^{-1}(\varepsilon) + \tau_{ph-e}^{-1}(\varepsilon)$  is the total loss rate for a phonon of energy  $\varepsilon$ , including the effects of phonon escape from the electrode, phonon pair breaking (if  $\varepsilon > 2\Delta$ ) and phonon absorption by qps. It represents a generalization of the Rothwarf-Taylor recombination coefficient<sup>82</sup> for the situation when each of colliding qps has an arbitrary energy. When both reside at a superconducting edge ( $m=s=0$ ), we obtain the Rothwarf-Taylor result  $R_{0,0}^* = 1/[4\bar{N}(0)\Delta\tau_0\Gamma(2\Delta)\tau_e(2\Delta)](2\Delta/k_B T_c)^3$ . The expressions for the elements of the matrix of tunnel rates are

$$\Gamma_{m \rightarrow m \pm \nu} = \frac{1}{\rho_m} \int_{\varepsilon_m}^{\varepsilon_{m+1}} d\varepsilon \rho(\varepsilon) \Gamma_l(\varepsilon \pm \nu \delta) \quad 4-12$$

with  $\Gamma_l(\varepsilon + eV_b) = (G/4e^2\bar{N}(0)\Omega_0)\rho(\varepsilon + eV_b)$ , where  $G$  is the conductance of a barrier and  $\Omega_0$  the electrode volume<sup>95</sup>. Finally,  $\tau_{g,s}$ , which is the rate of qp injection into the  $s$ th interval due to the energy accumulation in tunnelling cycles of direct and back tunnelling events<sup>79</sup>, is given by

$$\frac{1}{\tau_{g,s}} = \frac{2}{\pi\tau_0} \left( \frac{\Delta}{k_B T_c} \right)^3 \frac{1}{\rho_s} \int_{\varepsilon_m}^{\varepsilon_{m+1}} \frac{d\varepsilon'}{\Delta} \rho(\varepsilon') \int_{\varepsilon_s}^{\varepsilon_{s+1}} \frac{d\varepsilon''}{\Delta} \rho(\varepsilon'') \int_{\Delta}^{\varepsilon'' - \varepsilon' - \Delta} \frac{d\varepsilon'''}{\Delta} \rho(\varepsilon''') \rho(\varepsilon'' - \varepsilon' - \varepsilon''') \left( 1 - \frac{\Delta^2}{\varepsilon'' \varepsilon'''} \right) \Theta(\varepsilon'' - \varepsilon' - 2\Delta) \frac{B(\varepsilon' - \varepsilon'' - \varepsilon''', \varepsilon')}{\Gamma(\varepsilon'' - \varepsilon''') \tau_{ph}} \quad 4-13$$

The trapping time  $\tau_{m \rightarrow trap}$  describes the qp transition from a mobile state in the  $m$ th interval to the trap and is assumed to be proportional to the time for the spontaneous emission of a phonon of the same energy  $(m+t)\delta$ . Thus,

$$\frac{1}{\tau_{m \rightarrow \text{trap}}} = \frac{1}{\tau_{m+t \rightarrow 0}} \zeta_{\text{trap}} \quad 4-14$$

The magnitude of the proportionality coefficient  $\zeta_{\text{trap}}$  depends on the microscopic origin of the trap and has been introduced here as a fitting parameter. For de-trapping, we write

$$\frac{1}{\tau_{\text{de-trap}}} = \sum_{s=0}^M \frac{1}{\tau_{\text{trap} \rightarrow s}} \quad 4-15$$

where the de-trapping time  $\tau_{\text{trap} \rightarrow s}$  refers to transitions from the trap into the  $s$ th elementary interval ( $s=0, \dots, M$ ) due to the absorption of a thermal phonon with energy  $(s+t)\delta$ . The function  $K_{m,s}(t)$ , describing the de-trapping effect of subgap phonons, is given by

$$K_{m,s}(t) = \frac{1}{\pi \tau_{\text{ph}}} \left( \frac{\Delta}{k_B T_c} \right)^3 \frac{1}{N(0)\Delta} \int_{(m+t)\delta}^{s\delta} d\Omega \Omega^2 \rho(\Omega + \Delta_t) \exp \left[ -\frac{t}{\tau_e(\Omega)} \right] \int_{\varepsilon_s}^{\varepsilon_{s+1}} \frac{d\varepsilon'}{\Delta \rho_s} \rho(\varepsilon') \rho(\varepsilon' - \Omega) \left[ 1 - \frac{\Delta^2}{(\varepsilon' - \Omega)\varepsilon'} \right] \quad 4-16$$

where  $\tau_e(\Omega)$  is the loss time for subgap phonons in the STJ<sup>93,94</sup>. Then, the array of de-trapping coefficients relating to pair-breaking phonons emitted in the recombination process with participation of a trapped qp is

$$R_{\text{trap},s} = \frac{1}{4N(0)\Delta\tau_0} \left( \frac{\Delta}{k_B T_c} \right)^3 \int_{\varepsilon_s}^{\varepsilon_{s+1}} \frac{d\varepsilon}{\Delta} \frac{\rho(\varepsilon)}{\rho_m} B(\varepsilon, -t\delta) [\Gamma(\varepsilon + t\delta) \tau_{\text{ph-e}}(\varepsilon + \varepsilon')]^{-1} \quad 4-17$$

Finally, it is convenient to split the overall qp loss rate  $\tau_{l,s}^{-1}$  into two distinct components, one of which,  $\tau_{s \rightarrow \text{trap}}^{-1}$ , arises from trapping of qps by local traps and is a strong function of qp energy, and the second,  $\tau_{\text{res}}^{-1}$ , which describes residual losses resulting from bulk and surface recombination and out diffusion into leads, all essentially independent of energy. Hence, the residual loss rate can be represented as a sum of the two terms, one independent of the STJ size (bulk and surface recombination) and the other inversely proportional to  $L^2$  arising from the diffusive nature of qp transport leading to qp loss<sup>97,98</sup>. Thus,

$$\tau_{\text{res}}^{-1} = \tau_{\text{res},\infty}^{-1} \left( 1 + \frac{a}{L^2} \right) \quad 4-18$$

where  $\tau_{\text{res},\infty}^{-1}$  is the magnitude of the residual loss rate in the infinite sample ( $L=\infty$ ), that is, the residual bulk loss, and  $a$  is a numerical coefficient defining the relative magnitude of out diffusion versus bulk terms.

In the derivation of the spectral balance equations eq. 4-6, we have ignored electron-electron interactions and the energy exchange and equilibration terms originating from self-recombination followed by sequential pair breaking. In contrast to the quadratic terms leading to recombination, such processes conserve qp number. For this reason, they are not directly relevant to recombination and de-trapping and any effect arises indirectly through their modification of the qp spectral distribution. However, for non-equilibrium qp densities in typical photon absorption experiments, they are small and may be neglected.

## 4. Dynamics of nonequilibrium quasiparticles in narrow-gap superconducting tunnel junctions

### 4.4 Experiment and modelling

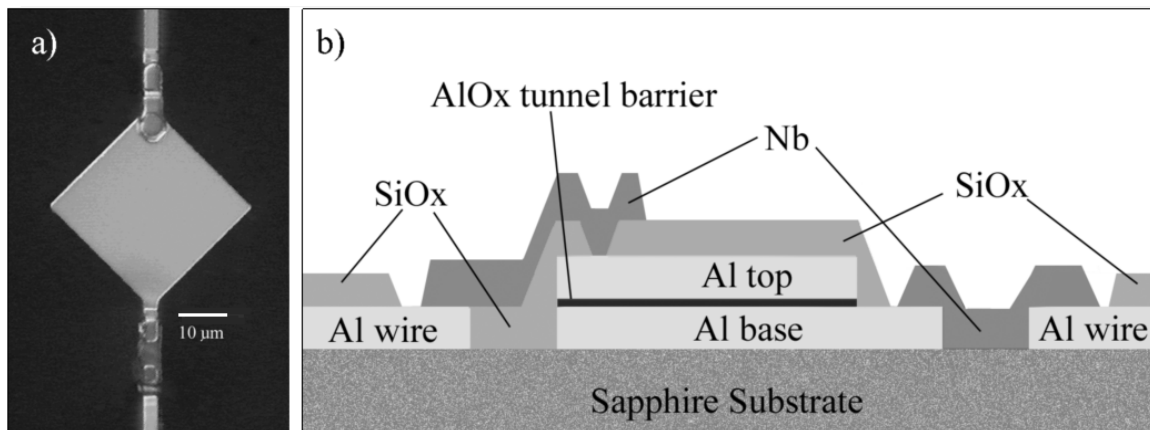


Figure 4-1 a) Micrograph of the 30  $\mu\text{m}$  STJ showing the Nb plugs in the leads. B) Layer structure of the STJ. Schematic side view from the left.

In order to demonstrate the application and success of the theoretical approach described above, we will present experimental results obtained for a series of narrow gap, multi-tunnelling, aluminium-based STJs and discuss their analysis in terms of our model. The STJs studied were square devices, of varying sizes  $L$ , 30, 50, and 70  $\mu\text{m}$  on a side, all fabricated on the same sapphire substrate with the same layer structure 100 nm Al/AlOx/50 nm Al on a single chip (chip set MUL 127). An image of a typical STJ is given in Figure 4-1, clearly showing the Nb plugs in the leads intended to limit qp loss through out diffusion. Measurements were made of dc current, photoresponsivity, and charge output rise time as a function of device bias voltage and, in addition, of the dependence of responsivity and rise time on temperature and photon energy. It is important to note that the current pulse itself is not observed. The measured quantity is the total charge detected, and the time scale over which the level of  $1-1/e$  of the total charge is reached, the so-called rise time, is identically equal to the current decay time<sup>23</sup>. Although sample measurements of  $IV$  curves, responsivity, and rise time are routinely made for all STJs on all chip sets, the complete data for all measurements in the full range of variation of photon energy, bias voltage, and temperature were available only for MUL 127, obtained specifically to test the theoretical model. Experiments were carried out at temperatures between 40 and 400 mK using either an adiabatic demagnetization cryostat (40–200 mK ) or a He sorption cooler (200–500 mK). Josephson effects were suppressed by application of a small ( $\sim 3$  mT) parallel magnetic field. The apparatus was carefully shielded to ensure that no fluxoids were present in the samples. The junctions were illuminated by monochromatic near IR (1–5 eV), multiple photon LED sources (2–30 eV), and a <sup>55</sup>Fe radioactive source (6 keV). Typical  $IV$  characteristics are shown in Figure 4-2, illustrating the effect of varying temperature and device size.

Measurements of responsivity and rise time for different sized STJs are shown later as a function of bias voltage, photon energy and temperature, in Figure 4-3-Figure 4-5, respectively. For each type of measurement, the data obtained are shown as experimental points with modelled results superimposed as continuous curves. It is important to stress that the model curves for all three devices are generated using the same, single set of parameters. In contrast, within a simpler model such as that of Rothwarf and Taylor<sup>82</sup>, a separate set of parameters, different for each STJ, would be required to model each data set, for each experiment. In addition, this model predicts monotonic decreases of both responsivity and rise time with bias voltage, which are not observed.

Table 4-1 STJ material characteristics used as parameters for the model

Symbol	Name	Value	Unit	Comment
$R_m$	Normal barrier resistivity	6.65	$\mu\Omega\text{cm}^2$	Measured
$\Delta$	Energy gap	180	$\mu\text{eV}$	Measured
$T$	Characteristic e=ph scattering time	440	ns	Reference 94
$N(0)$	Single spin normal state density of states at Fermi level	12.2	$10^{23}/\text{eVcm}^3$	Reference 94
$\tau_{ph}$	Characteristic pair-breaking time	0.242	ns	Reference 94
$\Delta_t$	Effective trap depth	84	$\mu\text{eV}$	Measured
$\Gamma_t(\infty)$	Tunnel rate	2.58	$10^6/\text{s}$	Calculated from $R_m$

In our model, the common parameters are of two types, first, material parameters, listed in Table 4-1 which are obtained either from standard BCS theory or previously published in the relevant literature, or directly measured by us using standard STJ characterization procedures. For instance, the value of the effective trap depth is determined from an independent measurement of the responsivity of any of the STJs as a function of temperature. Table 4-2 given later in Sec 4.5 contains specific parameters relating to the chip set, not previously known but obtained through the modelling procedure itself. They are  $n_t$ , the total number of traps,  $\zeta_{trap}$ , the trapping constant determining the residual loss time,  $\tau_{res}$ , the residual loss rate, and phonon escape times  $\tau_e$  and  $\tau_e(2\Delta)$  for subgap and for pair-breaking phonons, respectively. The values of these fitting parameters are totally realistic on physical grounds. The total number of traps determined by the modelling is found to be the same for all STJs, implying that they reside in an area of fixed size, such as the leads to a device. The quantities that vary with device size are residual loss time, which because of the diffusive nature of qp transport contains a quadratic dependence on device size as described earlier in eq. 4-18, and local trapping constant  $\zeta_{trap} \propto L^{-2}$ . The latter dependence is again due to the diffusive nature of qp transport delivering qps to the area where local traps reside, on the assumption that the number of local traps is independent of the STJ size. We believe that the excellent agreement between experimental results and modelled curves confirms that the behaviour of such STJs is determined primarily by a strongly non-equilibrium qp distribution.

## 4.5 Analysis and discussion of results

### 4.5.1 Bias voltage dependence of dc current

Typical dc  $IV$  characteristics for the 30  $\mu\text{m}$  device are given in Figure 4-2a, showing the comparison between measured and calculated curves at different temperatures. In Figure 4-2b, data for all three devices, 30, 50, and 70  $\mu\text{m}$ , are shown at the same temperature. Only the range above  $\sim 100\mu\text{V}$  is meaningful; the rising current below  $\sim 40\mu\text{V}$  toward zero bias is an imperfectly suppressed Josephson current, while the residual subgap current is due to leakage. We concentrate on the section of the  $IV$  characteristic over which the current increases rapidly by 3–4 orders of magnitude above the relatively smooth background level at around 100  $\mu\text{V}$  and show that it can be attributed to the excitation of qps across the gap through multi-tunneling. The exact bias voltage corresponding to the current edge should be very sensitive

#### 4. Dynamics of nonequilibrium quasiparticles in narrow-gap superconducting tunnel junctions

to the qp loss rate consistent with the observation that the current edge moved toward lower bias voltage with rise in temperature (Figure 4-2a) and increase in STJ size (Figure 4-2b), both corresponding to lower qp loss rates.

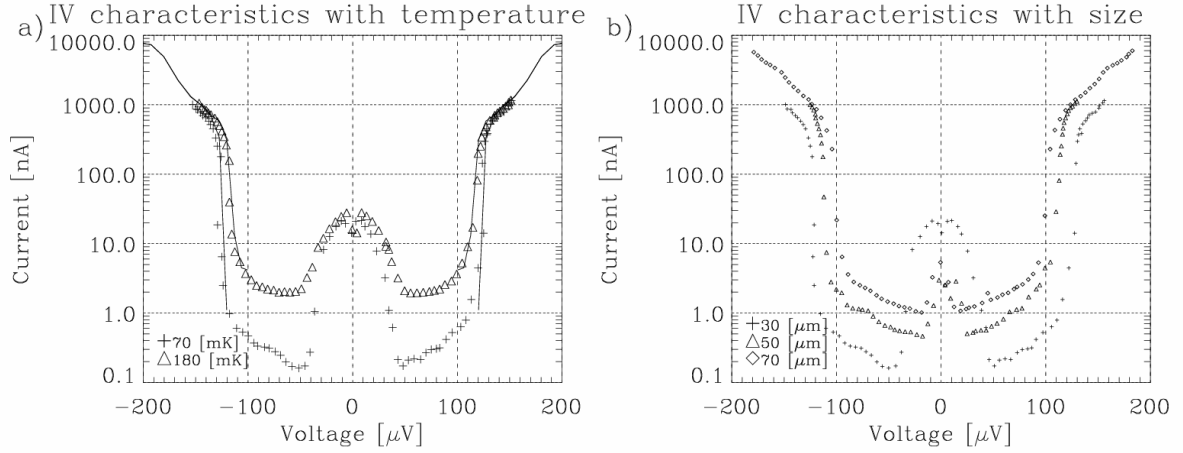


**Figure 4-2** *IV* curves in Al STJ: a)  $L=30 \mu\text{m}$ ,  $T=70 \text{ mK}$  (crosses) and  $T=180 \text{ mK}$  (triangles). Solid curves, theory. b)  $T=40 \text{ mK}$ ,  $L=30 \mu\text{m}$  (crosses),  $L=50 \mu\text{m}$  (triangles), and  $L=70 \mu\text{m}$  (diamonds).

In order to model the *IV* characteristic, the dynamic model described in Sec. 4.3 can be simplified significantly since in the stationary situation, all time derivatives are identically equal to zero. Thus, in eq. 4-6 and with  $\partial/\partial t=0$ , it is easy to solve the resulting system of algebraic equations to eliminate trap densities. The problem is then reduced to solving the closed system of spectral balance equations for mobile qps alone with appropriate terms to describe the interaction of qps with local traps. The latter includes de-trapping due to the absorption of both thermal and non-equilibrium phonons with energies exceeding the trap depth. Spectral balance equations are obtained from eq. 4-6 if  $\tau_{l,s}$  is replaced by  $\tau_{res,s}$  and the terms describing trapping and de-trapping in eq. 4-6 replaced by an effective trapping term  $\tau_{s \rightarrow trap}^{eff}$ . The resulting system of balance equations coincides with that of Ref. 79 but with the qp loss rate written as

$$\frac{1}{\tau_{l,s}} = \frac{1}{\tau_{res}} + \frac{1}{\tau_{s \rightarrow trap}^{eff}} \quad 4-19$$

The relation of the rise time (experimental mean loss time)  $\tau$  to  $\tau_{l,s}$  can only be found when it is simulated through the solution of spectral balance equations and the qp and phonon response to photon absorption calculated. The expression for  $\Gamma_{s \rightarrow trap}^{eff} = (\tau_{s \rightarrow trap}^{eff})^{-1}$  has the form

$$\Gamma_{s \rightarrow trap}^{eff} = \Gamma_{s \rightarrow trap} \left[ 1 + \frac{\sum_{s'} \Gamma_{s' \rightarrow trap}^{eff} P_{s'}^i}{\Gamma_{de-trap} + \sum_{s'} R_{l,s'} P_{s'}^i} \right] \quad 4-20$$

where  $\Gamma_{s \rightarrow trap} = 1/\tau_{s \rightarrow trap}$ . Finally, the de-trapping rate  $\Gamma_{de-trap}$  is expressed in terms of the complete distribution of phonons, including both thermal and non-equilibrium, which are capable of promoting a trapped qp into any mobile state. This rate is given by



$$\Gamma_{de-trap} = \frac{1}{\tau_0} \left( \frac{\Delta}{k_B T_c} \right)^3 \sum_{s'=0} N_{t+s'} (t+s')^2 \left( \frac{\delta}{\Delta} \right)^2 \left[ \sqrt{\left( \frac{\varepsilon_{s'+1}}{\Delta} \right)^2 - 1} - \sqrt{\left( \frac{\varepsilon_{s'}}{\Delta} \right)^2 - 1} \right] \quad 4-21$$

where the expression for the phonon distribution function  $N_s$  was obtained in the form<sup>79</sup>

$$N_s = N_{0,s} + \frac{2\tau_e(s\delta)}{\pi\tau_{ph}} \sum_{s'} \frac{P_{s'+s}^i}{\rho_{s'+s}} \int_{\varepsilon'_s}^{\varepsilon'_s+1} \frac{d\varepsilon'}{\Delta} \rho(\varepsilon') \rho(\varepsilon_s + \varepsilon') \left[ 1 - \frac{\Delta^2}{\varepsilon'(\varepsilon_s + \varepsilon')} \right] \quad 4-22$$

where  $N_{0,s}$  is the Planck distribution and subscript  $s$  denotes the phonon energy of  $s\delta$ . After the solution of the system of spectral balance equations for qp spectral densities  $P_m^i$ , the current through the STJ is found as

$$J = 2eN(0)\Delta V_{STJ} \sum_M \left( \Gamma_{m \rightarrow m+\nu} P_m^i - \Gamma_{m+\nu \rightarrow m} P_{m+\nu}^i + \Theta(m-\nu+0) \left[ \Gamma_{m \rightarrow m-\nu} P_m^i - \Gamma_{m-\nu \rightarrow m} P_{m-\nu}^i \right] \right) \quad 4-23$$

where  $V_{STJ}$  is the STJ volume.

#### 4.5.2 Responsivity and rise time: Bias voltage dependence

The dc, responsivity, and rise time are all calculated via a numerical solution of the spectral balance equations. However, while for dc the latter becomes a system of algebraic equations, the calculation of responsivity and rise time requires a full time-dependent solution. The simulation begins at an initial instant of time when the infinitesimally narrow initial distribution containing  $N_0=E/1.75\Delta$  qps, where  $E$  is the deposited energy, is taken at an arbitrary energy below  $3\Delta$ , to avoid any further qp generation. The exact energy and shape of the initial distribution are of no importance<sup>86</sup> because after a small number of tunnel events, the qp spectral distribution converges very rapidly to a stable shape, which remains unchanged during the remainder of the charge acquisition process, with only the total number of qps decreasing with time through losses. Hence, calculating the current flowing through the STJ according to eq. 4-23 but with  $P_m^i(t)$  as the instantaneous qp density in the  $m$ th spectral interval, we may find the integrated charge  $Q(t) = \int_0^t dt' J(t')$  and determine the responsivity and rise time as

$$R = Q(\infty) \Big|_{E=1eV} \quad 4-24$$

$$Q(\tau) = \left( 1 - \frac{1}{e} \right) Q(\infty)$$

Experimental results are shown in Figure 4-3a and Figure 4-3b. For the 30  $\mu\text{m}$  junction, the dependencies of the responsivity and rise time on the bias voltage are rather flat. The 50 and 70  $\mu\text{m}$  junctions, on the other hand, show strong effects. We note that the rise time of the pulse increases with the increase of bias voltage, implying that qp losses decrease with increasing bias voltage. As a consequence, the responsivity also increases because on average qps have more time to tunnel. A second noteworthy effect is that the responsivity rises faster than the rise time, showing that not only does the lifetime of qps increase with applied voltage but at the same time tunneling becomes faster. To understand how this is possible, we need to

## 4. Dynamics of nonequilibrium quasiparticles in narrow-gap superconducting tunnel junctions

consider the details of the quasiparticle dynamics and to examine the qp spectral distribution within the current pulse. While the bias voltage is small (well below the current edge on the  $IV$  characteristic), the qp spectral distribution, although increased in breadth, still remains concentrated below the  $3\Delta$  generation threshold for all STJs. However, with increasing bias voltage, the tail of the qp spectral distribution approaches the  $3\Delta$  threshold. With all parameters except qp losses being the same for all STJs, the high energy tail of the qp distribution in larger (lower loss) STJs contains significantly more qps than in smaller devices. When the qp numbers above the  $3\Delta$  threshold become sufficiently large, self-generation occurs, resulting in a significant increase of both responsivity and rise time.

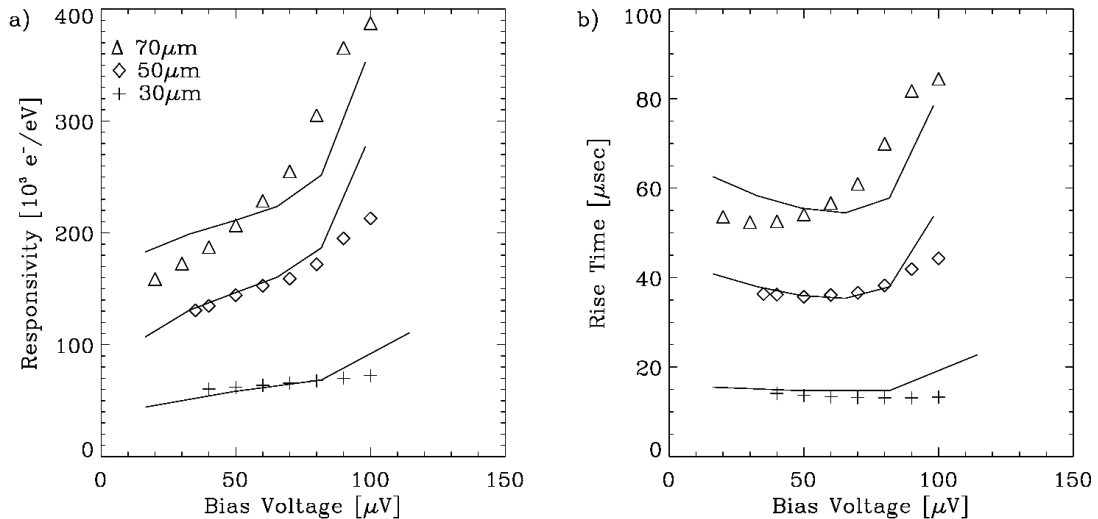


**Figure 4-3 a) Responsivity and b) rise time as a function of applied bias voltage for different device sizes at a temperature of 40 mK.**

As seen in Figure 4-3, this occurs when the bias voltage approaches the current edge in the dc  $IV$  curves and takes effect in the lowest loss 70  $\mu\text{m}$  STJ at the lowest bias voltages. The dc edge seen in the 30  $\mu\text{m}$  STJ occurs at 120  $\mu\text{V}$ , which was beyond the range of measurements of responsivity and rise time because of the developing current instability. Examining the qp distribution functions, we calculate that in the 70  $\mu\text{m}$  STJ, the fraction of qps above the  $3\Delta$  threshold is of the order of  $10^{-5}$  at 80  $\mu\text{V}$  bias. During the qp lifetime of approximately 100  $\mu\text{s}$ , there will be on average  $\sim 10^4$  spontaneous emissions of pair-breaking phonons resulting from qp inelastic transitions initially above the  $3\Delta$  threshold. Thus, by the time the initial distribution of qps has decayed, around 20% of it has been replaced due to self-generation, resulting in the observed behaviour of responsivity and rise time.

### 4.5.3 Responsivity and rise time: Photon energy dependence

Responsivity and rise time data were measured for the 30, 50, and 70  $\mu\text{m}$  junctions as a function of photon energy between 2 and 30 eV. The results of the experiments together with the modelled curves are shown in Figure 4-4. For the 30 and 50  $\mu\text{m}$  junctions, 6 keV data were also obtained. Nonlinearity in the optical domain arises from the fact that the number of active traps gradually saturates as the number of generated quasiparticles increases<sup>90</sup> and from this observation, it was possible to obtain an estimate of the total number of traps. The result of approximately  $8.8 \times 10^3$  was the same for each STJ regardless of size, confirming the earlier result that the traps do not reside in the bulk, nor are dispersed evenly along the device perimeter, but are concentrated at one or more well defined locations, presumably at the Nb

contacts. In contrast, the observed responsivity of STJs with Ta contacts is essentially independent of energy over in the same range, indicating either that traps are much more numerous than in junctions with Nb leads or that they are absent altogether. The sensitivity of the theoretical fit to trap density and trapping coefficient is good so that this experiment may be considered as essentially a measurement of these two parameters. However, in modelling the curves in Figure 4-4, theory uses also the trap depth as a parameter. The results of the simulations shown in Figure 4-4 are not critically dependent on the value of this parameter, and hence the determination of  $\zeta_{trap}$  and  $F^l$  remains slightly uncertain, in the absence of an independent determination of the trap depth. The latter was achieved by measuring the STJ responsivity in the appropriate range of temperature, as described below, since thermal phonons will activate the trapped qps and thus increase responsivity with increasing temperature<sup>91</sup>.

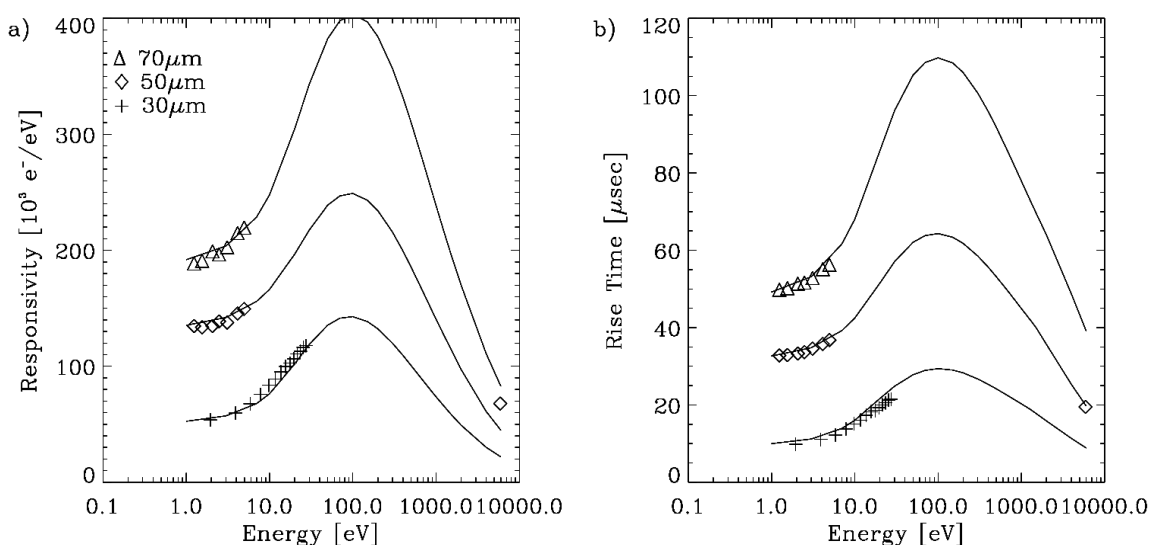


Figure 4-4 a) Measured responsivity and b) rise time of the 30 (crosses), 50 (diamonds), and 70 (triangles)  $\mu m$  Al junctions as a function of incoming photon energy.  $V=50 \mu V$ ,  $H_{||}=5 mT$ , and  $T=40 mK$ . The results of the simulations are shown by various curves.

#### 4.5.4 Responsivity and rise time: Temperature dependence

Finally, we have measured the temperature dependence of responsivity and rise time in the range of temperature 40–210 mK. The results of the experiments and theoretical modelling are shown in Figure 4-5, from which we were able to determine the trap depth  $\Delta_t$ . In Ref. 86, the de-trapping rate was proposed to be proportional to that of qp absorption from the initial state at the edge,  $\Delta$ , into a final state above this level corresponding to the trap depth. This assumption has never been tested experimentally before and needs refinement before a quantitative modelling can be carried out. The difference between the rate of de-trapping and that of phonon absorption arises from the different integrands in the expressions describing the transition rates. It is clear that absorbing a phonon of the energy exactly corresponding to the trap depth raises a trapped qp to a final state at the superconducting edge. In the BCS model, the latter is singular, leading to an enhanced de-trapping rate in comparison with that proposed in Ref. 86. A realistic description of both the density of states in the vicinity of the local trap as well as of the de-trapping rate requires an accurate model for the local trap. The general expression for the phonon absorption rate in an inhomogeneous superconducting system has the form<sup>95</sup>

#### 4. Dynamics of nonequilibrium quasiparticles in narrow-gap superconducting tunnel junctions

$$\Gamma_{abs}(x, \varepsilon) = \frac{1}{\tau_0 [k_B T_c(x)]^3} \int_0^{\Omega_D} d\Omega \Omega^2 N(\Omega) \left[ \text{Re} G(x, \varepsilon + \Omega) - \frac{\Delta(x)}{\varepsilon} \text{Im} F(x, \varepsilon + \Omega) \right] \quad 4-25$$

where  $x$  is a coordinate and  $\text{Re}G$ ,  $\Delta(x)$ , and  $\text{Im}F$  are position-dependent density of states, pair potential, and imaginary part of the anomalous Green function, respectively.

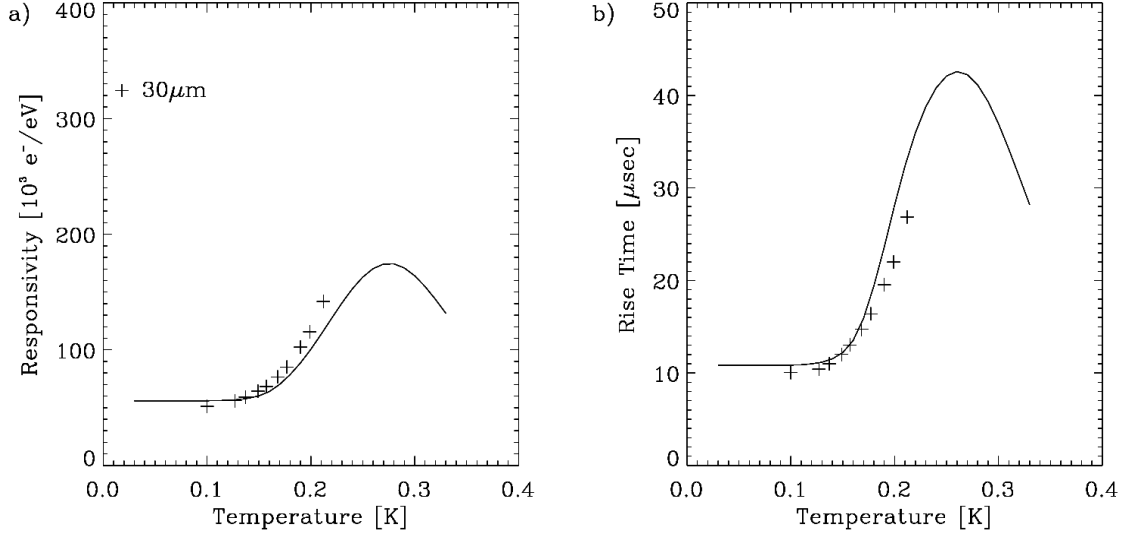


Figure 4-5 a) Responsivity and b) rise time versus temperature.  $V=85 \mu\text{V}$ .

To evaluate the de-trapping rate, we take the argument in the phonon absorption rate to be  $\varepsilon - \Delta_t$ . The singularity in the BCS density of states at the location of the local trap will be smoothed out because of the presence of the trap. However, in spite of this singularity, the integral is convergent, and hence we expect that the difference between the two expressions for the density of states does not play a significant role. Next is the problem of estimating the pair potential  $\Delta(x)$  at the location of the trap, taking account of the local suppression of the gap at the trap. Here, the result cannot be derived in a general form independent of the model of the local trap. If the trap is a normal region,  $\Delta(x)$  inside the trap is zero. However, the gap itself inside this normal region,  $\Delta - \Delta_t$ , still exists, while the pair potential is zero because  $\Delta(x) \sim \lambda F$ , where the electron-phonon coupling constant  $\lambda=0$  in the normal region. Thus, we have a finite  $F$  function and gap but zero  $\delta(x)$ , a common situation in proximized structures. Of course, the result depends on our assumption about the trap region, whether it is totally normal or whether it still retains some small electron-phonon coupling. Finally, our expression for the de-trapping rate is obtained from eq. 4-25 by using the BCS density of states and zero pair potential at the location of the trap,

$$\frac{1}{\tau_{de-trap}} = \frac{1}{\tau_0 (k_B T_c)^3} \int_0^{\Omega_D} d\Omega \Omega^2 N(\Omega) \rho(\varepsilon + \Omega) \quad 4-26$$

With this expression, we may model the temperature dependence of both responsivity and rise time and compare the results with experiment to establish the value of the parameter  $\Delta t$ . The steepness of the simulated curves on the rising side is greatly enhanced by the fact that dominant phonons excite the trapped qps into the states close to the edge where the BCS density of states is high. The results are shown in Figure 4-5. In view of the several

assumptions made, the agreement is promising. The general shape of the curve is similar to that observed for larger gap Ta/Al proximized junctions<sup>91</sup> in the region of higher temperatures, 200–800 mK, where the full curves can be measured experimentally. The responsivity and rise time curves reach maxima as a function of temperature because with rising temperature, thermal recombination first compensates for the effectively increased qp lifetimes while de-trapping becomes efficient, and then completely dominates, giving rise to enhanced loss, lower responsivity, and faster rise time.

**Table 4-2 Fitting parameters for the model (L in  $\mu\text{m}$ )**

Symbol	Name	Value	Unit
$\tau_e(2\Delta)$	Escape time for pairbreaking phonons	0.35	$10^{-9}\text{s}$
$\tau_e$	Escape time for subgap phonons	10	$10^{-9}\text{s}$
$\tau_{res}^{-1}$	Residual loss rate	$21.5/L^2+0.003$	$10^6\text{s}^{-1}$
$\zeta_{\text{trap}}$	Trapping constant	$72/L^2$	
$n_t$	Number of traps	$8.8 \cdot 10^3$	

Table 4-2 lists the fitting parameters which, together with the set of material parameters of Table 4-1, were found to model convincingly all the experimental results for all three devices. The good agreement of the model with experiment provides strong justification for the expressions used to describe loss and trapping in the STJs and therefore of the physics underlying them. The purely inverse quadratic dependence of the trapping constant, together with the observation that the number of traps is independent of STJ size, suggests strongly that the traps are localized in the Nb plugs at the connection with the leads. We also note that the magnitude of the bulk contribution (size independent) to the residual loss rate, corresponding to a rate of approximately  $300 \mu\text{s}$ , is not far removed from the figure of  $200 \mu\text{s}$  reported in Ref. 81 for an Al STJ with Ta plugs.

## 4.6 Summary

We have developed a theory to describe the formation and subsequent time evolution of the non-equilibrium qp state which is created in narrow gap, multiple tunnelling STJs by the absorption of an energetic photon. The theory is based on the system of coupled dynamic equations which link qp and phonon distributions via collision integrals describing all generation, interaction, tunnelling, and loss processes. No previous attempt has been successful in modelling this complex situation, which is a feature of the latest generation of high quality STJs for use at very low temperatures. For comparison, experimental measurements of responsivity and loss rate (rise time) were made on a series of Al STJs used as photon detectors. Our model was fully able to predict the responsivities and rise times and their dependence on experimental parameters such as temperature, bias voltage, and photon energy of all the related STJs in terms of a single set of material and device parameters. An important implication of the results is that local traps primarily responsible for qp loss in our Al STJs are located explicitly in the region of the Nb contacts. We believe that these studies provide important insight both into the physics of photon absorption processes in STJ detectors and specifically into non-equilibrium qp phenomena in superconductors

## Chapter 5

---

# Efficiency of quasiparticle creation in proximised superconducting photon detectors

---

R. A. Hijmering, P. Verhoeve, D.D.E. Martin, A. G. Kozorezov, J. K. Wigmore, R. Venn, P.J. Groot and I. Jerjen

J. Appl. Phys **105**, 123906 (2009)

*I*n previous work using thin superconducting films as photon detectors it has been assumed implicitly that the quasiparticle yield in proximised superconducting bilayers should be the same as for a pure superconducting layer with the same energy gap. The reasoning is that, following the energy down-conversion cascade, the resultant quasiparticles will all finish up at the edge of the density of states, which has the same energy throughout the whole structure regardless of whether it is pure or proximised. In this paper we show that, although the energy gap is the same, the actual density of quasiparticle states may vary considerably across a proximised structure, with a secondary peak at the energy of the higher gap material. Our calculations indicate that this peak can give rise to the generation of excess sub-gap phonons through which a larger portion of the original photon energy is lost from the quasiparticle system. The associated lower quasiparticle yield effectively reduces the responsivity of the proximised detector, and affects the limiting energy resolution. The predictions have been confirmed by experimental results obtained with a DROID (Distributed Read Out Imaging Detector) in which the response to photons absorbed in a pure Ta layer and in a Ta/Al proximised structure could be compared directly.

### 5.1 Introduction

Due to their spectroscopic properties superconducting detectors are ideal for use as photon counting spectro-photometers<sup>10,15,14</sup>. In these detectors the energy of the absorbed photon is converted into a large quantity of quasiparticles or phonons via a down conversion process which occurs in three stages<sup>47,48,49</sup>. Firstly the energy of the photon,  $E_0$ , is released into a photoelectron which excites secondary electrons and plasmons. This stage of the down conversion process is dominated by strong electron-electron interactions. The second stage starts at a lower energy  $E_1 \approx 1\text{eV}$ , when the electron-phonon interaction becomes dominant; the electrons begin to emit phonons with energy close to the Debye energy,  $\Omega_D$ . In the third stage the mixed distribution of phonons and quasiparticles evolves into a quasiparticle distribution at the edge of the energy gap of the superconductor. During this stage energy is lost via phonon loss into the substrate, mainly of phonons which do not have sufficient energy to break a Cooper pair and create two more quasiparticles.

Depositing one superconducting layer on top of a second superconducting layer of different material will modify the properties of both materials around the interface (the proximity effect). If the thicknesses of the layers is similar to or smaller than the coherence length the properties of both materials will be modified throughout the entire bi-layer. Although the density of states is broadened and will differ in the two materials, the energy gap will remain constant throughout the complete structure at a value intermediate between the energy gaps of the two individual materials determined by the relative layer thicknesses. Since after the down conversion process the quasiparticles will reside at the energy gap of the complete structure it is very often assumed that, although the devices are not BCS-type (following the theory as described by Bardeen, Cooper and Schrieffer<sup>40</sup>), the down conversion will progress in the same manner and the standard relation for the number of quasiparticles created would still be valid, eq. 5-1.

Quasiparticle dynamics and relaxation in superconductors are currently of great interest in numerous studies. Especially the discovery on an extra relaxation channel reducing the quasiparticle relaxation time and the likely involvement of magnetic impurities has provided a boost in this field<sup>91,100,101</sup>. In this paper we will look at the creation of quasiparticles and consider the final stage of down conversion process, where energy loss via subgap phonons is of importance, with particular reference to proximized superconducting tunnel junctions (STJs). The STJ consists of two thin layers of superconducting material separated by an insulating layer. As detectors they are sensitive to energies ranging from the near-infrared (NIR) up to X-rays, they can handle count rates up to tens of kHz and they provide each event with a sub-micro-second accurate time stamp. The photon energy which is absorbed in the superconducting material is converted, via the down conversion process, into a large number of quasiparticles. These quasiparticles can tunnel across the thin barrier and, by applying a DC bias voltage across the junctions, they can be detected as a measurable current pulse. To avoid a significant population of thermally excited quasiparticles the detector has to be cooled well below the critical temperature ( $T < 0.1T_c$ ) of the material, thereby constraining the operating temperature. For the widely used tantalum devices this operating temperature is around 400mK. Aluminium is often used in tantalum STJs, between the tantalum layer and tunnel barrier, in order to reduce the energy gap, thus improving the charge output, and to confine ('trap') the quasiparticles near the tunnel barrier, enhancing the tunnel rate<sup>26</sup>.

To increase the active area position sensitive configurations, DROIDS<sup>28</sup>, are being developed. In general these consist of a large absorber area with STJ detectors at the edges. The quasiparticles generated from absorption of a photon in the absorber will reach the detectors

## 5. Efficiency of quasiparticle creation in proximised superconducting photon detectors

via diffusion processes where they can be detected via tunnelling. The absorption position and incident energy can be reconstructed using the different signals from the detectors adjacent to the absorber. The DROIDS described in this paper consist of Ta/Al STJs and a pure tantalum absorber. The lower energy gap of the proximised STJs will confine the quasiparticles under the tunnel barrier, thus improving the energy resolution and position sensitivity. With the DROID geometry described in this paper this confinement of the quasiparticles in the STJ is not perfect: to some extent quasiparticles can diffuse out of the STJs back into the absorber.

In this paper we describe an investigation of the effect of the last stage of the down conversion process in proximised STJs on the quasiparticle yield. In this regime the down conversion involves relaxation of high energy quasiparticles by phonon emission and breaking of Cooper pairs by energetic phonons providing additional quasiparticles. Using calculated phonon emission rates we simulate the final stages of the down conversion process in proximised tantalum/aluminium bi-layers and compare the result with that of the hypothetical BCS counterpart with the same energy gap. To test the model we performed measurements of the ratio of charges from photon absorption in the proximised STJ and in the pure tantalum absorber immediately adjacent to the STJ of a DROID.

### 5.2 Quasiparticle relaxation in the final stage of the downconversion process

The quasiparticle density of states of a BCS-type superconductor, illustrated in Figure 5-1b, shows a singularity at the energy gap of the material and is constant throughout the layer thickness. Moving towards higher energy levels the quasiparticle density of states reduces asymptotically towards the value of  $2N_0$  (the normal state single spins density of states) of the material.

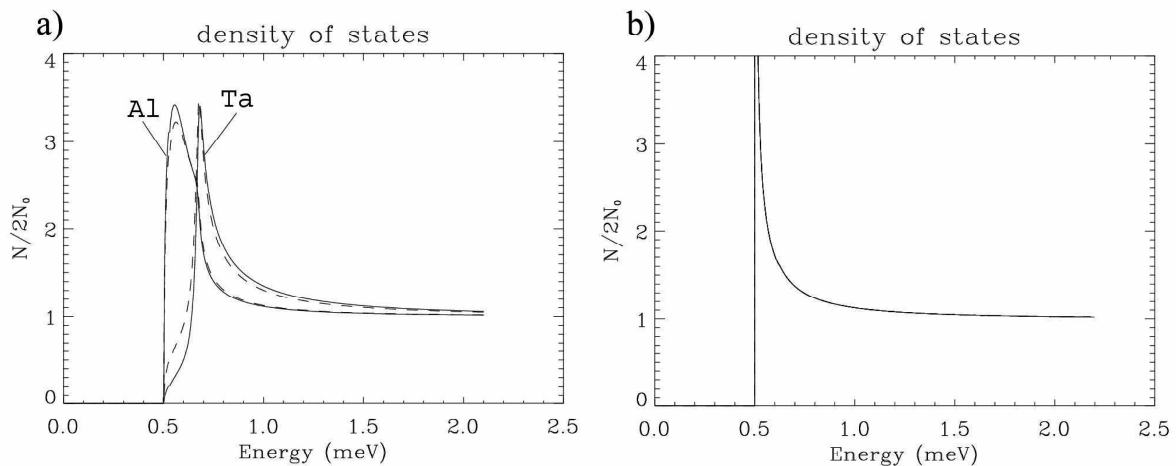


**Figure 5-1 a) The quasiparticle density of states in a proximised Ta/Al bi-layer with thicknesses 100/30nm. The solid lines show the density of states in the two materials at their free interfaces and the dashed lines show the quasiparticle density of states on either side of the interface between the two materials. The energy gap  $\Delta_{s1+s2}$  is equal to 500meV and the broadened peak in the tantalum layer is at  $\Delta_{s2}=\Delta_{Ta}=700$ meV, b) the BCS counterpart density of states which only shows a singularity at the energy gap.**

In a proximized superconducting material, the quasiparticle density of states, the Cooper pair density and the pair potential are all modified throughout the layers thickness. Brammertz *et al*<sup>102</sup> noted that the pair potential displays a step at the interface and the energy gap ( $\Delta_{s1+s2}$ ) is constant throughout the complete structure, if the layer thickness is in the order of a few



coherence lengths. The proximised quasiparticle density of states, illustrated in Figure 5-1a, is different in the two layers, varies across the thickness of the layers and is discontinuous at the interface. In the lower gap material ( $s_1$ ) the quasiparticle density of states shows a broadened peak at the energy gap of the complete structure and in the higher gap material ( $s_2$ ) a broadened peak is present at the energy gap of this material ( $\Delta_{s_2}$ ) with a shoulder towards  $\Delta_{s_1+s_2}$  creating the uniform energy gap throughout the two layers. Towards higher energies the density of states reduces asymptotically towards the value of  $2N_0$ , the single spin electronic density of states at the Fermi level, of the respective materials, identical to the BCS-type density of states.

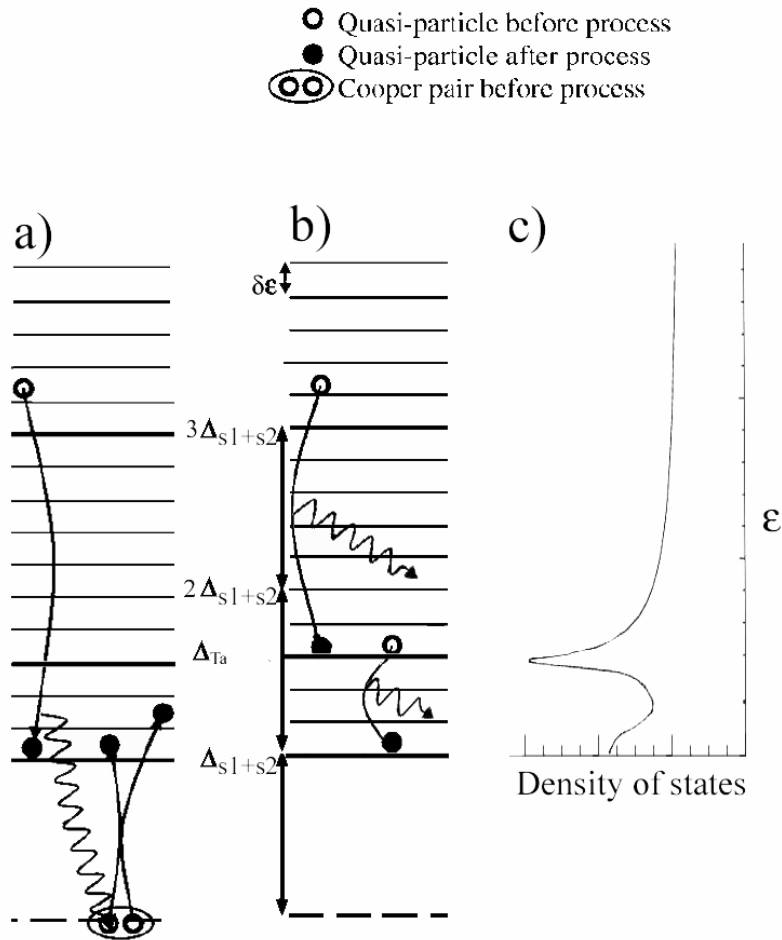


**Figure 5-2** The two routes of down conversion in a thin film proximised superconductor. a) Relaxation of a quasiparticle to the energy gap producing two extra quasiparticles. b) Relaxation of a quasiparticle towards the energy gap via the energy gap of the higher energy gap material producing no extra quasiparticles. c) A schematic representation of the quasiparticle density of states of a proximised superconducting bi-layer averaged over the bi-layer thickness.

The first two stages of the down conversion process occur at relatively high energies where the proximised structure and BCS-type structure appear identical and the down conversion will follow the same route. In the final stage of the down conversion the differences in quasiparticle density of states become more apparent. This stage is dominated by relatively slow relaxation of quasiparticles with release of a phonon. If  $\hbar\Omega_{\text{phonon}} > 2\Delta_{s_1+s_2}$ , with  $\hbar\Omega_{\text{phonon}}$  the energy of the released phonon, this phonon can break a Cooper pair releasing two more quasiparticles thus preserving the total energy. In contrast, sub-gap phonons

## 5. Efficiency of quasiparticle creation in proximised superconducting photon detectors

( $\hbar\Omega_{\text{phonon}} < 2\Delta_{s1+s2}$ ) cannot break Cooper pairs and the energy will be lost producing inefficiency in the energy preservation. This is accounted for by a factor  $1.75^{103}$  in the expression for calculating the number of created quasiparticles following the absorption of a photon with energy  $E_0$  in a BCS-type superconductor:

$$N = \frac{E_0}{1.75\Delta} \quad 5-1$$

with  $N$  the number of quasiparticles and  $1.75\Delta$  the average energy needed to break a Cooper pair.

The rate of spontaneous phonon emission is affected by the phonon density of states, which scales as  $\Omega^2$ . An extra power of the initial energy of a quasiparticle enters because the number of final states below the initial energy  $\varepsilon_\alpha$  is proportional to  $\varepsilon_\alpha$ . On the other hand the quasiparticle relaxation is also dependent on the density of electronic states. Since the quasiparticle density of states of a proximized superconductor is broadened and displays a maximum at  $\Delta_{s2}$  in  $s2$  this creates two possibilities. The first is emitting a high energy phonon and ending at an energy where the quasiparticle density of states is small (as in Figure 5-2a) and the second is emitting a lower energy phonon and ending at an energy where the quasiparticle density of states is large (as in Figure 5-2b). In the process depicted in Figure 5-2a relaxation from the initial state in the range  $3\Delta_{s1+s2} \rightarrow 2\Delta_{s1+s2} + \Delta_{s2}$  can produce a productive phonon,  $\hbar\Omega_{\text{phonon}} > 2\Delta_{s1+s2}$ , which results in the breaking of a Cooper pair. In contrast, in the process in Figure 5-2b where the energy of the emitted phonon is not sufficient,  $\hbar\Omega_{\text{phonon}} < 2\Delta_{s1+s2}$ , to generate extra quasiparticles and the system finally relaxes by emitting another non-productive phonon.

### 5.3 Phonon emission rate in BCS and proximised structures

Comparison of the phonon emission rate for a proximized thin film superconductor with its BCS-type counterpart will indicate if the less efficient route is of importance for the quasiparticle yield. The local phonon emission rate,  $\Gamma_{emi}$ , is calculated using the following expression<sup>102,99</sup>.

$$\Gamma_{emi}(x, \varepsilon_\alpha \rightarrow \Delta\varepsilon_\beta) = \frac{1}{\tau_0(x)[kT_c(x)]^3} \int_{\varepsilon_\alpha - \varepsilon_\beta - \delta\varepsilon/2}^{\varepsilon_\alpha - \varepsilon_\beta + \delta\varepsilon/2} \Omega^2 \left[ G(x, \varepsilon_\alpha - \Omega) - \frac{\Delta_1(x)}{\varepsilon_\alpha} \text{Im} F(x, \varepsilon_\alpha - \Omega) \right] [1 + n(\Omega)] d\Omega \quad 5-2$$

where  $x$  is the coordinate perpendicular to the interface between the two layers,  $\varepsilon_\alpha$  and  $\varepsilon_\beta$  the initial and final energies of the quasiparticle,  $\tau_0$  the electron-phonon interaction characteristic time,  $T_c$  the bulk critical temperature of the bi-layer, both taken from literature<sup>96</sup>.  $\Delta_1$  is the position dependent order parameter,  $G(x, \varepsilon)$  the quasiparticle density of states,  $\text{Im}F$  the imaginary part of the anomalous Green function, as explained in Ref 102, and  $n(\Omega)$  the phonon distribution function which is in most cases smaller than unity and can be neglected. In the geometries discussed below the quasiparticles traverse the bi-layer much faster than the time it takes to emit a phonon and the phonon emission rate can be averaged over the  $x$ -coordinate<sup>104</sup>.

$$\Gamma_{emi}(\varepsilon_\alpha \rightarrow \varepsilon_\beta) = \frac{\int_{electrode} N_0(x) G(x, \varepsilon_\alpha) \Gamma_{emi}(x, \varepsilon_\alpha \rightarrow \varepsilon_\beta) dx}{\int_{electrode} N_0(x) G(x, \varepsilon_\alpha) dx} \quad 5-3$$

For the numerical evaluation of this expression, energy intervals of width  $\delta\varepsilon$  (here chosen to be equal to  $\Delta_{s1+s2}/11$ ) are used and the phonon emission rate from energy level  $\varepsilon_\alpha$  to the energy interval  $\delta\varepsilon_\beta$  near the energy  $\varepsilon_\beta$  can be averaged over the interval  $[\varepsilon_\beta - \delta\varepsilon/2, \varepsilon_\beta + \delta\varepsilon/2]$ :

$$\Gamma_{emi}(\varepsilon_\alpha \rightarrow \delta\varepsilon_\beta) = \frac{\int_{\Delta\varepsilon_\alpha} \Gamma_{emi}(\varepsilon_\alpha \rightarrow \delta\varepsilon_\beta) d\varepsilon_\alpha}{\delta\varepsilon} \quad 5-4$$

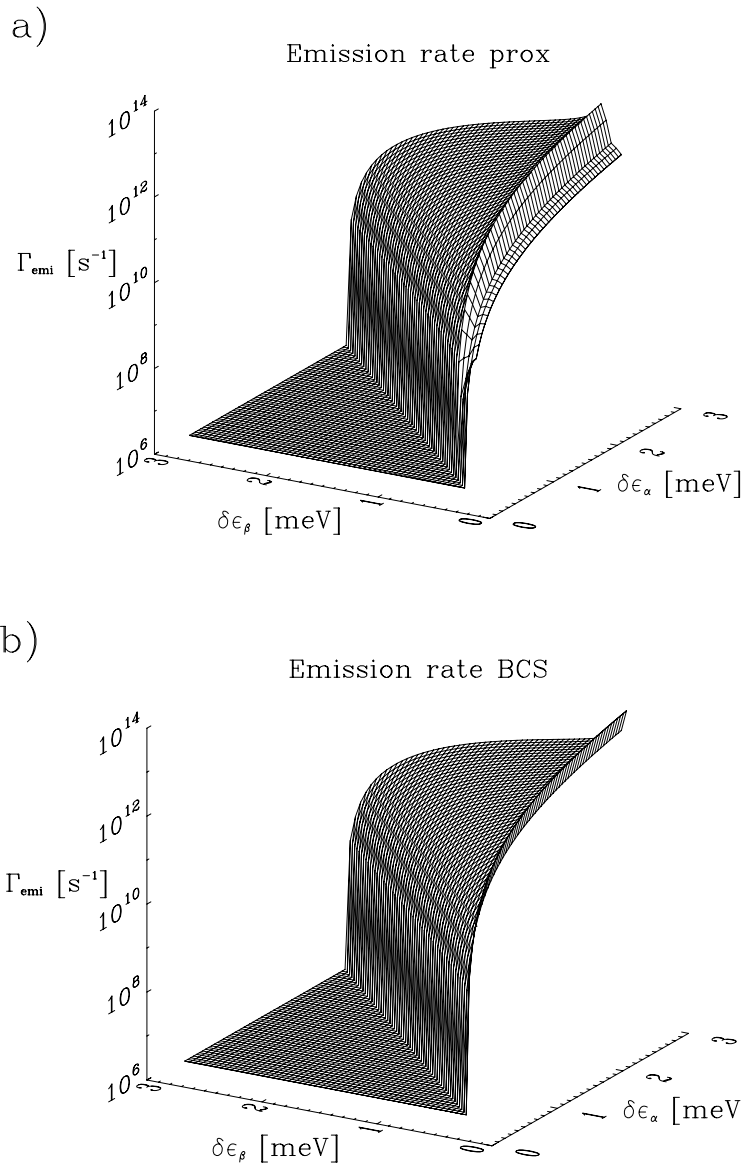


Figure 5-3 The rate of phonon emission resulting from relaxations of a quasiparticle from energy  $\varepsilon_\alpha$  to  $\varepsilon_\beta$  in the range  $\Delta$  to  $5\Delta$ , a) of a Ta/Al film 100/60nm with an energy gap of  $420\mu\text{eV}$ , b) of a BCS-type film with the same energy gap.

## 5. Efficiency of quasiparticle creation in proximised superconducting photon detectors

---

From these expressions the phonon emission rate in the energy range  $\Delta_{s1+s2}$  to  $5\Delta_{s1+s2}$  has been calculated for a proximised Ta/Al superconducting thin film with thickness 100/60nm (100nm of tantalum and 60nm of aluminium) and for the hypothetic BCS superconductor with the same energy gap ( $\Delta_{s1+s2} = 420\mu\text{eV}$ ). The significance of the interval  $\Delta_{s1+s2}$  to  $5\Delta_{s1+s2}$  is that the maximum energy of the emitted phonons is less than  $4\Delta_{s1+s2}$ , hence there may only be one pair-breaking phonon emitted during the relaxation.

Figure 5-3 shows the calculated emission rate from any energy level  $\varepsilon_\alpha$ , in the range  $\Delta$  to  $5\Delta$ , to any lower energy level  $\varepsilon_\beta$ . The BCS-type layers show the highest phonon emission rate, for all initial energy levels  $\varepsilon_\alpha$ , to the final energy level  $\varepsilon_\beta = \Delta_{s1+s2}$ , while the proximised bi-layer show the highest rate, for all initial energy levels  $\varepsilon_\alpha$ , to the final energy level  $\varepsilon_\beta = \Delta_{s2}$ . This indicates that indeed quasiparticle creation in a proximised superconducting thin film proceeds with high efficiency through the route shown in Figure 5-2b.

### 5.4 Quasiparticle creation efficiency

Using the phonon emission rate the final stage of down conversion can be modeled for the proximised and BCS-type superconductor thin films. The goal is to investigate if the efficiency of quasiparticle creation in a proximised structure is reduced in comparison with the efficiency of quasiparticle creation in a BCS structure with the same energy gap. For this comparison the number of quasiparticles created at the end of the down conversion process is of interest. The main reduction of the quasiparticle creation in a proximised superconductor will take place in the final relaxation towards the energy gap where the differences between the proximised and BCS density of states are the largest. This step is the relaxation from the range  $3\Delta_{s1+s2} < \varepsilon < 5\Delta_{s1+s2}$  in which the phonons emitted due to relaxation can only break a single Cooper pair at most. Below this range the emitted phonons will not possess Cooper pair breaking capabilities in either a proximised or a BCS-type superconductor thus not affecting the total number of quasiparticles. The energy dependent balance equation is given by<sup>105</sup>:

$$\frac{dN(\delta\varepsilon_\alpha)}{dt} = \sum_{\beta} \Gamma_{emi}(\delta\varepsilon_\beta \rightarrow \delta\varepsilon_\alpha) \cdot N(\delta\varepsilon_\beta) - \sum_{\beta} \Gamma_{emi}(\delta\varepsilon_\alpha \rightarrow \delta\varepsilon_\beta) \cdot N(\delta\varepsilon_\alpha) \quad 5-5$$

With  $N(\delta\varepsilon_\alpha)$  is the number of thermal quasiparticles in the energy interval  $\delta\varepsilon_\alpha$ . In order to account for quasiparticle creation due to breaking of Cooper pairs by high energetic phonons the number of emitted productive phonons ( $\hbar\Omega \geq 2\Delta$ ) is of importance. When a phonon resulting from the relaxation from energy level  $\varepsilon_\alpha$  to  $\varepsilon_\beta$  has Cooper pair breaking capabilities it can produce two extra quasiparticles positioned at energy levels  $\varepsilon_\gamma$  and  $\varepsilon_\alpha - \varepsilon_\beta - \varepsilon_\gamma$ . A small amount of the productive phonons will be lost into the substrate before they can break a Cooper pair, but this is assumed to be negligible. As mentioned above only the total number of quasiparticles at the end of the downconversion process is of interest and not the dynamics of the quasiparticle distribution, which makes it possible to simplify the simulation of this process further. In the model each relaxation with  $\varepsilon_\alpha - \varepsilon_\beta \geq 2\Delta$  is assumed to create two more quasiparticles, one of which is positioned at the energy gap and the other one is positioned at  $\varepsilon_\alpha - \varepsilon_\beta - \Delta_{s1+s2}$ . This simplification will produce a small error on the relaxation towards these energy levels because these levels will be more populated. However, in the required accuracy of the model this is negligible.

Using this model the final number of quasiparticles for different Ta/Al lay-outs has been calculated using the proximised and the BCS phonon emission rates. In this calculation we have used the density of states in Ta/Al bilayers as calculated with the model from Brammertz

*et al*<sup>102</sup>. The energy gaps predicted for the experimentally tested structures in Sec 5.5 were found in excellent agreement with the measured gaps. The density and energy gaps of the modelled geometries are only dependent on the layer thicknesses of the two materials. The rest of the parameters are the bulk values taken from literature<sup>96</sup>. The ratio of numbers of calculated created quasiparticles in the proximised structure and in the BCS counterpart ( $N_{prox}/N_{BCS}$ ) for the different geometries is shown as a function of tantalum layer thicknesses for three different aluminium thicknesses in Figure 5-4. In all cases the ratio  $N_{prox}/N_{BCS}$  is smaller than unity indicating that the calculated quasiparticle creation is indeed less efficient in proximised structures.

For tantalum thicknesses larger than a few coherence lengths ( $\xi_0 \sim 90$  nm) the proximised quasiparticle density of states will approach the quasiparticle density of states of pure tantalum and display a sharp peak near the energy gap of tantalum. In the proximised part of the structure the energy gap  $\Delta_{s1+s2}$  will be constant with tantalum thickness, in the non proximised tantalum the energy gap will be equal to  $\Delta_{Ta} (=700\mu\text{eV})$  and in between there will be an intermediate region where the energy gap changes from  $\Delta_{s1+s2}$  to  $\Delta_{Ta}$ . The effect of the proximised density of states will reduce with increasing tantalum thickness and the device will appear more like BCS tantalum with the ratio  $N_{prox}/N_{BCS}$  approaching  $\Delta_{s1+s2}/\Delta_{Ta}$  (0.71, 0.60 and 0.51 for Al thicknesses of 30 nm, 60 nm and 100 nm, respectively).

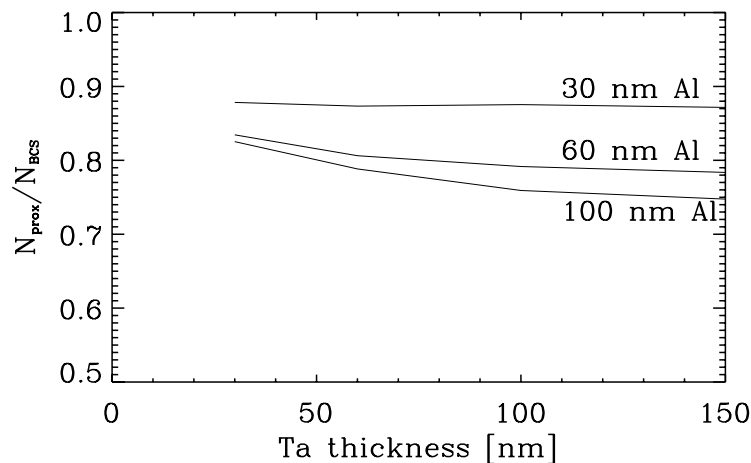


**Figure 5-4 Ratio of quasiparticle yield in a proximised Ta/Al bi-layer and in the BCS counterpart as a function of tantalum layer thickness for aluminium thicknesses 30, 60 and 100nm.**

Due to the finite bin size  $\delta\varepsilon$  in the numerical calculation of the averaged phonon emission rate (eq. 5-4), the number of states in the sharp peak at  $\Delta_{Ta}$  for thick Ta layers tends to get underestimated, and hence also the contribution of the relaxation through this channel. The efficiency of quasiparticle creation will be overestimated and the calculated ratio  $N_{prox}/N_{BCS}$  for thicker tantalum layer will be too large. For this reason we only display calculations for layer thicknesses up to a few coherence lengths. Note that the BCS quasiparticle density of states shows a similar sharp peak near the energy gap. However, in this case underestimation of the number of states in the peak has only a minor effect, since there is only a single relaxation channel.

### 5.5 Experimental investigation of the quasiparticle yield in the BCS absorber and proximised STJ of a DROID

To test the model we compared the charge outputs (defined as the number of tunnelled electrons) of photon absorption events occurring inside an STJ with those in the absorber immediately next to the STJ, in three DROID structures with different STJ layer structures. Within a DROID we can measure the charge output ( $e^-$ ) of a proximised superconductor (the STJ) and a BCS-type superconductor (the absorber) within a single experiment. Since the two types of superconductor are part of the same detector the measurement parameters such as film quality, operating temperature and magnetic field are identical. The DROIDS, produced by MicroFab Ltd<sup>21</sup> using high quality sputter targets (purity of 99.99%) and r-plane Sapphire substrates, have a length, including the STJs, of 400 $\mu\text{m}$  and a width of 30 $\mu\text{m}$ . The STJs are square in geometry with the sides equal to the width of the absorber. The tantalum layer of the base electrode of the STJ is an integral part of the pure BCS tantalum absorber (see Figure 5-5) which has an energy gap of 700 $\mu\text{eV}$ . The STJs are made out of a Ta/Al/AIO<sub>x</sub>/Al/Ta multilayer with thicknesses of 100/30/1/30/100nm, 100/60/1/60/100nm and 100/100/1/100/100nm, energy gaps, as measured from the IV curves, of 500, 420 and 360  $\mu\text{eV}$  and RRR (residual Resistivity Ratio) values of 50, 59 and 41, respectively. The confinement of the quasiparticles in the STJ improves with aluminium layer thickness due to the lower energy gap. For the 100nm aluminium layer the confinement is nearly perfect which means that the quasiparticles cannot escape from the STJ.

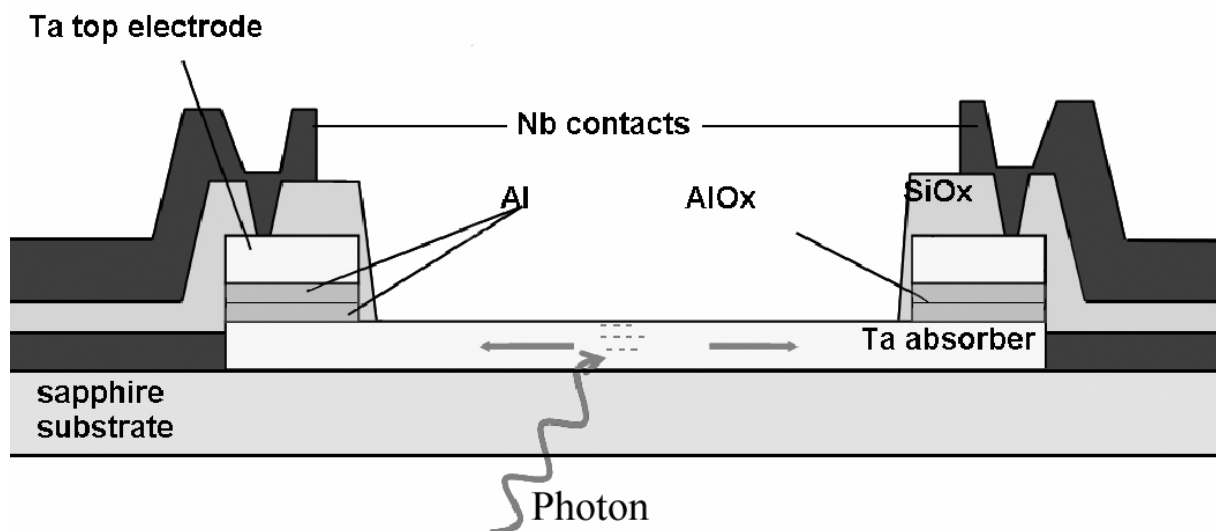


Figure 5-5 schematic representation of the DROID configuration.

A  $^3\text{He}$  sorption cooler has been used with a base temperature of 295mK, low enough to reduce the thermal current to a negligible level for all three devices. The cryostat is equipped with an optical fibre to illuminate the chip through the sapphire substrate with optical photons ( $E_\sigma=1-5\text{eV}$ ) from a double grating monochromator.

The signal pulses from the STJs are fed into a charge sensitive preamplifier and subsequently digitized in a computer oscilloscope card. In a DROID structure the generated quasiparticles will diffuse throughout the structure and are detected by tunnelling across the barrier in the STJs. The sum of the measured charge outputs  $Q_1+Q_2$  is a measure of the photon energy, while the normalised difference  $(Q_1-Q_2)/(Q_1+Q_2)$  refers to position of absorption along the

absorber. Figure 5-6 shows a scatter plot of individual photon signals in an energy versus position representation. Absorptions in the STJs can easily be distinguished from those in the absorber by their spatial separation. The pulses from a single position are averaged to reduce the noise and integrated to obtain the charge output. To ensure that the detected quasiparticles undergo the same loss due to diffusion the STJ charge output is compared to the charge output of an area on the absorber next to the STJ. This area should be sufficiently large so that the lateral proximity effect<sup>106</sup> has a negligible influence. Also it should not be big enough for the differences in loss due to diffusion through the absorber to become apparent. An area with a width of 33  $\mu\text{m}$  is chosen, which divides the absorber in 11 sections (see Figure 5-6). This is much larger than the extent of the lateral proximity effect, which is only for a few  $\mu\text{m}$ , and it is well within the position resolution of the devices used.

There are some differences between an absorption in the STJ and one in the absorber which have to be taken into consideration. For photon absorption in the STJ the quasiparticles will ultimately relax toward  $\Delta_{\text{STJ}}$ . Quasiparticles which are generated due to absorption in the absorber will ultimately relax towards  $\Delta_{\text{Ta}}$  and diffuse towards the STJs where they are injected into the STJ at  $\Delta_{\text{Ta}}$ . The relaxation time of these quasiparticles is much faster than the time required for diffusing into and out of the STJ and the quasiparticles will relax with emission of a phonon.

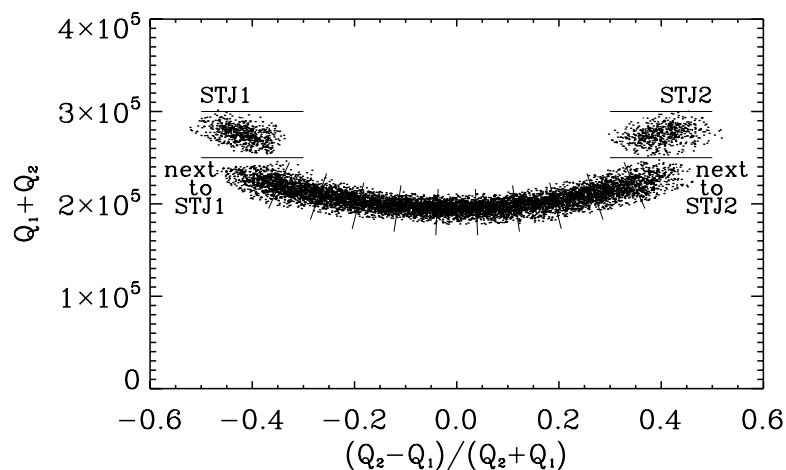


**Figure 5-6** Scatter plot of the total charge output, measuring a photon energy, against the ratio of the charges, measuring the position of absorption site, for the 100/30nm Ta/Al DROID and a wavelength of 300nm. The lines show a graphical representation of the selection of the different areas with the sections used to calculate the ratios indicated.

Under the influence of gain in energy due to sequential tunnelling, relaxation with emission of a phonon and the in- and out-flux of quasiparticles between the STJ and absorber a quasistationary spectral distribution of quasiparticles will be formed in both situations. This quasiparticle distribution will retain its spectral shape during the whole process of charge acquisition, while the number of non-equilibrium quasiparticles (area under the spectral distribution curve) decreases as quasiparticles are lost or recombine. The effect of the different initial conditions in distribution between absorption in the STJ and that in the absorber on the shape of the spectral distribution is expected to be negligible. However, the confinement of quasiparticles in the STJ could have an effect on the charge output ratio. E.g. with perfect confinement all quasiparticles generated resulting from an absorption in the STJ would remain in the STJ. While for an absorption in the absorber a fraction of the quasiparticles would diffuse towards the opposite STJ, experiencing the loss mechanisms in

## 5. Efficiency of quasiparticle creation in proximised superconducting photon detectors

the absorber. The confinement of quasiparticles is affected by the applied bias voltage. With each tunnel event a quasiparticle gains energy equal to the bias voltage, this is counteracted by relaxation, and with increasing bias voltage the confinement will reduce. If the confinement has an effect on the ratio of charges in the way explained above it should be visible in a scan over different bias voltages. Because with reduced confinement in the STJ the quasiparticles created in the STJ will be subjected to more losses (the losses in the absorber) the ratio  $Q_{STJ}/Q_{abs}$  should reduce with bias voltage. Figure 5-7 shows the ratio of the measured charge outputs for photon absorption in the STJ and for absorption in the absorber next to the STJ as a function of bias voltage. Even if the data of the thicker aluminium devices show a lot of scatter due to noise no trend is visible in all three situations and we conclude that the extra losses for quasiparticles produced by an absorption in the absorber immediately adjacent to the STJ are negligible.

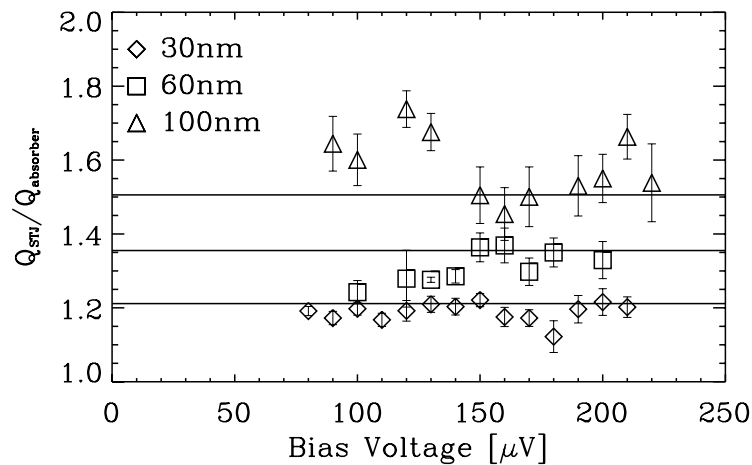


**Figure 5-7** Ratio of the charge output of absorption in the STJ and in the absorber right next to the STJ for the three lay-outs at different bias voltages. The three lines are the calculated ratios.

In the model the multiple tunnelling is seen as an amplification of the number of generated quasiparticles which is the same for absorption in the STJ and for absorption in the absorber. Thus in both situations the charge output is a measure of the number of quasiparticles generated and the ratio should be equal to the ratio of the number of created quasiparticles following the absorption of a photon on each position.

If the proximised STJs were acting like BCS-type STJs the ratio between the charge output in the STJ and the absorber section next to the STJ would simply be determined by the ratio of the energy gaps (cf. eq. 5-1).

$$\frac{Q_{STJ,BCS}}{Q_{abs}} = \frac{\Delta_{Ta}}{\Delta_{STJ}} \quad 5-6$$

Here  $Q_{STJ,BCS}$  is the charge output of a BCS-type STJ and  $Q_{abs}$  the charge output of the absorber. However, taking into account the lower quasiparticle yield in the proximised STJ we arrive at a lower ratio.



$$\frac{Q_{STJ,prox}}{Q_{abs}} = \frac{\Delta_{Ta}}{\Delta_{STJ}} \frac{N_{prox}}{N_{BCS}} \quad 5-7$$

Here  $Q_{STJ,prox}$  is the charge output of the proximised STJ, and  $N_{prox}/N_{BCS}$  is the calculated ratio of the numbers of created quasiparticles for a proximised and for a BCS-type density of states for the STJ, which can be calculated using the model explained in Sec 5.4. From eq. 5-7 the ratio  $Q_{STJ,prox}/Q_{abs}$  has been calculated for DROIDS with 30, 60 and 100nm thick aluminium layers in the STJs. The results are compared with the ratio of the charge output of the STJ and the part of the absorber immediately next to the STJ for different photon energies ranging from 1.5 to 5 eV for the different devices. The bias voltage was 100 $\mu$ V for the DROID with 30nm aluminium layers and 150 $\mu$ V for the DROIDS with 60 and 100 nm aluminium layers. For all three aluminium thicknesses the ratio is constant with photon energy and the ratios of a single energy scan have been averaged to increase the accuracy. The results are shown in Figure 5-8 where the points are the measured ratios, the dashed line is the ratio  $\Delta_{Ta}/\Delta_{STJ}$  and the solid line is the resulting ratio of the model.

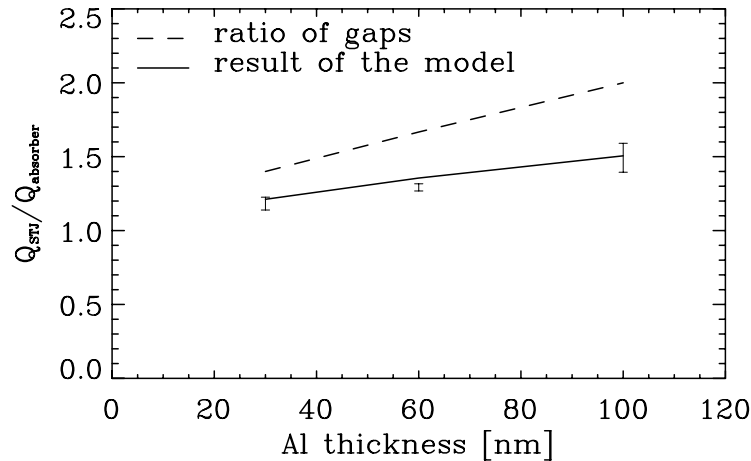


**Figure 5-8** Ratio of the charge output from the STJ and from the absorber just next to the STJ for the DROIDS with aluminium layer thickness of 30, 60 and 100nm, all with a tantalum layer thickness of 100nm. The dashed line is the predicted ratio for a BCS-type STJ with energy gap  $\Delta_{STJ}$ . The solid line is the ratio as calculated obtained with the model. The presented points are averages of the measured ratios at different photon energies in the range 1.5-5eV over which range the ratio is constant in all three cases. The ratios for the bi-layers with 30nm aluminium have been measured at a bias voltage of 100 $\mu$ V and the ratios for the bi-layers with 60 and 100nm aluminium have been measured at 150 $\mu$ V.

For all three DROIDS the measured ratios are well below the ratio  $\Delta_{Ta}/\Delta_{STJ}$  indicating the significance of different conditions for the quasiparticle creation. The simulated ratio convincingly fits the results in all three measurements.

## Discussion

We have investigated the final stage of down conversion in proximised thin film superconductors and clearly confirmed a lower efficiency in quasiparticle creation compared to the BCS counterpart. This lower efficiency is caused by the modified quasiparticle density of states of a proximised device (shown in Figure 5-1) which, contrary to the BCS quasiparticle density of states shows an increased number of states at  $\Delta_{s2}$  in the higher gap

## 5. Efficiency of quasiparticle creation in proximised superconducting photon detectors

---

material. In the final stage of the down conversion process of a proximised superconducting thin film, the result will be an increase in relaxation of high energy quasiparticles first toward  $\Delta_{s_2}$  followed by relaxation towards  $\Delta_{s_1+s_2}$ , instead of immediately relaxing towards  $\Delta_{s_1+s_2}$  as in a BCS-type superconductor. Quasiparticles from the energy range  $3\Delta_{s_1}$  to  $2\Delta_{s_1+s_2}+\Delta_{s_2}$  which relax to  $\Delta_{s_2}$  do not emit phonons with Cooper pair breaking capabilities while the phonons would be energetic enough to break a Cooper pair if the quasiparticle immediately would have relaxed to  $\Delta_{s_1+s_2}$ . This results in reduced quasiparticle creation efficiency in proximised superconducting thin films.

The reduced quasiparticle creation efficiency is confirmed in the measurements using DROIDS where we have compared the charge output of the proximised STJ with the charge output of the BCS absorber. Figure 5-8 clearly shows that the ratio of the two responsivities is lower than the ratio of the energy gaps. Using the model we have calculated the ratio as it would be with the lower efficiency in quasiparticle creation in the proximised STJ. In all three situations the calculated ratio closely fits the measured ratios. For the measurements it is assumed that the difference in loss of quasiparticles due to diffusion is negligible for these two locations. Although the quasiparticle diffusion and injection in the STJ are different for the two locations a constant distribution of quasiparticles is quickly formed, which is the same in shape but different in amplitude. The trapping of quasiparticles in the STJ could produce a lower loss rate for quasiparticles created in the STJ. However, a variation of the bias voltage, which changes the trapping efficiency of the STJs, has no effect on the ratio indicating this effect is negligible. The ratio of the responsivities is constant with photon energy in the optical range. With the absorption of an optical photon the quasiparticle concentration is too low to produce significant recombination between two mobile quasiparticles, which would reduce the charge output in both the STJ and absorber. Also the number of states available in the quasiparticle density of states is large enough to accommodate all generated quasiparticles close to the edge of the energy gap, such that no restriction in the relaxation of quasiparticles is introduced.

For photon detectors based on proximized superconductors, like STJs, the implication of this lower quasiparticle yield at the end of the downconversion is lower signal amplitude and a lower limiting energy resolving power. In the case of a DROID, where the absorber is made of a pure superconductor and the STJs are proximised superconductors, the charge output of the STJ will be lower than one would assume from the ratio of the energy gaps of the STJ and absorber. Also the resolution of the STJs will be affected accordingly.

### 5.6 Conclusion

In conclusion we have successfully clarified in significant detail the final stages of down conversion in proximised superconducting thin films, and compared them to the BCS counterpart with the same energy gap. The model has been tested using the ratio of the charge output of the proximised STJ and BCS-type absorber of three DROIDS with different aluminium trapping layer thicknesses in the proximised STJs. The experimental data agree closely with the model. We conclude that the quasiparticle creation in proximised devices compared with a BCS-type superconductor is indeed less efficient due to increased quasiparticle relaxation towards the energy gap of the higher gap material.

### *Acknowledgements*

We would like to thank Dr. A. A. Golubov from the Department of Applied Physics, University of Twente, Enschede, the Netherlands for the useful discussions.



## Chapter 6

---

# Position dependent spatial and spectral resolution measurement of distributed read-out superconducting imaging detectors

---

R. A. Hijmering, P. Verhoeve, A. G. Kozorezov, D.D.E. Martin, J. K. Wigmore, I. Jerjen, R. Venn and P.J. Groot

J. Appl. Phys. **103**, 083914 (2008)

We present direct measurements of spatial and spectral resolution of cryogenic Distributed Read Out Imaging Detectors (DROIDs). The spatial and spectral resolutions have been determined experimentally by scanning a 10 $\mu$ m spot of monochromatic visible light across the detector. The influences of the photon energy, bias voltage, and absorber length and width on the spatial and spectral resolution have been examined. The confinement of quasiparticles in the readout sensors (superconducting tunnel junctions (STJs)) as well as the detector's signal amplitude can be optimized by tuning the bias voltage, thereby improving both the spatial and spectral resolution. Changing the length of the absorber affects the spatial and spectral resolution in opposite manner making it an important parameter to optimize the DROID for the application at hand.

The results have been used to test expressions for photon energy, position, spatial and spectral resolution which have been derived using an existing 1-dimensional model.

The model is found to describe the experimental data accurately, but some limitations have been identified. In particular, the model's assumption that the two sensors have identical response characteristics and noise, the approximation of the detailed quasiparticle dynamics in the sensors by border conditions, and the use of a 1-D diffusion process is not always adequate.

### 6.1 Introduction

Cryogenic detectors are widely used in photon counting spectro-photometers because of their spectroscopic capabilities. A number of systems are currently under development that use superconductivity as the basis of photon detection. Transition Edge Sensors<sup>10</sup> (TES) are temperature biased on the superconducting-normal transition and measure the change in temperature due to the absorption of a photon through a change of resistance of the detector. Kinetic Inductance Detectors (KIDs)<sup>15</sup> rely on the change in inductance caused by the increase in number of quasi-particles (qps) excited by the absorbed photon. When placed inside a resonant circuit the change in inductance will create a change in resonance frequency of the circuit. A Superconducting Tunnel Junction (STJ) consists of two thin layers of superconducting material separated by an insulating layer. The excited qps tunnel through the insulating barrier to the opposite electrode and, in the presence of a DC bias voltage, produce a measurable current pulse. In each of these detectors the measurable quantities are proportional to the energy of the absorbed photon, thus providing the intrinsic spectroscopic capability. The best resolutions obtained with cryogenic detectors to date are 0.105eV at 2.48eV at optical wavelengths<sup>107</sup> using STJs, whilst in the X-ray part of the spectrum a resolution of 1.8eV at 6keV has recently been achieved by Bandler *et al*<sup>108</sup> using TESs. Whilst the development of individual devices, up to a few hundreds of microns in size, is well advanced, difficulties arise in the attempt to create larger area detectors which possess equivalent, high spatial and spectral resolution. The simplest approach is to fabricate close-packed arrays of individual detectors, each with their own signal wire, bias circuit and readout circuit. This route has been followed in the Superconducting tunnel junction CAMera (S-Cam) project at ESA, in which STJ arrays are being developed as imaging photon detectors for use in optical astronomy. With S-Cam 2 and S-Cam 3 a 6x6 array of 25x25 $\mu\text{m}$  STJs and a 10x12 array of 33x33 $\mu\text{m}$  STJs have successfully been used as optical photon counting spectrometers on the William Herschel Telescope (La Palma, Spain) and the Optical Ground Station<sup>22</sup> (Tenerife, Spain). The current camera can handle a count rate up to 8kHz/pixel and with a maximum resolving power of 14 at 500nm and micro-second timing accuracy. The thermal load from the signal wires on the cooling system, and the size of the readout electronics puts a practical limit on the number of pixels which can be read out in this way. A multiplexed readout in which several pixels share a single signal wire and readout electronics, can considerably extend this limit. In particular detectors which use SQUID-based readout systems such as TES's are well suited for this. STJs are usually read out with J-FETs at room temperature, which inhibits multiplexed readout, but SQUID readout has also been demonstrated<sup>126</sup>. The readout of KIDs can be conveniently multiplexed by using different resonance frequencies for each KID.

To further increase the sensitive area Distributed Read-Out Imaging Detector (DROID) configurations are being developed. In these devices the photon is absorbed in a single absorbing layer with two or more sensors, in the form of TESs, KIDs or STJs, at the edges. The resulting excited qps, or phonons in the case of TESs, diffuse rapidly throughout the film and are detected in the sensors. The position of absorption and the energy of the incident photon can be determined from the magnitudes of the sensor responses. Depending on the configuration of the sensor the signal carriers can be free to diffuse in and out of the sensor, be trapped inside the sensor or some intermediate situation can occur<sup>26</sup>. Trapping of signal carriers inside the sensor will decrease the crosstalk (signal carriers contributing to the signal in both sensors) between the two sensors and increase the signal amplitude of the DROID. This type of trapping should not be confused with local trapping<sup>105</sup> which immobilizes qps either due to the presence of localized states inside the superconductor gap or by localized

## 6. Position dependent spatial and spectral resolution measurement of distributed read-out superconducting imaging detectors

---

areas with suppressed gaps, e.g. due to impurities, keeping the qps away from the tunnel barrier. Whether or not such a detector is useful in practice depends on whether the spatial and spectral resolution of the measurements is at least comparable with that of a detector consisting of individual pixels. As will be described below in section 6.2, although there has been great interest in this area, there have been no previous measurements carried out on the dependence of spatial and spectral resolution of a DROID on the position of the photon absorption.

Although the results shown below are relevant to other types of detectors as well, they are obtained with DROIDS that use STJs as sensors. STJs are sensitive to photon energies ranging from the FIR ( $E > 2\Delta$ ) up to the X-ray wavelength range. Due to the low energy gap (typically below 1 meV) the absorption of a photon creates a large number of quasiparticles (qps), typically  $\sim 2000$  for the absorption of an optical photon. The number of qps created is proportional to the incident energy and is given by  $N = E_0/\varepsilon$  with  $N$  the number of qps,  $E_0$  the energy of the incident photon and  $\varepsilon = 1.75\Delta$  the average energy needed to break a Cooper pair. Here  $\Delta$  is the gap energy and the factor 1.75 arises from the efficiency of converting the absorbed photon energy into qps<sup>19</sup>. In its life time a qp can tunnel many times over the barrier producing an internal amplification<sup>58</sup>. This increases the signal output but adds an extra statistical fluctuation on the charge output. The energy resolution of a STJ is given by  $\Delta E(E_0) = 2.355((F+G+J+H)\varepsilon E_0 + (K_v + K_H)E_0^2)^{1/2}$  with  $F$  the Fano factor,  $G$  extra statistical fluctuation due to tunnelling and  $J$  a description of the statistical fluctuations on the converted energy due to losses of productive phonons into the substrate in thin films<sup>107</sup>. The cancellation factor  $H$  accounts for the statistical fluctuations in the ratio of direct and cancellation tunnel events<sup>29</sup>.  $K_v$ , the vertical inhomogeneity factor<sup>107</sup>, accounts for the dependence of the deposited energy on the distance between the absorption site and the phonon escape interface between the superconducting material and the substrate and the horizontal inhomogeneity factor  $K_H$  accounts for spatial variations in the responsivity over the area of the device<sup>110</sup>. In addition to these internal noise sources there are also external sources which influence the resolution such as the electronic noise associated with the readout and possible IR background load. To reduce the current of thermally excited qps the operating temperature must be well below the critical temperature of the material ( $T < 0.1T_c$ ). For the widely used tantalum STJs, with a  $\Delta = 700\mu\text{eV}$ , the operating temperature lies around 300mK.

In this paper we will describe measurements of both spectral and spatial resolution as a function of absorption position obtained by scanning a monochromatic optical beam with a diameter of  $10\mu\text{m}$  across the absorber. We used a DROID configuration consisting of an absorber strip of tantalum with an STJ with suppressed gap on each end. The relation between the spectral and spatial resolution was compared to the result of a 1D diffusion model of the DROID response by Kraus *et al*<sup>28</sup> and Jochum *et al*<sup>68</sup> from which we derived the expressions for the photon energy, absorption position, spectral resolution and spatial resolution. The measurements were performed as a function of various internal and external parameters to find the optimal conditions for both spectral and spatial resolution.

### 6.2 Modelling of DROID response

Many groups have studied the processes involved with position sensitive detector response and noise factors affecting its resolving power. Kraus *et al*<sup>28</sup> produced a widely used relation between the spectral and spatial resolution for DROIDS with perfect qp trapping in the STJs. Jochum *et al*<sup>68</sup> have produced a generalization of this model in order to include imperfect qp trapping in the STJs. This paper gives the expressions for the charge output for the right ( $R$ ) and left ( $L$ ) side STJ in the form:

$$Q_{R(+),L(-)} = \frac{E_0 c}{\varepsilon} \frac{\sinh \alpha \left( \frac{1}{2} \pm \frac{x_0}{L} \right) + \beta \cosh \alpha \left( \frac{1}{2} \pm \frac{x_0}{L} \right)}{(1 + \beta^2) \sinh \alpha + 2\beta \cosh \alpha} \quad 6-1$$

Here  $Q_{R,L}$  is a measure for the total number of tunnelled electrons collected by the right and left STJ with the ‘+’ sign for the right STJ and the ‘-’ sign for the left STJ,  $c$  is the proportionality factor which relates the observed charge to the number of qps reaching the STJ,  $L$  is the length of the absorber and  $x_0$  is the coordinate of the photon absorption position along the one-dimensional DROID. The characteristic parameter describing qp loss inside the absorber  $\alpha = L/\sqrt{D\tau_{loss,abs}}$  is given by the ratio between the length of the absorber and the square root of the product between the diffusion constant  $D$  and the loss time in the absorber  $\tau_{loss,abs}$ . The parameter  $\beta$ ,  $\beta = \sqrt{\tau_{tr}/\tau_{loss,abs}}$ , which is given by the square root of the ratio between the characteristic trapping time  $\tau_{tr}$  and the loss time in the absorber, has been introduced as a boundary condition to account for partial trapping of qps by the STJ. It describes which fraction of the qps is collected in the STJ and contributes to the measured signal. This is an approximation for the actual in and out flux of qps in the STJ because the dynamics of qps in the STJ is more complicated. Qps may be inelastically scattered, the process leading to their trapping, they also may diffuse back into the absorber, or they may tunnel, gain energy in the tunnel process and leave the STJ if after the tunnel process they emerge with sufficiently high energy to diffuse into the absorber. Further processes inside the STJ affecting the charge output as qps loss, trapping by local traps and multiple tunnelling are accounted for by the proportionality factor  $c$ .

Segall *et al*<sup>29</sup> developed a model for DROIDS with BCS type STJs which included the processes inside the STJs. Later they described the way to control out-diffusion in order to optimize the device<sup>111</sup>. Den Hartog *et al*<sup>72</sup> produced a 2D diffusion model without trapping based on the Rothwarf-Taylor equations<sup>82</sup> with which they modelled the current pulse resulting from X-ray absorptions. Ejrnaes *et al*<sup>112</sup> developed, using a different approach, a similar 2D diffusion model. Adrianov *et al*<sup>113</sup> have recently developed a 2D diffusion model which takes into account qp loss at the edges of the absorber and qp trapping in the STJs. Also recently Samedov *et al*<sup>114</sup> produced a 2D model which gives a relation for the spectral and spatial resolution, assuming perfect trapping of qp in the STJs. Furlan<sup>115</sup> *et al* used the model as derived by Jochum *et al*<sup>68</sup> to analyze the charge output of their devices which they illuminate using a pulsed LED to produce single and multiple photon events. To estimate the spectral resolution they used the thermodynamic limit on the resolution.

Based on the original result of Jochum<sup>68</sup> we have now derived all necessary expressions for comparison and interpretation of our experiments. We used an approach similar to that of Kraus<sup>28</sup> and found the expressions for the position of the absorption site, photon energy, spectral and spatial resolution. Specifically we have derived the relation between spatial and spectral resolution which is useful in the case of uniform illumination when only the spectral resolution can be directly determined. The absorption position depends only on the ratio of the two signals. Thus, rearranging the terms in eq. 6-1 and using hyperbolic relations gives the following expression for the position as function of the measured charge outputs.

$$x_0 = \frac{L}{2\alpha} \ln \left[ \frac{Q_R e^{\frac{\alpha}{2}} (1 + \beta) + Q_L e^{-\frac{\alpha}{2}} (1 - \beta)}{Q_R e^{-\frac{\alpha}{2}} (1 - \beta) + Q_L e^{\frac{\alpha}{2}} (1 + \beta)} \right] \quad 6-2$$

## 6. Position dependent spatial and spectral resolution measurement of distributed read-out superconducting imaging detectors

Summing the charge outputs in eq. 6-1 and rearranging the terms we obtain the following expression for the energy as function of the measured charge outputs.

$$E_0 = \frac{\varepsilon}{c} \sqrt{(Q_R^2 + Q_L^2)(1 - \beta^2) + 2Q_R Q_L [(1 + \beta^2) \cosh \alpha + 2\beta \sinh \alpha]} \quad 6-3$$

In order to derive spectral and spatial resolution we use the assumption<sup>28</sup> that the uncertainty in the charge measured by either STJ is the same,  $\Delta Q_L = \Delta Q_R = \Delta Q$ . In general this assumption can not always be justified but it can be justified e.g. in the case when electrical noise or the IR background is the dominant noise contribution. Implicit differentiation with the use of eq. 6-2 and eq. 6-3 yields the following expressions for spatial and spectral resolution:

$$\Delta x = \Delta Q \frac{\varepsilon}{E_0 c} \frac{L}{\alpha} \sqrt{[(1 + \beta^2) \cosh \alpha + 2\beta \sinh \alpha] \cosh \frac{2x_0 \alpha}{L} - (1 - \beta^2)} \quad 6-4$$

$$\Delta E = \Delta Q \frac{\varepsilon}{c} \sqrt{[(1 + \beta^2) \cosh \alpha + 2\beta \sinh \alpha] \cosh \frac{2x_0 \alpha}{L} + (1 - \beta^2)} \quad 6-5$$

The relation between the spatial and spectral resolution becomes:

$$\frac{E_0}{\Delta E} = \frac{L}{\Delta x \xi(x_0)} \quad 6-6$$

where  $\xi(x_0)$  is given by:

$$\xi(x_0) = \alpha \sqrt{\frac{[(1 + \beta^2) \cosh \alpha + 2\beta \sinh \alpha] \cosh \frac{2x_0 \alpha}{L} + (1 - \beta^2)}{[(1 + \beta^2) \cosh \alpha + 2\beta \sinh \alpha] \cosh \frac{2x_0 \alpha}{L} - (1 - \beta^2)}} \quad 6-7$$

When using this model some limitations need to be kept in mind. Firstly, the model describes a 1D diffusion process. However, for absorptions near the STJ (up to a distance of roughly the width of the absorber away from the STJ) the diffusion process is still 2D. For DROIDS with a smaller aspect ratio this 2-dimensionality becomes more evident. Secondly, the model assumes the responsivity of the two STJs to be equal. In practice there are always slight differences between the STJs due to the fabrication process limitations. This gain difference can not be corrected for due to the coupling between the two STJs. Thirdly, its validity depends on the assumption of equal noise densities in both STJs. The obvious advantage of the model is that it is simple and treats a general case in which imperfect trapping is taken into account. This situation applies for DROIDS with proximized STJs or KIDs as detectors at the ends of a linear absorber. When taking the limit of  $\beta \rightarrow 0$  the case for perfect trapping as given by Kraus<sup>28</sup> is retrieved, applicable if for example a DROID with a tantalum absorber and pure aluminium STJs, or if TESs are used as detectors.



### 6.3 Experimental details

We have measured the spatial and spectral resolution as function of photon energy, bias voltage, absorber length ( $L$ ) and width ( $w$ ). The experiments were focussed around three separate objectives. The first was to test experimentally the theoretical predictions published earlier by Kraus *et al*<sup>28</sup> and Jochum *et al*<sup>68</sup> and the resulting derivations in the present paper. Secondly, since the spectral resolution is largely fixed by internal physical processes, we aimed to explore the dependence of the spatial resolution on external variables such as photon energy and bias voltage. Finally we studied the effect of varying the design of the DROID, notably its length and width.

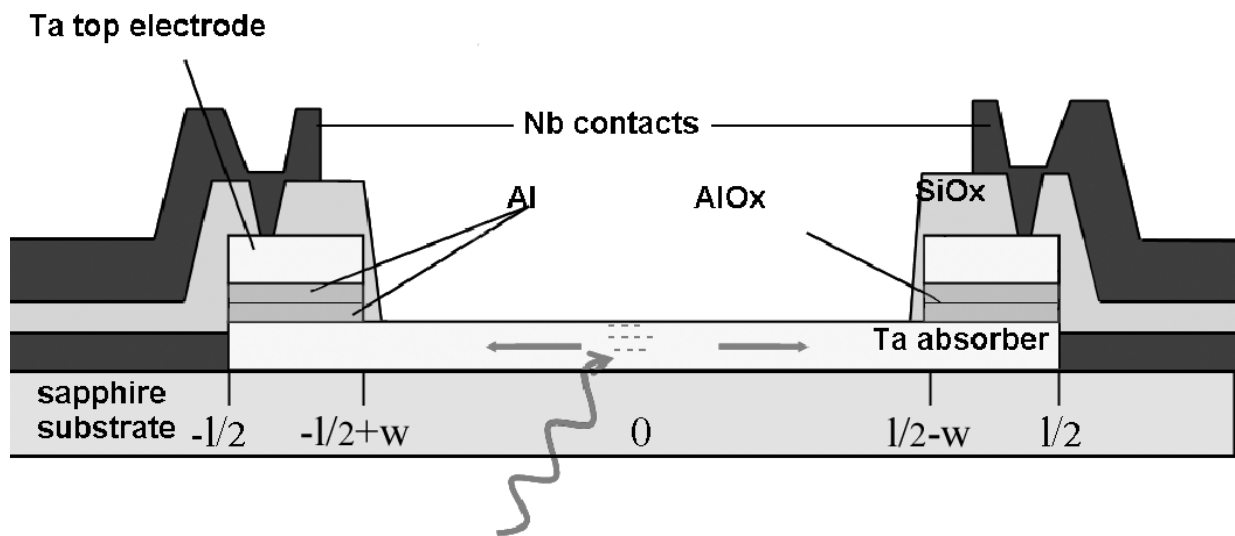


Figure 6-1 Schematic representation of the DROID configuration.

Several devices of different geometries were produced by Cambridge MicroFab Ltd<sup>87</sup> on a single chip so that variations between devices due to the production process are expected to be small. The devices consist of a 100nm thick absorber strip of tantalum with a proximized Ta/Al STJ on either end (see Figure 6-1). The STJs have a lay-out of Ta/Al/AlO<sub>x</sub>/Al/Ta with thicknesses of 100/60/1/60/100nm. The aluminium layer suppresses the energy gap from 700 $\mu$ eV to 420 $\mu$ eV providing mild trapping to confine the qps in the STJs area. The tantalum layer of the STJs base electrode is integral with the absorber. The devices have lengths ( $L_{DROID}$ ) ranging from 200-400 $\mu$ m, all lengths of the DROIDS are including STJs ( $L_{DROID}=L+2w$ ), and absorber widths ( $w$ ) of 20, 30 or 50 $\mu$ m. The STJs are square in geometry with the sides equal to the width of the absorber. The chip is illuminated with optical photons from the backside through the sapphire substrate. The charge output from each STJ is recorded via a pulse height analyzer consisting of a charge sensitive preamplifier followed by a pulse shaping stage, a peak detector and an AD converter. When signals are detected in the two pulse height analyzers within a time window of 30 $\mu$ s the signal is recorded as a single event with the two pulse height amplitudes and the time difference between the two pulses. For responsivity measurements this method is not ideal because the pulse profile changes with absorption position and the electronics have a fixed integrating time. To first order the effect will show up as an increased loss in the absorber, affecting the value for  $\alpha$ . But this should have no significant effect on the resulting spatial and spectral resolution. The experiments were carried out using a pumped <sup>4</sup>He cryostat with a <sup>3</sup>He sorption cooler having a base temperature of 295mK and a hold time of 6.5 hours. At this temperature there is

## 6. Position dependent spatial and spectral resolution measurement of distributed read-out superconducting imaging detectors

still some thermal current present, acting as an extra noise contribution. On average the subgap current reached a level of 400pA which is induced by both the thermal current and IR background. The cryostat is fitted with an optical window to allow external illumination with a set of three cold filters placed behind the window to reduce the IR radiation load on the detector. The IR filtering is not 100% efficient and there is still some IR radiation which reaches the detector, degrading the resolutions. However, it justifies the assumption  $\Delta Q_L = \Delta Q_R = \Delta Q$  allowing for a simplification to be made in the interpretation of the data. The available wavelength band is 350-750nm, limited by the IR filters.

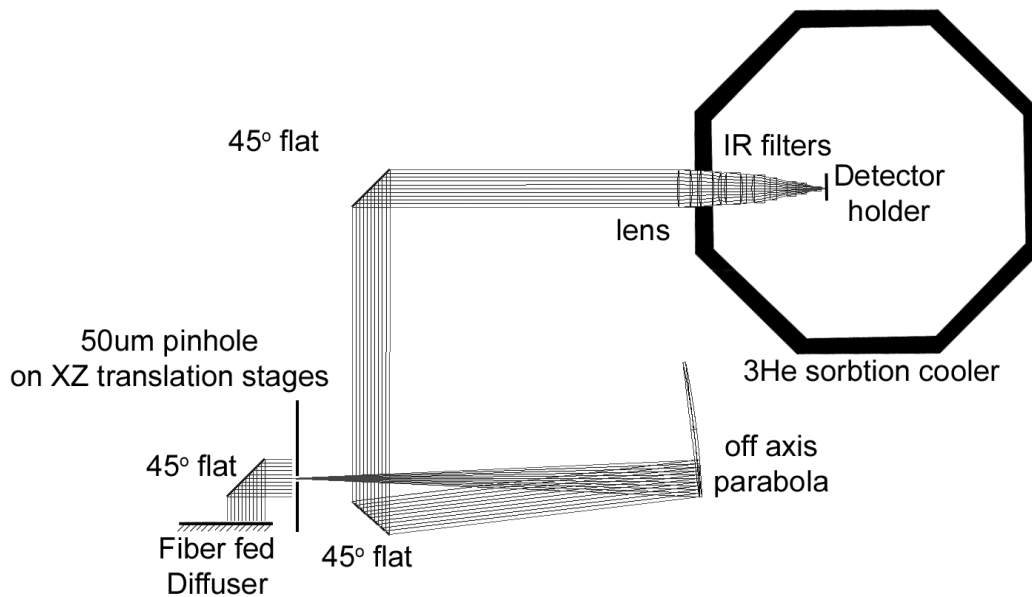


Figure 6-2 Schematic representation of setup.

The optical arrangement is shown in Figure 6-2<sup>116</sup>. The objective was to achieve a spot size of 10 $\mu\text{m}$ . Previous values for spatial resolution of a DROID with 30nm Al trapping layers estimated from the spectral resolution suggested a spatial resolution of  $\sim 40\mu\text{m}$ <sup>117</sup>. The spot size of 10 $\mu\text{m}$  should only have a small effect on the measured spatial resolution (3% with a spatial resolution of 40 $\mu\text{m}$ ). To produce this spot size on the detector the high quality optical relay system of the S-Cam 3 instrument has been used to image a pinhole on the absorber. A high quality lens was attached to the cryostat to focus the beam on the detector. The rest of the optics consists of two 45° flat mirrors to fold the beam, and an off-axis parabola with a 50 $\mu\text{m}$  pinhole in its focus. The pinhole was illuminated using a diffuser which was connected via an optical fiber to a double grating monochromator and a Xe lamp ( $\lambda=200\text{-}1000\text{nm}$ ), or alternatively to a HeNe laser ( $\lambda=633\text{nm}$ ) for a higher intensity. The pinhole was mounted on a set of translation stages in order to be able to move the spot over the detector chip. The throughput of the complete system was very low necessitating long integrating times due to the low count rate. With the reduction factor of the optical chain of 5.4 this setup should produce a 9.3 $\mu\text{m}$  spot on the detector. The actual size of the light spot has been determined from an intensity profile of a scan over the width of the absorber, in the  $y$  direction in Figure 6-3.

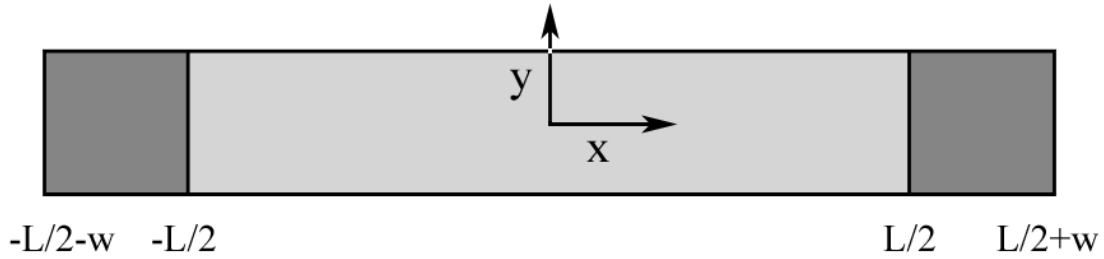


Figure 6-3 Schematic representation of the top view of a DROID to indicate the scan directions.

The resulting intensity profile describes the integration of the image profile with position in one direction. A model of the optical train has shown that the resulting spot profile has a sharp peak with very broad but low intensity wings. This profile has been approximated by a co-centric double 2D Gaussian profile of which the first describes the sharp peak and the second describes the broad wings. The resulting modelled spot profile is integrated in the  $x$  direction from  $-\infty$  to  $\infty$  (along the length of the absorber). The integration in the  $y$  direction between the limits  $y'-w/2$  to  $y'+w/2$  mimics the movement of the spot across the absorber width.

$$I(y') = \frac{1}{\sqrt{2\pi}} \int_{y'-w/2}^{y'+w/2} \left( \frac{1}{\sqrt{a}} e^{-y'^2/2a} + \varphi \frac{1}{\sqrt{b}} e^{-y'^2/2b} \right) dy \quad 6-8$$

Here is  $a$  the diameter of the first Gaussian representing the narrow spot and  $b$  the diameter of the second Gaussian representing the low intensity broad wings. The intensity of the second Gaussian is given by  $\varphi$  in percentages of the intensity of the first Gaussian. The factor  $\sqrt{2\pi}$  results from the integration in the  $x$ -direction. The measured intensity profile has been normalized to the intensity at the center of the absorber and the model has been fitted to the data, with the result shown in Figure 6-4.

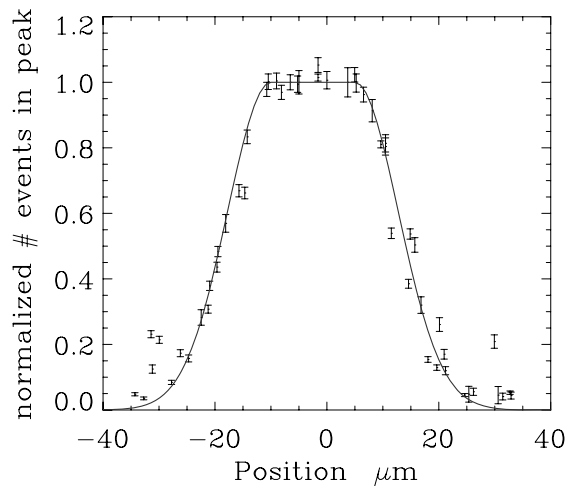


Figure 6-4 Measured intensity profile resulting from a scan of the pinhole image over the 30 $\mu$ m width of the absorber. The solid line is the result of a least-squares fit of the modeled intensity profile to the measured data.

## 6. Position dependent spatial and spectral resolution measurement of distributed read-out superconducting imaging detectors

The fitted spot profile resulted in a diameter of  $a=10\pm 1\mu\text{m}$  FWHM for the first, sharp Gaussian and  $b=300\pm 50\mu\text{m}$  FWHM for the second Gaussian which has an intensity of  $\varphi=0.02\pm 0.001$ . In practice the  $10\mu\text{m}$  FWHM is shown to be negligible compared to the spatial resolution of the measurements. The  $300\mu\text{m}$  wide Gaussian will show up as a low intensity background illumination. This spot profile has been used to illuminate the absorber locally on  $\sim 10$  positions with different  $x$ -coordinates (see Figure 6-3) along the absorber, referred to as a ‘scan’. The position of the spot is known from the translation stage settings and verified by detecting the ends of the absorber through a drop in intensity.

### 6.4 Results

The objectives of the experiments are to test the theoretical predictions and to find the optimal configuration of the external and internal parameters. The first of the experiments was carried out on a DROID of length  $400\mu\text{m}$  (including STJs) and width  $30\mu\text{m}$  with  $30\times 30\mu\text{m}$  STJs. Earlier results have shown this geometry to be a good trade off between sensitive area and signal to noise ratio at optical wavelengths<sup>117</sup>. The measurements were carried out using  $410\text{nm}$  ( $3.03\text{eV}$ ) photons, determined by optimal throughput of the optical system, with a bias voltage of  $120\mu\text{V}$  and at a temperature of  $295\text{mK}$ .

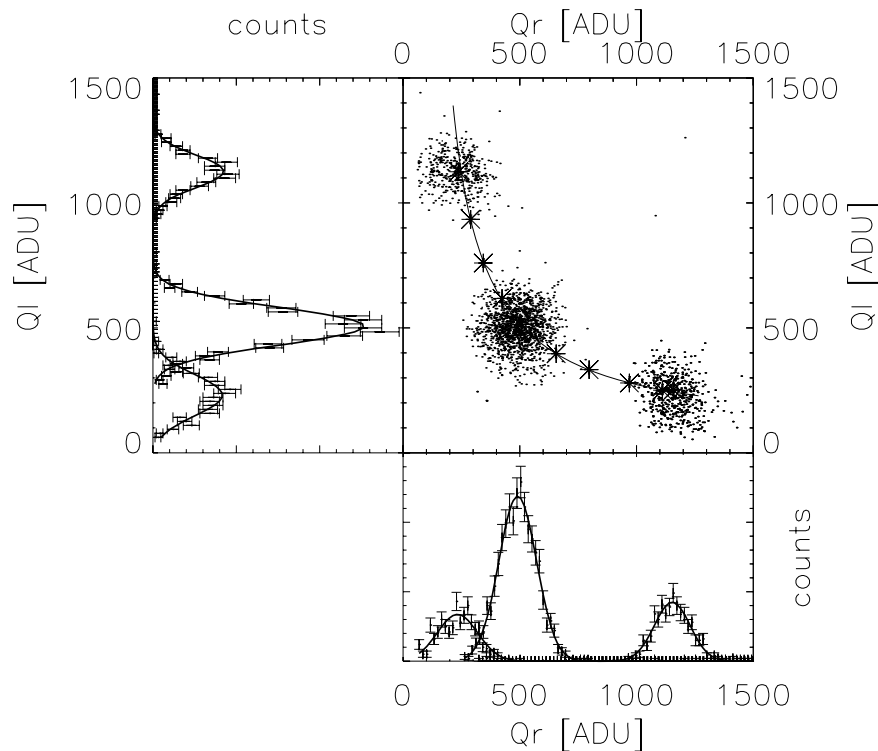


**Figure 6-5** Scatter plot of three measurements of a single device. The pulse height distributions of the two STJs are plotted on the axis together with the fitted gaussian profiles. The average charge outputs for the entire scan are shown by stars with the model to obtain the values for  $\alpha$  and  $\beta$  as a solid line.

Figure 6-5 shows an example of a scatter plot composed of three measurement points from a single scan. The pulse height distributions are displayed on the sides of the scatter plot. The intensity along the absorber, as indicated by the amplitude of the distribution, varies due to some vignetting in the optical system. A Gaussian profile has been fitted to the pulse height

distributions to obtain the charge detected at the left and right STJ. The mean values of the charge obtained for each measurement position in the whole scan are plotted in the Figure 6-5 as stars. The values of  $\alpha$  and  $\beta$  are determined by obtaining the best fit of eq. 6-1 to these charge outputs, also shown in Figure 6-5 as a solid line through the measurement points. Using the obtained values for  $\alpha=2.0\pm 0.1$ ,  $\beta=1.5\pm 0.1$ , and equations eq. 6-2 and eq. 6-3 we calculated the energy and position distributions from the measured data. The values for the mean and FWHM are determined by Gaussian fit to the spatial and spectral distributions, and the resulting resolutions are shown in Figure 6-6, together with the model results.

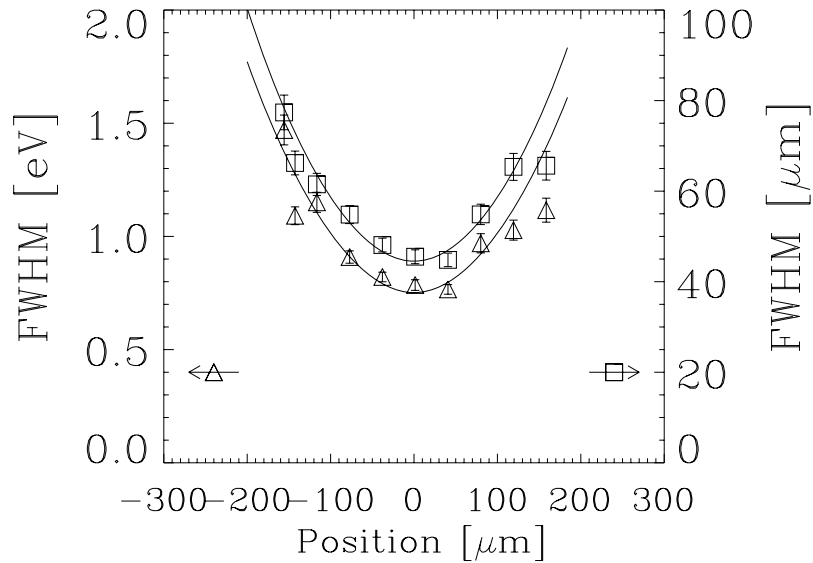


**Figure 6-6** The measured spectral resolution (triangles), and the measured spatial resolution (squares). The modeled predictions are shown as solid lines.

The spectral and spatial resolution are best in the centre of the absorber ( $0.77\pm 0.02$  eV and  $45\pm 2\mu\text{m}$ ), degrading towards the STJs ( $1.1\pm 0.04$ eV and  $65\pm 4\mu\text{m}$ ). The spectral resolution is relatively poor and limited by electronic noise and the residual IR load on the detector, which causes an effect similar to the electronic noise. Unlike the signal amplitude, the contributions of these noise sources are independent of absorption position, resulting in a strongly position dependent spectral and spatial resolution. With a spatial resolution of  $45\mu\text{m}$  the contribution of the spot size of  $10\mu\text{m}$  would be  $\sim 1\mu\text{m}$  and is indeed negligible. The solid lines in Fig.6 were plotted from eq. 6-4 and eq. 6-5 for best fit values of parameters  $\alpha$  and  $\beta$ . For  $\Delta Q$  in eq. 6-4 and eq. 6-5 we used an average FWHM of the pulse height distribution of the individual channels over all positions. The variations in the separate measurements are due to the small variations in  $\Delta Q$  in the different measurements. This variation is strongest near the STJs due to the low count rate caused by vignetting.

To test the relation between the spatial and spectral resolution the parameter  $\zeta(x)$  has been evaluated. The experimental values for  $\zeta(x)$  were determined from the measured spatial and spectral resolutions. The expected values for  $\zeta(x)$  from the model were calculated using eq. 6-6 and plotted in Figure 6-7. The modeled values for  $\zeta(x)$  agree well with the measurements showing that the relation between the spatial and spectral resolution, as given by eq. 6-6, is valid in case of imperfect trapping. For comparison,  $\xi(x)$  for the case of perfect trapping has also been plotted in Figure 6-6 (dashed line) to show the potential improvement in spatial resolution for the same spectral resolution.

## 6. Position dependent spatial and spectral resolution measurement of distributed read-out superconducting imaging detectors

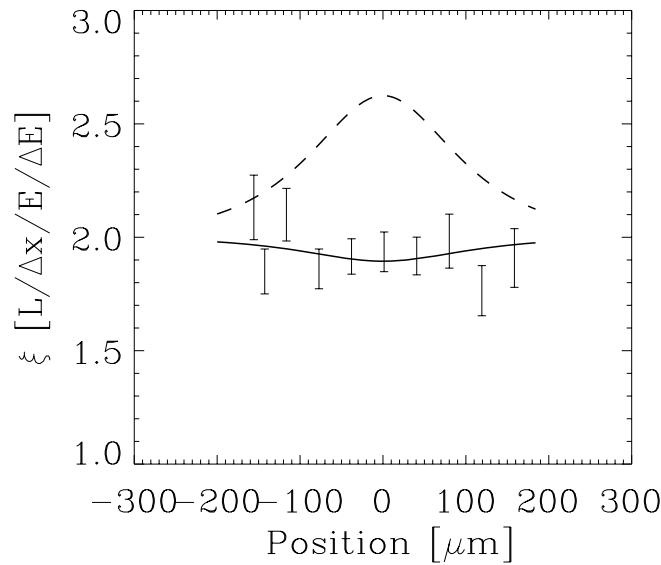


**Figure 6-7 Relation between the spatial and the spectral resolution with the prediction of the model as a solid line. The dashed line represents the case with perfect trapping ( $\beta=0$ ).**

The 30x400 $\mu\text{m}$  DROID has been scanned with different photon wavelengths; 410, 500 and 633nm (3.03, 2.48 and 1.97 eV, respectively) which are chosen for optimum throughput of the optical chain. The operating temperature was 295mK and the STJs were biased at 120 $\mu\text{V}$ . The resulting values of  $\alpha$ ,  $\beta$  and the proportionality constant  $c$  are shown in Table 6-1. The factor  $c$  from eq. 6-1 is the proportionality constant between the incident photon energy and the charge output indicating the linearity of the device.

**Table 6-1 Fitting parameters for different photon energy.**

$E_0$ [eV]	$\alpha$	$\beta$	$c$ [ADU/eV]
3.03	2.0 $\pm$ 0.1	1.5 $\pm$ 0.1	1.3 $\pm$ 0.04
2.48	2.1 $\pm$ 0.1	1.6 $\pm$ 0.1	1.4 $\pm$ 0.04
1.97	2.1 $\pm$ 0.1	2.0 $\pm$ 0.6	1.6 $\pm$ 0.2

The measured resolving powers ( $E_0/\Delta E$  and  $L/\Delta x$ ) for the different photon energies are shown in Figure 6-8. Both resolving powers increase with photon energy due to the higher charge output compared to the noise. The resolving powers have been over plotted with the predictions from the model using the values from Table 6-2.

The same DROID has been scanned with 410nm photons while biased at different voltages (70, 120 and 160 $\mu\text{V}$ ) at the operating temperature of 295mK. Table 6-2 shows the best fit values for  $\alpha$  and  $\beta$  from the different scans. The Ta/Al STJs have a lower energy gap than the pure tantalum absorber thus producing a mild trapping effect confining qps in the STJs. During the tunnel process the qps will gain energy by  $eV_b$  per tunnel, which is counteracted by relaxation with emission of a phonon. With increasing bias voltage the probability to reach an energy level above the bulk Ta gap, where the qps can diffuse into the absorber, increases, reducing the trapping effect. This is reflected by the change in the value of  $\beta$ . With decreasing trapping the probability for crosstalk increases, degrading the spatial resolution.

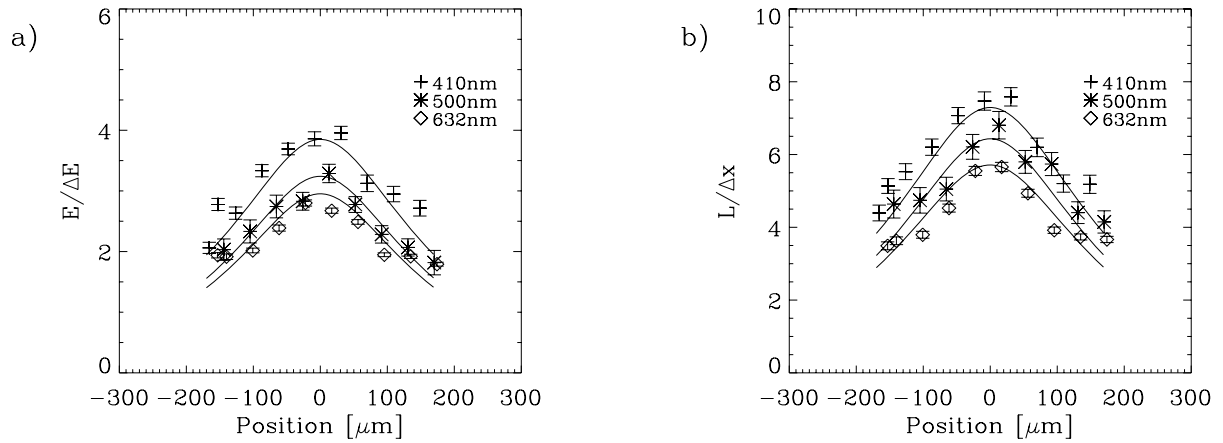


Figure 6-8 a) Spectral resolving power and b) spatial resolving power versus absorption position for different photon energies. The solid curves show the predictions of the model.

Table 6-2 Fitting parameters for different bias voltages.

$V_b$ [uV]	$\alpha$	$\beta$
70	$1.9 \pm 0.05$	$0.2 \pm 0.05$
120	$2.0 \pm 0.1$	$1.5 \pm 0.1$
160	$2.0 \pm 0.05$	$2.5 \pm 0.1$

Figure 6-9 shows that the effect is most noticeable with a bias voltage of  $70\mu\text{V}$ . At this bias voltage a qp needs 4 tunnels instead of 3 to reach an energy level above  $700\mu\text{V}$ . The spectral resolution is less affected because although the qps escape the STJ they still contribute to the signal in the opposite STJ.

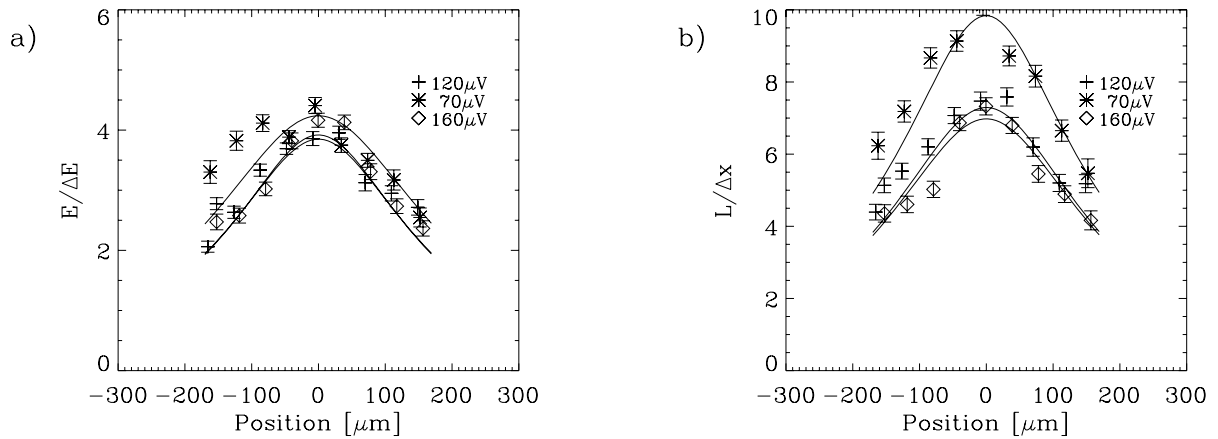


Figure 6-9 a) Spectral resolving power and b) spatial resolving power versus position at different bias voltages. The solid curves show the predictions of the model.

Figure 6-10 shows the relation  $\zeta(x)$  for the different bias voltages, and thus different trapping efficiencies, together with the modelled predictions. It is seen that the relation  $\zeta(x)$  indeed increases with improved trapping going towards the perfect trapping situation shown in Figure 6-7.

## 6. Position dependent spatial and spectral resolution measurement of distributed read-out superconducting imaging detectors

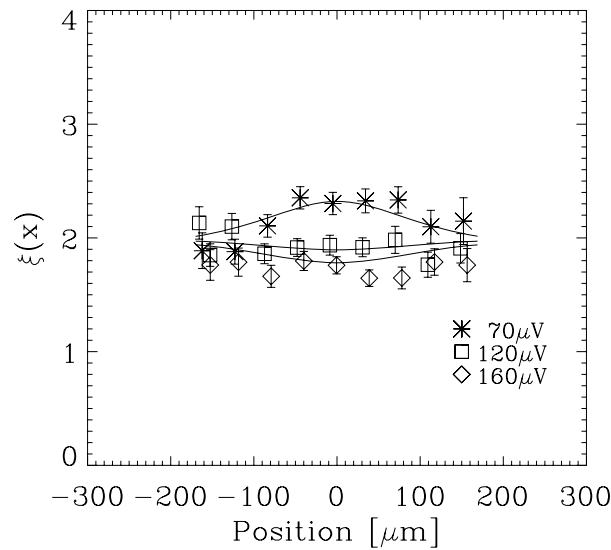


Figure 6-10 The ratio between the spatial and spectral resolving powers with position for the different bias voltages with the theoretical prediction of  $\zeta(x)$  plotted as solid lines.

The spatial and spectral resolution has been measured for three devices (on the same chip) with different DROID lengths, 200, 300 and 400  $\mu\text{m}$  (30x30  $\mu\text{m}$  STJs included) and a width of 30  $\mu\text{m}$ . The devices have been biased at 120  $\mu\text{V}$  and illuminated with 410nm photons at an operating temperature of 295mK. The resulting values for  $\alpha$  and  $\beta$  are shown in Table 6-3 together with the values for the corresponding characteristic diffusion length  $(D\tau_{loss,abs})^{1/2}$ .

Table 6-3 Fitting parameters for different absorber lengths

$L_{DROID}$ [ $\mu\text{m}$ ]	$\alpha$	$\beta$	$(D\tau_{loss,abs})^{1/2}$ [ $\mu\text{m}$ ]
200	$0.8 \pm 0.05$	$6.6 \pm 2$	$175 \pm 11$
300	$1.1 \pm 0.05$	$1.5 \pm 0.1$	$218 \pm 10$
400	$2.0 \pm 0.1$	$1.5 \pm 0.1$	$170 \pm 9$

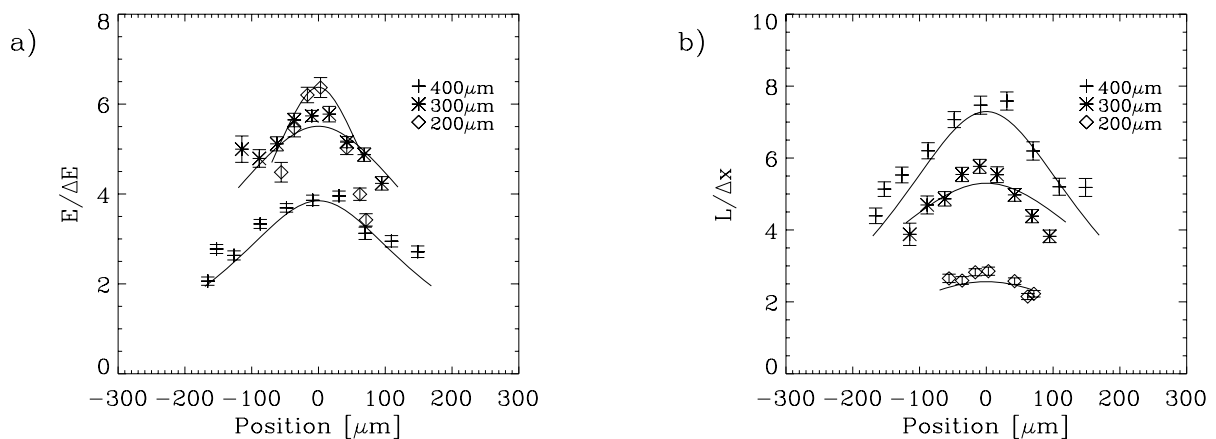
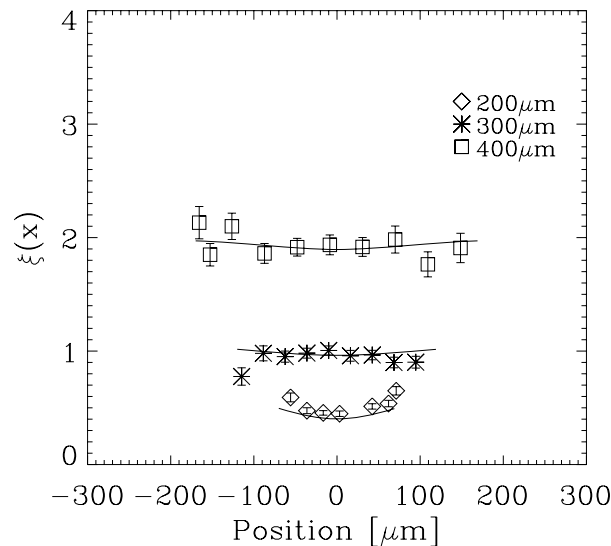


Figure 6-11 a) Spectral resolving power and b) spatial resolving power versus position for different absorber lengths. The predictions of the model are shown by the solid curves.



The resulting diffusion lengths for the 200 and 400 $\mu\text{m}$  DROID are in good agreement, while the 300 $\mu\text{m}$  device shows a slightly larger diffusion length. Comparing the measured resolving powers with the model results, as displayed in Figure 6-11, shows that the model does not exactly describe the experiment with the 300 $\mu\text{m}$  DROID. The 200 $\mu\text{m}$  device shows a high value for  $\beta$ . This device shows differences in the responses of both STJs which makes fitting the results using a single value for  $\beta$  inadequate. Tests conducted at X-ray energies, where we compared data sets obtained using the integrating electronics and data sets obtained using pulse sampling electronics, have shown that the value of  $\beta$  starts to deviate drastically above a value of 2.5 when using the integrating electronics. The true value for  $\beta$  for this measurement is expected to lie between 2.5 and 3.0 instead of at 6.6. This high value may be due to the smallest aspect ratio of this device (see also discussion below).

The spectral and spatial resolving power for the different absorber lengths are shown in Figure 6-11. The spectral resolving power degrades with increasing length while the spatial resolving power improves. This is clearly indicated by the change in the  $\zeta(x)$  for the different devices as shown in Figure 6-12. The larger losses in longer devices, due to the longer distance to reach the opposite STJ, have the effect of reducing the crosstalk between the STJs. This increases the ratio of the two signals, resulting in improved spatial resolving power. Although the spatial resolving power is increasing with length, the spatial resolution ( $\Delta x$ ) remains constant. The average spatial resolution is  $45 \pm 3 \mu\text{m}$  at the center of the absorbers for all three lengths. The spectral resolving power decreases with length. This is due to the reduced tunnel probability, and hence lower charge output of the longer devices, for which the STJs are a smaller fraction of the entire DROID area. In addition, the electronic noise contribution will remain the same and the IR noise contribution will increase for larger devices.



**Figure 6-12 Relation between the spatial and spectral resolution for the devices with different absorber length. The solid curves show the predictions of the model.**

The chip also contains DROIDS of different absorber widths and hence different STJ size. The spectral and spatial resolutions have been measured for three devices with absorber width of 20, 30 and 50 $\mu\text{m}$  and a total device length  $L_{DROID}=400\mu\text{m}$ . Note that effectively the absorber length  $L$  decreases slightly for wider DROIDS with the same length. The DROIDS are biased

## 6. Position dependent spatial and spectral resolution measurement of distributed read-out superconducting imaging detectors

at  $120\mu\text{V}$ , illuminated with  $410\text{nm}$  photons at a temperature of  $295\text{mK}$ . The resulting values for  $\alpha$ ,  $\beta$  and the diffusion length are listed in Table 6-4.

**Table 6-4 Fitting parameters for different absorber width.**

d [ $\mu\text{m}$ ]	$\alpha$	$\beta$	$(D\tau_{\text{loss,abs}})^{1/2}[\mu\text{m}]$
20	$2.1\pm 0.05$	$3.0\pm 0.5$	$171\pm 4$
30	$2.0\pm 0.1$	$1.5\pm 0.1$	$170\pm 9$
50	$1.4\pm 0.05$	$0.6\pm 0.05$	$214\pm 8$

The values for  $\alpha$  result in an average diffusion length of  $185\pm 25\mu\text{m}$  confirming the previously obtained value and the uniformity of the chip. The value of  $\alpha$  for the  $50\mu\text{m}$  device is lower than expected, resulting in a value for the diffusion length outside the error margins of the other devices. The values for  $\beta$  strongly decrease with absorber width. For the larger STJ sizes the qps spend more time in the STJ leading to a higher probability of inelastic scattering and trapping. On the other hand the tunnel probability is increased for larger STJs, which enhances the raising of qp energy and allows easier escape. Clearly, the processes inside the STJs need to be included into the model to understand exactly how STJ size influences the trapping probability.

Figure 6-13 shows the spectral and spatial resolving power as a function absorption position for the three different device widths. The  $50\mu\text{m}$  wide device clearly shows a discrepancy between the data points and the model. This could be caused by the smaller aspect ratio making the diffusion process more 2-dimensional.

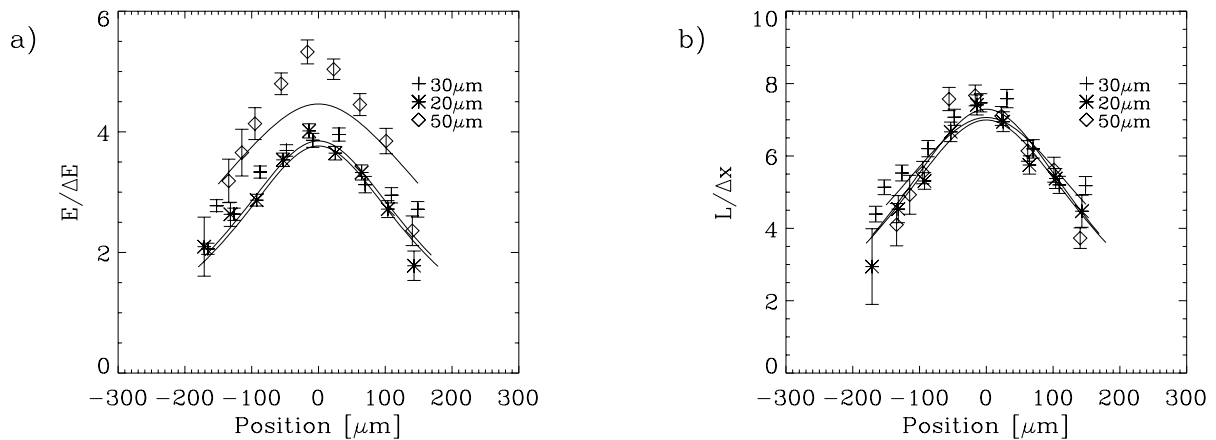


**Figure 6-13 a) Spectral resolving power and b) spatial resolving power versus position for different absorber widths. The solid curves show the predictions of the model.**

The resulting spectral resolving power shows no obvious difference between the 20 and  $30\mu\text{m}$  wide device in Figure 6-13. The  $50\mu\text{m}$  device shows improved resolution which is due to the increased charge output compared to the electronic and IR noise. Although the signal to noise ratio increases there is no noticeable improvement in the spatial resolution. The improvement in signal to noise with wider devices may be counteracted by the reduced losses due to the slightly shorter absorber length caused by the larger STJ size. Alternatively, if quasiparticle losses at the absorber edges are present in the system, these would be less relevant in wider devices and lead to reduced spatial resolution. For a better understanding of the influence of the absorber width and the presence of edge losses a more detailed investigation is needed.

## 6.5 Discussion

The experimental results in the previous section clearly show the influence of different parameters on the spatial and spectral resolution and provide a rigorous test of the simple model. Comparison between the experiment and simulation show good agreement for both the spectral and spatial resolution as function of absorption position in Figure 6-6, and also for the factor  $\zeta(x)$  in Figure 6-7. The latter is an important result validating the use of the model to determine the spatial resolution from the measured spectral resolution from a uniform illumination.

The linearity of the energy response of the DROID structure has been tested by using three different photon energies. The factor  $c$  in Figure 6-2 shows the DROID response to be fairly linear with photon energy. The model proved to be consistent in describing the DROID response to variations in photon energy, as shown in Figure 6-8. By varying other experimental parameters, such as bias voltage, absorber length and width, we were able to probe their effect on the detector performance and test the limitations of the model.

The geometry proves to be of great importance for optimization of the DROID performance. The absorber length is the only parameter with which the relation between the spatial and spectral resolution, as shown by  $\zeta(x)$  in Figure 6-12, clearly changes. This shows that the length of the absorber is limited by the requirements on the spatial and energy resolution. The different geometries also provide the clearest evidence on the limitation to the one-dimensionality of the model, which is evident in Figure 6-11 to Figure 6-13 for DROIDS with the smallest aspect ratios. The 1D model cannot account for the dimensionality effects in the results and for DROIDS with an aspect ratio below 10:1 a 2D model appears to be required. Although these limitations are obvious, nonetheless it is worth mentioning that the basic model is quite robust. The model gives good agreement with the experiments; however, in some cases the fitting parameters  $\alpha$  and  $\beta$  will need to go beyond the expected values, as seen with the different geometries. The inability of the model to deal with an asymmetric system is obvious but can easily be dealt with by introducing two separate  $\beta$ -parameters.

Confining the charge carriers inside the sensors is an important mechanism to optimize the spatial and spectral resolution. With the current DROID configuration, with mild trapping in the STJ, the trapping of qps can be fine tuned with the bias voltage, as shown by Figure 6-9. In the model this process is accounted for by the parameter  $\beta$  which describes the boundary condition just at the infinitesimally thin edge. However, the STJs are extended sensors with their own dynamical properties. The internal processes involving the qps inside the STJ can only be approximately accounted for by a single parameter  $\beta$ , as shown in Table 6-2 and in Table 6-4. Thus further development of a DROID model requires modelling of the qp dynamics inside the biased STJ including; qp injection, tunnelling and exchange between absorber and STJ. In addition STJs, and all other sensors, need to be treated as extended objects with appropriate conditions at all their boundaries. The observed dependences on bias voltage and on STJ size are examples since they do not only depend on the imperfect trapping but also on the combination of other parameters of the STJ. For physical reasons this dependence can be understood but cannot be predicted using the current simple model. Nonetheless the simple model is invaluable in setting up a basic framework for DROID optimisation.

The final limitation of the model is the assumption  $\Delta Q_R = \Delta Q_L$ , independent of position. In our experiments this limitation has been obscured by the presence of IR background, and electronic noise. Their contributions dominate the measured resolutions and they are independent on signal amplitude, ensuring that the assumption above is validated (as long as the STJs are identical). However, they induce a strong position dependency of the spectral and spatial resolution (cf. Figure 6-6), which is an unwanted property for a practical detector. The

## **6. Position dependent spatial and spectral resolution measurement of distributed read-out superconducting imaging detectors**

---

full scale problem of obtaining the best resolutions will become evident if the contribution of these external noise sources is reduced in an optimized experimental configuration, and the intrinsic noise sources (which scale with signal amplitude) become dominant. This is expected to reduce the position dependency of the resolutions. Then any further development on an improved model must rest on breaking down all contributing noise factors. For DROIDs with STJs as sensors such a breakdown will be in a similar form as with single STJs as shown in the introduction. All noise factors which are important for single STJs will of course play an important role when it becomes part of a DROID. However, additional noise sources will appear, some of which will be dependent on absorption position.

### **6.6 Conclusion**

In summary we have developed an experimental technique to measure the spectral and spatial resolution in Distributed Read-Out Imaging Detectors directly for each photon absorption position. Using this technique we have explored the influence of several parameters on the spatial and spectral resolution. Using the model of Jochem *et al* we have derived the expressions for photon energy, photon absorption position and the resolutions which give a satisfactory description of the experimental data. The limitations of the model were tested experimentally and major restrictions were identified pointing out the necessity for further development of the theoretical model along the described directions



## Chapter 7

---

# Experimental and theoretical response of Distributed Read-Out Imaging Devices with imperfect confinement

---

R. A. Hijmering, A. G. Kozorezov, P. Verhoeve, D.D.E. Martin, J. K. Wigmore, R. Venn and P.J. Groot

*submitted to J. Appl. Phys.*

We present a model to describe the responsivity of Distributed Read-Out Imaging Devices following photon absorption in the absorber or in the base or top film of the superconducting tunnel junctions at either end of the absorber. The model describes all processes relevant for photon detection, taking into account diffusion of quasiparticles across the absorber and imperfect confinement in the superconducting tunnel junctions via exchange of quasiparticles between absorber and the junction. It incorporates diffusion mismatch between STJ and absorber, possible asymmetry between the two junctions and asymmetry between base and top electrodes within each junction. We have conducted dedicated experiments in which different experimental conditions were varied in order to test the model. A good agreement was found between the experimental results and model predictions.

### 7.1 Introduction

Cryogenic detectors, detectors which operate at sub-Kelvin temperatures, are being developed as photon counting spectro-photometers due to their excellent spectroscopic capabilities in UV, optical and X-ray energies<sup>118</sup>. An important issue with these cryogenic detectors is to create a sufficiently large sensitive area while maintaining imaging capabilities and keeping the number of read-out channels within practical limits. Methods which are currently under investigation are multiplexed read-out of sensors and distributed read-out schemes which provide positional information within a sensor. Microcalorimeters with Transition Edge Sensors<sup>10</sup> (TES), which measure the change in temperature due to the absorption of a photon through a change of resistance in the sensor, are usually read-out with Superconducting Quantum Interference Devices (SQUIDs)<sup>10</sup>, which provide a relatively easy multiplexing scheme. Depending on the application, a few tens to a few hundred detectors may be read-out through a single read-out channel. Kinetic Inductance Detectors (KIDs)<sup>15</sup>, which rely on the change in inductance caused by the excitation of quasi-particles by the absorbed photon, can be grouped together on a single signal line by using a different resonance frequency for the read-out resonance circuit for each sensor. Superconducting Tunnel Junctions<sup>14</sup> (STJs) measure a photon-induced change in quasiparticle density as a tunnel current across a thin insulating barrier. Being high impedance devices, they are usually read-out with J-FET based charge sensitive preamplifiers, multiplexed read-out is not straightforward and distributed read-out is the more preferred approach. Distributed Read-Out Imaging Devices (DROIDs)<sup>28</sup> consist of superconducting absorber strip with an STJ at either end. A photon is absorbed in the absorber strip and the excited quasiparticles will diffuse towards the STJs where they tunnel across the barrier and produce a measurable current pulse. The sum of the signals will provide information on the energy of the absorbed photon and the ratio of the signals will provide information on the position of the absorption site. A similar geometry is used with TESs as sensors, named DROIDs<sup>119</sup> or POSition Sensitive TES (POSTs)<sup>120</sup>, or with MKIDs<sup>121</sup> as sensors. The first relies on heat conduction to produce the change in temperature in the TESs and the latter relies on the diffusion of quasiparticles to produce a change in inductance in the MKIDs.

In the distributed read-out devices diffusion plays a major role in the detection process. The carriers diffuse from the absorption site towards the sensors where they produce a measurable signal. If the trapping (confinement of the signal carriers in the sensors, applicable to quasiparticles) is perfect they will remain in the sensor adding to the signal. If trapping is imperfect they will be able to escape from the sensor and diffuse towards the opposite sensor producing a crosstalk signal. This will reduce the ratio of the two charges, the time the charge carriers contribute to the signal and expose the signal carriers more to the losses inside of the absorber. All these effects will influence the position and energy resolution of the detector negatively.

Several groups have proposed theoretical models describing the DROID response. Kraus *et al*<sup>28</sup> derived a widely used relation between the spectral and spatial resolution for DROIDs with perfect quasiparticle trapping in the STJs. Jochum *et al*<sup>68</sup> have generalised this model in order to include imperfect quasiparticle trapping in the STJs by using a characteristic trapping time. Both models focused on the diffusion process of the signal carriers but excluded description of processes involved with the signal detection in the sensors. Segall *et al*<sup>29,111</sup> developed a model for DROIDs which included the processes inside the STJs but assumes perfect trapping. Den Hartog *et al*<sup>72</sup> produced a 2D diffusion model of a DROID without trapping but accounting for quasiparticle dynamics in the STJ using Rothwarf-Taylor equations<sup>82</sup>. A similar model was developed by Ejrnaes *et al*<sup>112</sup> using a different approach.

## 7. Experimental and theoretical response of Distributed Read-Out Imaging Devices with imperfect charge confinement

In this paper we describe a model for the responsivity of a DROID with STJs as sensors and imperfect trapping which describes all relevant dynamical processes for all photon absorption sites within the DROID. It has been tested against a responsivity dataset from DROIDS with different geometries (Al thickness and absorber length) measured under varying operating conditions (bias voltage and temperature) using pulse sampling of the current pulses resulting from individual optical photons. The DROIDS used in this work consist of a pure tantalum absorber with a proximised Ta/Al STJ on either end.

### 7.2 Modelling of DROID response

We consider a DROID of length  $L$  (including the STJs) and width  $w$  consisting of a pure tantalum absorber with a Ta/Al STJ at either end, as shown in Figure 7-1. The bottom tantalum layer of the STJs and the absorber are produced as a single layer on top of which the aluminium layer, barrier and top electrode of the STJs are grown. The presence of the aluminium in the STJs will decrease the energy gap of the STJs due to the proximity effect and provide confinement of quasiparticles. The STJs are square in geometry with the sides equal to the width of the absorber, and the thickness of a single Ta/Al bi-layer is given by  $d$ . The coordinate along the length of the DROID is denoted by  $x$  and the position over the width of the DROID is denoted by  $y$ . The positions of the edges of the STJs in the  $x$  direction are at  $x_-^l = -L/2$ ,  $x_+^l = -L/2 + w$ ,  $x_-^r = L/2 - w$  and  $x_+^r = L/2$ .

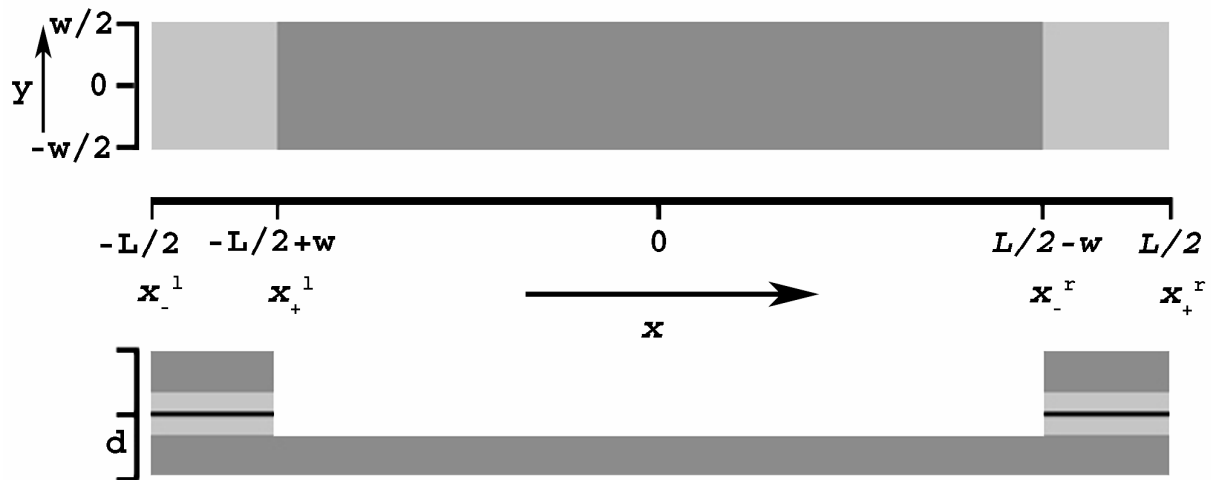
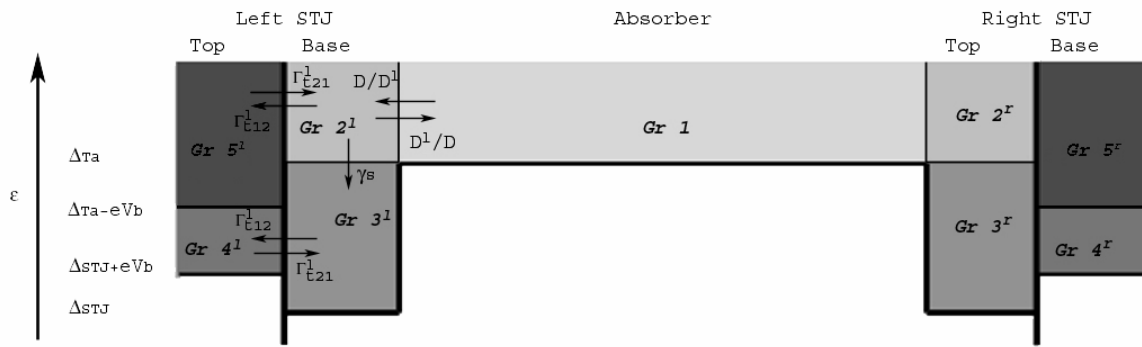


Figure 7-1 Schematic representation of the DROID geometry with a top and side view, the thickness of the layers is greatly exaggerated.

Differences in response between absorptions in the two STJs and/or between absorptions the top and base electrode of a single STJ may occur due to limitations in the fabrication process or initial experimental conditions. The parameters for either STJ are denoted by a superscript ( $i$ ), left:  $i=l$  and right:  $i=r$ . Similarly, subscript ( $j$ ) is used to denote the top,  $j=t$ , and base,  $j=b$ , electrode. We also distinguish between the tunnel rate from the base electrode ( $\Gamma_{t,b}^{(i)}$ ) and from the top electrode ( $\Gamma_{t,tb}^{(i)}$ ).





**Figure 7-2 Different groups of quasiparticles in a DROID which are determined by position in the DROID (horizontal scale) and energy (vertical scale).**

Within the complete system of the DROID we define different groups of quasiparticles divided by location and energy level. Figure 7-2 shows a schematic representation of the different groups of quasiparticles and, on the left hand side, the exchange routes between them. The first group are the quasiparticles inside the absorber (*Gr 1*). These quasiparticles do not directly produce a signal, are subjected to the losses in the pure Ta absorber, are free to diffuse towards the STJs and are in the energy range  $\varepsilon > \Delta_{Ta}$ . Secondly, quasiparticles inside the base electrode which have energies above the energy gap of the pure tantalum absorber form the second group (*Gr 2<sup>(i)</sup>*). This group of quasiparticles will directly contribute to the signal by tunnelling across to the opposite electrode, they are subjected to the loss mechanisms inside the STJ base electrode, and since they are above the energy gap of the absorber they are free to diffuse out of the STJ into the absorber. The third group is formed by the quasiparticles which are in the base electrode of the STJ with energy below the energy gap of the absorber (*Gr 3<sup>(i)</sup>*). Being confined within the STJ this group of quasiparticles differs from the previous group. Trapping efficiency of quasiparticles in the STJ affects the distribution of the quasiparticles between the second and third group. Quasiparticles from group 2 will feed group 3 via relaxation with emission of a phonon. This process, denoted by the relaxation rate  $\gamma_s^{(i)}$ , depends on the STJ proximation and can be calculated<sup>105</sup>. Due to sequential tunnelling quasiparticles gain energy, equal to twice the applied bias voltage ( $2eV_b$ ) with each tunnelling cycle, and after a sufficient number of cycles without relaxation the quasiparticles are promoted from group 3 into group 2. The number of tunnels needed to reach an energy above the energy gap of the absorber and thus to change the trapping efficiency can be adjusted for a given STJ lay-out with the bias voltage. In a biased STJ a quasi-stationary spectral distribution of quasiparticles is formed after one or two tunnelling events<sup>87</sup>. Therefore instead of modelling the complete dynamics in the STJ we ignore a short initial period and assume a quasi-stationary spectral distribution established instantly. Correspondingly for this distribution we divide the quasiparticles in the top film of the STJ into an energy group (*Gr 4<sup>(i)</sup>*) which after tunnelling enters group 3 and an energy group (*Gr 5<sup>(i)</sup>*) which after tunnelling enters group 2 and are free to diffuse into the absorber. The separation between these two groups is drawn at the energy  $\Delta_{Ta} - eV_b$ . We define  $\xi^{(i)}$  to be the fraction of quasiparticles in the top electrode of the STJ with an energy above  $\Delta_{Ta} - eV_b$ . The quasiparticles in both these groups are subjected to losses in the top electrode.

Due to the suppressed gap in the proximated STJs of a DROID the responsivity of a photon absorption in the STJs is higher than that of a photon absorption in the absorber. This increase in responsivity is accounted for by the parameter  $\chi$ . The efficiency of quasiparticle creation in

## 7. Experimental and theoretical response of Distributed Read-Out Imaging Devices with imperfect charge confinement

proximized superconductors is lower compared to pure BCS-superconductors with the same energy gap<sup>122</sup>.

At the boundary between the absorber and STJ the spectrum of electronic excitations in a superconductor undergoes a transition from BCS-like (on the absorber side) to that of a proximized bi-layer. As a result the transport parameters of quasiparticles will change on the scale of the coherence length. Particularly, a quasiparticle at an energy above  $\Delta_{Ta}$  when it crosses the boundary will have a different diffusion coefficient, even though its elastic scattering rates may remain unchanged. This occurs because with the change in electronic spectrum the group velocity of the quasiparticles changes, leading to a change in diffusion coefficient. With the quasiparticle flux across the boundary being continuous this diffusion mismatch will affect the effective trapping of the quasiparticles inside the STJs. When the diffusion constant in the STJ is larger than in the absorber the quasiparticle density at the STJ side of the boundary will be depleted. In order to keep the quasiparticle flux continuous there will be a corresponding build up of their density on the absorber side leading to an increased injection into the STJ. Effectively, this will enhance trapping of quasiparticles in the STJs. For a lower diffusion constant in the STJ there will be a build up of quasiparticles at the STJ side of the boundary reducing the flux of quasiparticles into the STJ and thus reducing the effective trapping.

The presented DROID model also includes the situation when absorption takes place inside the STJ either in the top or base electrode. If the photon is absorbed in the base electrode the quasiparticles above the energy gap of the absorber can escape from the STJ before tunnelling. Thus only the fraction of quasiparticles created in the range  $\Delta_g < \epsilon < \Delta_{Ta}$  are trapped within the STJ. The latter fraction is accounted for by the parameter  $\beta^{(i)}$ . If the absorption takes place in the top electrode of the STJ all quasiparticles must tunnel first before quasiparticles with sufficient energy can escape into the absorber increasing the responsivity. This additional contribution to the responsivity is accounted for by appropriate source terms in the Rothwarf-Taylor equations<sup>82</sup> describing photon absorption in the top or base electrode of the STJs. In the equation below the parameter  $\alpha$  determines if there is an absorption in the top ( $\alpha=0$ ) or base ( $\alpha=1$ ) electrode. The Rothwarf-Taylor equation for the quasiparticle density in the base Ta film (group 1 and group 2) is given by:

$$\frac{\partial n}{\partial t} - D\nabla^2 n + \gamma n + \sum_i \left[ \Gamma_{t,bl}^{(i)} n - \xi^{(i)} \Gamma_{t,lb}^{(i)} n_t^{(i)} + (D - D_b^{(i)}) \nabla^2 n - (\gamma - \gamma_s^{(i)} - \gamma_b^{(i)}) n \right] \Theta(x_{i+} - x) \Theta(x - x_{i-}) = \frac{N_0}{d} \delta(t) \delta(x - x_0) \left[ \Theta\left(\frac{L}{2} - w - |x|\right) + \alpha \left[ (1 - \beta^{(i)}) \Theta(x - x_-^{(i)}) \Theta(x_+^{(i)} - x) \right] \right] \quad 7-1$$

For group 3 of the base film in the STJ we have:

$$\frac{\partial n_b^{(i)}}{\partial t} - D_b^{(i)} \nabla^2 n_b^{(i)} + (\gamma_b^{(i)} + \Gamma_{t,bl}^{(i)}) n_b^{(i)} - \Gamma_{t,lb}^{(i)} (1 - \xi^{(i)}) n_t^{(i)} - \gamma_s^{(i)} n = \frac{\alpha}{d} \beta^{(i)} N_{0g}^{(i)} \delta(t) \delta(x - x_0) \Theta(x_0 - x_-^{(i)}) \Theta(x_+^{(i)} - x_0) \quad 7-2$$

Finally for the top film (group 4 and group 5):

$$\frac{\partial n_t^{(i)}}{\partial t} - D_t^{(i)} \nabla^2 n_t^{(i)} + (\gamma_t^{(i)} + \Gamma_{t,ab}^{(i)}) n_t^{(i)} - \Gamma_{t,bt}^{(i)} (n_b^{(i)} - n) = \frac{(1-\alpha)}{d} [\beta^{(i)} N_{0g}^{(i)} + (1-\beta^{(i)}) N_0] \delta(t) \delta(x-x_0) \Theta(x_0-x_-^{(i)}) \Theta(x_+^{(i)}-x_0) \quad 7-3$$

Here  $\Theta(x)$  is the Heaviside step function,  $\gamma$  and  $\gamma_{(j)}^{(i)}$  are the bulk loss rates in the absorber and in the base and top film of each STJ,  $\gamma_s$  is the inelastic relaxation rate of quasiparticles at  $\varepsilon=\Delta_{Ta}$ ,  $x_0$  is the absorption position coordinate and  $N_0$  and  $N_{0g}^{(i)}$  are the number of created quasiparticles for an absorption in the absorber and STJ ( $i$ ). Ideal edges at  $\pm L/2$  are assumed meaning that the flux at the edges is zero resulting in the boundary condition:

$$D \frac{du}{dx} \Big|_{\pm \frac{L}{2}} = 0$$

The diffusion mismatch at the boundaries between the absorber and STJs results in the following boundary conditions:

$$\begin{aligned} D \frac{du}{dx} \Big|_{\frac{L}{2}-w-\delta} &= D_b^l \frac{du}{dx} \Big|_{\frac{L}{2}-w+\delta} & , & & D \frac{du}{dx} \Big|_{-\frac{L}{2}+w+\delta} &= D_b^r \frac{du}{dx} \Big|_{-\frac{L}{2}+w-\delta} \\ u \Big|_{\frac{L}{2}-w-\delta} &= u \Big|_{\frac{L}{2}-w+\delta} & , & & u \Big|_{-\frac{L}{2}+w+\delta} &= u \Big|_{-\frac{L}{2}+w-\delta} \end{aligned}$$

In order to solve eq. 7-1 to 7-3 it is convenient to find an appropriate set of orthogonal functions satisfying the boundary conditions which we introduced above. These functions  $u$  satisfy the equation:

$$\frac{d}{dx} \left( D \frac{du}{dx} \right) + \kappa^2 Du = 0$$

For the set of orthogonal functions  $u$  we obtain the following expression:

$$u_m(x) = \sqrt{\frac{2}{L}} \left\{ \begin{array}{ll} \cos \kappa_m \left( \frac{L}{2} + x \right) + \left( 1 - \frac{D_b^l}{D} \right) \sin \kappa_m w \sin \kappa_m \left( \frac{L}{2} - w + x \right) & , |x| \leq \frac{L}{2} - w \\ \cos \kappa_m \left( x + \frac{L}{2} \right) & , -\frac{L}{2} \leq x \leq -\frac{L}{2} + w \\ \left[ \cos \kappa_m (L-w) + \left( 1 - \frac{D_b^r}{D} \right) \sin \kappa_m w \sin \kappa_m (L-2w) \right] \frac{\cos \kappa_m \left( x - \frac{L}{2} \right)}{\cos \kappa_m w} & , \frac{L}{2} - w \leq x \leq \frac{L}{2} \end{array} \right\} \quad 7-4$$

Here  $\kappa_m$  is the  $m^{th}$  solution of the dispersion relationship:

## 7. Experimental and theoretical response of Distributed Read-Out Imaging Devices with imperfect charge confinement

$$\sin \kappa_m L + \frac{1 - \frac{D_b^l D_b^r}{D^2}}{1 + \frac{D_b^l D_b^r}{D^2}} \sin \kappa_m (L - 2w) - \frac{\left(1 - \frac{D_b^l}{D}\right) \left(1 - \frac{D_b^r}{D}\right)}{1 + \frac{D_b^l D_b^r}{D^2}} \cos \kappa_m (L - 2w) \sin 2\kappa_m w = 0 \quad 7-5$$

To solve the equations for the DROID model eq. 7-1 to eq. 7-3 we look for the solutions in the form of an expansion over the functions  $u_m(x)$  for the  $x$ -direction and  $u_n(y)$  for the  $y$ -direction:

$$n(x, t) = \sum_{m, n} f_{m, n} \sqrt{\frac{D(x)}{D}} u_m(x) u_n(y) \quad 7-6$$

Here  $D(x)$  is the profile of diffusion constants across the DROID:

$$D(x) = D\Theta(L/2 - w - |x|) + D_b^l \Theta(x_+^l - x) \Theta(x - x_-^l) + D_b^r \Theta(x_+^r - x) \Theta(x - x_-^r) \quad 7-7$$

$\bar{D}$  is the mean diffusion constant given by:

$$\bar{D} = D \left[ (L - 2w)/L + w/L \left( (D_b^l + D_b^r)/D - 2 \right) \right] \quad 7-8$$

and

$$u_n(y) = \sqrt{\frac{2}{w}} \cos n\pi \left( \frac{1}{2} + \frac{x}{w} \right) \quad 7-9$$

For the STJs we may write:

$$n_{i/b}^{(i)}(\bar{x}, t) = \sum_{m, n} f_{b/i, m, n}^{(i)}(t) v_m \left( x - x_-^{(i)} - \frac{w}{2} \right) u_n(y) \Theta(x - x_-^{(i)}) \Theta(x_+^{(i)} - x) \quad 7-10$$

where  $v_m = (x - x_-^{(i)} - w/2)$  is another set of orthogonal functions for the range  $x_-^{(i)} < x < x_+^{(i)}$  defined by:

$$v_m = \sqrt{\frac{2}{w}} \cos m\pi \left( \frac{1}{2} + \frac{x - x_-^{(i)} - w/2}{w} \right) \quad 7-11$$

Inserting these expressions into eq. 7-1 we obtain for the coefficients  $f_{m0}$  of eq. 7-10 the following set of linear algebraic equations, in matrix notation:

$$\sum_{m'=1}^{\infty} \{ \delta_{m', m} A_{m-1, 0} - b(m-1, m'-1) \} F_{m'0} = g(m-1) \quad 7-12$$

where  $F_{mn}$  is the matrix representation of  $f_{mn}$ .  $A_{mn}$  and  $b(m, m')$  are given by:

$$A_{mn} = D\pi^2 \left( \frac{m^2}{L^2} + \frac{n^2}{w^2} \right) + \gamma \quad 7-13$$

$$b(m, m') = \frac{1}{V(m)} \sum_i \left[ \left( \Gamma_{t,bt}^{(i)} - A_{s,m'0}^{(i)} \right) \frac{D(x)}{D} J^{(i)}(m, m') - \xi^{(i)} \Gamma_{t,21}^{(i)} \sum_{m''} \frac{A_{b,m'0}^{(i)} \Gamma_{t,bt}^{(i)} + \gamma_s^{(i)} \Gamma_{t,bt}^{(i)}}{\left[ A_{b,m'0}^{(i)} A_{t,m'0}^{(i)} - \Gamma_{t,bt}^{(i)} \Gamma_{t,tb}^{(i)} (1 - \xi^{(i)}) \right] (1 + \delta_{m'0})} \frac{D(x)}{D} Y^{(i)}(m, m'') Y^{(i)}(m'', m') \right] \quad 7-14$$

and  $g(m)$  is given by:

$$g(m) = \frac{N_0}{V(m)} \frac{1}{4\pi d} \sqrt{\frac{2}{w}} \left\{ \frac{D(x_0)}{D} u_m(x_0) \left[ \Theta \left( \frac{L}{2} - w - |x_0| \right) + \alpha \sum_i (1 - \beta^{(i)}) \Theta(x_+^{(i)} - x_0) \Theta(x_0 - x_-^{(i)}) \right] + \sum_{(i)m'} \xi^{(i)} \Gamma_{t,tb}^{(i)} \frac{\left[ (1 - \alpha) (\beta^{(i)} \chi^{(i)} + 1 - \beta^{(i)}) A_{b,m'0}^{(i)} + \alpha \beta^{(i)} \chi^{(i)} \Gamma_{t,bt}^{(i)} \right]}{A_{b,m'0}^{(i)} A_{t,m'0}^{(i)} - \Gamma_{t,bt}^{(i)} \Gamma_{t,tb}^{(i)} (1 - \xi^{(i)})} \times \frac{v_{m'}^{(i)}(x_0) Y^{(i)}(m, m') D(x_0)}{1 - \delta_{m'0}} \frac{D(x_0)}{D} \Theta(x_+^{(i)} - x_0) \Theta(x_0 - x_-^{(i)}) \right] \quad 7-15$$

Here:

$$J^{(i)}(m, m') = \int_{x_-^{(i)}}^{x_+^{(i)}} dx u_{m'}(x) u_m(x) \quad 7-16$$

$$Y^{(i)}(m, m') = \int_{x_-^{(i)}}^{x_+^{(i)}} dx v_{m'}^{(i)}(x - x_-^{(i)} - w/2) u_m(x) \quad 7-17$$

$$A_{b/t, mn}^{(i)} = D_{b/t}^{(i)} \frac{(n^2 + m^2) \pi^2}{w^2} + \gamma_{b/t}^{(i)} + \Gamma_{t,bt/tb}^{(i)} \quad 7-18$$

$$A_{s, mn}^{(i)} = (D - D_b^{(i)}) \kappa_m^2 + \gamma - \gamma_s^{(i)} - \gamma_b^{(i)} \quad 7-19$$

and  $V(m)$  is the normalisation factor for the  $m^{\text{th}}$  harmonic  $u_m(x)$ :

$$V(m) = 2\delta_{m,0} \int_{-L/2}^{L/2} dx u_m^2(x)$$

In order to calculate the charge output of the two STJs we need to integrate the currents and find the total recorded charge. By definition the total recorded charge  $Q^{(i)}(t)$  at an instant  $t$  by STJ  $(i)$  is given by:

## 7. Experimental and theoretical response of Distributed Read-Out Imaging Devices with imperfect charge confinement

$$Q^{(i)}(t) = ed \int_0^t dt' \left( \Gamma_{t,bt} \int_{s^i} \int n(\bar{x}, t') d\bar{x} + \Gamma_{t,ib} \int_{s^i} \int n^{(i)}(\bar{x}, t') d\bar{x} + \right) \quad 7-20$$

Inserting eq. 7-6 and eq. 7-10 and integrating over the time we get the following expression for the total charge  $Q^{(i)}$  ( $t=\infty$ ) of STJ ( $i$ ) as a function of position:

$$Q^{(i)} = \pi ed \left\{ \sum_{m=0}^{\infty} f_{m,0}(0) \sqrt{wL} \Gamma_{t,bt} \int_{x_0^{(i)}}^{x_{i+}^{(i)}} dx \sqrt{\frac{D(x)}{D}} u_m(x) + 2w \Gamma_{t,ib} f_{b,00}^{(i)}(0) + 2w \Gamma_{t,ib} f_{i,00}^{(i)}(0) \right\} =$$

$$\left. \begin{aligned} & \sum_{m=0}^{\infty} f_{m,0} J \sqrt{wL} \left( \Gamma_{t,bt} + \Gamma_{t,ib} \left[ \frac{(\gamma_t + \Gamma_{t,ib}) \gamma_s + \Gamma_{t,ib} \Gamma_{t,bt} (1 - \xi) + \Gamma_{t,ib} (\gamma_b + \Gamma_{t,bt}) + \gamma_s \Gamma_{t,ib}}{(\gamma_b + \Gamma_{t,bt}) (\gamma_t + \Gamma_{t,ib}) - \Gamma_{t,bt} \Gamma_{t,ib} (1 - \xi)} \right] \right) + \\ & \frac{1}{2\pi d} \frac{\alpha \beta^{(i)} N_{0g} \Gamma_{t,bt} (\gamma_t + 2\Gamma_{t,ib}) + (1 - \alpha) (\beta^{(i)} N_{0g} + (1 - \beta^{(i)}) N_0) [(1 - \xi) \Gamma_{t,bt} + (\gamma_b + \Gamma_{t,bt})] \Gamma_{t,ib}}{(\gamma_b + \Gamma_{t,bt}) (\gamma_t + \Gamma_{t,ib}) - \Gamma_{t,bt} \Gamma_{t,ib} (1 - \xi)} \times \\ & \Theta(x_0 - x_{i-}) \Theta(x_{i+} - x_0) \end{aligned} \right\} \quad 7-21$$

The values for  $f_{m,0}$  are obtained by solving the set of linear algebraic equations of eq. 7-12

### 7.3 Experimental set-up and data reduction

DROIDS, produced by Cambridge MicroFab Ltd<sup>21</sup>, with different Ta/Al STJs have been used to test the described model. The STJs consist of a Ta/Al/AlO<sub>x</sub>/Al/Ta multilayer with thicknesses of: 100/30/1/30/100nm, 100/60/1/60/100nm and 100/100/1/100/100nm and energy gaps, as measured from the IV curves, of: 500, 420 and 360  $\mu$ eV, respectively. The *RRR* (Residual Resistance Ratio) values for the base Ta layer as measured using a dedicated structure on the chip are 37.2, 43.6 and 30.2 for the DROID with 30, 60 and 100nm thick Al trapping layer, respectively. For all three lay-ups a DROID of 400 $\mu$ m in length, including STJs, and a width of 30 $\mu$ m is used as a reference device. The STJs are square in geometry with the sides equal to the width of the absorber. The 100nm thick pure tantalum absorber and the tantalum layer of the base electrode of the STJs are part of the same epitaxial Ta layer (see Figure 7-1).

A <sup>3</sup>He sorption cooler with a base temperature of 280mK, low enough to reduce the thermal current to a negligible level for all three device structures, has been used to conduct the measurements. The cryostat is equipped with an optical fibre to illuminate the chip through the sapphire substrate with optical photons ( $E_0=1-5$ eV) from a Xe lamp filtered by a double grating monochromator. In this set-up it is only possible to illuminate the devices through the sapphire substrate and only the case where  $\alpha=0$  (base electrode illumination) could be investigated.

The signal pulses from the STJs are fed into a charge sensitive preamplifier with an RC time of 470 $\mu$ s at ambient temperature and subsequently digitized with a computer oscilloscope card (GaGe CS14100). With simulated shaping filters a measure of the responsivity can be obtained from the preamplifier signal to make a first selection of the events. Figure 7-3 shows a scatter plot of individual photon signals after the simulated shaping stages in an  $S_1+S_2$  (a measure for the energy with  $S_i$  the signal from STJ  $i$ ) versus  $(S_1-S_2)/(S_1+S_2)$  (a measure for the position) representation. The STJ events can easily be distinguished by their spatial and spectral separation. Using the results from the simulated shaping stage the noise events are

removed and the remaining events are divided into 13 sections based on the position (11 sections on the absorber and the two STJs). The preamplifier pulses of the events in a single section are averaged to obtain a low noise charge pulse. Averaging of the charge pulses is possible because the position resolving power ( $L/\Delta x$ ) of the absorber is below 11. From the average charge pulses the preamp response is de-convoluted to reduce the integration time and electronic noise. The resulting photo-current pulses, one per section, are integrated to obtain the true charge output.

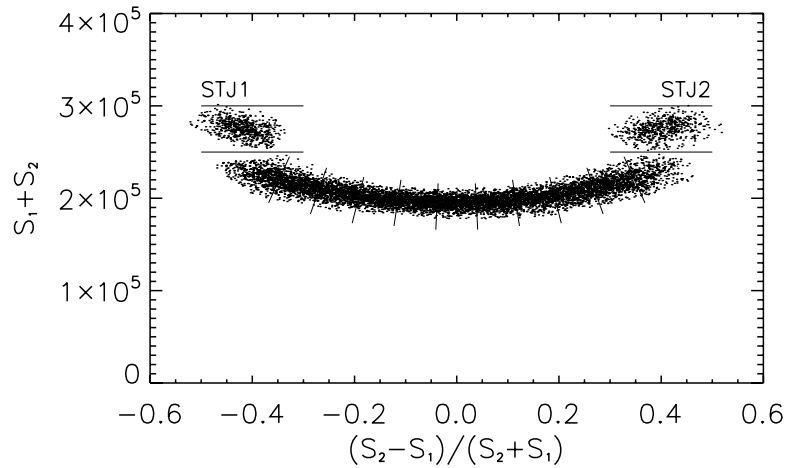


**Figure 7-3 Scatter plot of the sum versus normalized ratio of the result from the simulated shaping stages. Events from the STJs can be easily distinguished and selected by their spatial separation. The absorber events are divided into 11 sections along the position direction.**

These average values for the charge output are used to test the model. In order to obtain an objective fit of the model to the dataset a least squares fitting routine is used.

The model presented in this paper is described in the most generalised version with separate parameters for each of the groups described in the previous section and the possibility to distinguish between top and base illumination. With the current dataset it is not possible to distinguish between the top and base electrodes and the corresponding parameters for the two electrodes have therefore been replaced by a single common parameter. These parameters are the tunnel rates:  $\Gamma_t^{(i)} = \Gamma_{t,bt}^{(i)} = \Gamma_{t,tb}^{(i)}$ , the diffusion constants in the STJs:  $D^{(i)} = D_b^{(i)} = D_t^{(i)}$  and the loss rates in the STJs:  $\gamma^{(i)} = \gamma_b^{(i)} = \gamma_t^{(i)}$ . The parameters shown in Table 7-1 could be calculated or estimated and are kept fixed within the model. These are:  $\gamma_s^{(i)}$  the relaxation rate at  $\varepsilon = \Delta_{Ta}$ ,  $\beta^{(i)}$  the fraction of quasiparticles created in the range  $\Delta_g < \varepsilon < \Delta_{Ta}$ . The ratio between the responsivity of the STJ and absorber,  $\chi^{(i)}$ , are calculated using the models described in refs 105 and 122.

**Table 7-1 Values of the fixed parameters. The values are calculated separately using different models.**

	symbols	30nm	60nm	100nm
Relaxation rate	$\gamma_s^l, \gamma_s^r$	$1 \cdot 10^6 [s^{-1}]$	$2 \cdot 10^6 [s^{-1}]$	$3.5 \cdot 10^6 [s^{-1}]$
qps in $\Delta_g < \varepsilon < \Delta_{Ta}$	$\beta^l, \beta^r$	0.75	0.78	0.8
Ratio of responsivity	$\chi^l, \chi^r$	1.17	1.3	1.5

The operating and device parameters have been varied for devices of several geometries in order to thoroughly test the parameters of the model for their correct description of the processes.

## 7. Experimental and theoretical response of Distributed Read-Out Imaging Devices with imperfect charge confinement

### 7.4 Testing of the model with the experimentally obtained results

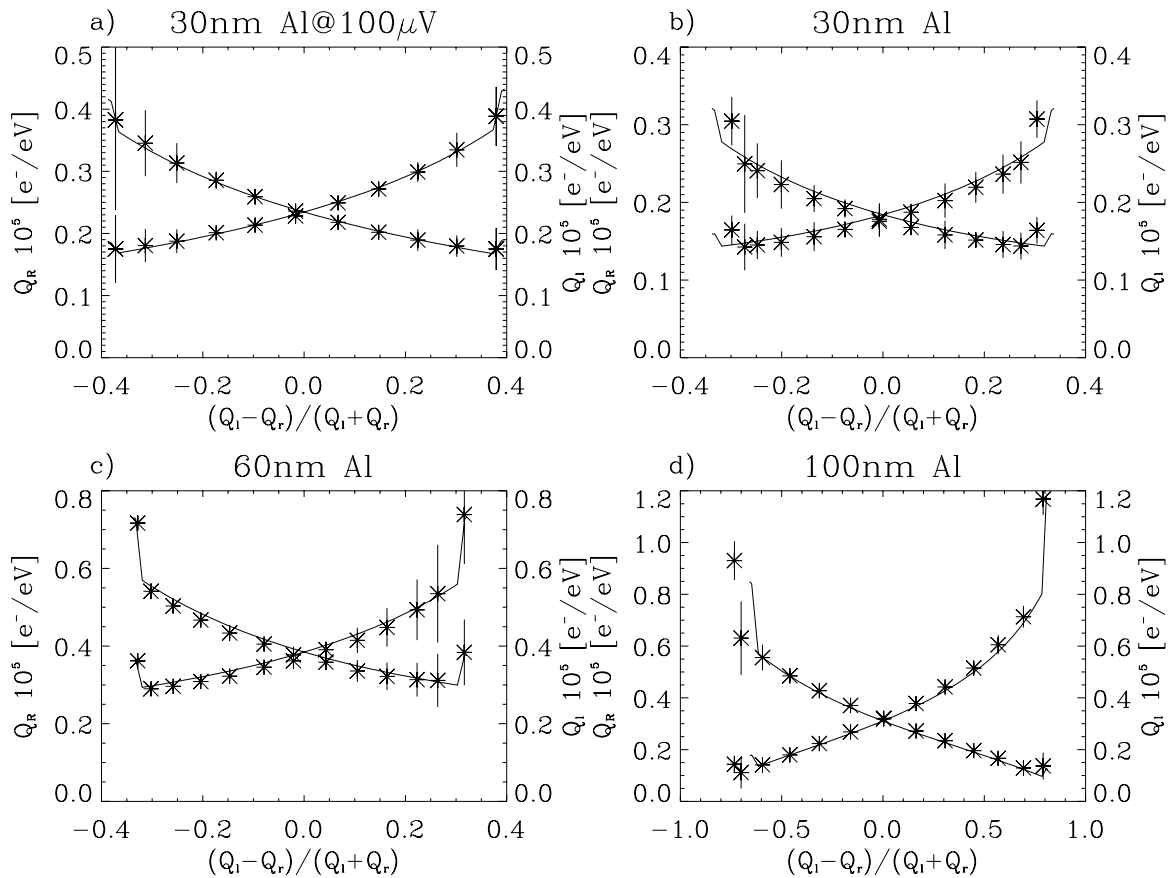


**Figure 7-4** The fit of the model to the measured charge output of the three DROID geometries. Each graph shows the charge output of the two STJs versus normalized charge ratio, (asterisk for  $Q_r$ , plus sign for  $Q_i$ ), with the fit of the model over plotted, solid lines. The dashed line is the calculated  $Q_i$  from the fit results. All measurements are from an illumination with 5eV photons at an operating temperature of 295mK. a) Shows the responsivity of the DROID with 30nm aluminium trapping layers at 100 $\mu$ V. b) shows a measurement from the same device with the same settings but biased at a voltage of 150 $\mu$ V for direct comparison with the other devices, c) and d) show measurements for the DROIDs with 60 and 100nm aluminium trapping layers respectively.

All three reference devices were illuminated by photon with energies within the range 1-5eV. The measurements have been conducted at an operating temperature of 295mK and at a bias voltage of 100 $\mu$ V in most of the tests on the DROID with 30nm aluminium trapping layers and 150 $\mu$ V for the DROIDs with 60 and 100nm aluminium trapping layers. This difference in bias voltage only affects the value of  $\zeta^{(i)}$  and a measurement with the DROID with 30nm aluminium trapping layers using a bias voltage of 150 $\mu$ V has been added to the results for comparison.

The model predicts the charge output of each STJ as a function of absorption position in the absorber or in the STJ. However, from the measurements only the two charges are known. In order to fit the results from the model to the measured data both are converted into a  $Q_r$  versus  $(Q_i - Q_r)/(Q_i + Q_r)$  graph, and fitted using a least squares fit. Figure 7-4 shows an example of fits of the model to measurements for the three reference devices at photon energy of 5eV. To



confirm the correctness of the fit the measured data is plotted as  $Q_l$  versus  $(Q_l - Q_r)/(Q_l + Q_r)$  with the result of the model, in the same representation, over plotted.

In all the cases the model satisfactorily describes the data points of the absorber events as well as the STJ events. The data from the DROID with 100nm aluminium (Figure 7-4d) trapping layer shows a significant asymmetry between the STJs, caused by an accidental difference in bias voltage, which is correctly described by the model as a variation of the value for  $\xi^r$ . This case also shows some discrepancy between the fit and the measurement due to the increased uncertainty on the measurement.

The results of the fit of the model to the data for different photon energies are constant within the accuracy of the measurement and the measured charge output is proportional to the input photon energies. Table 7-2 shows the average values for the parameters obtained from the fits of the model to the data sets obtained at different photon energies with the uncertainties being the standard deviations. The values of  $\xi^{(i)}$  for the 30nm aluminium trapping layer DROID corresponding with a measurement at 150 $\mu$ V have been added in parenthesis.

**Table 7-2 The average parameters resulting from the fit of the model to the experimental data obtained with the reference device at  $T=295\text{mK}$  and  $V_b=150\mu\text{V}$ , for 60 and 100nm Al layer, and  $V_b=100\mu\text{V}$ , for 30nm Al layer.**

	symbols	30nm	60nm	100nm
Tunnel rates	$\Gamma_l^l$ [ $10^5$ 1/s]	23 $\pm$ 1	26 $\pm$ 3	34 $\pm$ 3
	$\Gamma_l^r$ [ $10^5$ 1/s]	22 $\pm$ 1	27 $\pm$ 4	33 $\pm$ 3
Qp above $\Delta T_a - eV_b$	$\xi^l$	0.49 (0.6)* $\pm$ 0.02	0.36 $\pm$ 0.03	0.12 $\pm$ 0.01
	$\xi^r$	0.49 (0.6)* $\pm$ 0.02	0.35 $\pm$ 0.03	0.16 $\pm$ 0.01
Diffusion constant	$D$ [ $10^4$ cm <sup>2</sup> /s]	24.7 $\pm$ 0.8	23.1 $\pm$ 0.3	23.3 $\pm$ 0.3
	$D^l$ [ $10^4$ cm <sup>2</sup> /s]	24.3 $\pm$ 0.1	23.1 $\pm$ 0.7	24.2 $\pm$ 0.2
	$D^r$ [ $10^4$ cm <sup>2</sup> /s]	24.6 $\pm$ 0.1	23.1 $\pm$ 0.3	22.6 $\pm$ 0.5
Loss rates	$\gamma$ [1/s]	17900 $\pm$ 600	14200 $\pm$ 200	33000 $\pm$ 2000
	$\gamma^l$ [1/s]	5700 $\pm$ 2000	5500 $\pm$ 500	11000 $\pm$ 1000
	$\gamma^r$ [1/s]	6100 $\pm$ 2000	4500 $\pm$ 400	11500 $\pm$ 1600

\*For the 30nm aluminium trapping layer device the value for  $\xi^{(i)}$  at a bias voltage of 150 $\mu$ V has been added for comparison with the results from the other DROIDS.

Single STJs produced on the same wafer as the DROIDS enable an independent and more direct measurement of the tunnel rate. The values for the tunnel rate obtained from the fit to the DROID data and from single STJs of the same wafer agree within the uncertainties.

Thicker aluminium on top of the tantalum layer in the STJ reduces the energy gap in the STJ with respect to the bulk tantalum gap in the absorber. Therefore more quasiparticles will reside below  $\Delta T_a$  and the trapping efficiency is increased, such that fewer quasiparticles generated in one STJ can escape to the other STJ. In Figure 7-4 the effect of improved trapping with larger aluminium thickness can be seen as a larger separation of the two STJs along the  $(Q_l - Q_r)/(Q_l + Q_r)$  axis. Within the model this effect is described by the value for the fraction of quasiparticles above  $\Delta T_a - eV_b$ ,  $\xi^{(i)}$ , which decreases with increasing aluminium thickness, at a constant bias voltage.

## 7. Experimental and theoretical response of Distributed Read-Out Imaging Devices with imperfect charge confinement

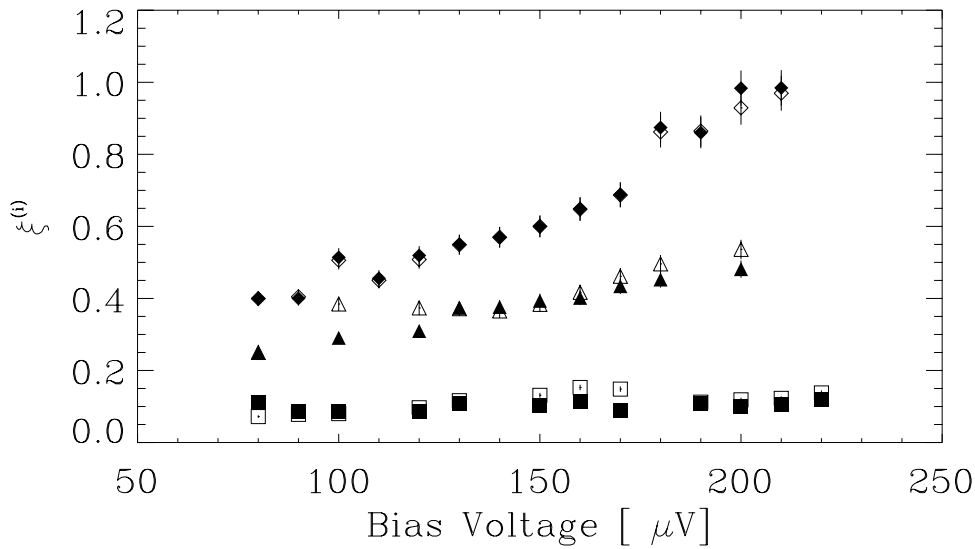


Figure 7-5 Fitted values for  $\zeta^{(i)}$  as a function of bias voltage for the DROIDS with 30nm (diamonds), 60nm (triangles) and 100nm (squares) aluminium trapping layers. The filled symbols are for the left STJ and the open symbols are for the right STJ.

Further confirmation of the correct description of the parameter  $\zeta^{(i)}$  is obtained from a scan in bias voltage for all three DROID geometries. These measurements have been conducted at an operating temperature of 295mK. The DROID with 30nm aluminium trapping layers was illuminated with 5eV photons while the 60 and 100nm were illuminated with 4.1eV photons. All parameters of the model are the same as in Table 7-2 within the uncertainties of the measurement, except for  $\zeta^{(i)}$  which increases with bias voltage (Figure 7-5) as expected. The value for  $\zeta^{(i)}$  for the DROID with 30nm aluminium layer increases from 0.4 at 90 $\mu$ V and reaches unity at 200 $\mu$ V, corresponding to a complete absence of confinement. This voltage is equal to the difference of the energy gaps of the STJ and absorber and all quasiparticles indeed remain above  $\Delta_{Ta}-eV_b$ .

For a photon absorption in one of the STJs of a DROID with perfect trapping ( $\zeta^{(i)}=0$ ) the charge output of the opposite STJ is equal to zero and in the representation of Figure 7-4 these events will occur on a single vertical line with  $(Q_l-Q_r)/(Q_l+Q_r)$  equal to 1 or -1. Any noise in the opposite STJ may give false triggers, of which only those with positive  $Q$  are registered. This can give rise to a small artificial shift of the STJ signal in the scatter plots away from the vertical line at  $\pm 1$ . For this reason it is expected that the trapping in the DROID with 100nm aluminium trapping layers is slightly underestimated (and hence the value of  $\zeta^{(i)}$  is overestimated), in particular at lower bias values.

The lack of variation in diffusion constant, as shown by the results in Table 7-2, between the three DROIDS indicates no connection between the  $RRR$  value, which is varying from device to device, and the non-equilibrium quasiparticle diffusion properties of the material. When quasiparticles thermalise while being in the absorber the following expression for the diffusion constant in the absorber would apply:

$$D \cong \frac{1}{3} \sqrt{\frac{2kT_{qp}}{\pi\Delta_{Ta}}} v_F \lambda_{300} RRR \quad 7-22$$

with  $T_{qp}$  the temperature of the quasiparticles in the absorber (taken equal to the operating temperature),  $v_F$  the Fermi velocity ( $0.67 \cdot 10^6$  m/s as taken from literature<sup>123</sup>) and  $\lambda_{300}$  the mean free path at room temperature (7 nm calculated using the Drude model<sup>124</sup> from the measured resistance).

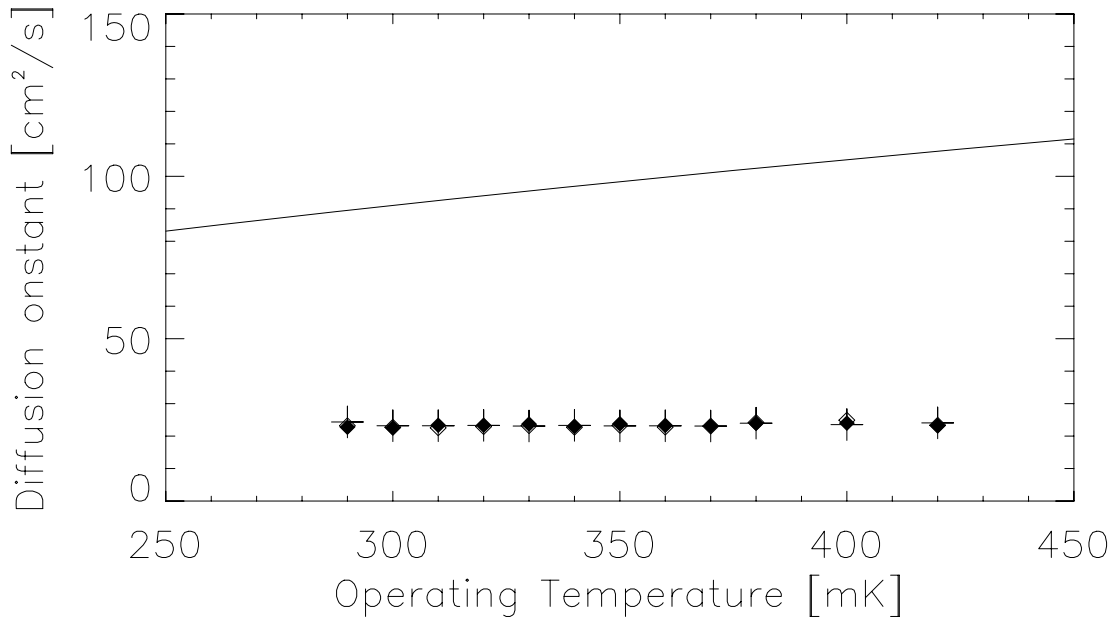


**Figure 7-6 Diffusion constant versus temperature for the DROID with 30nm aluminium trapping layers. The different symbols denote the diffusion constant in the absorber (crosses), left STJ (open diamonds) and right STJ (filled diamonds). The solid line denotes the theoretical diffusion constant as predicted by eq. 7-22.**

The DROID with 30nm aluminium trapping layers was illuminated using 5eV photons at bias voltage of  $100\mu\text{V}$  at different operating temperatures, limited by the base temperature of the cryostat at the low end and thermal noise contribution at the high end. Figure 7-6 shows the different diffusion constants resulting from the fit of the model to the data; all other parameters of the model remain the same within the uncertainties of the measurement as the values from Table 7-2. The solid line shows the theoretical prediction of eq. 7-22 which is well above the experimental values. However, the measured values are in agreement with previously obtained values on Ta/Al DROIDS from a different manufacturer<sup>125</sup> and with values obtained by other groups<sup>126-128</sup>.

## 7. Experimental and theoretical response of Distributed Read-Out Imaging Devices with imperfect charge confinement

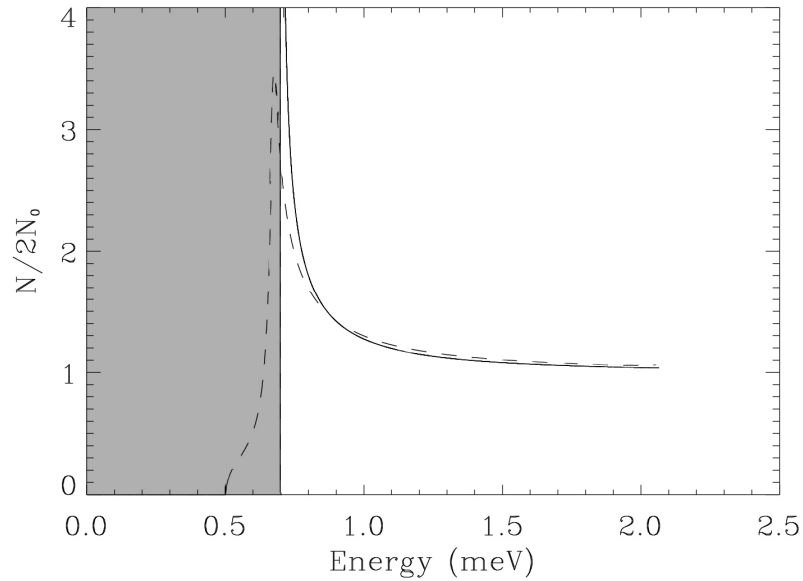
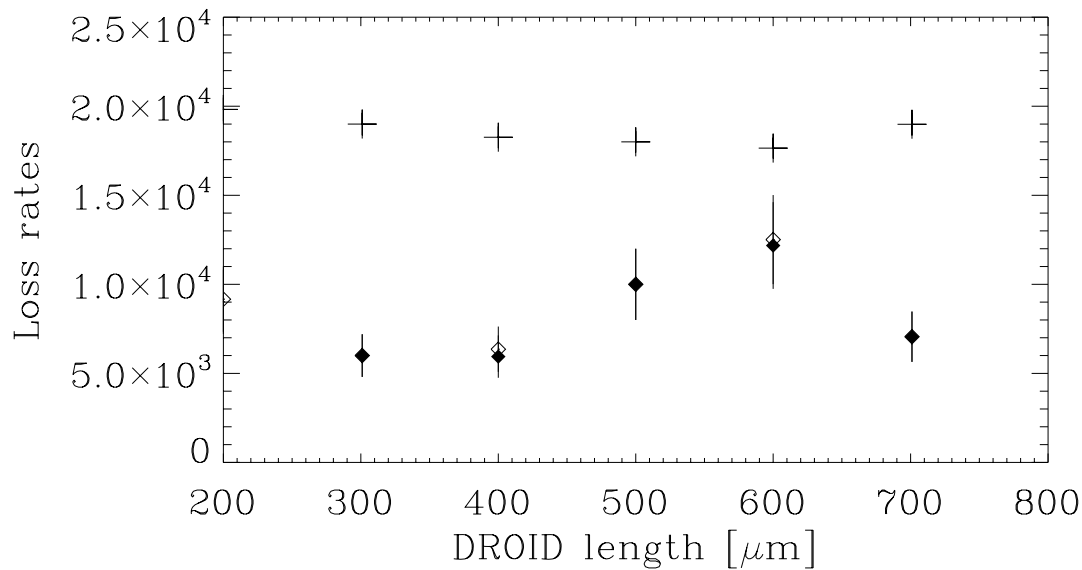


Figure 7-7 Density of states of the BCS tantalum absorber (solid line) and Ta/Al STJ (dashed line).

As seen in Table 7-2 there is no noticeable diffusion mismatch between the absorber and the STJs in any of the three DROID geometries. As described the tantalum absorber is only in contact to the tantalum layer of the base electrode and in order to estimate the diffusion mismatch between the absorber and the STJ only the quasiparticle energy distribution in the tantalum layer of the STJ above an energy equal to  $\Delta_{Ta}$  has to be compared to the energy distribution in the BCS-like tantalum absorber. Figure 7-7 shows the density of states for the BCS-like absorber and for a proximised Ta/Al bilayer with thicknesses 100/30nm. Both show a maximum at  $\Delta_{Ta}$  and rapid decay of the density of states towards high energy levels. In both situations the majority of the quasiparticles will remain near  $\Delta_{Ta}$  with rapid depletion at higher energies producing little difference in the quasiparticle distribution. We expect that the diffusion mismatch for this device will be below the accuracy of the dataset.

Previous results<sup>105</sup> on STJs have indicated that quasiparticle losses inside the STJ are due to bulk material losses and a concentration of loss centres near the leads, especially the plugs which are made of higher gap material to avoid out-diffusion of quasiparticles. Recent developments have indicated that quasiparticle losses in superconducting materials may be due to a very small amount of magnetic impurities in the high grade superconducting material<sup>129,130,100</sup>. The number of these impurities as well as the quality of the plugs, and thus the value of the loss rate are difficult to control in the production process, as indicated by the scatter in loss rate between the three devices. The DROID with 100nm Al trapping layer shows an increased loss rate in the absorber. This device has been produced in another but similar deposition system with a different sputter target. Compared with the STJ the loss rates in the absorber are much higher for all three devices indicating that the loss centres are mainly concentrated in the tantalum. The quasiparticles in the tantalum absorber are fully exposed to these loss centres while in the STJ the quasiparticles partly remain in the aluminium away from these loss centres. This is in agreement with our experience with pure aluminium devices which show extremely low loss rates.



**Figure 7-8** Loss rates in the DROIDS with different lengths from 30nm Al series. The loss rate in the absorber (crosses) is constant indicating homogeneous tantalum layer quality. The loss rate in the STJs (diamonds, open: left and filled: right) shows scatter between the DROIDS. This is caused by differences in plug quality.

Figure 7-8 shows the result of DROIDS of different lengths, ranging from 200 to 700 $\mu\text{m}$ , with 30nm aluminium layers in the STJs. The DROIDS were grown on a single chip and they have been measured within a single measurement run assuring similar fabrication and measurement conditions. The results can be described by the model using the parameters from Table 7-2 and changing the length of the DROID. The loss rate of the absorber remains constant for the different DROIDS indicating a homogeneous tantalum layer quality over the chip. However, the loss rate within the STJ varies from DROID to DROID indicating that the quality of the niobium plugs varies over the chip. This scatter in plug quality can also explain the absence of a correlation between the thickness of the aluminium layer and the difference of loss rate in the STJ and absorber.

## 7.5 Discussion

We have presented a theoretical model that describes all important processes involved with photon detection using DROIDS. We have tested the model against a set of experimental data of integrated signal charge from DROIDS using a least squares fitting method and found good agreement with the experimental results. Using this model and a single set of parameters for each DROID we were able to describe the dataset with all the DROID parameters within the expected range. The model correctly describes the DROID responsivity for absorption in both the absorber and the STJs with use of the separately calculated parameters  $\chi^{(i)}$  and  $\beta^{(i)}$ . The tunnel rates obtained for the different STJ geometries are in agreement with values obtained for single devices on the same wafer. Even asymmetry between the two STJs can easily be handled by the model as shown by the fit in Figure 7-4d.

The variation in the parameter  $\zeta^{(i)}$  shows increased trapping efficiency with increasing aluminium thickness, as expected due to the decrease of energy gap of the STJ (Table 7-2), and also with decreasing bias voltage (Figure 7-5), as expected from its definition, as the fraction of number of quasiparticles above  $\Delta_{\text{Ta}} - eV_b$ . The scan in bias voltage for the DROID

## 7. Experimental and theoretical response of Distributed Read-Out Imaging Devices with imperfect charge confinement

---

with 30nm aluminium trapping layer further provides proof of the correctness of these parameters. In this scan the parameter  $\zeta^{(i)}$  reaches unity at the bias voltage at which  $\Delta_{\text{Ta}} - eV_b$  is equal to the energy gap of the STJ.

The diffusion constants for the three DROIDs are found to be the same and show no dependence on operating temperature or *RRR* value. Although no correct theoretical description is available for the value of the diffusion constant the obtained value does agree with several other independent measurements of the diffusion constant in tantalum absorbers of DROIDs.

Unfortunately the quasiparticle distribution (Figure 7-7) shows little change at the interface between the absorber and STJ so no significant diffusion mismatch is present in this DROID geometry, which makes it impossible to test the role of this process.

Using a single parameter set, with exception of the loss rate in the STJ, the model was able to describe the results of several DROIDs of different lengths, located on a single chip and measured within a single run, showing the rigidity of the model. Within the fabrication process losses in the devices are still an important unknown factor, which makes the result uncertain from device to device. However, the behaviour of the loss rate within the different materials (low losses in the aluminium, higher losses in the tantalum and scatter in plug quality over the chip) agrees with our previous experiences.

### 7.6 Conclusion

We have developed a model to describe the integrated charge signal resulting from the detection of photons using DROIDs. The model incorporates all the important processes in the absorber and STJ involved with the photon detection. Tests of the model against responsivity data obtained from illumination with optical photons have shown the possibility of describing this dataset using a uniform parameter set. Tests of the individual model parameters have shown they respond as expected to changes in the experimental conditions. The model can be used to characterise and predict the behaviour of DROIDs used as photon detectors.



## Chapter 8

---

# First results of a cryogenic optical photon counting imaging spectrometer with use of a DROID array

---

R. A. Hijmering, P. Verhoeve, D.D.E. Martin, R. Venn, A. van Dordrecht and P.J. Groot

*submitted to A.&A.*

In this paper we present the first system test in which we demonstrate the concept of using an array of Distributed Read Out Imaging Devices (DROIDs) for optical photon detection. After the successful S-Cam 3 detector the next step in the development of a cryogenic optical photon counting imaging spectrometer under the S-Cam project is to increase the field of view using DROIDs. With this modification the field of view of the camera has been increased by a factor of  $\sim 5$  in area, while keeping the number of readout channels the same. The test has been performed using the flexible S-Cam 3 system and exchanging the 10x12 Superconducting Tunnel Junction (STJ) array for a 3x20 DROID array. The extra data reduction needed with DROIDs is performed offline. We show that, although responsivity (number of tunnelled quasiparticles per unit of absorbed photon energy,  $e^-/eV$ ) of the current array is too low for direct astronomical applications, the imaging quality is already good enough for pattern detection, and will improve further with increasing responsivity. The obtained knowledge can be used to optimise the system for the use of DROIDs.



## 8.1 Introduction

With the S-Cam project the Advanced Studies & Technology Preparation Division of the European Space Agency is developing a series of prototype cryogenic detectors to be used as optical photon counting imaging spectrometers for ground-based astronomy. The S-Cam detectors are using Superconducting Tunnel Junctions<sup>132,133,134</sup> as their detector technology. The merit of this and other cryogenic detectors<sup>135</sup> is that they combine single photon detection with sub-micron time resolution and intrinsic wavelength resolution, imaging and good detection efficiency in a single device.

STJs consist of 2 superconducting layers separated by a thin insulating layer acting as a tunnel barrier. With the absorption of a photon in the superconducting layer a large quantity (several thousands) of Cooper pairs are broken into quasiparticles which can tunnel across the barrier and, under the influence of an applied bias voltage, produce a measurable current pulse. The number of created quasiparticles is given by:  $N(E_0) = E_0/\varepsilon$ , with  $N(E_0)$  the number of created quasiparticles,  $E_0$  the energy of the absorbed photon and  $\varepsilon = 1.75\Delta_g$  the mean energy needed to create a quasiparticle<sup>19</sup> with  $\Delta_g$  the energy gap of the superconducting material. As shown the number of created quasiparticles, and hence the amplitude of corresponding tunnel current, is proportional to the energy of the absorbed photon, thus providing the detector with its spectrographic capabilities. The theoretical limit for the intrinsic spectral resolution is given by:  $\Delta E = 2.355\sqrt{\varepsilon E_0(F+G)}$ , where  $F$  is the Fano factor<sup>24</sup> ( $F = 0.2^{19,23}$ ) and  $G^{25}$  accounts for the statistical variations in the tunnel process. The energy gap,  $\Delta_g$ , of the used superconducting material is proportional to its critical temperature (temperature at which the phase changes from superconducting to normal metal,  $T_c$ ),  $\Delta_g = 1.764k_bT_c$  for a BCS type superconductor (usually elemental superconducting material which follows the theory developed by Bardeen, Cooper and Schrieffer<sup>40</sup>). A lower energy gap of the superconducting material will therefore increase the number of created quasiparticles and provide better spectrographic capabilities, but it also puts increasing constraints on the operating temperature ( $T_{op}$ ). This needs to be well below the critical temperature ( $T_c$ ) of the superconducting layer ( $T_{op} \sim 0.1T_c$ ) in order to sufficiently reduce the thermally excited quasiparticle population. For a more extended overview of the STJ technology the reader is referred to Peacock *et al*<sup>134</sup>.

Each STJ needs to be read out using a dedicated electronic chain which limits the maximum number of pixels that can be read out in a practical application<sup>136</sup>. To overcome this limitation the Distributed Read Out Imaging Device (DROID)<sup>28</sup> is being developed, see Figure 8-1. A DROID consists of a superconducting absorber strip with STJs on either end. The photon is absorbed in the absorber and the created quasiparticles diffuse towards the STJs where they tunnel. The sum of the tunnel signals of both STJs is a measure for the energy of the absorbed photon while the ratio is a measure for the absorption position. Depending on the position resolution of the DROID it can replace a number of single STJs and reduce the number of read out channels with sensitive area<sup>137</sup>.

Within the S-Cam project three prototype cameras have already successfully been used on telescopes such as the William Herschel Telescope (WHT) on La Palma and the Optical Ground Station (OGS) on Tenerife<sup>137</sup>. S-Cam 1<sup>3</sup> and 2<sup>30</sup> were based on a 6x6 pixel array (25x25 $\mu\text{m}^2$  pixels) with a wavelength resolving power of 6. S-Cam 3<sup>138,136</sup> was based on a 10x12 pixel array (35x35  $\mu\text{m}^2$  pixels), increasing the field of view on the WHT from 4"x4" to 10"x12". Also the covered wavelength range, operating temperature and resolving power ( $\sim 14@500\text{nm}$ ) had been enhanced with S-Cam 3. The applicability of this type of detector has been proven in the different observation campaigns in which several types of astronomical objects have been observed. The high time-resolution spectrally resolved S-Cam data has

## 8. First results of a cryogenic optical photon counting imaging spectrometer with use of a DROID array

provided strong constraints on the geometry of eclipsing binaries<sup>139,140,141</sup>. Precise timing of the Crab pulsar light curve has shown that the optical pulses lead the radio pulses with  $273 \pm 65 \mu\text{s}$ <sup>142,143</sup>. The spectral information provided by the STJs has enabled to directly determine the quasar redshifts<sup>144</sup> and stellar temperatures<sup>145</sup>.

The next step is to further increase the field of view with the use of DROIDS. Here we present the results of the first system test using a 3x20 DROID array as a detector.

### 8.2 Operation of the DROID array

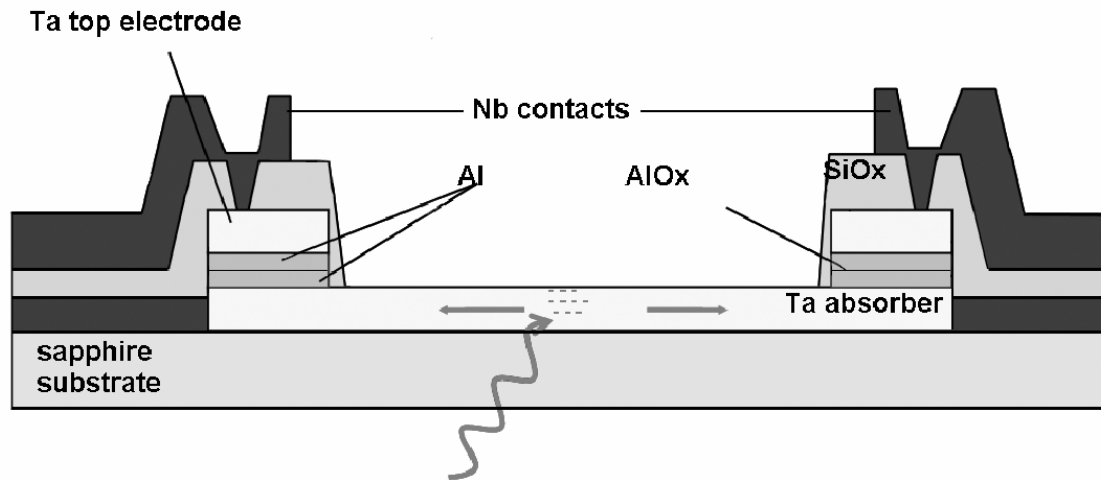


Figure 8-1 Schematic representation of the DROID geometry used in the DROID array.

The DROID array (Figure 8-2) is fabricated by MicroFab Ltd and is based on pure tantalum absorbers with Ta/Al STJs on the side. The lay-up of the STJs is Ta/Al/AlOx/Al/Ta with thicknesses of 100/30/1/30/100nm. The 100nm thick tantalum absorber of the DROID and the tantalum layer of the base electrode of the STJ (Figure 8-1) are made of a single layer of tantalum. The presence of the aluminium layer in the STJ reduces the energy gap due to the proximity effect<sup>26</sup> and provides confinement of quasiparticles inside the STJ, which enhances the performance. The confinement of quasiparticles using this method is not always 100% effective and quasiparticles which reside at higher energies,  $\epsilon > \Delta_{\text{Ta}}$ , are able to escape the STJ into the absorber. The DROIDS are  $33.5 \times 360 \mu\text{m}$  in size, including the  $33.5 \times 33.5 \mu\text{m}$  STJs. The DROIDS are separated by  $4 \mu\text{m}$  wide gaps to accommodate the interconnections between the base electrodes of the STJs, which share a common return wire. These interconnections are made of higher gap material (Nb,  $\Delta_{\text{Nb}} = 1550 \mu\text{eV}$ ) which prevents diffusion of quasiparticle across the interconnections, and thereby cross talk between DROIDS. The leads to the top electrodes of the STJs are routed over the front side of the DROIDS outwards. In order to electrically isolate the leads to the top electrodes from the rest of the DROID structure the complete array has been covered with SiOx. The array is divided into 4 electrically isolated groups of 3x5 DROIDS, each with a single common return lead. The devices are made on a transparent sapphire substrate which allows for backside illumination, through the sapphire. In this way the wiring routed over the absorber at the front side does not block any photons.

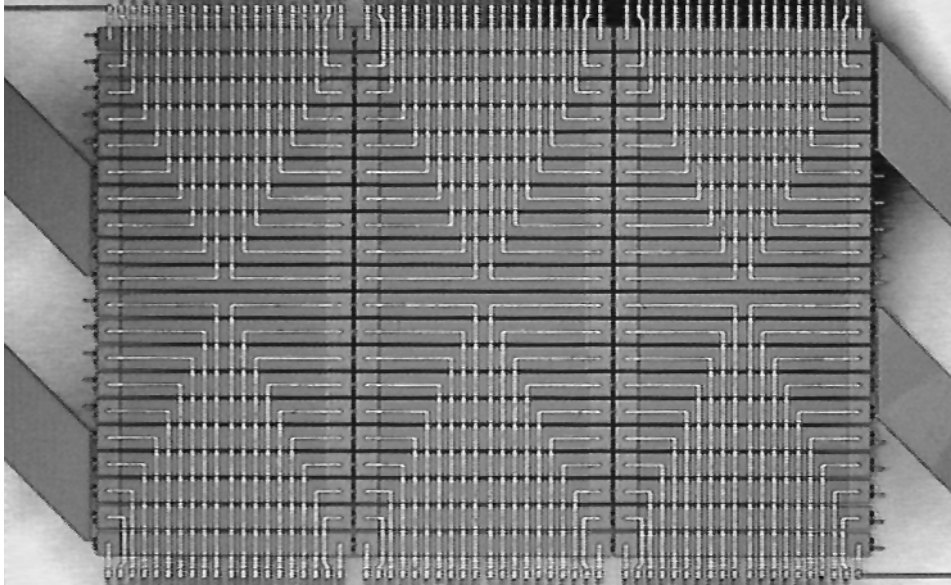


Figure 8-2 The 3x20 format DROID array fabricated by MicroFab Ltd. The leads for the read out of the STJs are visible running over the absorbers. The array is divided into 4 electrically isolated groups of 3x5 DROIDS of which the common ground leads can be identified as the two wide strips on either side of the array.

The individual DROIDS on the array have been characterised in a  $^3\text{He}$  sorption cooler in which we can read out two DROIDS at a time. In this cryostat the devices are effectively shielded from IR radiation using a closed shield surrounding the sample space and the chip can only be illuminated via an optical fibre. The electronics used to read out a single DROID at a time consist of two charge sensitive preamplifiers, with a RC time of  $470\mu\text{s}$ , each followed by a shaping stage. The two channels are linked in the sense that coincident events, defined as events in either STJ resulting from a photon absorption in the DROID which occur within  $30\mu\text{s}$  (the time window is defined by the electronics), can be identified and selected, while uncorrelated events are rejected. This efficiently reduces the noise-induced events as well. The resulting data for each event consists of the pulse height values of the two channels and the relative time of detection.

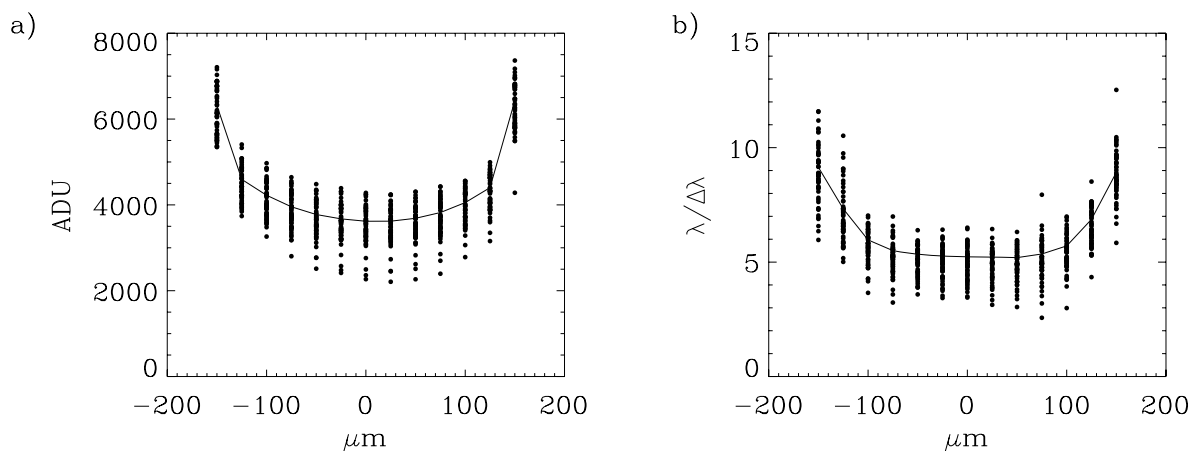


Figure 8-3 a) The relative responsivity for each of the DROIDS in the array (black dots) and the average responsivity (solid line) versus position along the absorber. b) The wavelength resolving power at 400nm of the individual DROIDS in the same representation. The outer group on either side represents the STJs.

## 8. First results of a cryogenic optical photon counting imaging spectrometer with use of a DROID array

---

The characterisation of the array showed that two DROIDS in the array were erroneously interconnected and one DROID showed increased subgap current levels. Figure 8-3a and b shows the relative pulse height (sum of the two STJ pulse heights) and wavelength resolving power  $\lambda/\Delta\lambda$ , respectively, of the DROIDS in the array as a function of position along the absorber (derived from the ratio of the two STJ pulse heights) under illumination with  $\lambda=400\text{nm}$  photons. The relative responsivity and resolving power of the DROIDS are determined by fitting a Gaussian to the single peak in pulse height spectrum. The responsivity across the array is rather non-uniform, with a standard deviation of 24%. This problem is related to the variable quality of the Nb interconnections between the base electrodes and solutions are currently under investigation. For practical use the absorber is divided into sections or virtual pixels. For S-Cam the size of a virtual pixel will be  $33\mu\text{m}$ , equal to the width of the absorber, and corresponding to the  $\sim 1\text{arcsec}$  seeing on the sky at the William Herschel Telescope and the Optical Ground Station. The average wavelength resolving power for the absorber events is  $6\pm 1$  (at  $\lambda=400\text{nm}$ ), and corresponds to an average position resolution of  $\Delta x \sim 35\mu\text{m}$ <sup>68,137</sup>, well matched to the size of a virtual pixel. The  $1\sigma$  variation in wavelength resolving power over the array is 16% (see Figure 8-3b) and is directly correlated to the variations in responsivity.

### 8.3 Full array test set-up

A full array test has been performed with the S-Cam 3 system<sup>138,136</sup> in which the complete array can be read out simultaneously and the array can be illuminated from the outside through a window. The optical chain, Figure 8-4, consists of an off axis parabolic mirror, two flat  $45^\circ$  mirrors to fold the beam, a high quality lens system to focus the beam on the detector and a set of 3 cold IR filters (inside the cryostat) to reduce the thermal load and IR background. The optical chain has a demagnification factor of 5.4 and the available wavelength band, limited by the IR filters, is 345-750nm. For laboratory tests the focal plain of the off axis parabolic mirror is illuminated, through a diffuser, with monochromatic light from a Xe lamp and grating monochromator through a UV-grade optical fibre. A pinhole can be moved into the focal plane to project spots of various size and shapes onto the chip. The chip is back illuminated through the sapphire substrate to avoid obscuration by the readout leads and to exploit the infrared absorption properties of sapphire.

The cryostat contains a liquid helium bath and uses a double stage  $^4\text{He}/^3\text{He}$  sorption cooler with a base temperature of 290mK and a hold time of  $\sim 28$  hours. The readout, which is similar to the one used with the measurements on one individual DROID, is performed using 120 charge sensitive preamplifiers grouped into the four electrically isolated groups, followed by analogue-to-digital converters and a programmable Finite Impulse Response (FIR) filter which acts as a shaping stage. The implemented filters produce a bipolar output pulse for each detected photon, of which both the positive and negative peak are sampled for offline evaluation. The ratio of positive and negative peak amplitude carries information on the original pulse shape and can be used to discriminate photon induced events from other disturbances. Each event in the STJ is labelled with a  $1\mu\text{s}$  accurate time stamp derived from a GPS (Global Positioning System) signal. The collected data for each detected event consists of the label of the STJ, the pulse height values for the positive and negative amplitudes and a time stamp.

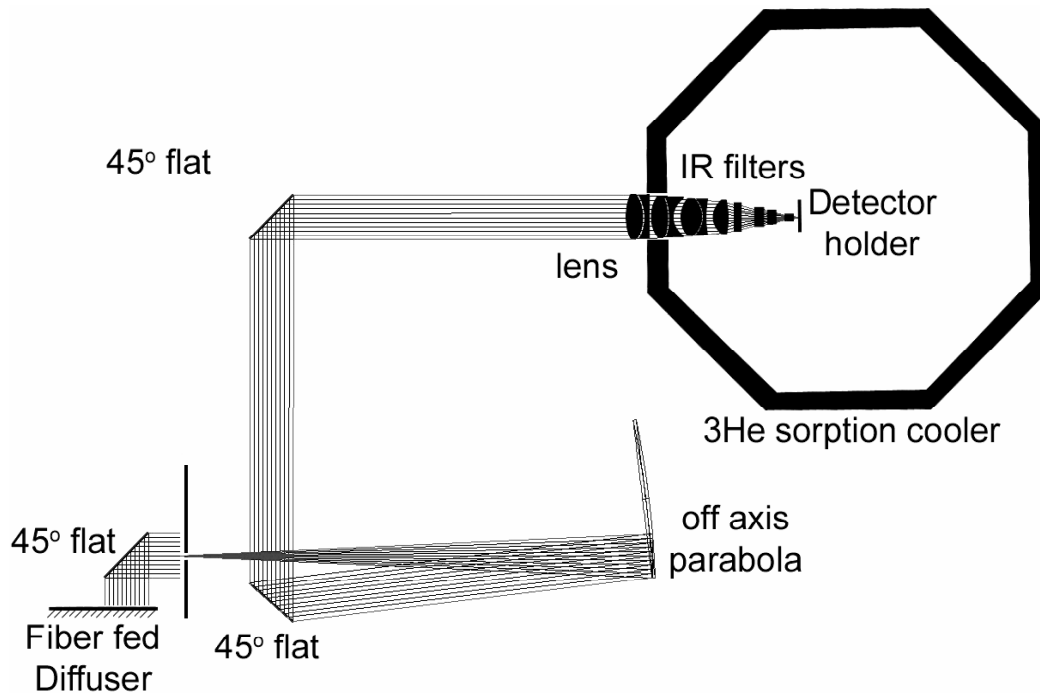


Figure 8-4 Schematic representation of the S-Cam 3 optical set-up.

Although the data acquisition system is very flexible it is currently geared towards the readout of an array of 120 single STJs, which introduces some complications for DROIDS. The signal in one of the STJs of a DROID decreases with distance between the absorption position and the STJ, and in order to detect the signals from absorptions near the far side STJ the thresholds for the individual channels need to be set sufficiently low, which introduces a large amount of noise-induced events. Identification and selection of coincident events in the two STJs of a DROID cannot be performed at hardware level yet and therefore all triggered events (including noise triggers) have to be recorded. Coincident event selection is then performed offline using the time stamps of the individual events.

Implementation of the DROID array and operation of the system proved to be not more difficult than the operation of the original 120 pixel S-Cam 3 detector array. Similar to previous experience the array was more sensitive to trapping of magnetic flux due to the larger superconducting area of the chip and multiple cool down cycles were required before an optimally functioning array was obtained. During the measurement four DROIDS were set inactive to allow stable operation: the two interconnected DROIDS, the DROID with increased subgap current levels and one DROID which remained flux trapped. For future use the interconnected DROIDS can be separated and improved magnetic shielding should remove the flux trapping entirely leaving only a single bad DROID in the array.

Because of the low responsivity of the DROID array only the shortest wavelengths in the available wavelength band could be used for illumination. Even so, the signal for some of the DROIDS did not reach above the detection threshold. For the current demonstration this results effectively in a non-uniform efficiency, which can be reduced using a flat field correction. However, because of the low responsivity the array is not useful for application on a telescope.

## 8.4 Data reduction

Despite the non-uniformity, the data of the DROIDS in the array shows fairly similar patterns and the off-line data reduction can easily be automated. The individual event data are initially filtered on the ratio of the positive and negative peak amplitudes (Figure 8-5a) which should be close to unity for true photon absorptions, see Martin 138. Coincident events are defined as events in the two STJs belonging to the same DROID which occur within  $\pm 40\mu\text{s}$ , of which the time window can be set manually in the offline data reduction. In this step  $\sim 95\%$  of the events, mainly noise-induced events, are filtered out making it the most important filtering step. Even with current computational power it takes several hours to complete this filtering on a file of several minutes' acquisition ( $\sim 35$  million events). Using the correlation between the ratio of charges  $(Q_r - Q_l)/(Q_r + Q_l)$  ( $Q_{r/l}$  being the pulse height value of the left or right STJ), which is related to the position along the absorber, and time difference of the two signals from the same event an extra filtering condition can be used (Figure 8-5b). This step is the second most important step with an additional  $\sim 70\%$  rejection efficiency. Finally the noise events at low pulse height are rejected by setting a lower threshold on the sum of the two signals  $(Q_r + Q_l)$ , see Figure 8-5c.

The STJ events can be discriminated from the absorber events by their spatial and spectral separation (Figure 8-5c). This is possible because the array is illuminated with monochromatic light. Part of the STJ events overlap with the outer absorber events in position and in case a broad band spectrum is used for illumination the spectral separation disappears. In order to calculate a correct measure for the photon energy and absorption position in the absorber the model of Jochum *et al*<sup>68</sup> is used (Figure 8-5d). Although this model is not complete in the description of all the processes involved with photon detection using DROIDS it provides an adequate and simple reconstruction method for the absorber events using only 2 fitting parameters<sup>137</sup>. The energy  $E_0$  and position of absorption  $x_0$  are derived from the measured signal amplitudes  $Q_r$  and  $Q_l$  as follows:

$$x_0 = \frac{L}{2\alpha} \ln \left[ \frac{Q_R e^{\frac{\alpha}{2}(1+\beta)} + Q_L e^{-\frac{\alpha}{2}(1-\beta)}}{Q_R e^{-\frac{\alpha}{2}(1-\beta)} + Q_L e^{\frac{\alpha}{2}(1+\beta)}} \right] \quad \text{8-1}$$

$$E_0 = c \sqrt{(Q_R^2 + Q_L^2)(1 - \beta^2) + 2Q_R Q_L [(1 + \beta^2) \cosh \alpha + 2\beta \sinh \alpha]} \quad \text{8-2}$$

Here  $c$  is the conversion factor between the measured charge and photon energy which can be obtained by calibration. The values for the fitting parameters  $\alpha$ , corresponding to loss in the absorber, and  $\beta$ , describing the trapping efficiency in the STJs, are determined from a least squares fit of the model to the data. The resulting values for  $\alpha$  and  $\beta$  for the DROIDS in the array are averaged to obtain a single value for  $\alpha = 1.4 \pm 0.3$  and  $\beta = 0.4 \pm 0.2$  which are then used for the correction. This is possible due to the homogeneity of the loss in the absorber and confinement of quasiparticles in the STJ in the DROIDS across the array. After this reconstruction is applied the absorber events are divided into 9 sections of which the area on the absorber are of roughly the same size as the STJs. The edges of the absorber in the data and the STJ events are determined by eye and the data points in between are separated in equidistant section. Each section will represent a virtual pixel in the final images.

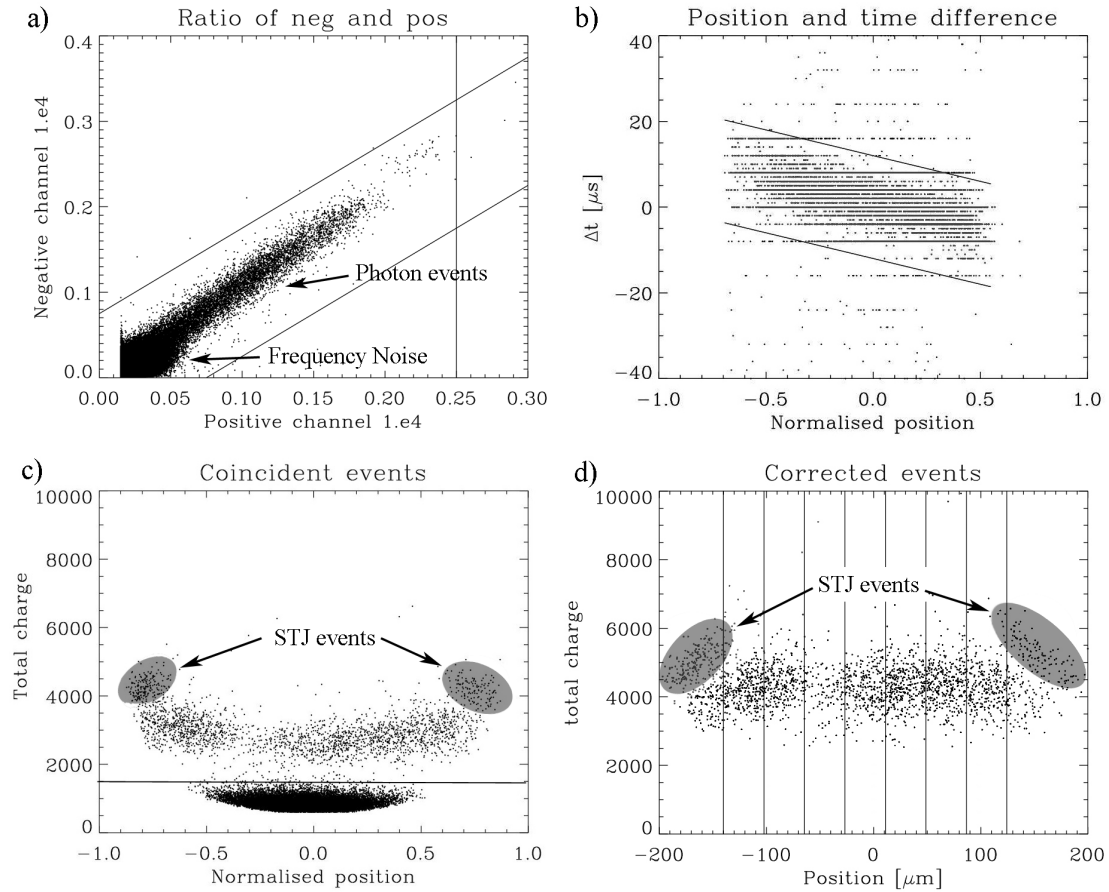


**Figure 8-5** Representation of the filtering procedures of the DROID array data. The data of the individual graphs is taken from different measurements to aid clarity of the complete process. a) Filtering on the ratio of the positive and negative peak which should lie close to unity. b) After identifying coincident events filtering on the correlation between the ratio of charges and difference in time stamp and c) removing the noise events with low pulse heights using the sum of the two signals. d) Shows the data after correction using the model from Jochum *et al* and divided into different sections. The gap in the absorber data of graphs c) and d) is caused by a mask in the focus of the optical system of which the result is shown in Figure 8-8.

## 8. First results of a cryogenic optical photon counting imaging spectrometer with use of a DROID array

### 8.5 Imaging quality of the DROID array detector

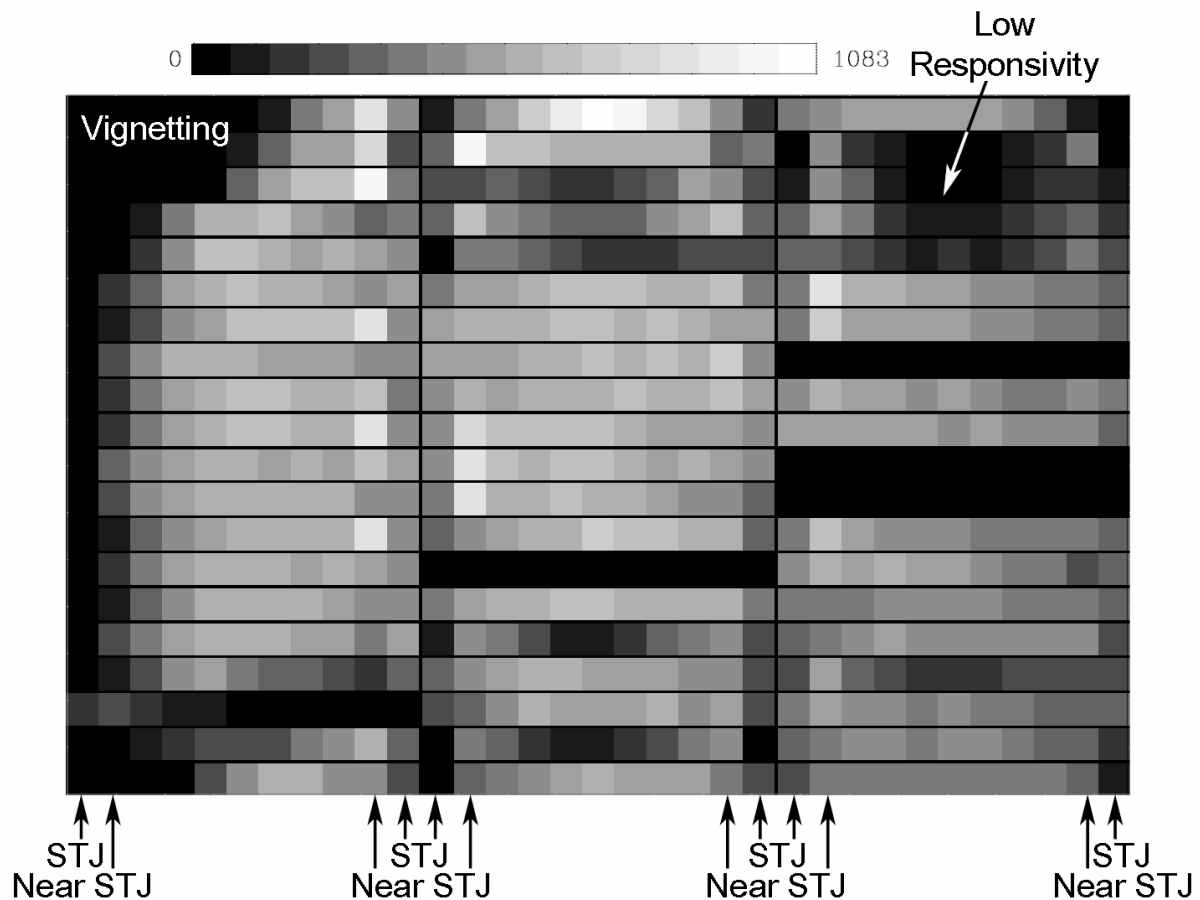
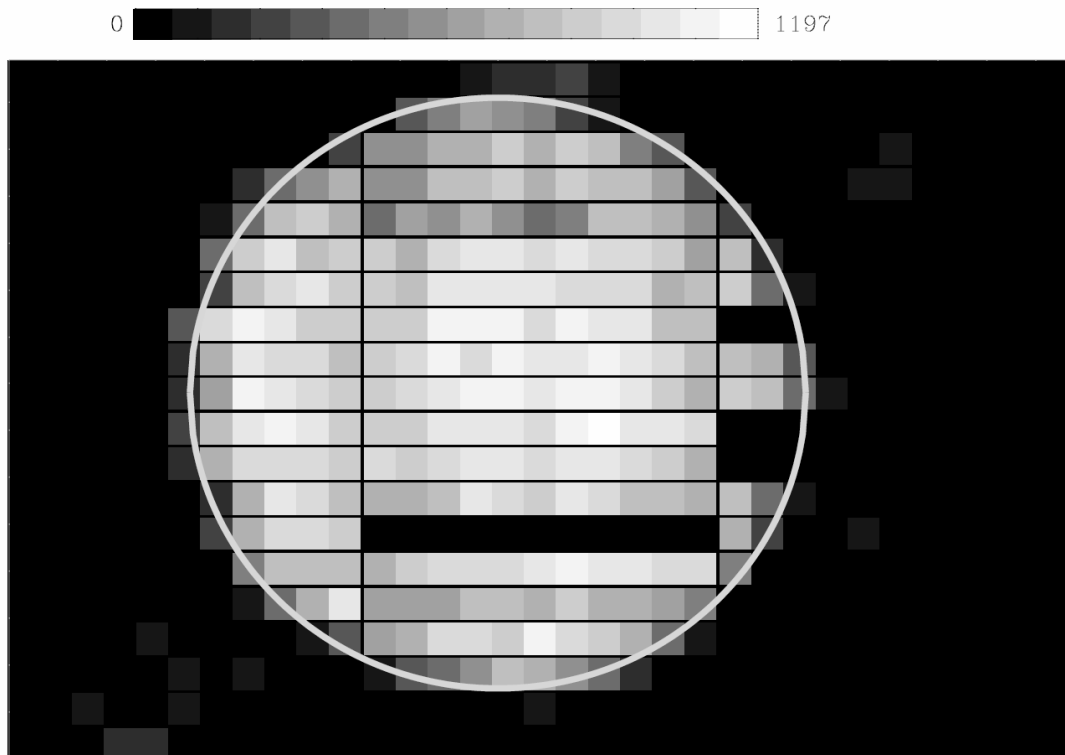


Figure 8-6 Image under full illumination used for the flat field correction. Each DROID corresponds to 11 virtual pixels in the horizontal direction. The left hand side shows dark areas due to vignetting. The DROIDS (2,7), (3,9), (3,10) and (3,13) are switched off.

An image of a full illumination of the array ( $\lambda=345\text{nm}$ , the lower limit of the available wavelength band) is shown in Figure 8-6 illustrating the non-uniform response of the array. The left hand side of the image is affected by vignetting from the lens assembly. This is more prominent compared to images shown below due to a side way shift of the lens assembly. Four DROIDS were switched off and appear as 11 black pixels in a row, one in the second column, line 7, and 3 in the third column, lines 9, 10 and 13. The remaining non-uniformity is caused by the low responsivity of the devices in the following manner. The responsivity of some devices, such as in the upper right corner, is too low to lift the sum signal from an optical photon absorbed in the middle of the DROID above the threshold set to reject the coincident noise triggers (see Figure 8-5c) and these events are erroneously rejected as noise producing dark areas in the image. If more energetic photons were used the signals of all events would rise above the thresholds and a much more uniform flat field would be obtained. The same holds for an array with higher responsivity.

As long as the threshold settings as well as the wavelength of illumination remain unchanged, the above image can be used for flat field corrections on other images. At the positions where the flat field shows no events, e.g. due to vignetting, the correction factor is set to unity and no correction is applied.





**Figure 8-7** Image of an illumination through a 3.4 mm aperture in the focus (after flat field correction with the image of Figure 8-6).

The imaging capabilities have been tested by illuminating the array through a set of masks positioned in the focus of the off axis parabolic mirror. Figure 8-7 shows a reconstructed image for the case when the array was illuminated through a 3.4mm  $\varnothing$  aperture in the focus of the off axis parabolic mirror, which should be projected as a 630 $\mu\text{m}$   $\varnothing$  image on the detectors. The circle, which represents the predicted size of the image, overlaps the boundaries of the image indicating correct scaling and the sharp drop-off of the intensity at the edges suggests a correctly focussed image and good position resolution along the DROID.

Secondly a mask with a double cross structure with line width of 0.1mm, corresponding to 16 $\mu\text{m}$  on the detector, was used. The spacing between the lines is 1.1 mm in the focus which should result in a spacing of 204 $\mu\text{m}$  at the detector. Figure 8-8 shows the resulting intensity plot with the projected image of the double cross represented by the lines. On the image the shadows of the double cross can be identified reasonably well and the lines overlap, showing the correct scaling.

## 8. First results of a cryogenic optical photon counting imaging spectrometer with use of a DROID array

---

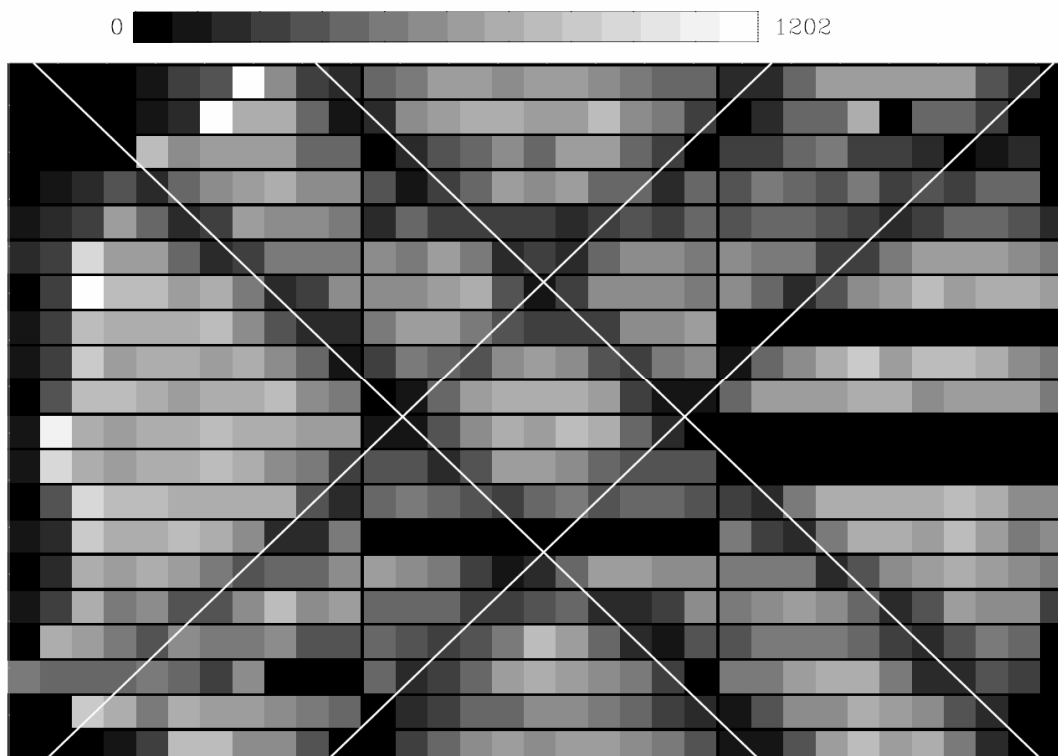


**Figure 8-8** Image of an illumination through a mask with of a double cross pattern with line width of 0.1mm and 1.1 mm separation (after flat field correction with the image of Figure 8-6).

S-Cam is being developed for applications in ground based astronomy. In order to simulate illumination from the sky a pinhole pattern has been located in the focus of the off axis parabola. Five  $50\mu\text{m}$   $\varnothing$  pinholes are located on an  $850\mu\text{m}$  grid which should result in five  $10\mu\text{m}$  spots, close to the limit of the optics resolution, on a  $160\mu\text{m}$  grid on the detector. Figure 8-9 shows the resulting image in negative. The pinhole pattern is deliberately projected on an area of the array with good responsivity. The predicted size and positions of the spots on the array are plotted over the image. The spots do not perfectly overlap because the position resolution in the vertical direction is determined by the width of the absorber. The upper and middle points show less broadening along the DROID length. These spots are located directly on a STJ where, due to the lower energy gap and quasiparticle confinement, the energy and position resolution is improved. The broadening of the other three points is slightly above a virtual pixel and corresponds with the position resolving power of  $35\mu\text{m}$  shown in section 8.2 as derived from the energy resolving power.

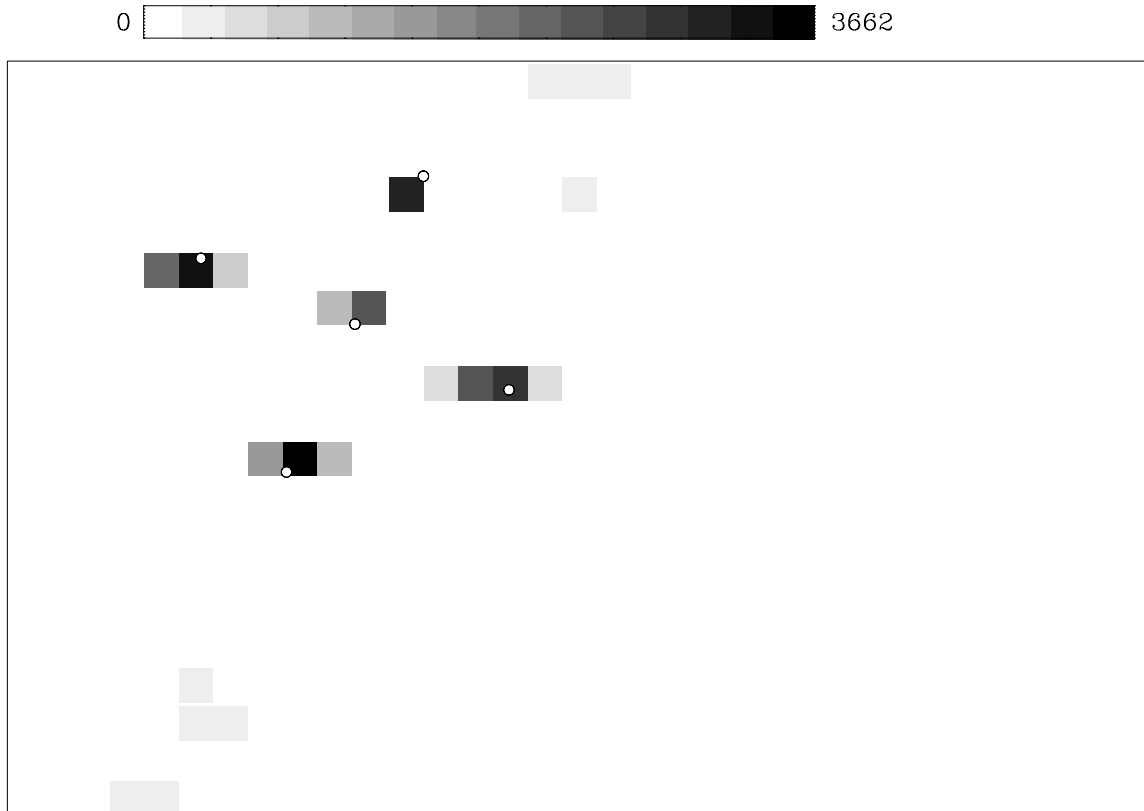


**Figure 8-9 Negative image of the 5 pinhole pattern. The five circles which represent the predicted pattern on the detector.**

## 8.6 Discussion

We have successfully demonstrated the feasibility of a DROID array as an imaging detector in the UV/visible. The S-Cam 3 10x12 individual STJ array could be easily exchanged for the 3x20 DROID array without introducing extra operating difficulties of the system. However, the larger superconducting area of the array appears to be more sensitive to trapping of magnetic flux and a better shielding inside the cryostat is required. The responsivity of the current array is too low for use on the telescope and only the shortest wavelengths in the available range of 340-740nm could be used. The responsivity is also non-uniform over the array, such that for some DROIDS not even the shortest wavelengths could be detected over the entire absorber. In order to reduce the effect on the images a flat field correction has been applied. The position resolution is found to be slightly larger than the absorber width as shown by illuminations with point sources as shown by Figure 8-9, and agrees with the position resolution of  $\sim 35\mu\text{m}$  calculated from the energy resolving power. This position resolution is just adequate to replace 11 individual STJs with a single DROID. This corresponds to an array of 660 virtual pixels using only 120 readout channels which would amount to a field of view of 20"x30" on the William Herschel Telescope. The imaging capability of the DROID array has been demonstrated by using a 3.4mm aperture and a 1.1mm separated double cross with 0.1mm wide lines, Figure 8-7 and Figure 8-8. Both images show a recognisable image of the introduced object as expected from the good position resolution.

## 8. First results of a cryogenic optical photon counting imaging spectrometer with use of a DROID array

---

The obvious first improvement on the DROID array for use on the telescope would be to increase the responsivity, which will automatically improve the energy and position resolution. This can be achieved by reducing the loss of quasiparticles inside the system. Experience has shown that the problem of low and variable responsivity appears to be related to the quality of the niobium interconnections between adjacent DROIDS and solutions are under investigation. In addition, increasing the thickness of the aluminium trapping layers in the STJ would improve the trapping of the quasiparticles in the STJs which will improve the responsivity thereby both energy and position resolution as well. Such performance has already been demonstrated in measurements on single DROIDS of identical geometry<sup>117,146</sup>. An aluminium layer thickness of 60nm is advised which is a good trade off between the trapping in the STJs and thermal noise with the current base temperature of just below 300mK. There is also margin for decreasing the base temperature with more advanced sorption coolers which will allow even thicker Al layers to be considered.

In addition to improvements on the DROID array some practical improvements can be introduced to the data acquisition system. Most important is to link the two readout chains for each DROID making it possible for the electronics to detect coincident events. If an event in one STJ is followed by an event in the other STJ within a user determined time window the event is passed on as valid, otherwise it is discarded. Secondly, because the threshold on a single channel must be set low in order to detect the low signals in case of absorption near the opposite STJ a lot of coincident noise events will be passed. These can be effectively filtered out by introducing an extra threshold on the sum of the two pulse heights, effectively setting an upper wavelength limit for detection. These two modifications to the system would improve noise filtering and offline data reduction time by orders of magnitude.

Finally the data could be converted into position and energy data instead of the charges of the STJs, by using for instance the model from Jochum *et al*<sup>68</sup>. However care has to be taken where this is implemented. In order not to jeopardise the raw data it could be implemented in the pipeline software that converts the raw data file into the final data file for the user in FITS<sup>147</sup> format (as for S-Cam 3). For the real time analysis this can be performed in a parallel route to the operating software, e.g. using a lookup table to convert pulse height ratio into virtual pixel to save calculation time. This would provide a highly desirable real time preliminary image reconstruction.

### 8.7 Conclusion

We have successfully demonstrated operation of an array of DROIDS as a photon counting and imaging detector in an astronomical instrument. Although the responsivity of the array was too low for practical use the resolving power and imaging capabilities, which will improve further with increasing responsivity, are already adequate. From this first system test we have obtained a good understanding on how to further optimise the system for photon detection with DROIDS.



## References

1. A. Chapman, *Astronomy & Geophysics*, **50**, Issue 1, pp. 1.27-1.33, 2009
2. G.F. Amelio, M.F. Tompsett, G.E. Smith, *Bell Syst. Tech. J.* **49**, pp. 593-600 (1970)
3. P. Verhoeve, N. Rando, A. Peacock, D. Martin, R. den Hartog, *Opt. Eng.* **41** (6), 1170 (2002)
4. C. Brofferio, *Nucl. Instr. And Meth. A* **520**, p. 151 (2004)
5. W.S. Holland, E.I. Robson, W.K. Gear, C.R. Cunningham, J.F. lightfoot, T. Jenness. R.J. Ivison, J.A. Stevens, P.A.R. Ade, M.J. Griffin, W.D. Duncan, J.A. Murphy, D.A. Naylor, *MNRAS* **303**, 659, (1999)
6. J.E. Ruhl, P.A.R. Ade, J.E. Carlstrom, H.M. Cho, T. Crawford, M. Dobbs, C.H. Greer, N.W. Halverson, W.L. Holzappel, T.M. Lanting, A.T. Lee, J. Leong, E.M. Leitch, W. Lu, M. Lueker, J. Mehl, S.S. Meyer, J.J. Mohr, S. Padin, T. Plagge, C. Pryke, D. Schwan, M.K. Sharp, M.C. Runyan, H. Spieler, Z. Staniszewski, A.A. Stark, *Proc. of the SPIE*, **5498**, 11 (2004)
7. G. Siringo, E. Kreysa, A. Kovács, F. Schuller, A. Weiß, W. Esch, H.P. Germünd, N. Jethava, G. Lundershausen, A. Colin, R. Güsten, K.M. Menten, A. Beelen, F. Bertoldi, J.W. Beeman, E.E. Haller, *A&A* **497**, 945 (2009)
8. M. Griffin, Alain, Abergel, P. Ade, P. André, J.-P. Baluteau, J. Bock, A. Franceschini, W. Gear, J. Glenn, D. Griffin, K. King, E. Lellouch, D. Naylor, G. Olofsson, I. Perez-Fournon, M. Rowan-Robinson, P. Saraceno, E. Sawyer, A. Smith, B. Swinyard, L. Vigroux, G. Wright, *Proc of the SPIE*, **6265**, 62650A, (2006)
9. A. Poglitsch, C. Waelkens, O. Bauer, J. Cepa, H. Feuchtgruber, T. Hennings, C. van Hoof, F. Kerschbaum, D. Lemke, E. Renotte, L. Rodriguez, P. Saraceno, B. Vandenbussche, *proc. of SPIE*, 6265, 62650B-1 (2006)
10. K.D. Irwin, *Appl. Phys. Lett.* **66**, 1998 (1995)
11. <http://ixo.gsfc.nasa.gov/>
12. R.W. Romani, A.J. Miller, B. Cabrera, S.W. Nam, J.M. Martinis, *The Astrophysical Journal*, **563**- 1, 221 (2001)
13. S. Shiki, H. Sato, Y. Takizawa, M. Kurakado, H. M. Shimizu, *Publ. Astron. Soc. Japan*, 56, L19, (2004)
14. A. Peacock, P. Verhoeve, N. Rando, A. van Dordrecht, B.G. Taylor, C. Erd, M.A.C. Perryman, R. Venn, J. Howlett, D.J. Goldie, J. Lumley, M. Wallis, *Nature* **381**, pp1 135-137 (1996)
15. P. Day, H. Leduc, B. Mazin, A. Vayonakis, and J. Zmuidzinas, *Nature (London)* **425**, 817 (2003)
16. D. Twerenbold, *Phys. Rev. Lett. B* **34**, 7748 (1986)
17. M.A.C. Perryman, C.L. Foden, A. Peacock, *Nucl. Instr. and Meth. A* **325**, Issue 1-2 pp. 319-325 (1993)
18. L. N. Cooper, *Phys. Rev.* 104, 1189 (1956)
19. M. Kurakado, H. Mazaki, *Nucl. Instr. and Meth.* 185, p. 141 (1981)
20. D. J. Josephson, *Phys. Lett.* **1**, 251 (1962)
21. D.D.E. Martin, PhD thesis, University Twente (2007)
22. D.D.E. Martin, P. Verhoeve, T. Oosterbroek, R.A. Hijmering, T. Peacock, R. Schulz, *Proceedings of SPIE* **6269**, pp. 62690O, (2006)
23. N. Rando, A. Peacock, A. van Dordrecht, C. L. Foden, R. Engelhardt, B. G. Taylor, P. Gare, J. Lumley, and C. Pereira, *Nucl. Instr. and Meth.*, **313**, 173 (1991).

24. U. Fano, *Phys. Rev.* **72**, 26 (1947)
25. C. Mears, S. E. Labov, and A. Barfknecht, *Appl. Phys. Lett.* **63**, 2961 (1993).
26. N.E. Booth, *Appl. Phys. Lett.* **50**, 293 (1987)
27. A.A. Golubov, E.P. Houwman, J.G. Gijsbertsen, V.M. Krasnov, M. Yu. Kupriyanov, J. Flokstra, and H. Rogalla, *Phys. Rev. B* **51**, 1073 (1995)
28. H. Kraus, F.v. Feilitzsch, J. Jochum, R.L. Mössbauer, Th. Peterreins, F. Pröbst, *Physics Lett. B* **231** 195 (1989)
29. K. Segall, Ph.D. thesis, Yale University, New Haven, Connecticut (2000)
30. N. Rando, S. Anderson, B. Collaudin, F. Favata, P. Gondoin A. Peacock, M. Perryman, J. Verveer, P. Verhoeve, D.J. Goldie, *Nucl. Instr. And Meth. A* **444**, 441 (2000)
31. P. Verhoeve, AIP Conference Proceedings 605, “Low Temperature detectors”, Edited by F.S. Porter, D. McCammon, M. Galeazzi, C.K. Stahle, 559 (2002)
32. M.A.C. Perryman, M. Cropper, G. Ramsay, F. Favata, A. Peacock, N. Rando, A. Reynolds, *Monthly Notice of the Royal Astronomical Society*, **324**, 899 (2001)
33. J.H.J. Bruijne, A.P. Reynolds, M.A.C. Perryman, F. Favata, D. Martin, P. Verhoeve, N. Rando, A. Peacock, *Galaxies: The Third Dimension*, ASP Conf. series **282**, 565, (2002)
34. D.D.E. Martin, P. Verhoeve, R.H. den Hartog J.H.J. de Bruijne, A.P. Reynolds, A. van Dordrecht, A.J. Peacock, *Proc. of SPIE* **4841**, 805 (2003)
35. M.A.C. Perryman, F. Favata, A. Peacock, N. Rando, B.G. Taylor, *A&A* **346**, 30, (1999)
36. T. Oosterbroek, J.H.J. de Bruijne, D. Martin, P. Verhoeve, M.A.C. Perryman, C. Erd, R. Schultz, *A&A*, **456**, 283 (2006)
37. H.K. Onnes, *Commun. Phys. Lab* **12**, p. 120 (1911)
38. W. Meissner, R. Ochsenfeld, *Naturwissenschaften* **21**, p. 787 (1933)
39. F. London, H. London, *Proc. Roy. Soc.* **A149**, p. 71 (1935)
40. J. Bardeen, L.N. Cooper, J.R. Schrieffer, *Phys. Rev.* **108**, p. 1175 (1957)
41. L.N. Cooper, *Phys. Rev.* **104**, 1189, (1956)
42. A.B. Pippard, *Proc. Roy. Soc.*, **A216**, 547 (1953)
43. T.E. Faber and A.B. Pippard, *Proc. Roy. Soc. (London)* **A231**, 336 (1955)
44. *Introduction to Superconductivity*, second edition, M. Tinkham, ISBN 0-486-43503-2 (2004)
45. N.N. Bogoliubov, *Nuovo Cimento* **7**, p. 794 (1958)
46. J.G. Valatin, *Nuovo Cimento* **7**, p. 843 (1958)
47. D. van Vechten, K. Wood, *Phys. Rev. B* **43**, pp. 12852-12860 (1991)
48. Yu. N. Ovchinnikov, V.Z. Kresin, *Phys. Rev. B* **58**, pp. 12416-12421 (1998)
49. A.G. Kozorezov, A.F. Volkov, J.K. Wigmore, A. Peacock, A. Poelaert, R. den Hartog, *Phys. Rev. B* **61**, pp. 11807-11819 (2000)
50. I. Giaever, *Phys. Rev. Lett.* **5**, p. 147 (1960)
51. I. Giaever, *Phys. Rev. Lett.* **5**, p. 464 (1960)
52. B.D. Josephson, *Phys. Lett.* **1**, 251 (1962)
53. V.L. Ginzburg, L.D. Landau, *Zh. Eksperim. i. Teor. Fiz.* **20**, 1064 (1950)
54. V. Ambegaokar, A. Baratoff, *Phys. Rev. Lett.* **10**, 11 (1963)
55. M.D. Fiske, *Rev. Mod. Phys.* **36**, 221 (1964)
56. D.D. Coon, M.D. Fiske, *Phys. Rev.* **138**, A744 (1965)
57. R.L. Peterson, *Cryogenics* **31**, 132 (1991)
58. K.E. Gray, *Appl. Phys. Lett.* **32**, pp. 392-395 (1978)
59. W. Eisenmenger, *Physical Acoustics* (eds. W.P. Mason and R.N. Thurston) **XII**, 80 (1976)

## References

---

60. Principles of Electron Tunneling spectroscopy, E.L. Wolf, ISBN 0-19-503417-1, (1985)
61. K.D. Usadel, Phys. Rev. Lett. **25**, 507 (1970)
62. Cambridge Microfab Ltd., Broadway, Bourne, Cambridge CD23 2TA, UK
63. PLansee SE, 6600 Reutte, Austria
64. Technical Materials Incorporated, 5 Wellington Rd., Lincoln, RI 02865, USA
65. Shipley Co, 245 Santa Ana Ct. Sunnyville, CA 94086, USA.
66. M. Yu. Kupriyanov and V.F. Lukichev, Zh. Esp. Teor. Fiz. **73**, 299 (1977) [Sov. Phys. JETP **41**, 960 (1977)]
67. J. le Grand, C. Mears, S. Labov, P. Jakobsen, P. Verhoeve, M. Bavdaz and A. Peacock, *Proc. of LTD 7*, 106, editor: S. Cooper (1997)
68. J. Jochum, H. Kraus, M. Gutsche, B. Kemmather, F.v. Feillitzsch and R.L. Mössbauer, Ann. Phys. (N.Y.) **2**, 611 (1993).
69. J.C. Mather, Nature **401**, 654 (1999)
70. C.A. Mears, S.E. Labov, M. Frank, M.A. Lindeman, L.J. Hiller, H. Netel, and A.T. Barfknecht, Nucl. Instrum. Methods Phys. Res. A **370**, 53 (1996).
71. P. Verhoeve, N. Rando, A. Peacock, A. van Dordrecht, and D. J. Goldie, Appl. Phys. Lett. **72**, 3359 (1998).
72. R.H. den Hartog, D. Martin, A. G. Kozorezov, P. Verhoeve, N. Rando, A. Peacock, G. Brammertz, M. Kramrey, D. Goldie, and R. Venn, Proc. SPIE **4012**, 237 (2000).
73. G. Angloher, B. Beckhoff, M. Bühler, F. v. Feilitzsch, T. Hertrich, P. Hettl, J. Höhne, M. Huber, J. Jochum, R. L. Mößbauer, J. Schnagl, F. Scholtze, and G. Ulm, Nucl. Instrum. Methods Phys. Res. A **444**, 214 (2000).
74. K.E. Gray, Appl. Phys. Lett. **32**, 392 (1978).
75. D.J. Goldie, P.L. Brink, C. Patel, N.E. Booth, and G.L. Salmon, Appl. Phys. Lett. **64**, 3169 (1994).
76. P. Verhoeve, R. den Hartog, A. Kozorezov, D. Martin, A. van Dordrecht, J. K. Wigmore, and A. Peacock, J. Appl. Phys. **92**, 6072 (2002).
77. L.J. Hiller, M.L. van den Berg, and S.E. Labov, Appl. Phys. Lett. **79**, 4441 (2001).
78. A.G. Kozorezov, J.K. Wigmore, A. Peacock, R. den Hartog, D. Martin, G. Brammertz, P. Verhoeve, and N. Rando, Europhys. Lett. **66**, 265 (2004).
79. A.G. Kozorezov, J.K. Wigmore, A. Peacock, R. den Hartog, D. Martin, G. Brammertz, P. Verhoeve, and N. Rando, Phys. Rev. B **69**, 184506 (2004).
80. C.M. Wilson, L. Frunzio, and D.E. Prober, Phys. Rev. Lett. **87**, 067004 (2001).
81. C.M. Wilson and D.E. Prober, Phys. Rev. B **69**, 094524 (2004).
82. A. Rothwarf and B.N. Taylor, Phys. Rev. Lett. **19**, 27 (1967).
83. A. Poelaert, A. Peacock, P. Verhoeve, A. van Dordrecht, A. Owens, N. Rando, A.G. Kozorezov, and J.K. Wigmore, Proc. SPIE **3445**, 9214 (1998).
84. K. Segall, C. Wilson, L. Frunzio, L. Li, S. Friedrich, M.C. Gaidis, and D.E. Prober, Appl. Phys. Lett. **76**, 3998 (2001)
85. K. Segall, C. Wilson, L. Li, L. Frunzio, S. Friedrich, M.C. Gaidis, and D.E. Prober, Phys. Rev. B **70**, 214520 (2004).
86. G. Brammertz, A.G. Kozorezov, J.K. Wigmore, R. den Hartog, P. Verhoeve, D. Martin, A. Peacock, A.A. Golubov, and H. Rogalla, J. Appl. Phys. **94**, 5854 (2003).
87. G. Brammertz, Ph.D. thesis, Universiteit Twente, 2003
88. V.F. Elesin and Yu. V. Kopaev, Sov. Phys. Usp. **24**, 116 (1981).
89. J.J. Chang, in *Nonequilibrium Superconductivity*, edited by D.N. Langenberg and A.I. Larkin Elsevier, Amsterdam, p. 459., (1986)
90. A. Poelaert, A.G. Kozorezov, A. Peacock, and J.K. Wigmore, Phys. Rev. Lett. **82**, 1257 (1999).



91. A.G. Kozorezov, J.K. Wigmore, A. Peacock, A. Poelaert, P. Verhoeve, R. den Hartog, and G. Brammertz, *Appl. Phys. Lett.* **78**, 3654 (2001).
92. A. Poelaert, Ph.D. thesis, Universiteit Twente, Enschede, 1999.
93. G. Fagas, A.G. Kozorezov, C.J. Lambert, J.K. Wigmore, A. Peacock, A. Poelaert, and R. den Hartog, *Phys. Rev. B* **60**, 6459 (1999).
94. A.G. Kozorezov, J.K. Wigmore, G. Brammertz, and A. Peacock, *Phys. Status Solidi C* **1**, 2816 (2004)
95. A.A. Golubov, E.P. Houwman, J.G. Gijsbertsen, J. Flokstra, H. Rogalla, J.B. le Grand, and P.A.J. de Korte, *Phys. Rev. B* **49**, 12953 (1994).
96. S.B. Kaplan, C.C. Chi, D.N. Langenberg, J.J. Chang, S. Yafarey, and D. Scalapino, *Phys. Rev. B* **14**, 4854 (1976).
97. A.G. Kozorezov, J.K. Wigmore, R. den Hartog, D. Martin, P. Verhoeve, and A. Peacock, *Phys. Rev. B* **66**, 094510 (2002).
98. R. den Hartog, A. G. Kozorezov, J. K. Wigmore, D. Martin, P. Verhoeve, A. Peacock, A. Poelaert, and G. Brammertz, *Phys. Rev. B* **66**, 094511 (2002).
99. A. A. Golubov, E. P. Houwman, J. G. Gijsbertsen, J. Flokstra, H. Rogalla, J. B. le Grand, and P. A. J. deKorte, *Phys. Rev. B* **49**, 12953 (1994).
100. R. Barends, J.J. Baselmans, S.J.C. Yates, J.R. Gao, J.N. Hovenier, T.M. Klapwijk, *Phys. Rev. Lett.* **100**, 257002 (2008)
101. A.V. Timofeev, C. Pascual Garcia, N.B. Kopnin, A.M., Savin, M. Maschke, F. Giazotto, J.P. Pekola, *Phys. Rev. Lett.* **102**, 017003 (2009)
102. G. Brammertz, A. Poelaert, A.A. Golubov, P. Verhoeve, A. Peacock, H. Rogalla, *J. Appl. Phys.* **90** 1, 355 (2001)
103. M. Kurakado, *Nucl. Instr. and Meth.* **196**, 275 (1982)
104. B.A. Aminov, A.A. Golubov, M. Yu. Kupriyanov, *Phys. Rev. B* **53**, 365 (1996)
105. A.G. Kozorezov, R.A. Hijmering, G. Brammertz, J.K. Wigmore, A. Peacock, D. Martin, P. Verhoeve, A.A. Golubov and H. Rogalla, *Phys. Rev. B* **77**, 014501 (2008) (*Chapter 4 in this thesis*)
106. R. den Hartog, A.A. Golubov, P. Verhoeve, A. Poelaert, D. Martin, A. Peacock, A. van Dordrecht and D.J. Goldie, *Phys.Rev. B* **63**, 214507 (2001)
107. D.D.E. Martin, P. Verhoeve, A. Peacock, A.G. Kozorezov, J.K. Wigmore, H. Rogalla, and R. Venn, *Appl. Phys. Lett.* **88**, 123510 (2006)
108. S. Bandler, R. Brekosky, A. Brown, J. Chervenak, E. Figueroa-Feliciano, F. Finkbeiner, N. Iyomoto, R. Kelly C. Kilbourne, F. Porter, J. Sadleir, S. Smith, *Journ. Of low. Temp.* **151**, 400 (2008)
109. C.A. Mears, S.E. Labov, M. Frank, H. Netel, L.J. Hiller, M.A. Lindeman, D. Chow, A.T. Barfknecht, *IEEE Trans. On Appl. Supercond.* **7**, issue 2, pp. 3415-3418 (1997)
110. P. Verhoeve, N. Rando, J. Verveer, A. Peacock, A. van Dordrecht, P. Videler, M. Bavdaz, D.J. Goldie, T. Lederer, F. Scholze, G. Ulm, R. Venn, *Phys. Rev. B* **53**, 809 (1996)
111. V. Savu, L. Li, A. Mukherjee, C.M. Wilson, L. Frunzio, D.E. Prober, R.J. Schoelkopf, *Nucl. Instr. and Meth.* **520**, 237 (2004)
112. M. Ejrnaes, C. Nappi, R.Cristiano, *Supercond. Sci. Technol.* **18**, 953 (2005)
113. V. Adrianov, L. Filippenko, V.P. Gorkov, V. Koshelets, *Journ. Of low. Temp.* **151**, 287 (2008)
114. V. Samedov, *Journ. Of low. Temp.* **151**, 333 (2008)
115. M. Furlan, E. Kirk, A. Zehnder, *J. Appl. Phys.*, **101**, 054501 (2007).
116. R.A. Hijmering, P. Verhoeve, D.D.E. Martin, I. Jerjen, A.G.Kozorezov, R.Venn, *Journ. Of low. Temp.* **151**, 298 (2008)

## References

---

117. R.A. Hijmering, P. Verhoeve, D.D.E. Martin, A. Peacock, A.G. Kozorezov, R. Venn, *Nucl. Instr. And Meth. A* **559** (2006) 692
118. N. Sullivan, H. Meyer, M. Paalanen (editors), *Proceedings of LTD12*, *J. Low Temp. Phys* **151** (2008)
119. S.J. Smith, C. Whitford, G.W. Fraser, A.D. Holland, D. Goldie, T.J.R. Ashton, R.J. Limpenny, T. Stevenson, *Nucl. Instr. and Meth A*, **520**, 449 (2004)
120. E. Figueroa-Feliciano, J. Chervenak, F. M. Finkbeiner, M. Li, M. A. lindeman, C. K. Stahle, C.M. Stahle, *AIP proc. of LTD 9*, **605**, 239 (2002)
121. B.A. Mazin, M.E. Eckhart, B. Bumble, S. Golwala, P.K. Day, I. Gao, J. Zmuidzinas, *proc. of LTD 12*, *J. Low Temp. Phys.* **151**, 537 (2008)
122. R.A. Hijmering, P. Verhoeve, D.D.E. Martin, A.G. Kozorezov, J.K. Wigmore, R. Venn, P.J. Groot and I. Jerjen, *J. Appl. Phys* **105**, 123906 (2009) (*Chapter 5 in this thesis*)
123. B. Chakraborty, W.E. Pickett, P.B. Allen, *Phys. Rev. B*, **14-8**, 3227 (1976)
124. P. Drude, *Ann. Phys.* **1**, 566, (1900)
125. R. den Hartog, A. Kozorezov, D. Martin, G. Brammertz, P. Verhoeve, A. Peacock, F. Scholze, D.J. Goldie, *AIP proc. of LTD 9*, **605**, 11 (2002)
126. M.L. van den Berg, PhD thesis, Utrecht University, chap. 2 and 6 (1999)
127. M.L. van den Berg, F.B. Kiewiet, M.P. Bruijn, O.J. Luiten, P.A.J. de Korte, J. Martin, R.P. Huebener, *Proc of ASC '98*, *IEEE Trans. Appl. Supercond.* **9**, 2951 (1999)
128. S. Friedrich, M.C. Gaidis, C.M. Wilson, D.E. Prober, A.E. Szymkowiak and S.H. Moseley. *Appl. Phys. Lett.* **71**, 3901 (1997)
129. R.A. Hijmering, A.G. Kozorezov, A.A. Golubov, P. Verhoeve, D.D.E. Martin, J.K. Wigmore and I. Jerjen, *Trans. Appl. Supercond.*, **19**, 1051 (2009)
130. A.G. Kozorezov, A.A. Golubov, J.K. Wigmore, D. Martin, P. Verhoeve, R.A. Hijmering, I. Jerjen, *Phys. Rev. B*, **V78**, 174501, 2008
131. R. Barends, J.J. Baselmans, S.J.C. Yates, J.R. Gao, J.N. Hovenier, T.M. Klapwijk, *Phys. Rev. Lett.* **100**, 257002 (2008)
132. S. Friedrich, P. Lerch, E. Kirk, *Nucl. Instr. And Meth. A* **559**, 4779 (2006)
133. D.E. Prober, J.D. Teufel, L. Frunzio, C.M. Wilson, R.J. Schoelkopf, *Nucl. Instr. And Meth. A* **559**, 676 (2006)
134. T. Peacock, P. Verhoeve, N. Rando, M.A.C. Perryman, B.G. Taylor, P. Jakobsen, *A&A* **127**, 581 (1996)
135. R.W. Romani, A.J. Miller, B. Cabrera, E. Figueroa-Feliciano, *Astrophys. J.* **521**, L153 (1999)
136. D.D.E. Martin, P. Verhoeve, T. Oosterbroek, R.A. Hijmering, T. Peacock, R. Schulz, 2006, *Proc. of SPIE* **6269**, pp. 626900
137. R.A. Hijmering, P. Verhoeve, A.G. Kozorezov, D.D.E. Martin, J.K. Wigmore, I. Jerjen, R. Venn, P.J. Groot, *J. Appl. Phys* **103**, 083914 (2008) (*Chapter 6 in this thesis*) D.D.E. Martin, P. Verhoeve, A. Peacock, A. van Dordrecht, J. Verveer, R.A. Hijmering, *Nucl. Instr. And Meth. A* **520**, 512 (2004)
138. D.D.E. Martin, 2007, PhD thesis, University Twente
139. M.A.C. Perryman, M. Cropper, G. Ramsay, F. Favata, A. Peacock, N. Rando, A. Reynolds, *Monthly Notice of the Royal Astronomical Society* **324**, 899 (2001)
140. J.H.J. de Bruijne, A.P. Reynolds, M.A.C. Perryman, F. Favata, D. Martin, P. Verhoeve, N. Rando, A. Peacock, *Galaxies: The Third Dimension*, *ASP Conf. Series* **282**, 565, (2002)
141. D.D.E. Martin, P. Verhoeve, R.H. den Hartog, J.H.J. de Bruijne, A.P. Reynolds, A. van Dordrecht, J. Verveer, A.J. Peacock, *Proc. of SPIE* **4841**, 805 (2003)

- <sup>142.</sup> M.A.C. Perryman, F. Favata, A. Peacock, N. Rando, B.G. Taylor, *A&A* **346**, 30 (1999)
- <sup>143.</sup> T. Oosterbroek, J.H.J. de Bruijne, D. Martin, P. Verhove, M.A.C. Perryman, C. Erd, R. Schulz, *A&A* **456**, 283 (2006)
- <sup>144.</sup> J.H.J. de Bruijne, A.P. Reynolds, M.A.C. Perryman, A. Peacock, F. Favata, N. Rando, D. Martin, P. Verhove, N. Christlieb, *A&A* **381**, 57 (2002)
- <sup>145.</sup> A.P. Reynolds, J.H.J. de Bruijne, M.A.C. Perryman, A. Peacock, C.M. Bridge, *A&A* **400**, 1209 (2003)
- <sup>146.</sup> R.A. Hijmering, A.G. Kozorezvo, P. Verhove, D.D.E. Martin, J.K. Wigmore, R. Venn, P.J. Groot, *submitted to J. Appl. Phys* (2009) (*Chapter 7 in this thesis*)
- <sup>147.</sup> FITS, Flexible Image Transfer System, <http://fits.gsfc.nasa.gov/>

# Summary

---

Superconducting detectors possess the capability to register the energy, arrival time and position simultaneously of each detected photon and they are being developed as the next generation of photon detectors. Superconducting tunnel junctions (STJs) are sensitive to photon energies ranging from infrared to X-ray. They consist of two superconducting layers, with sizes of several tens of micrometers and thicknesses of several hundreds of nanometres, separated by an insulating barrier of  $\sim 1$ nm thickness. When a superconductor is cooled below its critical temperature the electrons start to form pairs named Cooper pairs. By absorption of energy, for instance from a photon, these Cooper pairs are broken into two quasiparticles which tunnel across the insulating barrier and, under the influence of an applied bias voltage, produce a measurable tunnel current. The binding energy  $2\Delta$  (where  $\Delta$  is the energy gap of the superconductor) of the Cooper pairs is of the order of a meV, which is about 3 orders of magnitude lower than for semiconductors. Because of this low excitation energy the absorption of a single optical photon will generate a considerable number of quasiparticles,  $\sim 1000$ , of which the number is proportional to the absorbed photon energy. This provides the detector with its spectrographic capabilities even at low photon energies. In order to exploit these properties optimally the thermally excited quasiparticle current needs to be suppressed, and one needs to operate these detectors at a temperature  $< 0.1T_c$ , where  $T_c$  is the critical temperature of the superconducting material. For the widely used tantalum this operating temperature is  $\sim 300$ mK. A superconductor with lower energy gap will generate more quasiparticles per unit absorbed energy but since the critical temperature scales with the energy gap it puts heavier constraints on the operating temperature. Arranging the STJs in an array formation and correlating each photon's trigger signal with a GPS receiver for accurate timing produces a spectrographic photon counting imaging detector which provides each detected photon with a  $1\mu\text{s}$  accurate time stamp.

For read out each STJ needs a dedicated electronic readout chain and the number of STJs in the array is limited by the signal wires running from ambient temperature into the cryogenic environment and the volume of the readout electronics. The largest array size used up to date is the S-Cam 3 array which consists of 120 STJs in a  $10 \times 12$  format. In order to overcome the limitation in array size the Distributed Read-Out Imaging Device (DROID) is being developed. The DROID consists of a superconducting absorber strip with a STJ at either side. The photon is absorbed in the absorber strip and the generated quasiparticles diffuse towards the STJs where they tunnel and produce the desired tunnel current. The sum of the two STJ signals is a measure for the absorbed photon energy. The ratio of the tunnelled charges is a measure of absorption position providing the detector with positional sensitivity. The positional sensitivity makes it possible for a single DROID to replace a large number of single STJs using only two signal wires with corresponding readout electronics.

With the S-Cam project the Advanced Studies & Technology Preparation Division of the European Space Agency is developing a series of prototype cameras with STJs as the detection technology to be used as optical photon counting spectrometers for ground based astronomy. After the successful S-Cam 1, S-Cam 2, both based on a  $6 \times 6$  STJ array, and S-Cam 3, based on a  $10 \times 12$  STJ array, the next step is to increase the field of view using DROIDS. In this thesis we present the development of a DROID array for the S-Cam 4 detector.

The DROIDS described in this thesis consist of a pure tantalum absorber with proximised Ta/Al STJs, which have a lower energy gap than the absorber. The lower energy gap produces a potential well. This helps to confine the quasiparticles in the STJ (trapping of quasiparticles) and to prevent them from escaping from the STJ into the absorber, away from the tunnel barrier. The quasiparticles which escape from the STJ can either be lost inside the absorber, which reduces the total signal from the detector, or they can diffuse to the opposite STJ where they add to the tunnel signal. The latter reduces the ratio of the signals from the two STJs thereby degrading the position resolution of the detector. This is important since the position resolution dictates the number of single STJs that can be replaced by a DROID. The added aluminium layer, of which the energy gap is below the energy gap of tantalum ( $\Delta_{\text{Ta}}=700\text{meV}$  and  $\Delta_{\text{Al}}=180\text{meV}$ ), modifies the properties of both materials (Ta and Al) in the STJs. The layer thicknesses are of the order of the coherence length and a constant energy gap is established throughout the bi-layer, the value of which lies in-between the bulk value for the energy gaps of the two materials. Moreover, the quasiparticle energy density of states (DoS) changes compared to the DoS of the pure superconducting material and is different in either material. In the aluminium a broadened peak is present near the energy gap of the bi-layer while in the tantalum layer a broadened peak is present near the bulk value of the energy gap of tantalum with a shoulder towards the energy gap of the bi-layer.

The work in this thesis has started with the continuation of the development of a model which describes the dynamics of the non-equilibrium quasiparticles in a proximised STJ resulting from the absorption of a photon. The algorithms to calculate the model were refined such that they could be used in the BCS limit to describe experimental data from pure aluminium STJs. The main new process which was identified in these devices was the self generation of quasiparticles, quasiparticles which gain enough energy to emit a pair breaking phonon when relaxing and producing additional quasiparticles, in these low gap devices.

Use of this model also showed a different phenomenon which was important for the use of proximised STJs in DROIDS. The change in DoS in proximised STJs is of importance for the trapping efficiency. The excited quasiparticles in a STJ resulting from the absorption of a photon form a stable distribution in energy. Due to the presence of an increased number of states at the energy gap of tantalum in the tantalum layer, a large fraction of the quasiparticles in the STJ will reside at an energy equal to or greater than the energy gap of tantalum. These quasiparticles are free to diffuse into the tantalum absorber, which reduces the trapping efficiency. The fraction of quasiparticles which reside above the energy gap of tantalum, and thus the trapping efficiency, can be influenced with the bias voltage. With each tunnel across the tunnel barrier quasiparticles gain energy equal to  $eV_b$ , with  $V_b$  the applied bias voltage and  $e$  the elementary charge of an electron. This process is counteracted by relaxation of quasiparticles with emission of a phonon with energy equal to the difference of the initial and final energy state of the quasiparticle. The larger the bias voltage the larger the step in energy with each tunnel and the more quasiparticles will reach an energy above the energy gap of tantalum before they emit a phonon and relax.

The presence of the increased DoS near the energy gap of tantalum in the tantalum part of the bilayer also facilitates an extra loss channel in the conversion of photon energy to number of quasiparticles. The final stage of this conversion process consists of high energy quasiparticles which relax and emit high energy phonons. When these phonons' energies are equal to or greater than  $2\Delta$  they will break other Cooper pairs into two quasiparticles. On one side this process is driven by emitting the most energetic phonon and on the other side by occupation of the quasiparticle of the energy level at the maximum of the density of states. In the case of pure superconductors both drive for relaxation towards the energy gap where the maximum in the DoS is located. But for proximized devices this maximum is located near the energy gap of the higher gap material producing increased relaxation towards this energy

## Summary

---

level. One can imagine a quasiparticle which would emit a  $2\Delta$  phonon when it relaxes towards the energy gap but emits a sub- $2\Delta$  phonon when relaxing to the maximum in the density of states near the high gap material energy gap, resulting in a reduced quasiparticle generation efficiency. This could be tested experimentally in DROIDs, which allow a direct comparison of the responsivity of a proximised Ta/Al STJ at the end of the absorber, and the responsivity of the pure tantalum absorber immediately adjacent to the STJ. The reduced quasiparticle yield was confirmed and at least a qualitative agreement between the experimental results and the predicted efficiencies for different STJs was obtained

The spatial resolution is of importance for a DROID because it defines the maximum number of STJs it can replace without losing position sensitivity. Because the position is derived from the signals from the two STJs there is a relation between the spatial resolution and spectral resolution. This relation is given by Kraus for perfect confinement of quasiparticles in the STJ and a generalisation has been made by Jochum which applies to DROIDs with imperfect confinement in the STJs. For long only this relation was used to determine the spatial resolution theoretically from the measured energy resolution. In order to test this relation experimentally we have developed a new technique to measure the spatial resolution directly. In this technique we project a  $10\mu\text{m}$  light spot which we can scan across the DROID to locally illuminate different positions on the DROID. The model as developed by Jochum has been verified.

Although the model from Jochum, and the limit to perfect confinement by Kraus, perfectly described the responsivity, as well as the spatial and spectral resolution of the absorber strip, it is not complete in the description of the physical processes. For instance the processes in the STJs were not taken into account and trapping was described by a so-called trapping rate instead of the gain in energy and relaxation by quasiparticles in the STJs. To get a proper description of the relevant processes we developed a new model for DROIDs with imperfect confinement in the STJs. The model takes into account diffusion of quasiparticles across the absorber and imperfect trapping in the superconducting tunnel junctions via exchange of quasiparticles between absorber and the junction by considering separately the population of quasiparticles above the energy gap of tantalum. It also incorporates diffusion mismatch between STJ and absorber, as well as possible asymmetry between the two junctions and asymmetry between base and top electrodes within each junction. The model was tested against an extended data set of illuminations of DROIDs in varying geometries and under varying experimental conditions. In order to obtain the true responsivity we performed the measurements of the signal using sampling of the current pulses from absorption of optical photons at the output of a charge sensitive preamplifier and deconvolution of the signal. The model accurately describes the obtained dataset.

Finally, a prototype of a S-Cam 4 DROID array has been produced and tested in the S-Cam 3 set-up. The system level test with this array has demonstrated the feasibility of such an array to be used as an imaging spectrometer. Although the responsivity of the array was too low to be used on the telescope, the experience gained together with the already obtained knowledge provides a good understanding of DROID arrays and the production of the S-Cam 4 cryogenic optical photon counting spectrometers fit for ground based astronomy is within reach.



# Samenvatting

---

Supergeleidende detectoren hebben de mogelijkheid om gelijktijdig de energie, aankomsttijd en absorptiepositie van elk gedetecteerd foton te registreren. Daarom worden zij dan ook ontwikkeld als de volgende generatie foton detectoren. Supergeleidende Tunnel Juncties (STJs) zijn gevoelig voor fotonen met een energie variërend van infrarood tot het röntgen gebied. Een STJ bestaat uit twee lagen van supergeleidend materiaal, doorgaands met een afmeting van tientallen micrometers en dikte van een paar honderd nanometer. De twee supergeleidende lagen worden gescheiden door een  $\sim 1$ nm dikke isolerende barrière. Wanneer de temperatuur van een supergeleider lager is dan zijn kritische temperatuur beginnen de elektronen paren te vormen, genaamd Cooper paren. De absorptie van energie, van bijvoorbeeld een foton, breekt deze Cooper paren in twee quasideeltjes. Deze quasideeltjes tunnelen door de isolerende barrière en, onder de invloed van een aangelegde bias spanning, zal dit een meetbare stroom produceren. De bindingsenergie  $2\Delta$  (waarbij  $\Delta$  het energiegat van de supergeleider is) van een Cooper paar is van de orde van een meV, wat ongeveer 3 orders van grootte lager is dan bij halfgeleiders en de absorptie van één enkel optisch foton produceert een aanzienlijk aantal quasideeltjes,  $\sim 1000$ . Door de lage bindingsenergie is het aantal quasideeltjes dat geproduceerd wordt door de absorptie van een foton evenredig aan de geabsorbeerde fotonenergie. Dit geeft de detector zijn spectrografische mogelijkheden, zelfs bij fotonen met een lage energie. Om deze detectoren optimaal te kunnen gebruiken moet stroom van thermisch opgewekte quasideeltjes voldoende worden gereduceerd. Hiervoor moet de temperatuur waarbij de STJs gebruikt worden gelijk zijn aan of kleiner zijn dan  $0.1T_c$ , met  $T_c$  (kritische temperatuur) de temperatuur waarbij de supergeleider van normaal geleidend naar supergeleidend verandert. Het veel gebruikte tantaal moet bijvoorbeeld worden gekoeld tot een temperatuur van  $\sim 300$ mK. Bij een supergeleider met een lagere bindingsenergie zullen er ook meer quasideeltjes worden geproduceerd per eenheid geabsorbeerde energie. Maar aangezien de overgangstemperatuur ( $T_c$ ) schaal met de bindingsenergie zullen deze materialen ook gekoeld moeten worden tot een lagere temperatuur wat zware beperkingen op de meetopstelling veroorzaakt. Wanneer de STJs in een matrix worden geplaatst en het signaal geproduceerd door de absorptie van een foton wordt gekoppeld aan een GPS ontvanger, voor nauwkeurige tijds bepaling, krijgt men een beeldvormende detector welke elk gedetecteerd foton labelt met zijn energie, positie en een  $1\mu$ s nauwkeurig tijdstip.

Voor de uitlezing heeft elke STJ een individuele signaaldraad en bijbehorende electronicaketen nodig. Dit levert een beperking op het aantal STJs op waaruit een matrix kan bestaan en hiermee in de afmeting van de plaatschaal. De beperking wordt veroorzaakt door het aantal signaaldraden dat van kamertemperatuur naar de cryogene omgeving loopt en het volume van de uitleeselectronica. De grootste matrix die tot op heden is gebruikt is die van de S-Cam 3 detector. Deze bestaat uit 120 STJs in een  $10 \times 12$  formatie. Om de beperking in de afmeting van de plaatschaal te overwinnen wordt het Distributed Read-Out Imaging Device (DROID) ontwikkeld. De DROID bestaat uit een supergeleidende absorberende strip met een STJ aan beide uiteinden. Het foton wordt geabsorbeerd in de strip en de geproduceerde quasideeltjes verspreiden zich door diffusie naar de STJs waar zij tunnelen en de gewenste tunnelstroom veroorzaken. Het totaal van de getunnelde lading van de twee STJs is een maatstaf voor de geabsorbeerde fotonenergie. De verhouding van de getunnelde lading in



beide STJs is een maatstaf voor de absorptiepositie. Hierdoor geeft de detector positionele informatie en dit maakt het mogelijk voor een enkele DROID om een aantal STJs te vervangen, terwijl er toch maar twee signaal draden en bijbehorende uitlees elektronica gebruikt worden.

Met het S-Cam project ontwikkelt de Advanced Studies & Technology Preparation Division van het Europese ruimtevaart agentschap (ESA) een reeks van prototype camera's, waarbij STJs als de detectie technologie gebruikt wordt. Deze detectoren zijn bedoeld om als optische foton-tellende spectrometers gebruikt te worden voor astronomie vanaf de grond. Na het succes van S-Cam 1, S-Cam 2, beide gebaseerd op een 6x6 STJ matrix, en S-Cam 3, gebaseerd op een 10x12 STJ matrix, is het vergroten van de plaatsaal door gebruik te maken van DROIDS de volgende stap. In dit proefschrift presenteren wij de ontwikkeling van een DROID matrix voor de S-Cam 4 detector.

De DROIDS die gebruikt werden voor dit proefschrift bestaan uit een absorberende strip van zuiver tantaal met STJs bestaande uit geproximiseerde Ta/Al, met een lager energiegat dan de absorberende strip. Het lagere energiegat van de STJs resulteert in een potentiaal put waarin de quasideeltjes gevangen worden. Dit voorkomt dat quasideeltjes ontsnappen uit de STJs naar de absorberende strip, weg van de tunnel barrière. Quasideeltjes die uit de STJs ontsnappen, kunnen verloren gaan in de absorberende strip, hetgeen het totale signaal van de detector vermindert. Zij kunnen ook diffunderen naar de tegenovergestelde STJ waar zij signaal toevoegen aan het tunnelsignaal van die STJ. Dit laatste vermindert de verhouding tussen de signalen van twee STJs en daarmee wordt de positie resolutie van de detector aangetast. Aangezien de positie resolutie het aantal STJs definieert wat een enkele DROID kan vervangen, is deze van groot belang. Door het proximatie effect beïnvloeden de aanwezigheid van de aluminium laag, waarvan het energiegat lager is dan het energiegat van tantaal ( $\Delta_{\text{Ta}}=700\text{meV}$  en  $\Delta_{\text{Al}}=180\text{meV}$ ), en de tantaal laag elkaar wederzijds. De diktes van de individuele lagen zijn in de orde van de coherentie lengte van de materialen waardoor in de gehele dubbellaag een constant energiegat ontstaat waarvan de waarde tussen de waarden van de energiegapen van de individuele materialen in ligt. Daarnaast verandert de dichtheid van energie toestanden van de quasideeltjes (Density of States, DoS) ten opzichte van de dichtheid van energie toestanden van het zuivere supergeleidende materiaal. De dichtheid van energie toestanden is in de twee materialen van de Ta/Al STJ ook verschillend in vorm. In het aluminium is een verbrede piek aanwezig bij het energiegat van de dubbellaag. In de tantaal laag is ook een verbrede piek aanwezig maar bij de waarde van het energiegat van tantaal. Aan de lagere energie zijde van deze verbrede piek is een schouder welke reikt tot het energiegat van de dubbellaag.

Het werk in dit proefschrift is gestart met het voortzetten van een model dat de dynamiek beschrijft van een systeem van quasiparticles in een geproximiseerde STJ, welke geëxciteerd zijn als gevolg van de absorptie van een foton. De software algoritmes waarmee het model werd uitgerekend zijn verfijnd voor de toepassing in de BCS limiet zodat de resultaten van een STJ gemaakt van zuiver aluminium gemodelleerd konden worden. Het belangrijkste proces wat hierbij gemodelleerd werd is de zelfgeneratie van quasideeltjes in deze STJs met een laag energiegat. Het zelfgeneratie proces bestaat uit quasideeltjes die tijdens het tunnelen genoeg in energie niveau stijgen zodat ze, als zij terug vallen in energie, een fonon uitzenden dat een Cooper paar kan verbreken en zo twee additionele quasideeltjes creëren.

Dit model toonde ook een ander fenomeen aan dat belangrijk is bij het gebruik van geproximiseerde STJs in DROIDS. De verandering in energietoestandsdichtheid bij geproximiseerde STJs is van belang voor het rendement waarmee quasideeltjes in de STJ worden opgesloten. De quasideeltjes in een STJ welke geëxciteerd zijn als gevolg van de absorptie van een foton vormen een stabiele distributie in energie. Door de aanwezigheid van het verhoogd aantal energietoestanden in de tantaal laag bij het energiegat van tantaal zal een

groot gedeelte van de quasideeltjes in STJ zich in een energie toestand bevinden welke gelijk is aan of groter is dan het energiegat van tantaal. Deze quasideeltjes zijn vrij om de absorberende tantaal strip in te diffunderen en het opsluit rendement is verminderd. Boven op de vermindering van het opsluit rendement van quasideeltjes in de STJ door de geometrie van de twee lagen kan deze ook worden beïnvloed door de bias spanning over de tunnel junctie. Met elke tunnel door de tunnelbarrière verhoogt de energietoestand van een quasideeltje met een energie gelijk aan  $eV_b$ , waarbij  $V_b$  de spanning over de tunnel junctie en  $e$  de elementaire lading van een elektron is. Dit proces wordt tegengewerkt door het terugvallen in energie toestand van quasideeltjes waarbij zij een fonon uitzenden met een energie die gelijk is aan het verschil tussen de oorspronkelijke energietoestand en de uiteindelijke energie toestand van het quasideeltje. Als er een grotere spanning over de tunnel junctie wordt gezet neemt bij elke tunnel de energietoestand van een quasideeltje met een grotere stap toe. Quasideeltjes zullen dus minder stappen nodig hebben om een energietoestand boven het energiegat van tantaal te bereiken en meer quasideeltjes zullen dit volbrengen voordat zij een fonon uitzenden en terugvallen in energie.

De aanwezigheid van de verbrede piek in de dichtheid van energietoestanden in het tantaal versterkt ook een extra verlies kanaal in het proces waarbij de energie van het foton wordt omgezet in een groot aantal quasideeltjes. Het laatste stadium van dit omzettingsproces bestaat uit het terugvallen in energie van hoog energetische quasideeltjes onder het uitzenden van een energetisch fonon. Wanneer de energie van dit fonon groter is dan de bindingsenergie van een Cooper paar zal er een Cooper paar gebroken worden door absorptie van dit fonon. Enerzijds wordt dit proces gedreven door een voorkeur voor het uitzenden van het meest energetische fonon en anderzijds door een voorkeur voor het bezetten van het energieniveau met de hoogste energietoestandsdichtheid. Bij zuivere supergeleiders resulteren deze beide drijfveren tot terugval tot het energieniveau bij het energiegat aangezien dit het energieniveau is met de laagst mogelijke energie, waar zich ook de hoogste dichtheid van energietoestanden bevindt. Bij geproximiseerde Ta/Al supergeleiders ligt het energieniveau met de hoogste energietoestand dichtheid bij het energiegat van tantaal. Dit veroorzaakt een verhoogde terugval naar dit energieniveau. Men kan een quasideeltje veronderstellen welke een  $2\Delta$  fonon zou uitzenden wanneer het zou terugvallen naar het energiegat van de dubbellaag. Maar wanneer deze zou terugvallen naar de energie toestand met de hoogste dichtheid, gelegen bij het energiegat van tantaal, zal het een sub- $2\Delta$  fonon uitzenden waarmee de productie van quasideeltjes vermindert. Dit kon experimenteel geverifieerd worden met behulp van DROIDS. Met DROIDS kan de responsiviteit van de geproximiseerde TA/Al STJ aan het eind van de absorberende strip direct vergeleken worden met de responsiviteit van de zuivere absorberende strip net naast de STJ waardoor dit effect geverifieerd kon worden. De vermindering in de creatie van quasideeltjes was aangetoond en een kwantitatieve overeenkomst tussen de experimentele resultaten en de voorspelde efficiëntie voor de verschillende STJs was verkregen.

De spatiële resolutie van een DROID is van belang omdat deze het maximum aantal STJs bepaalt dat de DROID kan vervangen zonder dat er positie gevoeligheid verloren gaat. Omdat de positie wordt bepaald uit de signalen van de twee STJs is er een directe relatie tussen de spectrale resolutie en de spatiële resolutie. Voor DROIDS met perfecte opsluiting van quasideeltjes in de STJ is deze relatie gegeven door Kraus. Jochum heeft dit model zodanig aangepast dat het ook van toepassing is op DROIDS met imperfecte opsluiting in de STJs. Doorgaans wordt alleen deze theoretische relatie gebruikt om de spatiële resolutie van DROIDS te bepalen met gebruik van de gemeten spectrale resolutie. Om deze relatie te testen hebben wij een nieuwe techniek ontwikkeld waarmee de spatiële resolutie direct gemeten kan worden. Hierbij projecteren we een  $10\mu\text{m}$  grote lichtvlek die we over de DROID kunnen

verschuiven om zo verschillende posities lokaal te kunnen belichten. Hiermee is het model van Jochum geverifieerd.

Hoewel het model van Jochum, en de limiet met perfecte opsluiting van Kraus, de responsiviteit, spectrale en positionele resolutie van een DROID perfect beschrijft is het niet compleet in de beschrijving van de onderliggende fysische processen. Bijvoorbeeld de processen in de STJ zijn buiten beschouwing gelaten en het opsluiten van de quasideeltjes in de STJs is beschreven door een snelheid waarmee de quasideeltjes opgesloten worden in plaats van een beschrijving van de toename in energie en relaxatie van quasideeltjes in de STJs. Om een juiste beschrijving van de verschillende relevante processen te krijgen hebben we een nieuw model ontwikkeld voor DROIDS met imperfecte opsluiting van quasideeltjes in de STJs. Het model beschrijft de diffusie van de quasideeltjes door de absorberende strip en de imperfecte opsluiting van quasideeltjes in de STJs. Dit laatste gebeurt door middel van het uitwisselen van quasideeltjes tussen de absorberende strip en STJ waarbij met name de extra populatie van quasideeltjes met een energie toestand boven het energiegat van tantaal in acht wordt genomen. Het model neemt ook het mogelijke verschil in diffusiesnelheid tussen de STJ en absorberende strip, de mogelijke asymmetrie tussen de STJs en de mogelijke asymmetrie tussen de twee elektrodes van een enkele STJ in acht. Om dit model te testen hebben we een grote experimentele dataset geproduceerd waarbij DROIDS met verschillende geometrie zijn belicht onder verschillende experimentele omstandigheden. Om de responsiviteit van de DROIDS zo nauwkeurig mogelijk te meten hebben we de daadwerkelijke stroom pulsen aan de uitgang van de voorversterker gemeten en deze gedeconvolveerd. De gehele dataset wordt goed beschreven door het theoretische model.

Tenslotte is er een prototype van een S-Cam 4 DROID matrix geproduceerd en getest in de S-Cam 3 opstelling. Deze tests gaven aan dat dit soort detector met succes gebruikt kan worden als beeldvormende spectrograaf. Hoewel de responsiviteit van deze DROID matrix te laag was om gebruikt te worden aan een telescoop, heeft de ervaring samen met de verkregen kennis een goed inzicht gegeven en ligt de productie van de S-Cam 4 cryogene optische foton tellende spectrometer voor astronomische doeleinden binnen bereik

# Acknowledgements

---

The research, preparation and finalisation of this thesis have been possible thanks to a lot of people both personal and professional.

First I like to thank my parents, family and friends whom I neglected too much to pursue this research. However, they understood and I had their fullest support. And I like to thank all people at ESA and RUN who were interested in my PhD research and gave their support.

I like to thank the technical people from SCI-PAI for helping with all the technical problems. From bending clamps, making electronics schematics, soldering wires to upgrading and changing complete cryogenic systems. Especially I want to mention Jacques Verveer who shared his knowledge on cryogenic systems with me and Axel van Dordrecht who shared his electronic expertise. Georges Sirbi with whom I enjoyed sharing an office and working with and who was a good source for all sorts of software. Bart Butler who I enjoyed working with on cryogenic systems and who helped me with keeping my motorcycle and car on the road.

I like to thank Hans Smit for the software he developed and talks on music, books and movies. Roland den Hartog for sharing our birthday, good advice on numerical methods for the simulations and long discussions on topics varying from music, books or movies to global warming, economy or politics and of course also some work relating topics. We did not always share our opinions but that just made the discussions more interesting. I like to thank Alan Owens who, together with his wife Cecilia Nelson, gave the best parties. Thanks to the memorable red dwarf nights I developed a fine taste for British humor programs and of course the fine English ale. But also thanks for the good talks over tea. And I like to thank Alex Jeanes, Tina Jeanes and Diane Barton for making me a part of the Aurora team, arranging a good working environment and of course the delicious and wonderful Aurora dinners.

I like to thank Rob Venn for great work on producing the devices used in this research and explaining the methods used. Guy Brammertz for the help and the research he performed which I could follow up. Christian Erd for the help with analyses several methods. Iwan Jerjen for the discussions and cooperation. Alex Golubov for the discussions we had on STJs and DROIDS and theoretical explanations. Keith Wigmore for the discussions we had on STJs and DROIDS and reading my papers with a reviewer's eye. This was always a tough challenge from which I learned a lot.

I would like to thank my promotor Paul Groot for the supervision from Nijmegen, for making the time and effort to visit ESA to keep everything in order. I like to thank Alex Kozorezov for his theoretical supervisions, the great theoretical descriptions and the patience to explain them to me. Next to the theoretical explanations you also explained many other physical processes and showed me a different point of view on many subjects. For the guidance at ESA I like to thank Peter Verhoeve and for sharing his knowledge on STJs and DROIDS and guiding me in the different skills needed as a scientist. And also for having the patience to read through all my articles, correcting the many, many errors. And I like to thank Didier Martin for the faith in me for doing the research and making it possible to perform my PhD research at ESA. Next to the scientific research I got the chance to learn much more and evolve further than I hoped to. But also thanks for always having the time to explain all sorts of things.

And last but not least my beloved Celesta who had to endure all the stress, late night puzzling on problems, crankiness and time away from home. But you always stood behind me to cheer me up and supported me fully. Thank you all very, very much!



## List of Publications

---

### First Author:

- Imaging spectroscopy with Ta/Al DROIDS: Performance for different Al trapping layer thicknesses, R.A. Hijmering, P. Verhoeve, D.D.E. Martin, A. Peacock, A.G. Kozorezov, *Nucl. Instrum. Methods Phys. A*, 559, 689 (2006)
- Imaging spectroscopy with Ta/Al DROIDS: Performance for different absorber lengths, R.A. Hijmering, P. Verhoeve, D.D.E. Martin, A. Peacock, A.G. Kozorezov, R. Venn, *Nucl. Instrum. Methods Phys.*, 559, 692 (2006)
- Imaging spectroscopy with Ta/Al DROIDS: performance for different geometries, R.A. Hijmering, I. Jerjen, P. Verhoeve, D.D.E. Martin, A. Peacock, A.G. Kozorezov, R. Venn, *Proc. of SPIE*, 6276, 47 (2006)
- Direct position resolution measurement with DROIDS at optical wavelengths, R.A. Hijmering, P. Verhoeve, D.D.E. Martin, I. Jerjen, A.G. Kozorezov, R. Venn, *Low Temp. Phys.*, 151, 298 (2008)
- Position dependent spatial and spectral resolution measurement of distributed read out superconducting imaging detectors, R.A. Hijmering, P. Verhoeve, A.G. Kozorezov, D.D.E. Martin, J.K. Wigmore, I. Jerjen, R. Venn, P.J. Groot, *J. Appl. Phys.*, 103, 083914 (2008)
- Modelling of local trapping states in superconducting tunnel junctions with Kondo impurities, R.A. Hijmering, A.G. Kozorezov, A.A. Golubov, P. Verhoeve, D.D.E. Martin, J.K. Wigmore, I. Jerjen, *trans. Sup. Cond.*, 19, 3, 423 (2009)
- Efficiency of quasiparticle creation in proximised superconducting photon detectors, R.A. Hijmering, P. Verhoeve, D.D.E. Martin, A.G. Kozorezov, J.K. Wigmore, R. Venn, P.J. Groot, I. Jerjen, *J. Appl. Phys.*, 105, 123906 (2009)
- Experimental and theoretical response of Distributed Read Out Imaging Devices with imperfect charge confinement, R.A. Hijmering, A.G. Kozorezov, P. Verhoeve, D.D.E. Martin, J.K. Wigmore, R. Venn, P.J. Groot, *submitted to J. Appl. Phys.*(2009)
- First results of cryogenic photon counting imaging spectrometer with use of a DROID array, R.A. Hijmering, P. Verhoeve, D.D.E. Martin, R. Venn, P.J. Groot, *submitted to A&A* (2009)
- Model on DROID response with imperfect trapping tested on experimental results, R.A. Hijmering, A.G. Kozorezov, P. Verhoeve, D.D.E. Martin, J.K. Wigmore, R. Venn, *accepted for publication in Proc. of LTD-13* (2009)
- First results on the imaging capabilities of a DROID array in the UV/VIS, R.A. Hijmering, P. Verhoeve, D.D.E. Martin, R. Venn, P.J. Groot, *accepted for publication in Proc. of LTD-13* (2009)

### Second Author:

- Superconducting Tunnel Junction detector for soft X-ray astrophysics, P. Verhoeve, R.A. Hijmering, D.D.E. Martin, I. Jerjen, A. Peacock, R. Venn, *Proc of SPIE*, 6276, 13 (2006)
- Evaluation of a CdZnTa pixel array for X- and  $\gamma$ -ray spectroscopic imaging, F. Quarati, R.A. Hijmering, G. Maehlum, A. Owens, E. Welter, *Nucl. Instrum. Methods Phys. A*, 568, 446 (2006)
- Dynamics of nonequilibrium quasiparticles in narrow-gap superconducting tunnel junctions, A.G. Kozorezov, R.A. Hijmering, G. Brammertz, J.K. Wigmore, A. Peacock, D. Martin, P. Verhoeve, A.A. Golubov, H. Rogella, *Phys. Rev. B*, 77, 014501 (2008)
- Determination of the photon impact position within a DROID, I. Jerjen, R.A. Hijmering, P. Verhoeve, D.D.E. Martin, A.G. Kozorezov, R. Venn, *Low Temp. Phys.*, 151, 322 (2008)

### Co-Author:

- Photon counting cryogenic detectors for ground-based and space telescopes, P. Verhoeve, D. Martin, G. Brammertz, R.A. Hijmering, A. Peacock, *Proc. of conf. space Opt.*, 781 (2004)
- A 12x10 pixels superconducting tunnel junction array based spectro-photometer for optical astronomy, D.D.E. Martin, P. Verhoeve, A. Peacock, A. van Dordrecht, J. Verveer, R. Hijmering, *Nucl. Instr. Meth. A*, 520, 512 (2004)
- Accurate time-resolved optical photospectroscopy with superconducting tunnel junction arrays, D.D.E. Martin, P. Verhoeve, T. Oosterbroek, R. Hijmering, A. Peacock, R. Schulz, *proc. of SPIE*, 6962, 22 (2006)
- Quasiparticle dynamics in superconducting tunnel junctions, A.G. Kozorezov, G. Brammertz, R.A. Hijmering, J.K. Wigmore, A. Peacock, D. Martin, P. Verhoeve, A.A. Golubov, H. Rogella, *Nucl. Instr. Meth. A*, 559, 695 (2006)
- S-Cam 3: Optical astronomy with a STJ-based imaging spectrophotometer, P. Verhoeve, D.D.E. Martin, R.A. Hijmering, J. Verveer, A. van Dordrecht, G. Sirbi, T. Oosterbroek, A. Peacock, *Nucl. Instr. Meth. A*, 559, 598 (2006)
- Electron-phonon interaction in a superconductor with Kondo scattering, A.G. Kozorezov, A.A. Golubov, J.K. Wigmore, D. Martin, P. Verhoeve, R.A. Hijmering, *EPL*, 86, 47009 (2009)
- Inelastic scattering of quasiparticles in a superconductor with magnetic impurities, Kozorezov, A.A. Golubov, J.K. Wigmore, D. Martin, P. Verhoeve, R.A. Hijmering, I. Jerjen, *Phys. Rev. B*, 78, 174501 (2008)
- The effect of magnetic impurities on the response of superconducting photon detectors, A.G. Kozorezov, A.A. Golubov, J.K. Wigmore, D. Martin, P. Verhoeve, R.A. Hijmering, I. Jerjen, *trans. Sup. Cond.*, 19, 3, 440 (2009)

# Curriculum Vitae

---

Richard Hijmering was born on 7 September 1978 in Boxmeer, the Netherlands, where he spent the first years of his life. At a later age he moved to Nijmegen where he attended Atheneum at the Stedelijke Scholen gemeenschap Nijmegen.

In 1997 Richard went to the Catholic University Nijmegen (KUN, now the Radboud University Nijmegen, RUN) where he studied Applied Physics. In his final year at the university Richard spent half a year at the telescopes of the Isaac Newton Group (ING) in La Palma, Spain, for his Master Thesis Project. He worked in the detector group, under supervision of Simon Tulloch, on quality control measurements of the different CCD detectors present at ING. During his stay at ING Richard came in contact with the S-Cam project from the European Space Agency (ESA), who developed a cryogenic photon counting imaging spectrograph for UV/VIS based on Superconducting Tunnel Junctions (STJs). He was able to arrange that he could spend 6 month at ESTEC/ESA with this project for the final part of his Maser Thesis Project. Richard worked on the data processing part of the project in support of the astronomers under supervision of, Dr. Jos de Bruijne and Prof. Michael Perryman. He developed a quick look tool to determine the quality of the obtained data directly after the observation on the telescope.

After his graduation under supervision of Prof. Jan Kuijpers, at the newly founded astronomy department of the KUN, Richard got the opportunity to continue his work on the S-Cam 3 detector at ESA and perform a PhD research in the development of S-Cam 4, the next prototype in the S-Cam series using DROIDS to increase the field of view, under supervision of Dr. Peter Verhoeve and Dr. Didier Martin. The PhD research was in cooperation with the RUN with Prof. Paul Groot as promotor and this thesis is the result of this research.



The printing of this book was sponsored by:



The research described in this thesis was performed in the laboratories of the Advanced Studies & Technology Preparation Division within the Directorate of Science & Robotic Exploration of the European Space Agency in Noordwijk, The Netherlands.

